THESE DE DOCTORAT DE

L'ECOLE NATIONALE SUPERIEURE
DE TECHNIQUES AVANCEES BRETAGNE

ECOLE DOCTORALE N° 648
Sciences pour l'Ingénieur et le Numérique
Spécialité : Mécanique des Solides, des Matériaux, des Structures et des Surfaces

Par

Laure CIVIER

Characterization and modelling of the fatigue and durability of polyamide mooring lines for offshore floating wind turbines

Thèse présentée et soutenue le 28/11/2023 à l'IFREMER, Plouzané
Unité de recherche : Institut de Recherche Dupuy de Lôme - UMR CNRS 6027

Rapporteurs avant soutenance :

Emmanuelle VIDAL-SALLE   Professeur des universités, LamCoS, INSA Lyon
Laurent ORGEAS   Directeur de recherche CNRS, Univ. Grenoble Alpes - CNRS - Grenoble INP

Composition du Jury :

Président :
    Samuel Forest   Directeur de Recherche CNRS, Centre des Matériaux, Mines ParisTech
Examinateurs :
    Emmanuelle Vidal-Sallé   Professeur des universités, LamCoS, INSA Lyon
    Laurent Orgéas   Directeur de recherche CNRS, Univ. Grenoble Alpes
    Damien Durville   Chargé de recherche CNRS, LMPS, Paris-Saclay
    Alba Marcellan   Maître de conférences, SIMM, Sorbonne Université
Dir. de thèse :
    Yann Marco   Professeur des universités, IRDL, ENSTA Bretagne, Brest
Co-dir. de thèse :
    Peter Davies   Dr Ingénieur. HDR, Laboratoire SMASH, IFREMER, Brest
Encadrement. de thèse :
    Guilhem Bles   Maitre de conférences, IRDL, ENSTA Bretagne, Brest

Invité(s)
    Guillaume Damblans   Expert en interactions fluide-structure, France Energies Marines, Plouzané

Remerciements / Acknowledgements

Table of Contents

List of Figures

List of Tables

List of Symbols and Abbreviations

PA6	Polyamide 6 (or nylon 6)	SEM	Scanning electrons microscopy
HMPE	High modulus polyethylene	DSC	Dynamic scanning calorimetry
PET	Polyester terephthalate	T_f	Melting temperature
MRE	Marine renewable energy	T_g	Glass transition temperature
FOWT	Floating Offshore Wind Turbine	S-N curve	Stress-Number of cycles curve
4T sub-rope sample	Sub-rope with a minimal breaking load of 40 kN	W_h	Hysteresis energy
7T sub-rope sample	Sub-rope with a minimal breaking load of 70 kN	T	Temperature
MBL	Minimal breaking load	Δ (chapter 5)	Intrinsic dissipation
tex	g/km (Unity for textile)	Δ^*	Global dissipation per cycle
BI procedure	Bedding-in procedure	θ	Mean temperature variation
POLYAMOOR law	1D rheological constitutive law	f	frequency
L	Length	$\tilde{F}$	deformation gradient tensor
L_0	Initial Gauge length	$\tilde{R}$	Proper rotation
D	Diameter	$\tilde{U}$	Pure strain
α	Twist/lay angle	$\tilde{D}$	tensor of the rate of strain or stretching tensor
ε	Strain	$\tilde{L}$	the gradient of the velocity of the deformation
ε_{log}	Logarithmic strain	J	Change of volume
ε_e	Elastic strain	$\tilde{S}$	the second stress tensor of Piola-Kirchhoff
ε_v	Viscous strain	ψ	Specific free energy
ε_p	Plastic strain	s	entropy
ε_{FRB}	Fully relaxed behaviour strain	φ_1 (chapter 6)	Intrinsic dissipation
$\dot{\varepsilon}$	Strain rate	FiBuLa law	Fibre Bundle Law
Σ	Specific Stress in N/tex	$\widehat{LnU_{ab}}$	Transversal shear strain invariant in the FiBuLa law
Σ_2	Time-independent specific stress	$\tilde{\varepsilon}_\delta$	Axial shear strain invariant in the FiBuLa law
Σ_v	Viscous (Time-dependent) specific stress	LnU_c	Axial elongation strain invariant in the FiBuLa law
E	Young modulus	$\ln J$	Change-of-volume invariant in the FiBuLa law
E_{inst}	Instantaneous modulus	W_a	Energy potential for a strain mode
M_{FRB}	Fully relaxed behaviour modulus	Z-twist	a clockwise twist
E_s	Secant modulus	S-twist	a counter-clockwise twist
ρ_t	Density kg/m³	A	Logarithmic creep rate
$\bar{\bar{\rho}}_t$	Linear density kg/m	ε_c	Creep strain
$\tilde{T}$	The Cauchy Stress tensor	ε_r	Recovery strain
F	Force	TS/TRS	Total strain/Total recovered strain
τ	Characteristic time	IS/IRS	Instantaneous strain /Instantaneous recovered strain
c	Specific heat	VS/VRS	Viscous strain/ Viscous recovered strain

Introduction

Offshore wind is well established in Europe with the largest operational wind farms for both fixed and floating foundation technologies (Offshore Wind Europe, 2021). There is currently 28 GW of grid connected capacity and 123 offshore windfarms in 12 European Countries. The target ambitions of the European Government are to deliver up to 160 GW of wind capacity by 2030 (Offshore Wind Europe, 2021). Furthermore, The European Green Deal target is to make Europe climate neutral (no net emissions of greenhouse gases) by 2050. Hence, the development of this technology is essential and research is needed to allow reductions of wind farm installation costs. In France, the first three Mediterranean floating wind turbines are in construction and are to be installed in the year 2024 by SBM. The proposed technology is a tension leg platform (TLP), historically used in the oil & gas production, with low motion. Also, the pilot project, FLOATGEN, was installed at the SEM-REV Atlantic site in 2018 and proposes a mooring system using 6 polyamide mooring lines. The number of projects is increasing and turbine manufacturers develop a range of models, mooring systems and materials for different wind and buoyancy conditions (Heiberg et al., 2021). Figure 0.1 represents the four main technologies proposed for the floating wind market (Amaral, 2020):

- Spar Platform: a large vertical buoy cylinder with high density material that increases the stability.
- Tension-leg platform: vertically moored floating structure for which no motion is allowed.
- Semi-submersible platform: a floating structure characterized by a large deck. The stiffness will depend on the buoyancy and on the mooring system.
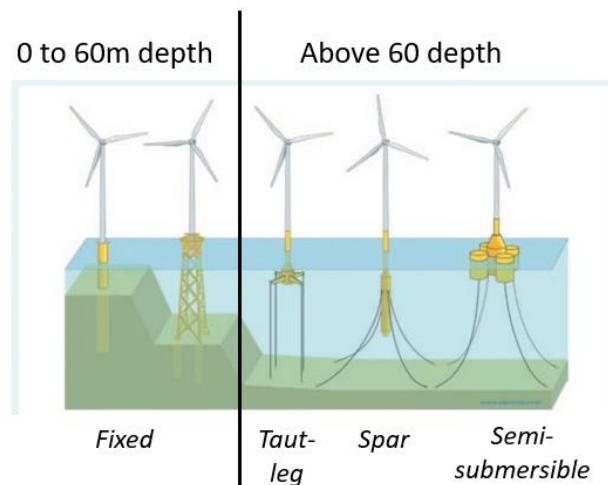
Figure 0.1 - Common fixed and floating offshore wind structure designs (University of Strathclyde, 2019)

Two main types of mooring systems are associated with these technologies (Woellwarth, 2020):

- Tension leg system where the mooring lines are composed of a stiff material (i.e chain) and are under high tension loads. No motion of the floater is allowed.
- Spread mooring systems with catenary, semi-taut, or taut-lines are used for mooring semi-submersible and spar structures. The lines can be composed of chain or synthetic fibres such as polyester or polyamide 6. The chosen materials will strongly influence the design of the rest of the floating system, hence, its cost.

There is a need to accelerate the delivery of cost-effective solutions. This requires innovative mooring solutions and improved the knowledge of failure modes, prevention and monitoring.

Offshore floating wind turbines will be located in exposed sites with significant environmental loading due to waves and wind. They will require mooring lines that maintain the floater position and withstand the environmental loads (Chailleux & Davies, 2003; Flory, Banfield, et al., 2007). Synthetic fibre ropes have become extremely attractive as an alternative to steel chain and wire ropes due to their light weight, easier handling for installation and as they offer the possibility to reduce the overall footprint by using semi-taut to taut mooring arrangements. The high compliance and viscosity of synthetic ropes will lower the line tension and provide damping. Polyamide 6 (PA6) fibres are well-suited for this type of application in shallow water thanks to their low stiffness, good tensile strength and their viscous behaviour. Polyester mooring lines could be used but they are too stiff and don't damp shock impacts and loadings. Polyamide 6 ropes are already used in other marine applications but their visco-elasto-plastic behaviour is not fully understood, and they are limited to temporary applications such as offloading operations or harbour berthing. This limitation is due to an insufficient lifetime for permanent applications and ropes must be renewed every two years. The mooring lines will be under tension throughout their service life and subjected to cyclic loading due to the waves and the movements of the platform. Hence, they should show durability in terms of creep, fatigue life and ageing.

Recent research suggests that an optimized rope architecture of polyamide rope and the use of appropriate internal coating allow fatigue lifetimes higher than the operation life of an offshore wind turbine to be reached (Banfield & Ridge, 2017; Chevillotte, 2020). Bureau Veritas and DNV are currently working to assess the feasibility and robustness of polyamide rope for long-term floating wind turbine moorings. Several test campaigns for polyamide ropes have been performed by developers and rope manufacturers (Heiberg et al., 2021). Key aspects of polyamide rope behaviour are still being investigated; the present study is part of a project, called MONAMOOR, which was proposed to extend the knowledge on the complex behaviour of polyamide 6 ropes in order to improve the reliability of such mooring lines. This project is piloted by France Energies Marines. It is the direct continuation of a previous project, POLYAMOOR, which started investigating some key R&D challenges; Yoan Chevillotte's PhD was part of that project (Chevillotte, 2020).

The first chapter of this thesis proposes an introduction to synthetic fibre ropes (history, construction, type of fibres). Then, it focuses on the mechanical behaviour of synthetic fibres and fibres assemblies and, more specifically, of polyamide 6 fibre ropes. Several studies on their complex responses, both due to the viscoelasticity of the material filaments, and on the influence on the construction and scale, are presented. The current knowledge on the creep and recovery behaviour is then described. This is followed by a presentation of the knowledge of their fatigue behaviour. Finally, a review on the different modelling approaches proposed in the literature for synthetic ropes is presented. This chapter concludes with a description of the context and motivations of the present study.

The second chapter is devoted to the presentation of the materials and the experimental methods used in this study.

Then chapter 3 of this thesis is devoted to the first key R&D challenge which is the description and understanding of the elasto-visco-plastic behaviour of rope made of polyamide 6 fibres. It presents the 1D constitutive law developed by Chevillotte (Chevillotte, 2020) during the POLYAMOOR project and proposes new identifications and validations of this law. A specific

investigation of a sub-rope after long term creep is performed using the identification of the parameters of the law.

Chapter 4 treats the long term creep and recovery behaviour of polyamide 6 sub-ropes. This behaviour is complicated to investigate on sub-ropes as the experimental set-ups for this scale of tests are rare. They must allow a constant load to be maintained for long periods of time.

Chapter 5 focuses on a fatigue investigation. The fatigue lifetime of sub-ropes is studied by extending an existing S-N curve to higher numbers of cycles. The heat build-up method is investigated to determine if it is reliable for predicting fatigue lifetime in a reduced amount of experimental time. The mechanical response and the damage and failure mechanisms are also studied.

Finally, chapter 6 describes the development of an innovative 3D meso-scale model, inspired by the work of Charmetant *et al.* (Charmetant et al., 2011), to allow a deeper understanding of the complex mechanical behaviour of ropes and to provide a quantification of the friction due to the relative movement of the components during loading.

Chapter 1. Bibliography

1.1. Introduction

This work addresses the mechanical behaviour of synthetic fibre ropes and more specifically, of polyamide 6 fibre ropes, for their use as mooring lines. The knowledge of the complex non-linear elasto-visco-plastic behaviour of polyamide 6 ropes in water is of primary interest, especially, their long term creep behaviour and their fatigue resistance, to ensure that they will keep their integrity over their lifetime. This chapter focuses on the state of the art of synthetic fibre ropes; it highlights that the knowledge of the long term creep behaviour and the durability of polyamide 6 fibre is not complete, strongly depends on the construction of the rope, and should be improved. It also highlights the complexity of the modelling both for dimensioning (phenomenological approach) and for understanding (mechanical approach).

1.2. Generalities on synthetic fibre ropes

1.2.1. History

Synthetic fibre ropes are structural elements characterized by their ability to resist high axial loadings compared to their small flexion and torsion stiffnesses. The need to hold and lift started as soon as the exploitable properties of ropes was discovered. However, animals were the first to use ropes. For example, the monkeys used the liana, long strands of plants, to climb trees and swing from one branch to another. These natural "ropes" are oriented hierarchical assemblies of strong fibres in a softer matrix (McKenna et al., 2004). At different times and in different parts of the world, men and women found that they could take fibres or coarse strands found in nature, and design long strong ropes by twisting the yarns together. Very few artefacts remain, because natural fibre ropes only survive in very dry conditions. One example was found by British troops in 1942 in Tura Caves on the banks of the Nile. It is a large papyrus rope, presented in Figure 1.1, made in 500 BC. The hierarchical structure is comparable to the modern ones: seven fibres twisted together to form yarns; 40 yarns twisted together to form strands and 3 strands twisted to form the rope (McKenna et al., 2004).

Figure 1.1 - A papyrus rope made in 500 BC. From Tyson (1966) (McKenna et al., 2004)

1.2.2. Fibre ropes for marine applications

More recently, synthetic fibre ropes have become extremely attractive as an alternative to steel chain and wire ropes for the cost-effective design of marine mooring systems. The development of high tenacity fibres allowed fibre ropes to be designed with a ratio resistance/weight ten times higher than their metallic alternatives. These ropes are already used in a wide range of surface and sub-sea installations thanks to their low stiffness, good tensile strength and their viscous behaviour (Weller, Johanning, et al., 2015). The stress-strain curves of different types of fibre ropes used in marine applications, and which could be used for MRE (Marine Renewable Energy) mooring applications, are presented in Figure 1.2. Some examples of applications are:

- Polyester for mooring lines of deepwater offshore applications;
- Polyamide for single point moorings for tankers and for towing applications;
- Aramid ropes (*Kevlar, Technora*) for towing and oceanography;
- High modulus polyethylene fibres for mooring and rigging.
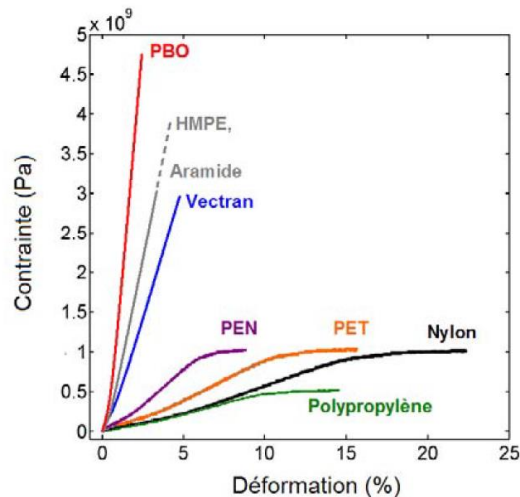
Figure 1.2 - Stress-strain behaviour of different type of fibres used in marine applications. These are families of available fibres. For each type of family, various grades with a range of properties (different drawing ratios, temperatures...) are commercially available (Lechat, 2007)

1.2.3. Construction

The construction of a rope is the particular arrangement of the strands and the sub-elements that makes up its structure. Two main constructions are used (Figure 1.3): braided and twisted. Each type of construction has advantages and drawbacks. The braided constructions have a more balanced geometry. Therefore, no torsion couple is present during tensile loading (Davies et al., 2016). By contrast, the twisted geometry is not balanced; a torsion is induced during tensile loading (Leech & Hearle, 1993; Raoof & Kraincanic, 1998). However, twisted constructions are more adapted for mooring line applications as they reduce the abrasion and friction, which are associated with reduced fatigue lifetime of ropes. In fact, stress concentrations are observed for braided construction at crossover points and these lead to higher friction and reduced fatigue lifetimes.
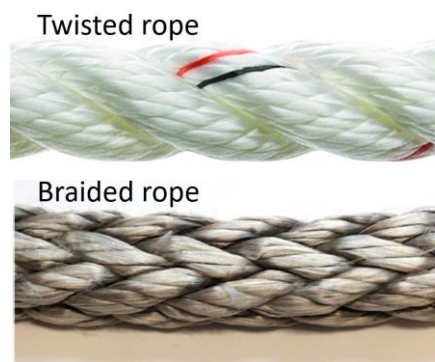
Figure 1.3 - Two widely used rope constructions (Bain, 2020)

The polyamide sub-rope we are studying is a 3-strand twisted sub-rope. The hierarchical structure of twisted rope is characterized by filaments that are twisted together to form yarns, themselves twisted together to form rope-yarns; the rope-yarns are then twisted to form strands. The strands are finally twisted to form the sub-rope. The final rope is composed of parallel sub-ropes grouped together in a protective jacket. There are two ways to twist elements together (Figure 1.4):

- The Z-twist is a clockwise twist or right lay twist
- The S-twist is a counter-clockwise twist or left-lay
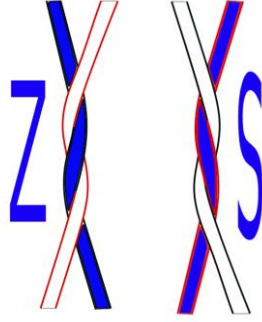
Figure 1.4 - Illustration of Z-twist (left) and S-twist (Right)

To balance a twisted structure, S-Twist and Z-twist are alternatively used at the different scales of a sub-rope. For example, our studied sub-rope has its rope-yarns Z-twisted to form a strand and then, its strands are S-twisted to form the sub-rope. Figure 1.5 is an illustration of a 3-stranded rope. We observe the strands or yarns have changed their shape from an assumed cylinder to wedges and truncated wedges. These are the conforming shapes for transversely soft components (Leech, 2002).
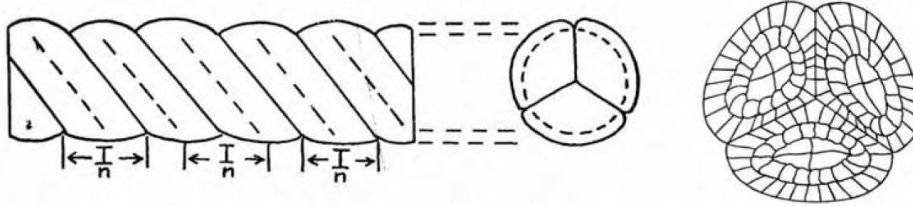
Figure 1.5 - Example of three-stranded rope structures (McKenna et al., 2004)

Other parameters are important when designing a rope:

- The number of sub-elements composing each scale (for example, the number of rope-yarns in a strand);
- The diameters of the elements;
- The different twist angles of each scale (twist angle of the rope-yarns to form the strand; or of the strand to form the sub-rope);
- The lay-length.

If we approximate the structure by a helix, the lay-length P, radius r and twist angle α are inter-dependent following this expression (Eq. 1):

$$P = \frac{2\pi r}{\tan \alpha}$$

Eq. 1

The construction parameters have significant effects on the behaviour and durability of the rope and research has been performed to understand their impact (Del Vecchio, 1992; Ghoreishi, 2005; Lechat, 2007). Friction plays a major role in a twisted rope response, it is the inter-fibre friction that give the yarns their stability. Studies on friction are numerous, Leech *et al.* investigated the different friction modes between the fibres and proposed some models to describe them (Leech, 2002). Bain *et al.* performed an experimental evaluation of the main parameters influencing friction between polyamide fibres and also showed that the direction of twist (S or Z) has a strong influence on the result (Bain, Davies, et al., 2022).

1.2.4. Terminations

To transmit force, a rope needs a termination. It can be temporary using knots or wraps around a cylinder, or permanent using splices, sockets or mechanical grips. It is essential, yet complicated, to have an effective termination for every application that puts the rope under tension. The rope is as strong as its weakest link and it is often at its termination that the rope will fail. Local stress concentrations and disturbances are observed at the termination. Also, during dynamic loadings, abrasion and slippage may occur in the termination. Both these phenomena lead to a gradual loss of strength and failure.

The main termination systems for synthetic fibres are represented in Figure 1.6 and are (Lechat, 2007; McKenna et al., 2004):

- Splices: these terminations are manually made and require some training. They are the most efficient and the most widely used. The drawbacks of splices are that they require very long samples and thus, important stroke for the test machines.
- Capstan: the end of the rope is wrapped around a cylindrical part several times before being fixed. These terminations allow the stress to be distributed uniformly to the sub-elements. They are associated with abrasion during dynamic loading.
- Conical jaws: the end of the rope is put inside a conical part and held in place using a resin or with conical pins. These terminations are relatively short but induce important stress concentrations.
- Compression sleeves that are very quick to install but are associated with a risk of slipping and abrasion.
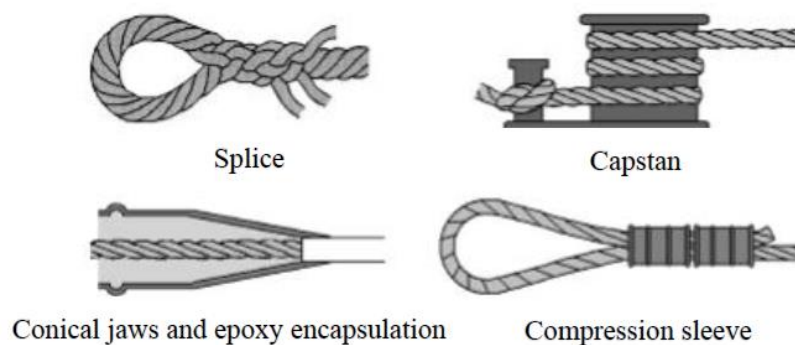
Figure 1.6 - Diagram of different methods of terminating synthetic ropes (Lechat, 2007)

1.3. Structure and complex behaviour of polyamide 6 fibres

Polyamide 6 ropes are already used in other marine applications but their visco-elasto-plastic behaviour and response to cyclic loads are not fully understood, and they are limited to temporary applications. Work has been performed to investigate the complex non-linear mechanical behaviour of polyamide 6 fibres but a deeper understanding is essential to use these lines for permanent mooring applications. The following section will discuss the complex behaviour of polyamide 6 ropes due both to their fibre structure and properties, and also to their hierarchical organization and construction.

Polyamide 6 fibres, and more broadly, synthetic fibres, are characterized by a time-dependent load-elongation behaviour and a non-linear viscoelastic and viscoplastic behaviour Figure 1.7 (Chailleux & Davies, 2005). We observe, on Figure 1.7, the characteristic behaviour of a

polyamide 6 rope, which includes: an elongation under a constant load called 'creep' or recovery (C and D) characteristic of a time dependent viscous behaviour; an hysteresis that highlights the ability to absorb and dissipate energy during dynamic loading; a permanent extension due to initial loading of a new rope (E) characteristic of a viscoplastic behaviour and a construction rearrangement of the rope (Weller, Johanning, et al., 2015).
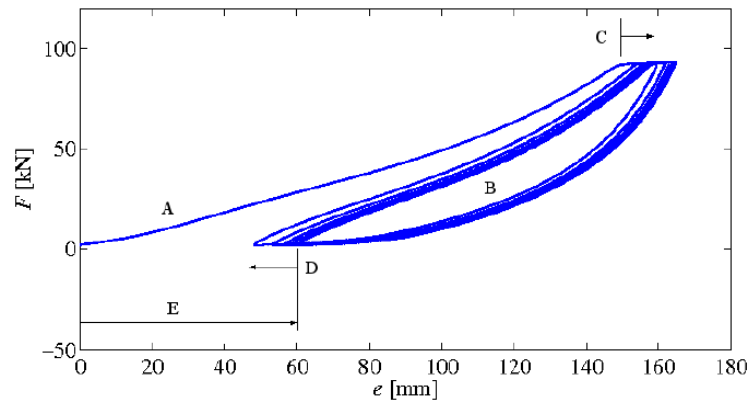
Figure 1.7 - Load-extension behaviour of a new polyamide mooring rope subjected to 10 cycles of bedding-in. A) Initial Loading B) hysteresis during cycles C)creep D) Recovery E) Permanent Extension (Weller, Johanning, et al., 2015)
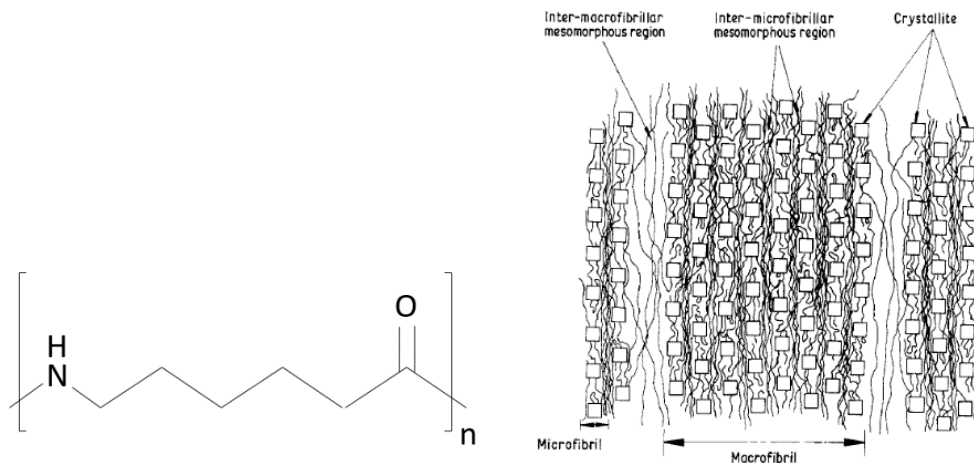
Figure 1.8 – left: Polyamide 6 structure Right: macro-fibrillar structure Right: microfibrillar structure proposed by Oudet and Bunsell (Oudet & Bunsell, 1987)

This complex behaviour is due to both the polymeric nature of the filaments and also to their hierarchical structure and construction. The polyamide 6 structure is shown in Figure 1.8. As its name implies, a polyamide linkage (-NHCO-) can be seen. The polyamide 6 structure is governed by strong hydrogen-bonded chain segments and weak van der Waals forces that are more easily deformable and susceptible to changes in crystallization condition and applied external forces (Mukhopadhyay, 2009). Polyamide 6 fibres are semi-crystalline due to their manufacturing process (melt-spinning, drawing). Their structure is described as microfibrillar with a regular stacking of alternate amorphous and crystalline regions. This microfibrillar description was first proposed by Outdet for polyester fibres (Figure 1.8) (Oudet & Bunsell, 1987). Marcellan *et al.* used macrofibrillar entities to describe the mechanical behaviour of polyamide fibres (Marcellan et al., 2006). The mechanical behaviour of polyamide 6 fibres depends on their molecular weight, their structural morphologies, and the orientation of their molecular chains.
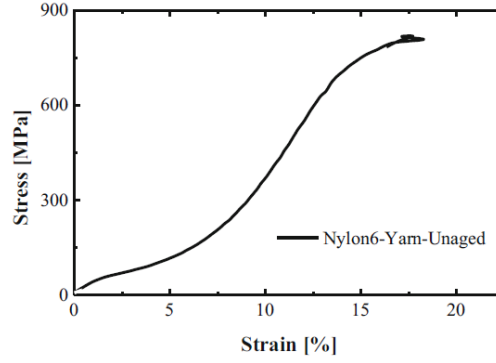
Figure 1.9 - Typical stress-strain curve of polyamide 6 yarns during quasi static tensile test (Humeau et al., 2018)

A typical stress-strain profile of polyamide 6 is shown Figure 1.9. We observe an S-shaped profile that can be divided into 3 parts. This is a behaviour we often observe for melt-spun fibres. Four domains can be identified here (Marcellan et al., 2006):

- At small strains, from 0% to 3.5%, the progressive alignment of the amorphous region is responsible for the strain while the crystalline domain is still unloaded. Moreover, stress induced crystallization is observed with a visible increase of the crystalline part.
- Between 3.5% and 10%, it is the end of the amorphous domain orientation.
- From 10% to 15%, the crystalline regions are highly loaded which causes breakage of their chains. In the meantime, C-C bonds form crystals and oriented domains continue to elongate. We consider that these mechanisms are associated with viscoelastic deformations and 'rubber-like' behaviour.
- Above 15% strain, viscoplastic mechanisms are activated which seem to be due to macrofibril sliding as many ruptures of the macrofibrils on the fibre surface are observed.

The mooring line application requires knowledge of the behaviour of polyamide 6 fibres in water. Humeau *et al.* showed that these fibres are very sensitive to water (Humeau, 2017). A significant water uptake is noted during immersion, which induces a plasticizing effect as shown in Figure 1.10 for creep tests under different humid conditions.
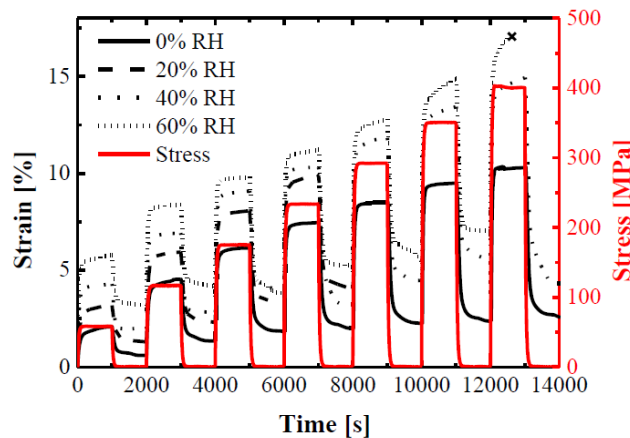
Figure 1.10 - Creep tests performed under different humid conditions from 0% to 60% relative humidity (Humeau, 2017)

The glass transition temperature T_g will differ in the wet and dry states. Humeau *et al.* studied the variation of T_g as a function of the relative humidity and showed it was below 0° for a 100% humidity condition. This means that the state of the amorphous part of the polymer will pass from glassy to rubbery during immersion.

1.4. Effect of scale and construction

The visco-elasto-plastic behaviour of ropes for mooring lines is the result of the material properties of polyamide 6 fibres. However, the effects of the rope construction must also be considered as they play a major role in the response of a rope. The construction impacts the stabilization of the whole structure when the rope is first loaded (François & Davies, 2008); it also has a strong effect on the fatigue lifetime. The main parameters influencing the behaviour of twisted rope will be the lay-length and the twist angles. Lechat *et al.* studied different components of a twisted polyester rope. They showed that a similar nonlinear behaviour was observed at all scales, but the higher scale presented a loss of strength and modulus. For that twisted structure, this loss was related to the number of fundamental elements and the twisting angles (Lechat et al., 2006).

For station-keeping applications, a process called 'bedding-in' allows the properties of the rope to be stabilized. It consists of a procedure with a chosen sequence of loading to allow the permanent strain, due to construction modifications and amorphous regions of fibre reorientations, to occur before the installation. Lian *et al.* (Lian et al., 2018) showed that, depending on the bedding-in applied to a rope, different values of strain, initial creep and stiffness could be observed. Bain *et al.* (Bain et al., 2020) studied the influence of bedding-on loading on HMPE braided rope performance and showed that applying a pre-loading of at least 30% of the break load improves the rope properties. Depending on the rope material, different loading procedures can be found but recommendations are proposed, for example, by Bureau Veritas (NI 432 Dt R02 E, 2007) .

1.5. Creep behaviour of synthetic fibre ropes

To use synthetic fibres with confidence, it is essential to characterize the visco-elasto-plastic behaviour which could be revealed as an increasing elongation with time under load (creep). Creep effects could impose modifying fairlead chains in the line or periodic re-tensionning (Davies et al., 2000). Also, at high loads, creep rupture can occur, though this can be prevented with adequate safety factors. Lastly, at high loads, creep effects can dominate the cyclic fatigue behaviour (Mandell, 1987; Davies et al., 2000).

The following bibliographic section will discuss the literature on creep and recovery of fibres and fibres assemblies. It will then describe the existing experimental set-ups to test polyamide sub-ropes in water under creep and recovery conditions.

1.5.1. Creep of fibres, fibre assemblies and ropes

Creep is defined as the strain under a constant load (McKenna et al., 2004) and creep failure is considered as a quasi-static mechanism where the rope breaks after a certain duration at a constant load (Chevillotte, 2020). Mooring lines are subjected to almost constant load for most of their service life. Hence, the investigation of the creep mechanisms of fibres ropes is and has been a priority (Chimisso, 2009). A typical creep response curve for polymers is shown in Figure 1.11. Three different regimes are visible; primary creep occurs at low stresses and is recoverable when load is removed. During primary creep, the creep rate is high and it decreases when approaching the secondary creep. Secondary creep at higher stresses or longer times is non-recoverable and shows a lower creep rate. The tertiary creep regime is the ultimate one before failure and can be identified with an increasing creep rate (McKenna et al., 2004).
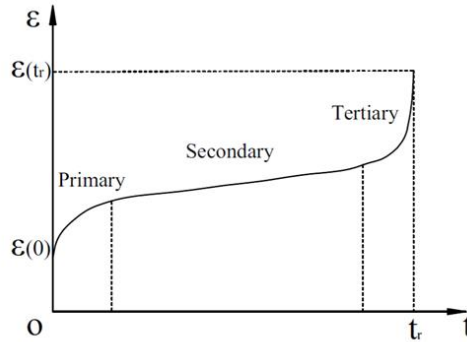
Figure 1.11 - A typical strain–time curve in polymer creep–rupture tests

Studies of high tenacity and high modulus fibres for deep mooring lines are numerous, as the Oil and Gas sector has developed new solutions for their deep-water mooring lines (Chimisso, 2009; Del Vecchio, 1992). Values for various fibres have been gathered in (McKenna et al., 2004) and show that aramid fibres are the most resistant to creep followed by polyester fibres. Davies *et al.* (Davies et al., 2000) presented a study of polyester creep behaviour. Creep tests were performed on fibres, yarns, sub-ropes and ropes. It was shown that polyester can be characterized by a linear evolution of the creep strain as a function of the logarithm of time. The creep rate of the polyester sub-rope in water was evaluated at 0.10 %/decade. The creep was slowing down with time on a logarithmic scale. A study of aramid fibres by Burgoyne (Guimarães & Burgoyne, 1992) highlights that creep and recovery for aramid fibres could also be adequately described by a logarithmic time law and that the creep rate was dependent on the stress. High modulus polyethylene (HMPE) fibres are more sensitive to creep and creep rupture and are an exception; most HMPE fibres show a linear creep strain-time response though a recent grade has significantly reduced creep sensitivity (McKenna et al., 2004; Pal et al., 2007; Vlasblom et al., 2012). Creep rupture of these fibres can occur after around one hundred days at only 30% of their minimal breaking load (30 %MBL) (Chimisso, 2009; Lian et al., 2015).

Polyamide fibres are a more flexible type of fibres than HMPE and show a large amount of primary creep (recoverable with time). Polyamide fibre can fail in less than a day at 50 %MBL load level (McKenna et al., 2004). Pal *et al.* (Pal et al., 2007) studied braided polyamide 6,6 and measured a total strain of 13.3% after 17 days of continuous loading at 32 %MBL. Instantaneous elongations were around 80% of the total elongation. However, polyamide 6 fibres exhibit lower creep rates than polyamide 6,6 (McKenna et al., 2004).

1.5.2. Difficulties to study long term creep on polyamide 6 ropes

A complete study and understanding of ropes and cables requires the characterization of each of their scale. Local scale tests allow us to identify the material (fibre) contribution to creep, whereas macroscopic scale (sub-rope, rope) tests include the construction contributions to creep. Long term creep and creep rupture tests at a higher scale than the filaments or yarns are scarce due to the technical challenges and cost. It requires a machine able to hold high loads for a long duration (months or years).

To simulate the operational response of mooring lines, tests should be performed in water. Water adds the constraint of keeping the water temperature quite constant for months or years and measuring the local strain in water. Therefore, studies of creep in water are rare. One example is a study performed by Humeau on filaments, using dynamic mechanical analysis (DMA) equipment which controls the relative humidity (Humeau et al., 2018).

Another difficulty is the load introduction attachments. The recommended terminations for ropes are splices. This imposes a long sample as splices have to be long enough to distribute the load uniformly inside the rope, without slipping.

Due to high polyamide flexibility, the test machine must have a long stroke. A study on ropes described in (Pal et al., 2007) used a set-up consisting of hanging the rope with one end knotted on an iron bar of a 20 m high frame and the other end near the ground was knotted to the desired weight assembly.

To avoid the difficulties associated with long testing times, some research has focused on ageing the material either at higher temperature using time-temperature equivalence (Lechat et al., 2011; Lian et al., 2015; Pang & Fancey, 2006), or under higher loads using time-stress superposition (Fancey, 2005).

More recently, Chevillotte designed a specific experimental set-up to test sub-rope samples in water for long term creep tests (Chevillotte, 2020). Long term creep and recovery tests were started and a first analysis was performed. These long-term tests lasted already one year for the first analysis proposed in Chevillotte's work. The tests were kept running and a full analysis and investigation of the experimental results is proposed in chapter 4 of this manuscript.

1.6. Fatigue behaviour of synthetic fibre ropes

The term fatigue refers to the degradation and failure of a material induced by a repeated loading. A fatigue test consists of applying a cyclic mechanical stress to a material and measuring the number of cycles to failure. Mooring lines will be subjected to fatigue loading caused by the swell and the movement of the platform.

A typical stress-strain curve under cyclic stress for a viscoelastic material is characterized by an unloading curve located below the loading curve. The area contained in the cycle is called the hysteresis loop and will depend on the type of inelasticity. This area is characteristic of a dissipation of energy by the material during the loading-unloading cycle. The changes in the shape of this loop with the number of cycles gives information on the mechanical state of the material. We will focus our study on force-controlled fatigue tests.

Such repeated loads are associated with rearrangements and structural modifications at different scales: at the sub-rope scale (rearrangement of strands, rope-yarns and yarns) and at the fibre material scale (microstructural rearrangement). The final response to fatigue loading is a combination of the responses at the different scales. Furthermore, depending on the loading range and the mean tension, the mechanisms of degradation and failure may not be the same (Ramirez et al., 2006).

This section reports the studies found in literature on fatigue behaviour and fatigue lifetime at different scales: filament, yarns, rope-yarns and sub-rope scales for synthetic fibre ropes (mainly polyester and polyamide).

1.6.1. Study of fatigue at the filament scale and failure mechanisms

The fatigue behaviour of individual fibres has been the subject of many studies. At the fibre scale, three failure modes have been observed on polyamide (Kenney et al., 1985):

- Polyamide has a large hysteresis loop (larger than polyester) and poor thermal conductivity. Therefore, as a result of internal hysteretic heating, it may fail thermally.
- It may fail due to the static loading at the mean tension of the cyclic loading, hence showing a failure similar to a creep failure.
- It may fail due to crack initiation and stable propagation.
- It may fail due to filament fatigue in tension-compression, in flexure or rotation.

Bunsell *et al.* (Bunsell & Hearle, 1971) were the first to develop a machine able to perform load-controlled fatigue tests on fibres at high frequencies (50 Hz). This apparatus was then used in several fatigue test programs on polyamide (Colomban et al., 2006; Ramirez et al., 2006), polyester (Le Clerc et al., 2007; Lechat et al., 2006) and higher stiffness fibres (Davies et al., 2010). Using this test machine Bunsell *et al.* revealed a specific fatigue failure mechanism for polyamide fibres. It is characterized by a distinctive fracture morphology that they investigated using scanning electron microscopy. Figure 1.12 and Figure 1.13 present, respectively, the morphology of creep rupture in static tensile testing of polyamide, and the fatigue failure morphology under cyclic tension loading obtained by Bunsell *et al*. The main differences between these two modes of failure are the rate and direction of crack propagations. The creep failure mode is a fast crack propagation mainly in the radial direction. The fatigue mechanism happens in three steps: an initiation zone appears on the surface of the axis fibres; after a radial propagation, the crack deviates sharply and starts propagating along the fibre axial direction but with a penetration angle inside the fibre; finally, the cracks will propagate radially until the remaining section can no longer support the applied stress and a normal tensile fracture completes the break (Bunsell & Hearle, 1971).
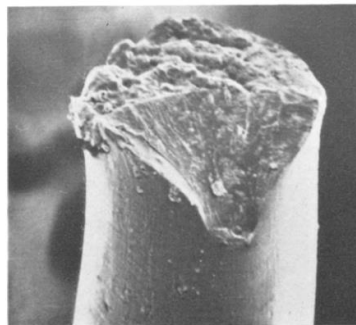
Figure 1.12 - Example of creep rupture morphology (Bunsell & Hearle, 1971)
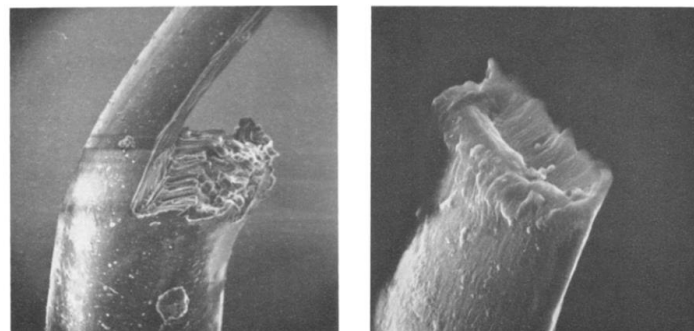
Figure 1.13 - Example of fatigue rupture morphology. Left: root of the tail. Right: Tip of the tail (Bunsell & Hearle, 1971)

Further studies were performed to understand this fatigue failure mode in more detail. Herrera (Herrera-Ramirez, 2004) studied the mechanical behaviour of fibres under cyclic loading. His work examined the minimal, and maximal, load influence on the failure mode and fatigue lifetime of polyester and polyamide 6,6 fibres. It revealed the existence of a minimal load threshold, above which the failure is caused by the creep mechanism. Herrera (Herrera-Ramirez, 2004) also studied the microstructural mechanisms governing the fatigue failure of polyamide 66 fibres using wide angle X-ray scattering. His study illustrated that molecular movements in the fibre occurred under cyclic loading through changes of the crystalline perfection and of the anisotropic and isotropic amorphous phases. Studying two types of PA66 fibres, Herrera showed the microstructure had a quantitative impact on the fatigue behaviours. Finally, he supposed that the minimum load threshold level in fatigue and fatigue crack initiation could be the transition from tension to compression. If the global load is low enough, the fibre surface region will be subjected to compression, hence, facilitating crack initiation. He proposed a scheme of structural modification of polyamide 66 fibre during cyclic loading which is shown in Figure 1.14.
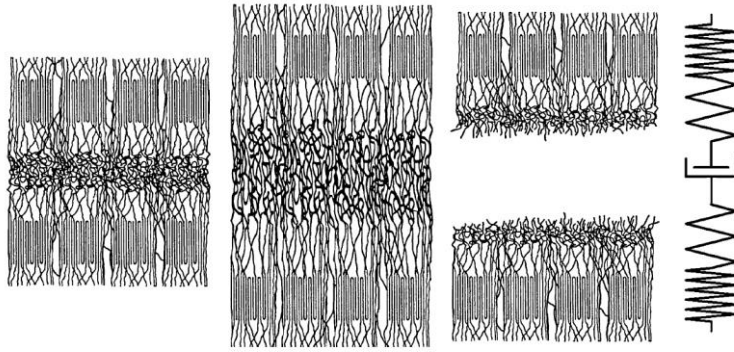
Figure 1.14 - Fibres structure in different conditions: Left: Fabrication state: Middle: During a cyclic loading. Right: After fatigue failure (Herrera-Ramirez, 2004)

These molecular changes are associated with a local heating and hysteresis due to the interaction and friction of the amorphous chains. Lowering the minimal load encourages the interaction of amorphous chains and leads to structural rearrangements with heat production. Figure 1.15 presents the measured energy of hysteresis for a PA66 fibre. Further studies on the hysteresis and self-heating at the sub-rope scale will be presented in the next section.
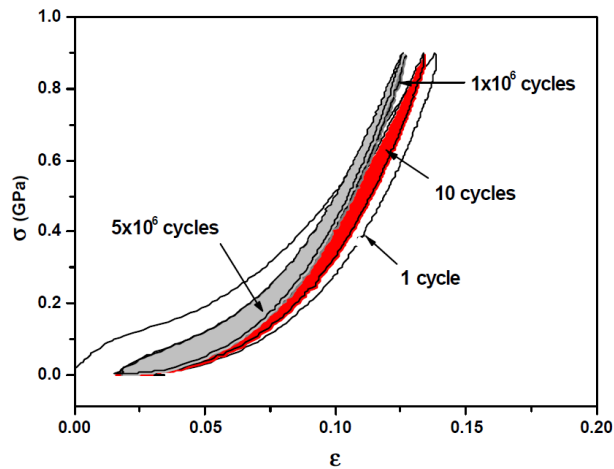
Figure 1.15 - Superposition of the hysteresis loop for different number of cycles of a PA66 fibre tested under non-damaging conditions (Herrera-Ramirez, 2004)

1.6.2. Fatigue study of higher scale fibre assemblies

The experimental requirements to perform fatigue tests, on synthetic fibre sub-ropes and ropes, are complicated. One difficulty is to control the failure zone in the gauge length using the right terminations. In section 1.2.4, four terminations were described. Splices are the most used as they allow the load distribution to be controlled and secure the failure in the gauge length. However, the splices have to respect a minimum length with regards to the gauge length of the rope studied. Moreover, a minimum number of pitches has to be present in the gauge length. These constraints result in long samples which require large test machines with long stroke. Also, the strain at rupture reached for polyamide 6 is around 20% which increases the minimum stroke required even more. The results at these scales are precious and hard to obtain.

During rope tests, two mechanisms are observed at the filament/fibre scales:

- Creep, which is the elongation under a constant load of the rope construction and its constituent fibres or filaments.
- Fatigue, in tension-compression, in flexure or rotation.

Other mechanisms related to the multiscale nature of ropes must be considered (Parsey, 1983):

- The hysteresis due to the energy build up due to internal heating within the rope and its constituents.
- Structural fatigue due to the successive internal realignments of the rope structure.
- Internal abrasion between the sub-components of the rope at each scale (filaments, yarns, rope yarns and strands).

1.6.2.1. Hysteresis internal heating

Parsey (Parsey, 1983) proposed an investigation of the internal hysteresis heating mechanism that can cause failure under specific cyclic loading sequences. Their study focused on single point mooring hawsers made of polyamide and polyester in dry and wet conditions. The hysteresis observed on a rope can be due to dissipation of energy because of inter-yarn effects (flattening, twist migration and abrasive wear). It can also be linked to a plastic deformation of the rope and filament structure. Parsey monitored the internal temperature and hysteresis on such ropes. He found that the maximum temperature rises for a new dry polyamide, or polyester line (made of 6 sub-ropes and loaded between 10%MBL and 28%MBL) did not exceed 45°C and could be ignored. But for larger diameter hawsers in dry conditions (24 sub-ropes), the temperature could exceed 150 °C and reduce the strength if exposed too long. He also concluded that prior wetting could marginally reduce the maximum temperatures. In that study, he showed that hysteresis heating effects are important on large hawsers under continuous cycling or at high or resonant frequencies. They cause failure by progressive degradation, by creep or by melting of the material. In a separate study, he summarised the data then available on the fatigue life man-made fibre ropes and concluded that wet cross-plaited polyester hawsers were more resistant in fatigue than wet polyamide hawsers. That study also highlights the importance of the environment as, in water, the temperature rise is significantly reduced, limiting the cause of failure due to hysteresis heating.

1.6.2.2. Fatigue failure piloted by creep

Kenney *et al.* (Kenney et al., 1985) performed fatigue tests characterized by cycling between a maximum load, ranging from 50%MBL to 95%MBL, and one-tenth of this value (load ratio of 0.1) and at a frequency of 1Hz. They obtained S-N fatigue plots for polyamide 6.6 single fibres, yarns and braided sub-ropes (in dry conditions). The fatigue resistance was shown to be nearly identical when plotted on a normalized S-N curve for the three different scales. Kenney *et al.*

showed that creep rupture was the dominant mechanism in fatigue failure at all these scales. Hence, they suggested that the creep behaviour of a single fibre may determine the fatigue resistance at each level of structure studied. They proposed a creep rupture model for the fatigue resistance based on the assumption that the creep rupture mode was dependent on the total time under load rather than on the number of cycles.

Mandell *et al.* (Mandell, 1987) worked on the fatigue data for polyamide and polyester from several test programs. They analysed data of fibres, yarns and ropes. They also concluded that the failures at loads above 30-40%MBL, for polyamide, can be predicted by a model based on the creep rupture behaviour of individual fibres and yarns.

The literature presented above showed that, at high loads, the creep rupture is dominant and that, at high or resonant frequencies, hysteresis will be dominant.

1.6.2.3. Abrasion mechanisms

Mandell *et al.* (Mandell, 1987) investigated the internal and external abrasion degradation mechanisms during fatigue testing. They defined 'external abrasion' by the wear between the rope and the bollard at the termination region (eye-splice); 'internal abrasion' was defined by the wear between strands on inner and outer braids, in the splice or along the free part of the rope. They showed failures at lower loads and higher cycles usually occur by external or internal abrasion. Their work focused more on external abrasion and they proposed a model considering the loss of material to predict fatigue lifetime.

Seo *et al.* (Seo et al., 1997) completed this analysis of internal wear and fatigue of polyamide and polyester. They highlighted the tensile fatigue superiority of polyester, dry and wet, compared with braided polyamide. They showed that hysteretic thermal effects in rope structures are caused by both intrinsic mechanical hysteresis of the polymer fibres and by frictional interactions between the yarns and strands of the tensioned rope. Internal wear is caused by the relative motion of rope elements during tensile cycling loading or during bending and unbending.

A specific experimental set-up and test, called the yarn-on-yarn test, can be used to study the friction between the components of a rope. ASTM (American Society for Testing and Materials) standard tests uses this set-up to provide an indication of the abrasion durability. It was developed to check the coating on yarns for hawsers and has been further analysed in the literature (Goskoy, 1986). It has recently been adapted to estimate the yarn-on-yarn friction coefficient (Bain, Davies, et al., 2022; Hobbs & Ridge, 2018).

Seo *et al.* (Seo et al., 1997) obtained yarn-on-yarn (YoY) abrasion data which indicated that, while polyamide 66 fibres showed better durability than polyester when dry, when tests were run wet, the polyamide 66 showed significant reduction in wear resistance whereas polyester did not. They found that wet YoY wear life exceeded that of dry YoY tests for both polyamide and polyester at high loads. In the case of polyamide, for lower loads, the differences between dry and wet reverse. They also concluded that comparisons of YoY wear between polyamide and polyester vary significantly with the loading condition. Polyamides are superior at very high tensions whereas at low tensions polyester lifetimes exceed those of polyamide. They concluded that the coefficient of yarn friction is influential in structural rearrangements under tension. They highlighted the importance the coating can have on rope strength and fatigue durability as it prolongs the YoY wear life.

Bain *et al.* (Bain, Davies, et al., 2022) proposed an experimental evaluation of the main parameters influencing friction between polyamide fibres. They also studied the influence of friction on the abrasion resistance. They performed tests, in immersed conditions (rope-yarns

immersed in a container filled with natural water), based on the ASTM yarn-on-yarn standard test for the characterization of abrasion durability. They adapted this test to the rope-yarns scale (higher scale). They concluded that two parameters were controlling the friction coefficient between fibres (Figure 1.16):

- The inter-fibres angle δ: an increase of this angle is associated with a decrease of friction coefficient;
- The friction angle $\theta = \frac{\delta}{2}$: an increase of this angle is also associated with a decrease of the friction coefficient slightly less sharp.
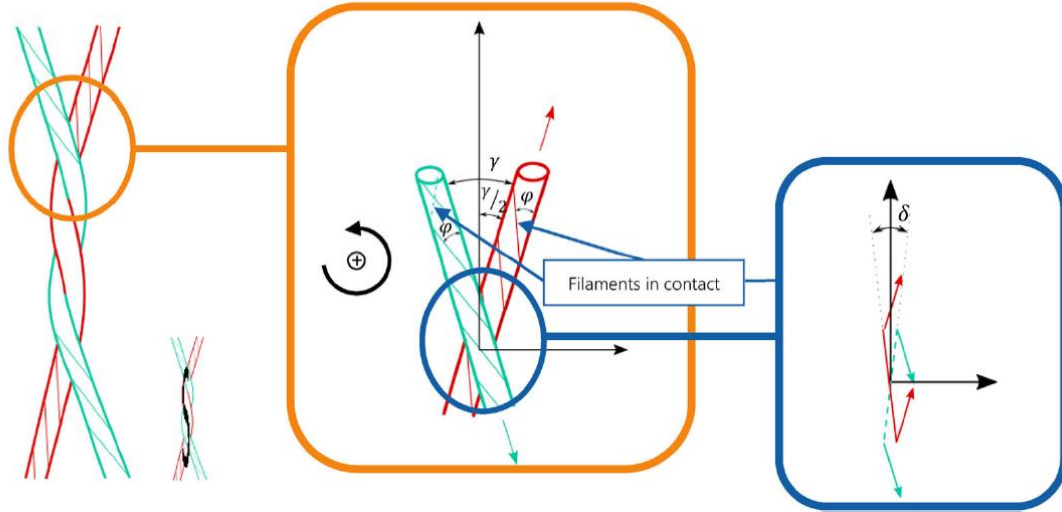
Figure 1.16 - S-wrapped area for S-twisted rope and parameters influencing the friction (Bain, Davies, et al., 2022)

In their study, they also showed that the direction of twist (S or Z) has a strong influence on the result. The friction coefficients for Z-wrapped are significantly lower than those for S-wrapped. The number of cycles to failure for Z-wrap were shown to be much higher than those of S-wrap. Finally, they highlighted that the friction coefficient is one of the main parameters controlling rope durability.

Friction and abrasion will depend on the construction of a rope. The first studies presented (Kenney et al., 1985; Mandell, 1987; Seo et al., 1997) concluded that braided polyamide ropes had poor fatigue performance in comparison with polyester. For the use of polyamide as mooring lines, fatigue durability is an indispensable asset. Until now, polyamide fibre-based rope has only been used for short term applications (< 3 years) as their construction (braided, plaited) and coating were not designed to assure good fatigue resistance.

Considerable efforts have therefore been made to propose rope constructions and coatings that can provide a suitable fatigue lifetime for long term moorings. Twisted polyamide 6 ropes with special coating have been shown to be good candidate. Banfield *et al.* (Banfield & Ridge, 2017) studied a twisted polyamide 6 rope characterized by a long lay-length and a new coating (marine finish) in wet conditions. They showed that fatigue results were greatly improved. In fact, improved coating and a longer lay-length will both reduce inter-strand abrasion, which has been shown to be the most critical mechanism in fatigue durability. More specifically, inter-strand abrasion is the main failure mechanism during high amplitude cycling at low loads (Mandell, 1987). The strands, during a cyclic loading, will slide over each other to open the helix angle and slide back during the unloading to go back to the initial helix angle.

Weller *et al.* (Weller, Davies, et al., 2015; Weller et al., 2014) examined new polyamide mooring constructions subjected to highly dynamic loading conditions in dry conditions. Their results demonstrated that the applied load history and operating conditions both have an impact on the instantaneous properties of the rope. The influence of aging was also investigated. The aged ropes demonstrated larger average strain and strain amplitudes, and were characterized by a reduced axial stiffness. They concluded that these observations were symptomatic of abrasion wear caused by tension-tension fatigue cycling.

Chevillotte (Chevillotte, 2020; Chevillotte et al., 2018) studied twisted polyamide 6 sub-ropes (4T scale and 7T scale) supplied by BEXCO (also studied in this manuscript and presented in chapter 2 section 2.3). In their study, they performed fatigue tests and yarn on yarn tests in wet conditions. The yarn on yarn tests showed that a proper coating could increase the abrasion resistance. However, the fibre coating condition has to be controlled as it affects the fatigue performance. The fatigue tests on sub-ropes showed results that suggested polyamide ropes could have a fatigue durability close to that of polyester. They concluded that, thanks to the coating and construction, the studied polyamide sub-rope fulfilled the standards BV recommended for fatigue lifetime for their use as mooring lines (Figure 1.17). Chevillotte *et al.* also highlighted that two major failure mechanisms were observed under cyclic loading: the melting of fibres on a large area and the peeling of individual fibres. The peeling was associated with the abrasion mechanisms.
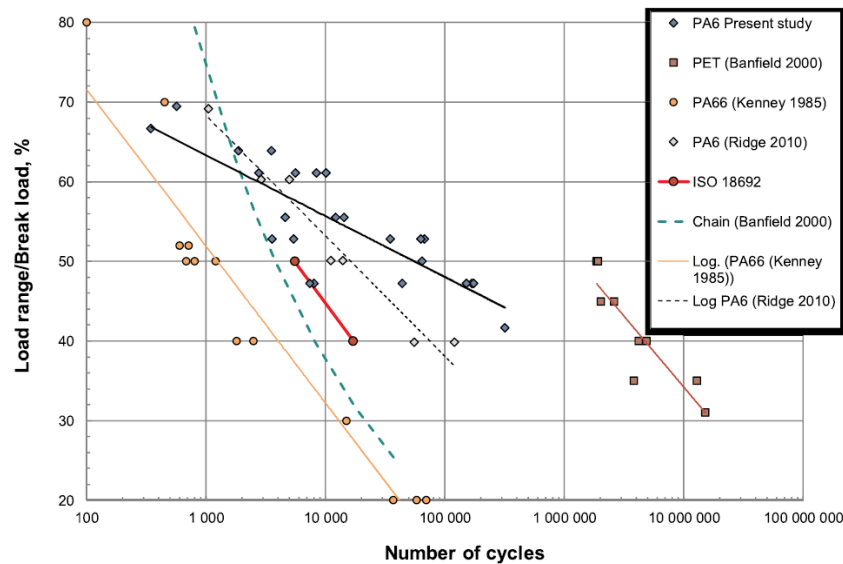
Figure 1.17 - Overview of fatigue results on 8T sub-ropes by Chevillotte, compared to previous tests on polyamide, polyester and steel chain (Chevillotte et al., 2018)

More recently, to improve the confidence in polyamide 6 rope for mooring applications, Sorum *et al.* (Sørum et al., 2023) analysed the performance of polyamide versus PET-fibre based rope. They performed experimental tests with complex loading to identify the parameters of the SYROPE model (presented in chapter 1 section 1.7.1). They ran a fatigue damage analysis using the Syrope model applied in fully coupled load calculations carried out with two different time domain computer programs. They showed that polyamide 6 lifetime could exceed polyester for specific configurations in which polyamide lines are to be used. However, they propose a T-N curve only based on one experimental point (made following the "thousand cycle load level test", TCLL) and on numerical analysis.

1.6.2.4. Failure and damage mechanisms investigations

To study the failure mode at the fibre scale, SEM observations are often used (Bunsell & Hearle, 1971; Herrera-Ramirez, 2004). Tomography scans can also be used to study the damage mechanisms of ropes. Oland *et al.* published a review of the condition monitoring technologies for synthetic fibres ropes and presented the computed X-ray tomography as one possible technology (Oland et al., 2020). Davies *et al.* (Davies et al., 2013) performed x-ray tomography after a cyclic rope bending over a sheave (CBOS) test and they revealed that fibres had melted together during use which increased the rope's density. Also, Heinze and Michael (Schmieder et al., 2015) used tomography in-situ during a CBOS test and revealed internal abrasion associated with reduced rope diameter.

1.6.2.5. Heat build-up prediction method

In his work, Chevillotte (Chevillotte, 2020, 2020) attempted to use a heat build-up measurement protocol to evaluate the fatigue properties of ropes rapidly. An evaluation of the cyclic dissipated energy from the temperature measurements by an infrared camera was proposed. Chevillotte chose a stationary state analysis approach (Jegou et al., 2013). The thermal response of the diameter of the rope is recorded over the full loading steps and averaged over the cable and over the surrounding environment. The stationary state approach leads to an expression of the dissipative energy following Eq. 2 :

$$\Delta^* = \frac{\rho c \bar{\theta}}{f_r \tau_{eq}}$$

Eq. 2

With ρ the density, c the specific heat depending on the wetting protocol, Δ^* the dissipative energy and τ_{eq} the cooling characteristic time and f_r the frequency. The two parameters τ_{eq} and $\bar{\theta}$ are identified using a saturating exponential function to fit the obtained relative evolution of the temperature with time of the sub-rope. They performed this heat-build up method on two scales: a 4T sub-rope scale and a 7T sub-rope scale. A graphical approach based on the calculated dissipative energy allows a fatigue lifetime prediction to be obtained. These predictions are empirical and experimental data from higher numbers of cycles are required to validate them. Further understanding of the dissipation mechanisms of the sub-rope is also needed to improve the graphical approach of this method.

1.7. Modelling of synthetic fibre ropes

The design of mooring lines has been the main motivation to develop models that describe the complex non-linear behaviour of synthetic ropes. Since lines are already in service offshore, guidance documents have been proposed (François & Davies, 2008). Dynamic stiffness tests are often employed for the characterization of rope behaviour. The dynamic stiffnesses are measured by cyclic loading around a mean value. Apparent spring constants are determined, and viscoelastic parameters can be analytically calculated to implement three-parameter models (Lechat et al., 2006). Currently in the offshore industry, the viscoelastic and viscoplastic behaviour of mooring lines is accounted for by stiffness values related to two tension load cases, quasi-static and dynamic. The latter is due to the response of lines under wave loading or due to the movements of the platform. This description is very limiting when designing offshore floating wind turbine floaters and mooring lines as they will be subjected to more complex constraints. Hence, to be able to design properly and precisely these complex structures and their response, there is a need to introduce a model describing the complex behaviour of polyamide 6 mooring lines. The model should also describe the effect of the loading history on the rope's response, for time-domain numerical simulations.

Various approaches for modelling the behaviour of synthetic fibres are proposed in the literature. They are distinguished by their consideration of the fibre structure.

1.7.1. Phenomenological approach

Phenomenological models consider the fibres as a homogeneous nonlinear viscoelastic material. François and Davies (François & Davies, 2008) proposed a model which defines the rope properties with several separate terms in order to simulate the behaviour of PET ropes. These terms correspond to different responses of the rope:

- A mean elongation (system pretension and permanent load),
- A visco-elastic response due to slow variations of mean load, which is modelled by a quasi-static stiffness,
- A dynamic response which is modelled by the dynamic stiffness, that depends on the mean load.

The quasi-static stiffness defined by François *et al.* is determined using a cyclic test between two chosen tension levels with a constant load plateau at each level during which creep and recovery occur. This model consists of the summation of three strains: one for the fully relaxed behaviour, one for the non-recoverable strain and one for the viscoelastic behaviour. Therefore, the rope strain is a function of both the current tension and the maximum tension undergone by the rope (this approach provided a good description of the polyester rope behaviour observed experimentally). François and Davies considered that a fully relaxed behaviour exists for an 'infinitely slow' rate of loading. The advantage of this approach is that it can be used in current mooring line software. However, a true 'time domain' rheological model is needed and requires further work.

Falkenberg *et al.* developed the 'Syrope' model to describe the tension-stretch and axial stiffness characteristics of polyester ropes (Falkenberg et al., 2017). It is based on experimental testing. It is now included in the recommended practices by DNV (DNVGL-RP-E305, 2015). This model consists of (Figure 1.18):

- An original curve which represents the tension versus elongation during the first loading of a new rope;
- The original working curve, corresponding to the stationary working point if the rope is at its historical highest mean tension and when the permanent stretch has been taken out;
- The working curve which represents the working point when the curve is at a lower mean tension than the preceding maximum mean tension.
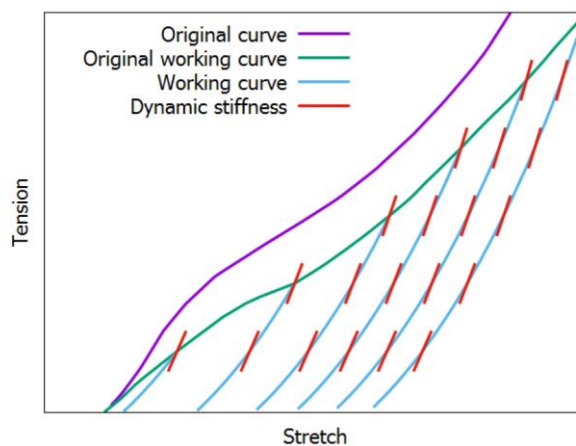
Figure 1.18 - The SYROPE model (Falkenberg et al., 2017)

Falkenberg *et al.* recommended choosing an adequate working curve, considering the maximal tension the rope had been through, for static mooring analysis. The use of a pertinent dynamic stiffness model to calculate the tension responses of the line is a requirement of the DNVGL-RP-E305. For this reason, further work was performed to use different and more precise stiffness models for structure excursions and tension response analysis.

Sorum *et al.* proposed using the Syrope stiffness and the bi-linear stiffness model to predict fatigue lifetime of polyester mooring lines (Sorum et al., 2023). In their study, the Syrope model accounts for the quasi-static stiffness and permanent rope elongation while the bi-linear model applies both the quasi-static and dynamic stiffness in the dynamic analyses.

Recent studies from Huntley on a wire-lay-3-strand polyamide rope showed that the dynamic stiffness of the polyamide rope depends on both the applied mean tension and the tension amplitude (Huntley, 2016). Hence, Pham *et al.* (Pham et al., 2019) proposed a practical mooring analysis procedure to capture the tension amplitude effect on the dynamic mooring analysis. In this procedure, an empirical expression of the dynamic stiffness, that considers the mean tension and the tension amplitude, is proposed for polyamide:

$$Krd = a \cdot T_m - b \cdot T_a + c \qquad \textit{Eq. 3}$$

Where T_m is the mean tension, T_a is the tension amplitude and a, b c, are determined from multiple linear regression on polyamide dynamic stiffness testing data.

More recently, François *et al.* presented an empirical model to predict the response of a polyamide 6 mooring line under stochastic loading (Francois & Davies, 2023). It is a pseudo-elastic model that can reproduce specific features of the response of a fully wetted polyamide 6 sub-rope. For extreme values, it provides a better prediction than the linear "dynamic stiffness" model.

None of these models can be used for analysing the viscoelastic and viscoplastic behaviours of fibre mooring ropes. These time-dependent behaviours need to be precisely evaluated in the design of taut or semi-taut mooring systems. They are even more crucial for polyamide 6 mooring lines that are characterized by an important viscous behaviour.

One of the first macroscopic quantitative models for mooring ropes was proposed by Chailleux and Davies to describe the creep and recovery behaviour of polyester and aramid fibres (Chailleux and Davies, 2005). It is an adaptation of Schapery's non-linear viscoelastic and viscoplastic constitutive model (based on the modification of the generalized Boltzmann integral). This work was continued by Huang *et al.* who employed Schapery's single integral constitutive model to describe the viscoelastic behaviour and a one-dimensional dashpot-slider-spring model to represent the viscoplastic behaviour (Huang et al., 2013, 2015). Huang *et al.* chose the Prony series to describe the transient compliance to improve the description in comparison with Chailleux and Davies' logarithmic proposition. In their work, they proposed two complete identification methods depending on the need to simulate the creep-recovery or the need to simulate cyclic loading conditions. Their model can be implemented in finite element analysis, following the method described in the work of (Lai & Bakker, 1996) to implement Schapery's representation. Humeau *et al.* (Humeau et al., 2018) used the same approach to study creep at high loads on polyamide 6 yarns for both dry and immersed conditions.

Flory *et al.* developed a spring and dashpot model aiming to describe the complex change in-length characteristic of polyester ropes (Flory *et al* 2007) (Figure 1.19). Their model integrates the visco-elasto-plastic behaviour of the material as well as the construction response that will

include twisting, elongation, friction, packing and locking, which Flory called the 'construction stretch'. This model is phenomenological and does not aim at representing the actual components of the rope. The model is composed of four units in series:

- The creep, associated with polymer stretch, represented by the separate dashpot unit (4),
- A parallel spring and ratchet unit represents the construction stretch (3),
- A parallel spring and dashpot unit represents the slow response to tension and is associated with the working stretch (2),
- A separate spring unit represents the fast response to tension and is responsible for the dynamic stretch (1).
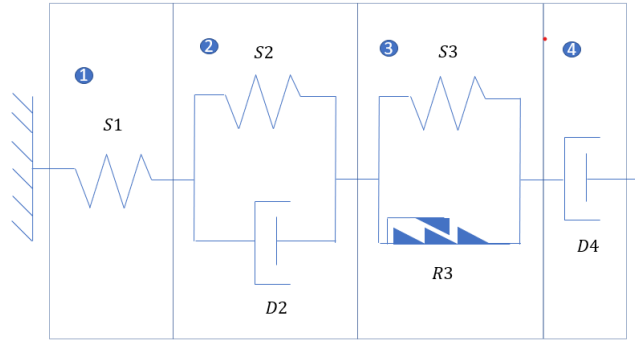
Figure 1.19 - Flory's spring and dashpot model (based on Weller et al., 2018)

This physical unit model can be used for qualitative explanation but, if the parameters can be identified, it could also be used as a quantitative analytical tool for the mechanical behaviour of synthetic fibre ropes under complex loading history. In that work, the equations of the model were not detailed, and no simulation was shown. Weller *et al.* (Weller et al., 2018) published a paper on a preliminary study of the identification of parameters related to the different elements of Flory's model. They considered a fully bedded-in rope that would not have any further significant construction stretch. Therefore, they chose to remove the parallel spring dashpot unit, leading to a four-parameter Burger model. This simplified model allowed the change-in length of the rope to be examined but was not sufficient to fully represent the complex time-dependent behaviour.

Chevillotte (Chevillotte, 2020) developed a constitutive law, called the POLYAMOOR law, based on Flory's proposal (Figure 1.19). Its development is based on the characterization of a polyamide 6 sub-rope in water and under representative conditions for different loadings. The identification method is direct and does not use any inverse identification approach as Weller *et al.* did. This allows more control over the model. Huang *et al.* proposed a model which describes with good agreement the creep-recovery and cyclic behaviour of polyester ropes but two distinct identifications method are required (Huang et al. 2013; 2015). Hence, the same set of parameters cannot be used to simulate both the cyclic loading conditions and creep-recovery conditions. The POLYAMOOR phenomenological law aims to describe the complex visco-elasto-plastic behaviour of polyamide 6 lines during loading at sea with creep-recovery and cycling, and considering the history of loading, with one set of parameters and one identification method. It should describe the real complex behaviour of the rope during loading at sea. The proposed model is also implementable in the one-dimensional finite element analyses used in industry (using software such as ®Deeplines, ®Orcaflex, ®Flexcom, ®Sima …). The law was developed on a small-scale sub-rope and identified only for a virgin material.

1.7.2. Micro/meso mechanical approach

A large literature also exists on twisted ropes, based on analytical models, and dealing with wire ropes. Often, the main objective is to assess the global elastic properties of twisted ropes and the distribution of stresses among components. These models use assumptions on the geometry of the twisted rope components, usually approximated by helices. An experimental study on the distributions of the orientations of fibres within yarns was led by Sibellas *et al.* to propose a detailed description of the filament trajectories. Their approach combined tomography image acquisition and image processing techniques to reconstruct these trajectories (Sibellas et al., 2019). This study was followed by an investigation of the variable fibre packing role in the mechanical response of continuous-filament yarns (Sibellas et al., 2020). Hence, these innovative studies can help to improve the modelling of fibres assemblies as the trajectories and a variable packing have important consequences on the mechanical properties of such structural multi-scale materials. Goreishi *et al.* (Ghoreishi, Cartraud, et al., 2007; Ghoreishi, Davies, et al., 2007) adapted the available models and proposed a mechanical approach which assumes the complex hierarchical structure to be a continuum formed by a set of coaxial helixes only characterized by their external angle and corresponding radius (Figure 1.20). This proposed approach allows the mechanical properties in tension and torsion to be assessed for 1+6 twisted ropes and for multi-layered structures. In this approach the constitutive material is assumed to be linear and the inter-fibre friction effects are neglected.
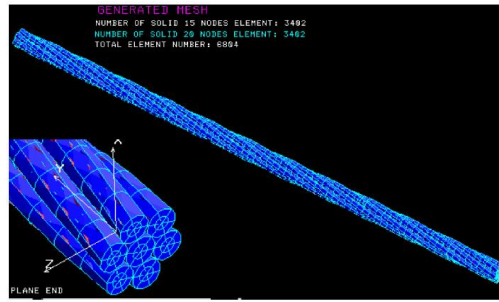
Figure 1.20 - Mesh of a Twisted rope modelled by (Ghoreishi, 2005)

Leech (Leech, 2002) proposed an analysis of the rope structures and the various friction modes. To introduce friction effect, the sliding and movements between the sub-components (yarns, strands, ...) contact points must be described. There exist several sliding modes, Leech presented 6 main sliding modes: the axial slip mode, the component twist, the scissoring, the sawing, the dilation and the distorsional. For a twisted cable in axial tension, Leech *et al.* 1993, showed that the axial slip had the largest contribution to the mechanical behaviour of the cable.

Durville (Durville, 2012) proposed a meso-mechanical approach with a description of contact-friction interactions between beams in large transformations. The aim is to model the behaviour of fibre structures by considering the contacts at the mesoscopic scale between the base components (fibres or yarns). The theoretical background solves the mechanical equilibrium of beam assemblies subjected to large transformations, and develops contact-friction interactions. The yarns are modelled by finite strain beam elements and the contact-friction interactions between the yarns is detected and modelled (Figure 1.21). The detection of the contacts and the construction of contact elements can be time consuming depending on the number of yarns considered.
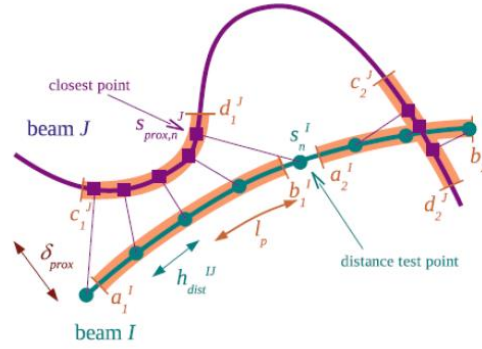
Figure 1.21 - Determination of proximity zones between two beams (Durville 2011)

This model was developed for braided synthetic rope (Figure 1.22) in the work of Vu *et al.* (Vu et al., 2015). Vu *et al.* performed a sensitivity analysis to examine the influence of the friction coefficient between yarns on the response of the braided rope. This type of model is a first way to analyse the impact of construction and friction between components in the response of a rope. In this type of model, the contact-pair management is one of the difficult points as there are numerous contact possibilities (Durville, 2012; Wang et al., 2022; Wielhorski & Durville, 2015). Because of this, the tensile behaviour of the components is limited (for example visco-elasto-plasticity). For polyamide 6 ropes, visco-elasto-plastic tensile behaviour of the polymer filaments will have a significant contribution and must be considered.
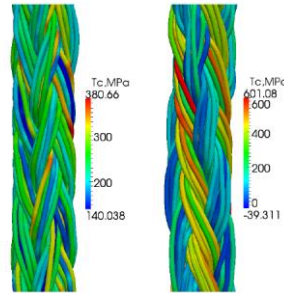
Figure 1.22 - Configuration of HMPE rope braided under a tension of 40 kN for two different parameters of construction (VU, 2014)

Other modelling approaches for fibrous and textile materials, based on hyper-elastic laws, that avoid the numerous contact interaction management, are proposed in the literature. Research effort to develop hyperelastic model for anisotropic materials which undergo large transformation have been made. Terzolo *et al.* proposed a micro-mechanical hyperelastic model for human vocal-fold sublayers able to describe the 3D fibrous architecture and to predict their nonlinear and anisotropic mechanical behaviour under the most important physiological loading (compression, tension, shear) (Terzolo et al., 2022). Their study highlighted the major role of the fibre orientation in the mechanical response of human vocal folds. Another hyperelastic law has been proposed by Gasser *et al.* for biological materials (Gasser et al., 2006). These tissues are composed of an elastic matrix and two different type of fibres. Each fibre type consists of fibres with a specific orientation. These materials present an isotropic transverse symmetry in large transformations. Guo *et al.* (Guo et al., 2007) also developed an hyperelastic law for porous elastomers. The porosities have a cylinder shape and are parallel. Hence, this material presents a transverse isotropic symmetry and undergo large transformations.

The previous hyperelastic models presented are defined as a function of the classical invariants and elongations of the materials. On the contrary, Charmetant *et al.* proposed an anisotropic hyperelastic model based on specific physically motivated invariants for the mechanical

behaviour of textile composite reinforcements (Charmetant et al., 2011). In Charmetant's work, the working scale corresponds to the yarn which is considered as a transverse-isotropic material. The hyperelastic law developed by Charmetant *et al.* was then used to simulate composite reinforcement deformation based on X-ray computed tomography in the work of Naouar *et al.* (Figure 1.23) (Naouar et al., 2016). Chapter 6 of this manuscript proposes an adaption of this model for 3-stranded polyamide sub-ropes.
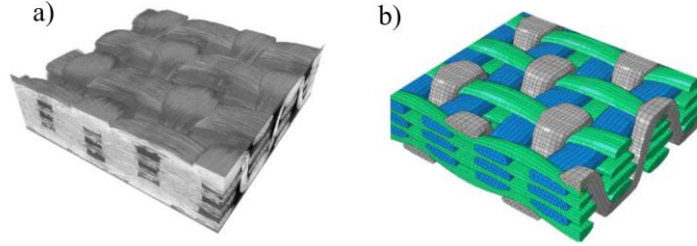
Figure 1.23 - Comparison of a tomography and a simulation of a 3D woven. a) Tomography 3D compacted at 22% c)
Simulation of the 3D woven compacted at 22% (Naouar et al., 2016)

1.8. Study overview

Based on this overview of existing knowledge, a scientific approach is proposed to answer some of the remaining questions related to the long term creep and recovery behaviour, the durability and fatigue lifetime and the modelling of ropes. Our approach is summarized by the schematic diagram given in Figure 1.24.

Chapter 3 of this thesis is devoted to the first key R&D challenge which is the description, understanding and modelling, of the elasto-visco-plastic behaviour of ropes made of polyamide 6. The design of mooring lines has been the main motivation to develop models that describe the complex non-linear behaviour of synthetic ropes. Floating offshore systems already use synthetic mooring lines and therefore guidance documents have been proposed (François & Davies, 2008). However, a true 'time domain' rheological model is needed and is crucial for polyamide 6 mooring lines that are characterized by significant viscous behaviour. In this context, Chevillotte has developed a 1D constitutive law (Chevillotte, 2020). The law has been implemented in *DeepLines* software. The present study focuses on the validation of this law. The law is first identified on a 4T sub-rope (small scale) after long term creep testing to evaluate changes to the parameters of the law, and to mechanical properties of the sub-rope, with creep. Then, the law is identified at a higher scale with a more representative construction (7T). Validation is done on loading sequences different from the specific multi-relaxation test devoted to the identification of law parameters. Respectively in Chapters 4 and 5, the law is compared to long term creep and fatigue test results. A paper based on this work is submitted and under review at Ocean Engineering (Civier et al., 2023).

Chapter 4 of this thesis focuses on the long-term creep behaviour of polyamide 6 mooring lines in water. This study was started during Chevillotte's thesis (Chevillotte, 2020) allowing experimental results lasting two to three years to be obtained during the present thesis. The use of a simple model to fit the data is examined and a comparison with the prediction of the POLYAMOOR law is made. A comparison between creep and recovery kinetics is discussed. Short term creep tests are also performed, in order to conclude on the need to perform long term creep tests. This work is published in Ocean Engineering (Civier et al., 2022).

Chapter 5 investigates the fatigue durability which is another key aspect for future applications. The literature review showed that efforts have been made to propose a construction and a coating that can provide a suitable fatigue lifetime. Chevillotte performed fatigue studies on 4T and 7T polyamide sub-rope samples and the results suggested that polyamide line could have a fatigue durability close to that of polyester (Chevillotte et al., 2020). The present study proposes to extend this work to reach higher numbers of cycles and for lower loads (closer to the application) on a 4T sub-rope scale. An investigation of the failure and damage mechanisms is performed to improve our understanding of the degradation at lower loads. There is still a need to investigate the mechanical response of sub-ropes under fatigue loading. A fatigue test with strain monitoring is therefore performed, and several questions on the impact of the construction and terminations (splices) on the fatigue response and evolution of the hysteresis are raised. Also, during his PhD work, Chevillotte used the self-heating method to allow a fast prediction of the fatigue lifetime. This was quite an exploratory study and the present work aims at validating the repeatability of the experimental protocol and data treatment (both complex) and at comparing the first self-heating prediction to the extended fatigue curve of a 4T sub-rope.

Another key R&D challenge is the understanding of the construction impact on the mechanical, the creep and the fatigue responses of polyamide ropes. Chapter 6 of this manuscript proposes the development of a 3D model, called meso-scale model, of a rope structure. The model should describe:

- The behaviour of polyamide 6 material at the rope-yarn scale: that includes the elasto-visco-plasticity of the material; the inter-rope-yarns friction and their reorganisation;
- The behaviour at the strands scale: that includes the inter-strand friction and the evolution of the geometries at this scale.

The approach chosen is a development of Charmetant's model (Charmetant et al., 2011), developed for composite fabrics, and its adaptation for another type of material. It should allow the separation of the dissipation due to the friction between the sub-components of a sub-rope (the inter-strand's friction and the inter-rope-yarns friction) from the dissipation due to the polyamide material.
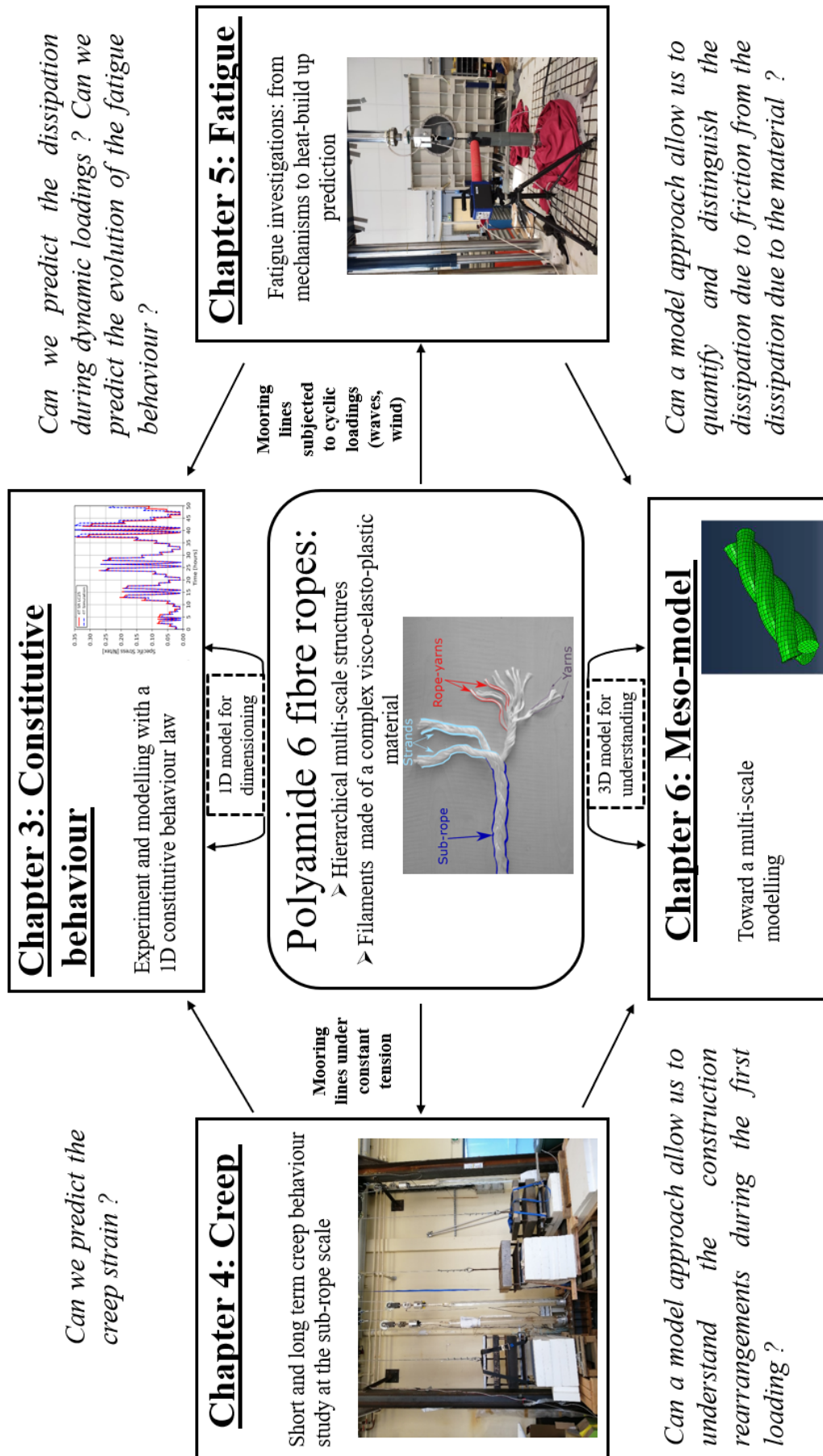
Figure 1.24 - Scheme of the proposed study

Chapter 2. Materials and methods

2.1. Introduction

This chapter describes the polyamide 6 sub-ropes under study, together with all the experimental test methods that are used. A complete understanding of ropes is complicated by their multiscale nature. Each scale contributes to the mechanical behaviour differently and so, ideally, each scale should be characterized. Local scale tests allow us to identify the material (fibre) contribution, whereas macroscopic scale (sub-rope, rope) tests include the construction contributions to the behaviour. Each scale is characterized by a different range of displacements and loads, so each scale requires a specific experimental set-up. In addition, the mooring line application requires knowledge of the behaviour of polyamide 6 fibre in water. Humeau *et al.* showed that these fibres are very sensitive to water (Humeau et al., 2018). A significant water uptake is noted during immersion, which induces a plasticizing effect. Also, water acts as a lubricant between the different sub-components of a rope which reduces the friction and changes the overall response of the rope. Therefore, an effort has been made to perform most of the experimental tests either in water or on wet samples.

2.2. Ropes specifics: units, stress and strain measurements

The multiscale hierarchical structure of ropes has led to specific units of measure and quantities that are different from those usually employed in material engineering; these define rope dimensions and their mechanical properties.

The size of a rope cross-section is defined by its linear density which is its mass per unit of length. One traditional textile unit of measure for the linear density of fibres and yarns is the '**tex**', one gram per kilometre. The strict SI unit is **kg/m** and **1 kg/m =1 Mtex**.

With most engineering materials, specimens of different cross-sections are compared using the Cauchy stress defined by the applied force divided by the cross-section area. The complex structure of synthetic fibre ropes complicates the use of the usual Cauchy stress because of the uncertainty of the cross-section measurement. Hence, it is preferred to work with a specific stress, namely force divided by linear density. A specific stress tensor $\widetilde{\Sigma}$ based on the density of the material is therefore used:

$$\widetilde{\Sigma} = \frac{\widetilde{T}}{\rho_t}$$

Eq. 4

with ρ_t the density in kg/m³ and $\widetilde{T}$ the Cauchy stress tensor in Pa.

In the one-dimensional case (rope case), this specific stress leads to:

$$\Sigma = \frac{F}{\overline{\overline{\rho_t}}}$$

Eq. 5

with $\overline{\overline{\rho_t}}$ the linear density in kg/m and F the tensile force in Newton.

The SI specific stress unit is N.m/kg (= J/kg). The textile industry uses a specific unit N/tex with:

$$1\frac{N}{tex} = 10^6 \frac{J}{kg} = 10^3 \frac{Pa}{g/m^3}$$

Eq. 6

where 1 tex = 1 g/km.

In addition, in the rope and cable industry, loads applied are often given as a percentage of the minimum breaking load noted '%MBL'. In this study, the loads are often given in %MBL but their equivalent in kilonewtons (kN) or newtons (N) are also given.

For defining and measuring a strain, one needs a reference mechanical state, which defines the reference length L_0. In the case of rigid materials like metals, this reference state is usually chosen at rest, before any loading. In the case of textile materials, the mechanical state at rest, i.e., without any loading, has very variable geometric dimensions. Indeed, without any loading, this type of material has very low rigidity and we can easily modify its dimensions during handling. So, the state at rest cannot be used as a reference mechanical state, because of the high uncertainty of the reference length L_0. In order to overcome this difficulty, a simple solution is to apply a low load to the material in order to stabilize its dimensions. Then, this lightly-loaded mechanical state can be used as a reference state for L_0.

The logarithmic strain will be used for this study:

$$\varepsilon_{log} = \log\left(\frac{L}{L_0}\right)$$

Eq. 7

with L the current length, L_0 the reference length and $\log$ the natural logarithm.

In this study, the reference mechanical state is chosen at the end of a *bedding-in* loading, described at section 2.4.

2.3. Materials

The polyamide 6 yarns used in this study are manufactured by Nexis fibres (reference 1880 f 280). Their linear density is 188 tex. This fibre is characterized by a measured crystallinity of 40%, and a measured melting temperature T_f of 220 °C. The glass transition temperature T_g in the dry state is different to that measured in the wet state: Humeau et al. 2018 measured a T_g of 60°C in the dry state and estimated a Tg of around -17°C for an 80% relative humidity state. This indicates that, in the dry state and at ambient temperature, the material is below the glass transition, hence, in the glassy state. In the wet state, the material is above the glass transition, hence, in the rubbery state.

The synthetic ropes studied are reduced scale models of a polyamide sub-rope developed for mooring lines by Bexco, Hamme Belgium. Two reduced-scale three-strands sub-ropes are studied in this manuscript and both were specially manufactured for the research project.

The first is a three-strand rope with a diameter of around 11.5 mm, a lay-length of 50mm, an MBL of 40 kN and a linear density of 90 000 tex (g/km), it will be referred in this study as '4T sub-rope' (Figure 2.1). Each strand is composed of 10 twisted rope-yarns and each rope-yarn is composed of 13 twisted yarns. A proprietary coating has been applied on the rope-yarns by the rope manufacturer Bexco. This coating aims to reduce the internal abrasion, improving its fatigue durability (the target fatigue lifetime for FOWT is 20 years) (Chevillotte, 2020). The dimensions and properties of this 4T sub-rope and its components are gathered in Table 2.1. The description of the tested 4T sub-rope samples is given at Figure 2.1.
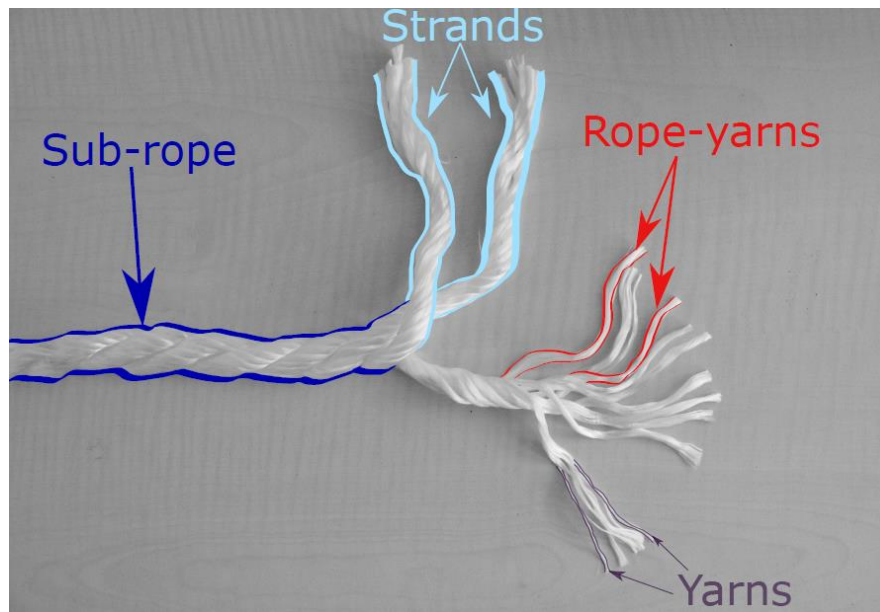
Figure 2.1 - The different scales of a model 3-strand sub-rope

Table 2.1 - Dimensions and other parameters of the 4T-sub-rope supplied by BEXCO and its components

	Quantity in the immediate upper scale	Average diameter (mm)	Linear density (tex)	Lay length (mm)	Z or S twists	Measured Minimal breaking load (kN) and N/tex
Sub-rope 4T	Several in parallel in a rope	11.5	90 000	50	S	40
Strand	3	9	27 000	47	Z	14
Rope-yarns	10	2	2600	46	S	1.6
Yarns	13	0.27	190.5	-	-	
Fibres	280	0,026	-	-	-	-

The second reduced-scale sub-rope is a three-strand rope of outer diameter around 15 millimetres for a minimal breaking load of 75 kN. It will be referred as '7T sub-rope' in this study. The lay length is similar to polyester sub-rope constructions for deep-water mooring ropes and imposes splices of more than 2 meters at each end of the rope. Each strand is composed of yarns twisted together into rope-yarns. The rope-yarns are twisted together to form strands. No further information can be given on this 7T sub-rope for confidentiality reasons. The tested 7T sub-rope samples are six-meters-long (pin to pin), leaving a 1.5-meter central area between splices.

2.4. Bedding-in procedure

For station-keeping applications, a bedding-in process is performed to stabilize the properties of the rope as explained in section 1.4 of the bibliography.

A pre-loading sequence proposed specifically for the project is described in Table 2.2. It was applied with a loading rate equivalent to the ISO test. The mean tension experienced by the floating wind turbine mooring lines is estimated at 15 %MBL. Hence, the bedding-in was chosen to be representative of these low loading conditions and does not follow the ISO recommendation which requires higher loads (NI 432 Dt R02 E, 2007).

Sequence order	Loading/unloading rate	Reached loading value [N/tex (%MBL)]	Creep/recovery duration [s] at this loading value
1	$5 \cdot 10^{-4} s^{-1}$	0.07 (14)	3600
2	$-5 \cdot 10^{-4} s^{-1}$	0.01 (2)	3600

These two steps were applied before all tests unless otherwise specified. The mechanical state at the end of this pre-loading was defined as the reference state for all strain measurements.

In the following study, each time this bedding-in was applied, it will be mentioned with a reference to this section for further details.

2.5. Methods

The experimental procedures used in this project are presented in this section.

2.5.1. Crystallinity measurements

Polyamide 6 fibres are semi-crystalline and their crystallinity ratio will strongly influence the mechanical behaviour of polyamide 6 ropes. The material crystallinity was determined here using differential scanning calorimetry analyses (DSC). This thermomechanical technique measures the difference between the amounts of heat required to increase the temperature of a sample and reference as a function of the temperature. The sample mass was between 7 and 8 mg. The samples were heated from -10°C to 300°C at a rate of 10°C/min. These analyses were performed on a Q200 DSC equipment from TA Instruments®.

Material crystallinity was calculated using Eq. 8:

$$X_{cr} = \frac{H_{ms}}{H_{m0}}$$

Eq. 8

Where X_{cr} is the crystalline fraction of the material and H_{ms} and H_{m0} are the enthalpies of fusion of the sample and the entirely crystalline material, respectively. The theoretical enthalpy of fusion of 100% crystalline polyamide 6, H_{m0} , was taken as equal to 188 J/g in this study (value from (Humeau, 2017)).

2.5.2. Linear density measurements

Linear density measurements require first to measure the length of a sample and then, to weigh it. The linear density is then given by Eq. 9:

$$\bar{\bar{\rho}}_t = \frac{m}{l}$$

Eq. 9

With $\bar{\bar{\rho}}_t$ the linear density in g/km, l the measured length in km and m the mass in g.

The length was measured using a ruler and by putting the sample straight on a table, without tension. We also could have applied a tension to measure the length. However, it would have required a long sample and a specific set-up to apply a 2%MBL load on this sample. Hence, we preferred to measure the length without tension in this study.

The final linear density measured for rope-yarns, strands and sub-ropes are gathered in Table 2.1 in the column 'Linear Density (tex)'. These linear densities were used to calculate the specific stress defined by Eq. 8.

2.5.3. Sub-rope sample testing 4T and 7T

2.5.3.1. Splice Terminations

The recommended terminations for ropes are eye-splices. Splices tighten the structure and stabilize the tension in each strand. This imposes long samples as splices have to be long enough to distribute the load uniformly inside the rope, without slipping.
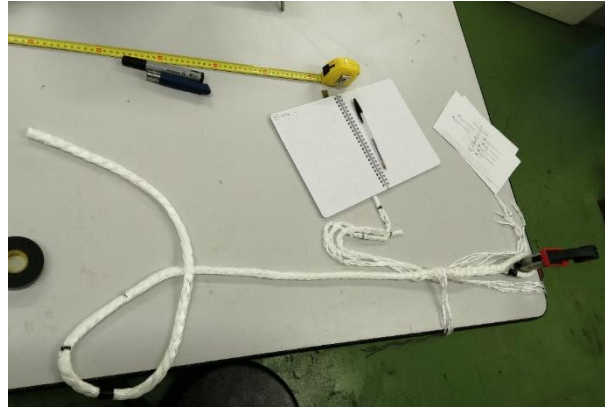
Figure 2.2 - Splicing of a 4T-sub-rope sample

The properties of splices are dependent on the type of experiment and the experimental set-up associated. The 4T smaller scale sub-rope is more adapted to laboratory experiments and the splices can be prepared in the laboratory (without having to ask the supplier) (Figure 2.2). This allowed more experiments to be performed, as the cost is also reduced and the autonomy in the splicing result in more samples and shorter delays. I realized all the splices for the 4T sub-rope samples tested in this study. Two types of splices were used for 4T sub-rope sample:

- For fatigue tests (section 2.5.3.3; presented chapter 5), 1-meter long samples were tested. The strand lay-length of the 4T sub-rope imposes splices of around 300 mm, leaving 300 mm in the central section (Figure 2.3).
- For creep tests and multi-relaxation tests on longer sample (2.5.3.4 and 2.5.3.5; presented chapter 4), 1.80-meter long samples were used. The length of the splices is around 500 mm leaving a central section of 770 mm.
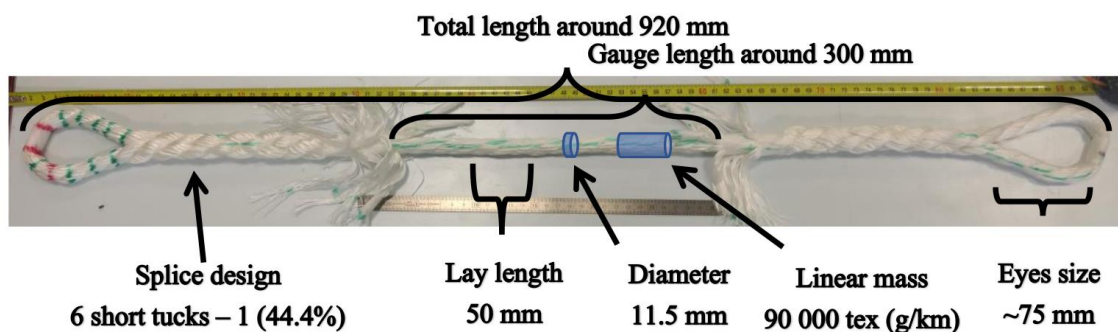
Figure 2.3 - 4T sub-rope sample splices construction and dimensions (Chevillotte, 2020)

The lay length of the 7T sub-rope sample (studied in chapter 3) is similar to polyester sub-rope constructions for deep-water mooring ropes and imposes splices of more than 2 meters at each end of the rope, leaving a 1.5-meter central area. These higher scale samples were supplied by BEXCO with the splices already made.

2.5.3.2. Quasi-static tensile test on dry samples

The quasi-static tests on 4T sub-ropes were performed on a 200 kN capacity ROELL KORTHAUS model RKM250 (Figure 2.4). A load cell of 200 kN was used. There were no tests with wet samples on this machine as no set-up was available to allow a water protection of the machine. The motor of this machine is at the bottom of the frame and water could have damaged it seriously.

Figure 2.4 - Quasi-static test on 4T sub-rope samples: experimental set up using an electromechanical test machine

The samples were attached to the testing machine using loading pins of 35 mm diameter. Two black markers were placed on the sample. The relative displacement of the markers was measured by image correlation analysis. Two Basler cameras with 2040x1080 pixel resolution were used. The loading rate of the test was 50 mm.min^{-1}. Only four tests on dry 4T sub-ropes were performed during this work to investigate the effect of the lay-length on the mechanical properties of a sub-rope during a tensile loading to rupture. These tests are presented in chapter 3 section 3.3.2.3.

2.5.3.3. Fatigue characterization on 4T sub-rope samples

Self-heating (Heat build-up measurement protocol) and fatigue (Fatigue tests) tests were performed on 4T sub-rope samples to study the fatigue behaviour and to develop the self-heating prediction method. The results from this investigation are presented in chapter 5 of this manuscript.

A large displacement stroke is required for testing polyamide 6 sub-rope samples. A hydraulic machine developed for compression tests at high rates (Figure 2.5) called 'Servotest' allowed one-meter long samples to be tested. This Servotest machine could also be used for quasi-static tensile tests, having a piston stroke of 600 mm. The maximum displacement rate is 100 mm.s^{-1} for quasi-static tests. The sample splices were linked to the machine by two 35-mm diameter loading pins.

Figure 2.5 - Servotest test hydraulic machine at ENSTA Bretagne

This is a vertical testing machine. As noted previously, the experimental tests should be performed in water (when possible). Following immersion in water for 16 hours, the samples were kept wet during the test by a system producing a constant and controlled vertical gravitational water flow around the sub-rope (Chevillotte, 2020). This consists of a volumetric pump with a low flow rate (around 1 litre.min^{-1}) that brings tap water near the top of the sample through a spiral-shaped pierced tube covered by a knitted fabric (Figure 2.9). This provides a homogeneous flow around the sub-rope section. The water then flows along the sample length by gravity. The lower loading pin was surrounded by a PVC tube to collect the sample water and return it to a tank. The HBM load cell has a range of ±50 kN and a resolution of 2 mV/V leading to a precision of around 10 N.

2.5.3.3.1. Heat build-up measurement protocol

The heat build-up measurement protocol is a fast method to evaluate the fatigue properties of materials (Doudard et al., 2005; Marco et al., 2017). An evaluation of the cyclic dissipated energy from the temperature measurements by an infrared camera allows a prediction of the fatigue lifetime of a material to be made. Chevillotte (Chevillotte, 2020) first developed this technique on 4T sub-ropes and this study (presented in Chapter 5) aims at completing this work.

The heat build-up tests were performed on the Servotest testing device. To improve the self-heating measurement, the emissivity of the polyamide 6 rope has to be as close to 1 as possible, hence a black paint was applied to improve emissivity (Figure 2.6).

Figure 2.6 - 4T sub-rope sample with black paint on the gauge length to increase self-emissivity of the material

The sample was then immersed for 16 hours in a water tank. A High-Moddulus Polyethylene (HMPE) fabric was wrapped around the eye-splices to avoid abrasion between the sub-rope eye-splice and the steel pin, hence avoiding a failure in the eye. The sample was then attached to the loading pins and the watering system described above was activated.

The environment affects thermal measurements; hence a custom plastic box was used in order to control the reflection conditions and to simplify the thermal measurements. A sheet was also placed around the samples and the box (Figure 2.7). The self-heating measurements were performed using a Flir Systems infrared camera (reference Phoenix SC7600-BB). The integration time was set at 2000 µs. The thermal precision was evaluated around 40 mK.

Figure 2.7 - Experimental set-up on the Servotest testing machine for fatigue test with self-heating measurement. a) plastic box and infrared camera installed. b) Sheet placed around the sample.

A bedding-in sequence (*section 2.4*) was applied before each heat build-up test. The heat build-up test procedure consisted of several loading steps of 90 cycles, at 0.1 Hz, between 2% MBL (800N) and a chosen maximal tension level ranging from 20% to 70% of MBL (Figure 2.8). After each loading step, a load plateau, at the mean tension of the previous cycles, was held for 8 minutes to reach the stabilized state after cooling (Figure 2.8). The detailed procedures applied are described in Table 2.3.
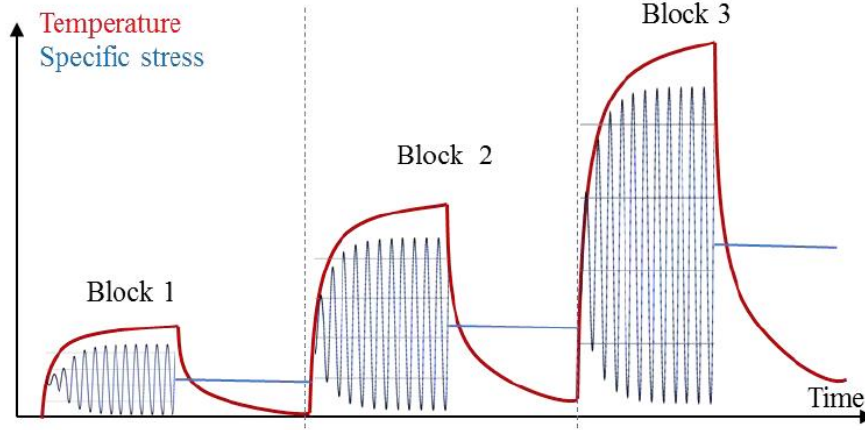
Figure 2.8 - Scheme of a self-heating test: Red curve: measured temperature evolution versus time. Blue curve: Specific stress evolution versus time

Table 2.3 - Loading sequences of cycle blocks for heat-build up on 4T sub-rope samples

Test Name	Self-heating blocks: maximal value (%MBL) during load step
1	20 – 25 – 30 – 40 – 45 – 50 – 55 – 60 – 65 – 67.5 – 70
2	20 – 20 - 25 – 25 – 30 – 30 – 40 – 40 – 45 – 45 – 50 – 50 – 60 – 60 – 70 – 70

The analysis of self-heating temperature, applied for this study, investigated the evolution of the dissipated energy, which is an intrinsic parameter. We considered a stationary state analysis (Jegou et al., 2013) which allowed measurement of the thermal response of the full section of the ropes. The thermal evolution of the sub-rope sample and the surrounding box were recorded during the total duration of a loading step and a load plateau. An in-house developed software called Celenos® was used (Le Saux, 2017) to calculate the average temperature over the full rope diameter and the average temperature of the surrounding box. If necessary, the changes of the ambient temperature could be compensated. The relative evolution of the temperature with time during the loading step is schematized in Figure 2.8 and can be identified as a saturating exponential function following Eq. 10:

$$T(t) = (\overline{\theta_{MAX}}) \times \left(1 - e^{-t/\tau_m}\right)$$

Eq. 10

With $\overline{\theta_{MAX}}$ the maximal stabilized temperature, τ_m the characteristic time during heating.

The evolution with time during the unloading and the plateau can be identified using Eq. 11 :

$$T(t) = \overline{\theta_{moy}} \times e^{-t/\tau_d}$$

Eq. 11

With $\overline{\theta_{moy}}$ the mean stabilized temperature, τ_d the characteristic time during cooling.

Finally, the cyclic dissipated energy Δ^* is deduced according to Eq. 12:

$$\Delta^* = \left(\frac{\rho c \overline{\theta_{MAX}}}{f_r \tau_d}\right)$$

Eq. 12

With ρ the density, c the specific heat capacity, f_r the frequency of the test.

2.5.3.3.2. Fatigue tests

Two different fatigue test procedures are described in this section. These fatigue tests were performed on the Servotest testing device using the same experimental set-up as the heat build-up test described above, with the watering system.

- *Fatigue test with self-heating measurement*

Several fatigue tests, with one self-heating measurement performed at the beginning of the test, were performed on the Servotest testing machine with the same set-up as for heat build-up protocol described in the previous part (section 2.5.3.3.1). The self-heating measurement prevents a strain measurement (a red sheet and a plastic box hide the sub-rope so no image correlation analysis can be performed).

The bedding-in sequence of 2 hours, presented in *section 2.4,* was performed before each fatigue test. For all the fatigue tests, the minimal tension level was kept fixed at 2% MBL (800N). The maximal tension level was modified, so the R ratio was not fixed for this fatigue campaign. The fatigue tests performed are described in Table 2.4 and were all performed at a frequency of 0.1 Hz. This frequency was chosen to be representative of the wave swell frequency because of the mooring application. The self-heating measurement was performed during the first 90 cycles (around 15 minutes) to be sure to reach the stationary state.

N.B. Some of these tests were performed by Cédric Bain during his post-doctoral research, which was part of the MONAMOOR project, as detailed in Table 2.4 below.

Table 2.4 - Fatigue tests performed during the MONAMOOR PhD (PhD) and post-doctoral research (PSD)

Minimal tension level (%MBL - kN)	Maximal Tension level (%MBL – kN)	Ratio R
2 – 0.8 (PSD)	70 - 28	0.029
2 – 0.8 (PSD)	53 – 21.2	0.038
2 – 0.8 (PSD)	45 – 18	0.44
2 – 0.8 (PSD)	42 – 16.8	0.48
2 – 0.8 (PSD)	36 – 14.4	0.56
2 – 0.8 (PSD)	35 – 14	0.57
2 – 0.8 (PhD)	34 – 13.6	0.058
2 – 0.8 (PhD)	33 – 13.2	0.060
2 – 0.8 (PhD)	32 – 12.8	0.062
2 – 0.8 (PhD)	29 – 11.6	0.068
2 – 0.8 (PhD)	25 – 10.0	0.080

- *Interrupted fatigue test with strain measurement*

Only one interrupted fatigue test with strain measurement is presented in this study. This test will be presented in chapter 5. The procedure is similar to the one of the previous fatigue tests. The 4T-sub-rope sample was immersed for 16h in a water tank. An HMPE fabric was wrapped around the eye-splice, then the sample was installed and the watering system was activated. A pre-load of 800 N was applied and black markers were placed on the sample. The displacement of the markers was followed by image correlation analysis using a Meyer Instruments CCD camera RETIGA 6000 (Figure 2.9). The two-hours bedding-in sequence described in *section 2.4* was performed before the fatigue test. The frequency of acquisition of the camera was 2 Hz. The cyclic frequency was 0.1 Hz and the cyclic amplitude was between 2% of MBL (800 N) and 45% of MBL (17 500N). The R-ratio of this fatigue test was 0.044. The fatigue test was interrupted, before failure, at 830 cycles and was followed by a recovery of 3 hours at 900 N.
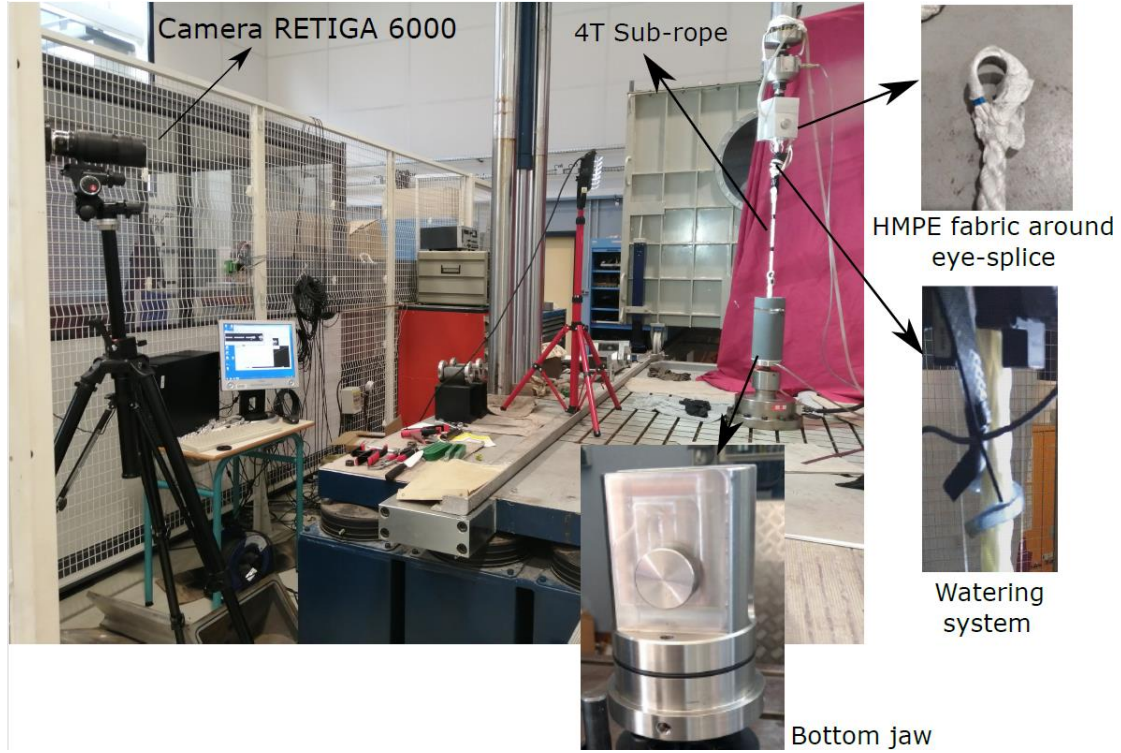
Figure 2.9 - Experimental set-up for the fatigue tests with strain measurement by image correlation analysis using a CCD camera and with a vertical watering system

2.5.3.4. Constitutive response and behaviour law

Multi-relaxation tests were performed on 4T sub-rope samples and on a 7T sub-rope sample to investigate the viscoelastic and viscoplastic properties of the polyamide 6 sub-rope and to identify a one-dimensional behaviour law. The procedure applied to each sample includes cyclic loading, relaxations, recoveries and a complex loading history with various maximum loading states (Figure 2.10). This enables most of the elasto-visco-plastic behaviour to be described. A stochastic test on a 7T sub-rope sample was also performed and used as a second validation test of the law. This study is presented in Chapter 3.

2.5.3.4.1. Multi-relaxation tests

During this study, multi-relaxation tests were performed on long samples to investigate the viscoelastic and viscoplastic properties of the polyamide 6 sub-rope. The results are detailed in chapter 3.
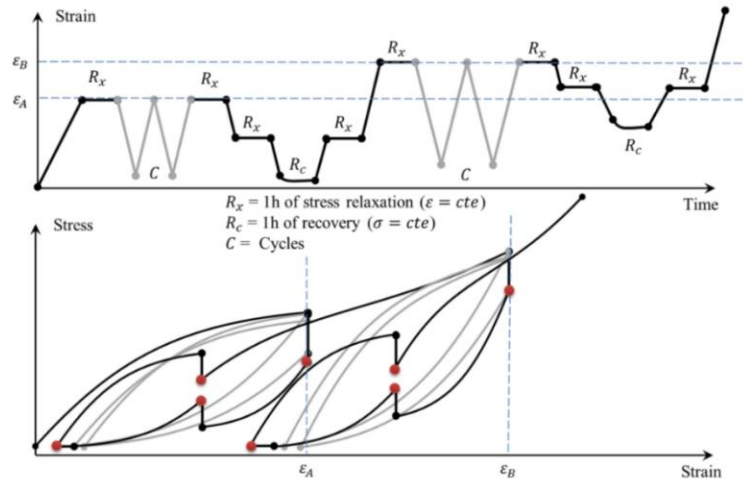
Figure 2.10 - Scheme of the loading path of the multi-relaxation tests (Chevillotte, 2020)

The samples were two 2-meter-long 4T sub-rope samples and one 6-meter-long 7T sub-rope sample. Therefore, they cannot be tested on the Servotest testing device. These samples were tested at IFREMER using a servo hydraulic machine with a load capacity of 300 ± 1 kN and a piston stroke of 3 m. The loading pin diameter was 80 mm. Samples were immersed for 16h before testing and sprayed with water during the tests as shown in Figure 2.11. The strain in the section between splices was determined using two wire displacement transducers (WS10-500 R1K-SB0-D8 and WS10-1000-R1K-SB0-D8) attached to points about 1 meter or 2 meters apart. The acquisition frequency was 10 Hz.

Figure 2.11 - Servo-hydraulic machine with 300 kN capacity: (left) 6-meter-long 7T sub-rope sample installed on the testing machine, (right) 4T sub-rope sample installed on the testing machine.

Two multi-relaxation tests were performed on two 4T sub-rope samples (one virgin and one collected after creep duration of 2 years). The 2-meter 4T sub-rope samples are too small for this testing machine. Hence, an extension was added to link the sub-rope to the pins.

These tensile tests were preceded by the bedding-in procedure described in *section 2.4*. The procedure is shown schematically in Figure 2.10 and can be described as follows:

- The cyclic loading was piloted by piston displacement at a strain rate around $8 \cdot 10^{-5}\ s^{-1}$ (0.08 mm.s^{-1})
- The unloading before recovery at 900N was controlled by force at an unloading rate of $10\ kN.s^{-1}$
- Relaxation of 1 hour (by maintaining the piston position) at different strains during the cyclic loading

One multi-relaxation test was performed on a 6-meter-long 7T sub-rope sample. This tensile test was preceded by the bedding-in procedure described in *section 2.4*. The procedure for the 7T sub-rope was the following:

- The cyclic loading was piloted by piston displacement at a strain rate around $1 \cdot 10^{-5}\ s^{-1}$ (0.08 mm.s^{-1})
- The unloading before recovery at 900N was controlled by force at an unloading rate of $10\ kN.s^{-1}$
- Relaxation of 1 hour (by maintaining the piston position) at different strains during the cyclic loading

2.5.3.4.2. Stochastic loading on 7T sub-rope sample

A stochastic test was performed on a 7T sub-rope sample to validate a behaviour law under more representative in-service conditions. The experimental set-up is the same as for the multi-relaxation test (Figure 2.11). The test sequence was a 1-hour random amplitude time series, extracted from the results of simulations on a FOWT permanent mooring, and scaled to the sub-rope size. The procedure was the following:

- A bedding-in of 100 cycles between 14kN and 17kN
- A load spectrum characterized by a mean tension of 15.3 kN and a tension range of 10 kN.

Unfortunately, due to the small number of 7T sub-ropes available, the same sample had been through other load series before this one. In fact, the maximum load it had seen was 40kN and in addition, this sequence was performed after the sub-rope had been held in recovery at 2%MBL for three weeks. One could therefore consider that the sub-rope had nearly completely recovered from the previous test sequences. Nevertheless, this history of loading had an impact on the response the polyamide 6 sub-rope. This stochastic loading will be investigated in chapter 3 section 3.4.2.

2.5.3.5. Creep behaviour characterization

A creep behaviour study is presented in chapter 4 of this manuscript and the experimental protocols used are presented in this section.

2.5.3.5.1. Long term creep

A specific test frame was designed and built for long term creep tests, during the preceding project POLYAMOOR. It is a one-piece steel module made of a linear vertical system with pulleys. The pulley system imposes a force on the sample, that is twice the steel weights (Figure 2.12). To attach the splice termination to the machine, special grips with pins have been made. The pin diameter is 35 mm. Loads can be applied with modular steel weights which slide on the support. The load is measured above each upper pin by a 3000 daN load sensor (FSB251 from Tei technologies). Samples were immersed for 10 hours before testing and then tested in watertight tubes full of tap water. The water is directly pumped from a thermally controlled tank inside which the temperature is maintained at 20 ± 5 °C using three heaters (Eheim Jäger Thermocontrol™ 2048 100Watt).
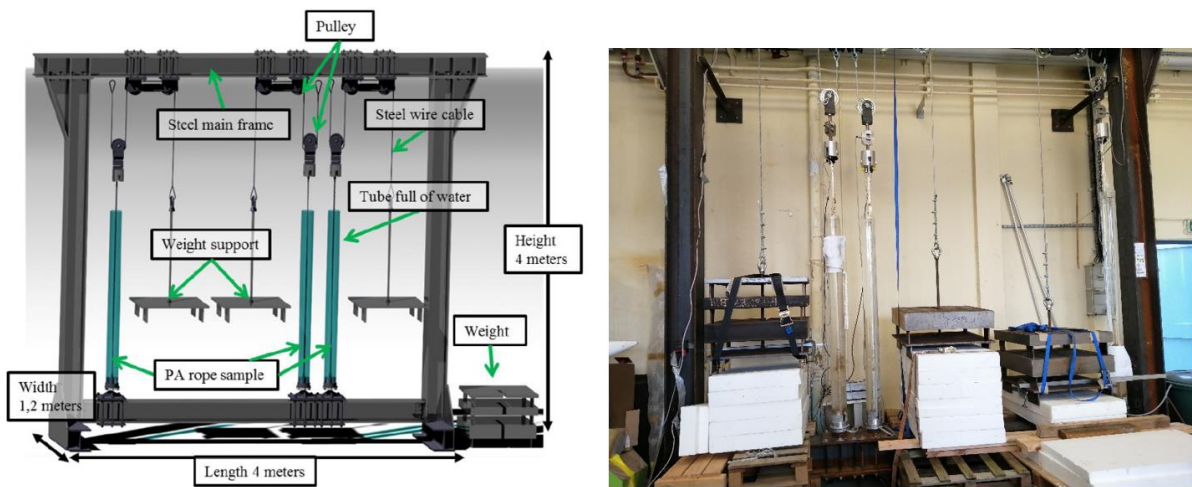
Figure 2.12 - a) Schematic diagram of the long-term creep test frame (Y. Chevillotte's PhD). b) Long term creep test frame

The water temperature of 20 ±5°C was set because it is an easy temperature to achieve throughout the year (different seasons) in Brest. It is also close to the mean ocean temperature (17.5 °C). Higher temperatures could have been used to accelerate creep, but analysis of results would then require the multiplication of tests to determine acceleration factors, so for this series a single representative temperature was preferred.
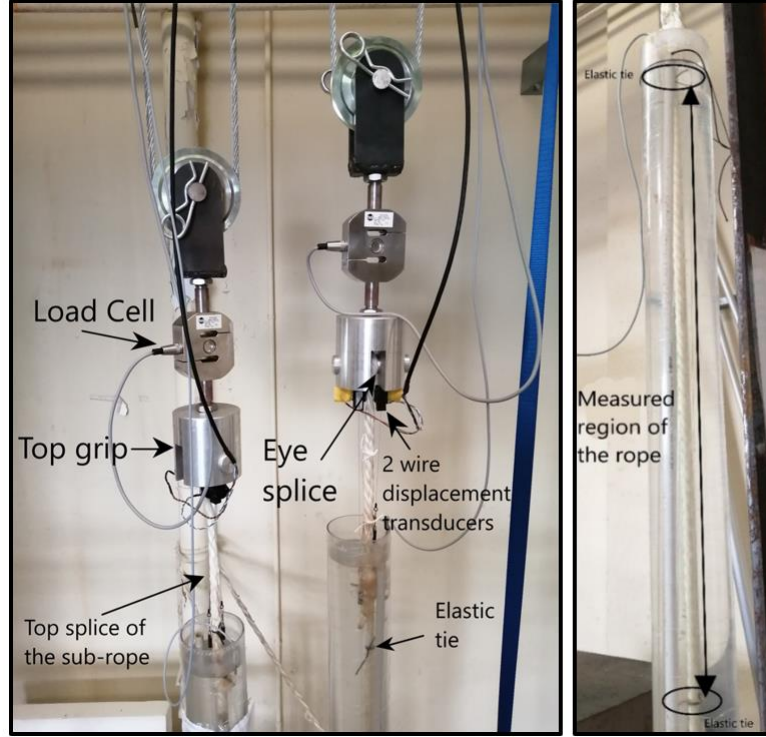
Figure 2.13 - a) Picture of the measurement system. b) Measured region of the rope

The bottom grip enables the water flowing down the rope to be collected and returned to the tank. Regulation was generally satisfactory during the two-year test period except for two peaks; a cold one during 3 days in February 2021 and a hot one during four days in July 2021. These temperature variations did not have a visible effect on the creep curves. The elongation was measured using two wire displacement transducers attached to the top of the set-up (WPS-500-MK30-P10 and WPS-750-MK30-P10) fixed to the central part of the sub-rope at two points with 2mm diameter elastic ties. A minimal distance of at least 100 mm from the end of the splice was respected to fix the elastic ties so as not to be affected by the splices. The average length between the two measurement points was around 900 mm (Figure 2.13-b). The elongation of the rope is defined by Eq. 13:

$$\frac{\Delta L}{L_0} = \frac{(C1 - C1_0) - (C2 - C2_0)}{L_0} \qquad \textit{Eq. 13}$$

L_0 being the length between the two elastic ties taken after the 10 hours of immersion. $C1$ and $C2$ are the measurements of the two wire displacement transducers. $C1_0$ and $C2_0$ are the values of the sensors when the length is L_0.

For the loading phases (beginning of the tests and reloading for some tests), the acquisition system was set with a high acquisition frequency (10 Hz) for one day. This was then changed to an acquisition rate better adapted to long term measurements: three acquisition periods per day, each of 10 minutes at 1 Hz. The acquisition system was shut down in between the measurements to be sure the sensor's conditioning would not evolve, as it calibrated each time it was switched on.

The tests performed during the first part of the long-term creep campaign are presented in Table 2.5. Test LC45$_B$ was performed with the bedding-in procedure described in *section Bedding-in procedure*. Test LC45$_A$ is the same test but the sample did not undergo the bedding-in. The comparison of these two tests allowed us to study the effect of the bedding-in (BI) procedure.

Table 2.5 - Procedure for long term creep tests. For test LC45B, we performed the bedding-in sequence detailed in section 2.4

Test names	Creep phase				Recovery phase		Second Creep phase	
	Load (kN)	Load (N/tex)	Load (%MBL)	Duration (days)	Unload (kN)	Duration (days)	Load (%MBL)	Duration (days)
$LC45_B$ With BI	18	0.20	45	405	1.08	672	45	281
$LC45_A$	18	0.20	45	0.16	Stopped	Stopped	Stopped	Stopped
$LC25$	9.9	0.11	25	424	1.08	414	Stopped	Stopped
$LC39$	15.750	0.175	39	1316	/	/	Still in first creep	Still in first creep

One specific test was performed to simulate a creep during a storm. The aim of this experiment was to investigate if short term creep at high loads is more important than long-term creep at service tension load. The procedure for this test is described in Table 2.6:

Table 2.6 - Specific procedure for storm effect creep tests, also called 'Cyclic creep' test

Step	Description	Duration	Comment
1	Load to 39% MBL (as close as possible to this value)	1 hour	Storm/pre-stretch
2	Reduced load to 25%MBL (as close as possible to this value and without dropping load to below 25%MBL)	83 days	Pre-tension
3	Load to 39% MBL (as close as possible to this value)	1 hour	Storm/pre-stretch
4	Reduced load to 25%MBL (as close as possible to this value and without dropping load to below 25%MBL)	393 days	Pre-tension

2.5.3.5.2. Short-term creep

Short-term creep tests were performed at IFREMER on the servo-hydraulic machine presented in section 2.5.3.4. The samples were immersed for 16 hours before testing and sprayed with water during the tests. The samples are of exactly the same geometry as long-term creep samples (1.80 meters long and with identical splices). The strain in the section between splices was determined using two wire displacement transducers (WS10-500-R1K-SB0-D8 and WS10-1000-R1K-SB0-D8) attached to points about 800 mm apart.

The tests performed during the short-term creep campaign are presented in Table 2.7.

Table 2.7 - Procedure for the short-term creep tests

Test names	Creep phase				Recovery phase	
	Load (kN)	Load (N/tex)	Load (%MBL)	Duration (days)	Unload (kN)	Duration (days)
$SC25$	9.9	0.11	25	0.125	1.08	0.125
$SC39$	15.750	0.175	39	0.125	1.08	0.125
$SC45$	18	0.20	45	0.125	1.08	0.125

2.5.4. Tensile testing of strands and rope-yarns

2.5.4.1. Capstan Terminations and capstan grips

For the sub-scales of a 4T-sub-rope samples, such as strands and rope-yarns, splices cannot be easily made. A recommended loading device for testing at these scales is the capstan. Capstans are cylinders around which we can wrap a rope, a strand, a rope-yarn or a yarn and block it in a fastening system. Ropes are often tensioned by capstans in the offshore sector.

A capstan termination uses the friction between the rope and the cylinder to hold the sample (Flory & Hagedorn, 2003). The increase of tension in a rope wrapped around a capstan is:

$$\frac{T_{high}}{T_{low}} = 2.718^{2\pi n\mu}$$

Eq. 14

With T_{high} the tension of the high side (here the sample gauge length), T_{low} the tension in the low side (here the clamp), n the number of wraps and μ the friction coefficient.

Figure 2.14 - Capstan grips

The higher the number of wraps, the lower the tension in the clamp. If insufficient turns are applied, the rope cannot be held by back tension in the clamp.

The advantage of a capstan termination is that the cylinder shape results in a homogeneous distribution of the tension in the gauge section at the exit of the capstan (Flory & Hagedorn, 2003; McKenna et al., 2004). The capstan diameter must be chosen with respect to the range of tension of interest. Because the capstan diameter adds to the number of turns needed, the samples studied can be long. In addition, some elongation will take place around the cylinder, requiring a test machine with high stroke or using a small gauge length.

For this study, split capstan grips were ordered from the Sofia High Tech company (Figure 2.14). The maximal force applicable to the sample attached to the fixtures is 50 kN which allows testing of rope-yarns (MBL of 1.2 kN) as well as strands (MBL of 14 kN). The minimum diameter of a specimen is 2 mm and the maximum diameter is 12 mm. These grips are made in stainless steel so they can be used in water (section 2.5.4.4).

2.5.4.2. Sample preparation

The samples studied were taken from the 4T sub-rope samples. The strands are extracted first by un-stranding the sub-rope into three strands. During this procedure, the aim is to keep the strand lay-lengths intact. The sub-rope was placed on a table. Then, the strands were slowly disentangled (Figure 2.15). The rope-yarn scale could then be extracted from the strand scale by the same un-stranding procedure.

Figure 2.15 - Strand sample preparation: disentanglement of the 3-strand 4T sub-rope

2.5.4.3. Quasi-static tensile tests on dry rope-yarns and strands

The mechanical behaviour of dry rope-yarns and strands were investigated with tensile tests to failure (see chapter 3). The capstan grips were mounted on a 200 kN capacity ROELL & KORTHAUS model RKM250 testing machine. A load cell of 200 kN was used. Only one wrap around the capstan is enough to hold a rope-yarn during a tensile test to failure. Two wraps around the capstan were needed for testing a strand to failure. The test loading rate was 50 mm. min^{-1}. Two black markers were placed on the sample. The displacement of these markers was measured by image correlation analysis. Two Basler cameras of 2040x1080 pixels resolution allowed each marker to be followed during the tests. The distance between the capstan grips was 300 mm, leading to a gauge length (distance between markers) around 230 mm (Figure 2.16). The acquisition frequency was 1Hz for the cameras and 10 Hz for the load cell. No bedding-in sequence was applied before these tensile tests for time constraint reasons. Also, a bedding-in on this electromechanical machine with low loads (for strand and rope-yarn) is not recommended.

Figure 2.16 - Experimental set-up during a quasi-static tensile test on a strand with capstan grips. The same set-up is used for the rope-yarns.

2.5.4.4. Quasi-static tensile tests in water on rope-yarns

Quasi-static tests in water were performed on rope-yarns. The capstan grips were mounted on an MTS hydraulic tensile testing machine model 322.31 with a maximal load capacity of 250 kN (Figure 2.17). The load was measured using a 250 kN load cell.

This machine was used for two reasons:

- The hydraulic actuator is placed above the experimental set-up, which allows tests to be performed in a water tank without the risk of water reaching any critical part of the machine;
- The hydraulic actuator is also more suitable for cyclic tests (see next section).

The drawback of using this machine is its short stroke (300 mm). Only one wrap around the capstan grips could be applied for both the rope-yarns and the strands. The strands slip when the load reaches 10 kN. Hence, it was not possible to measure the load to failure in water for the strand scale.

Figure 2.17 - Hydraulic testing machine used for the test on rope-yarns and strands in water: actuator of the machine is Figure 2.17above, hence, no risk of water damaging critical parts.

The rope-yarn samples were immersed in water for 4 hours. Then, the samples were placed in water in a parallelepiped shaped tank made of Plexiglas placed on the tensile testing machine (Figure 2.18). This tank was designed specifically for these tests during this PhD. The dimensions were chosen so that the capstan grips would fit in the tank.

Two black markers were fixed on the samples. The displacement of these markers was measured by image correlation analysis. Two Basler cameras of 2040x1080 pixel resolution allowed each marker to be tracked during the tests. It was first verified that the Plexiglass did not generate any optical defects without water. Then, adding water, we checked using a ruler attached to the top jaw, that the measured displacement of the ruler was the same as the jaw displacement. The distance between the grips could not be higher than 200 mm, because of the short stroke, leading to a gauge length (distance between the markers) of around 120 mm. The acquisition frequency of the Basler cameras was 2 Hz. The acquisition frequency of the load cell was 4 Hz.

2.5.4.5. Tensile cyclic test in water on rope-yarns and strands

Tensile cyclic tests using similar load blocks to those for the self-heating procedure (presented in section Fatigue characterization on 4T sub-rope samples), adapted to rope-yarns and strands, were performed. Results from these tests are used to develop a meso-structural FEM model at the rope-yarn scale of a sub-rope during self-heating test (chapter 6). The tests on strands are validation tests for this meso-structural model.

The same experimental set-up as in section 2.5.4.4 was used. For tests on strands, rotation of the hydraulic actuator was blocked using two wooden beams attached to the machine frame. The rotation was induced by the torque applied by the strands to the actuator, due to their laid construction (Figure 2.18-right).

The longitudinal strain evolution during the tests was again followed by image correlation analysis. For this experiment, a measurement of the transverse strain (i.e the evolution of the section diameter) was also performed. This measurement is needed to investigate the "poisson effect". One *Ids camera* of 3469x3469 pixels resolution was placed close to the tank (Figure 2.18). The measurement was made by image analysis. The contrast between the white colour of polyamide 6 and a black background allowed the value of the section in pixels to be calculated during the tests. The section was measured along all the captured length and the average section was calculated and used to obtain the transverse strain. To allow this measurement, a specific software was programmed to automatically measure the section on all the captured length and to calculate the average. The acquisition frequency of the *Ids camera and the Basler cameras* was 2 Hz. The acquisition frequency of the load cell was 4 Hz.
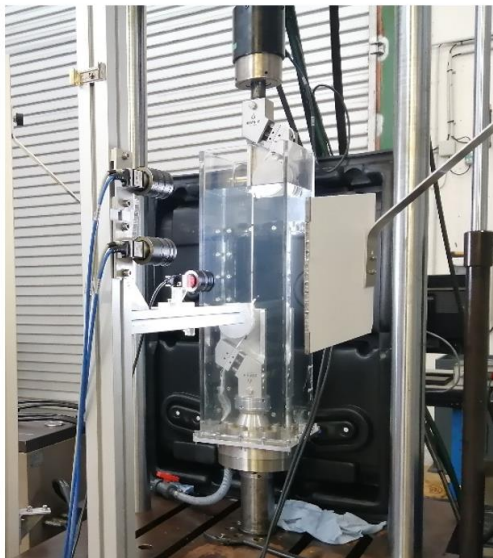
Test on rope-yarn   Test on strand
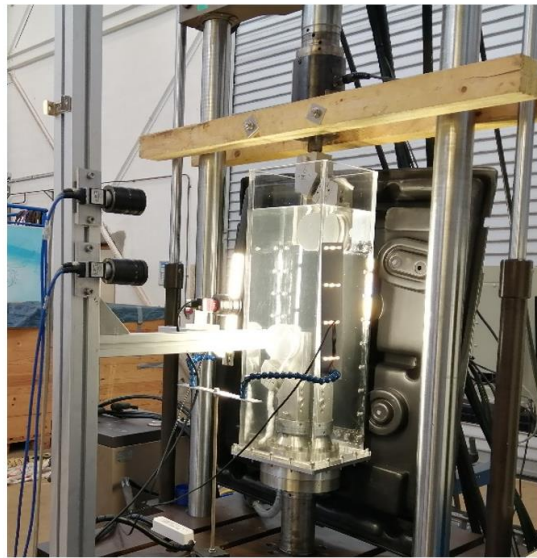
Figure 2.18 - Experimental set-up for cyclic tests in water with a plane-diopter tank and three cameras: two cameras for axial strain measurement; one camera for transversal strain measurement. Left: Test on rope-yarn scale. Right: Test on the strand scale (wood beams to block the actuator rotation).

Before testing, the samples were immersed in water during 4 hours for the rope-yarns and 16 hours for the strands.

A bedding-in sequence (section 2.4) of two hours was applied before each test. After the bedding-in, the test loading consisted of applying several cycle blocks of increasing load. Each block consisted of cycling between a fixed percentage of the minimal breaking load and a maximal load chosen for each block. The frequency for the cycles of each block was 0.1 Hz.

Figure 2.19 - Picture of the Vectran braided sheath (yellow) placed around the rope-yarns (white) for reducing the friction damage on contact with the capstan.

The procedure for the rope-yarns consisted of 50 cycles per blocks. Between two blocks, a load plateau at the mean load of the previous block was applied for 8 minutes. A ramp to failure at a rate of 50 mm.min^{-1} was performed after the last block. The rope-yarn was protected by a Vectran braided sheath (Figure 2.19). Without this protection, the friction between the rope-yarns and the capstan cylinder is too high and failure occurs prematurely due to friction before the end of the procedure.

The procedure is described in Table 2.8:

Table 2.8 - Load sequence applied during the cyclic tests in water on the rope-yarn scale

Block number	Minimal load (%MBL – kN)	Maximal load (%MBL – kN)	Load at plateau (%MBL – kN)
1	5 - 0.06	30 - 0.33	18 - 0.20
2	5 - 0.06	40 - 0.45	23 - 0.26
3	5 - 0.06	50 - 0.56	28 - 0.31
4	5 - 0.06	60 - 0.67	33 - 0.37
5	5 - 0.06	70 - 0.78	38 - 0.42

The loads are expressed as a percentage of the minimal breaking load of the sample. The measured minimal breaking load for the rope-yarns in water is 1.12 kN.

The procedure for the strands is not the same as for the rope-yarns. Adding a sheath to the strand leads to slippage in the clamp (the friction is not high enough to hold the sample in the clamp). Hence, as we could not avoid the friction, we chose to shorten the test procedure. The number of cycles per blocks was decreased to 25 cycles per block. A load plateau at the mean load of the previous block was performed for 3 minutes. No ramp to failure was performed because the test was ended by failure due to friction before reaching the ramp.

The procedure is described in Table 2.9:

Table 2.9 - Load sequence applied during the cyclic tests on the strand scale

Block number	Minimal load (%MBL – kN)	Maximal load (%MBL – kN)	Number of cycles	Load at the plateau (kN)
1	3 – 0.42	20 – 2.8	25	1.6
2	3 – 0.42	30 – 4.2	25	2.3
3	3 – 0.42	40 – 5.6	25	3.0
4	3 – 0.42	50 – 7.0	10 to 20 (then rupture)	-

The loads are expressed as a percentage of the minimal breaking load of the sample. No breaking load in water could be measured for strands. Hence, a minimal breaking load of 14 kN measured on dry sample was taken.

2.5.4.6. Diametral compression tests on dry strands

The investigation of the diametral compression behaviour of a strand is necessary to develop the meso-structural FEM model of a sub-rope at the rope-yarn scale (chapter 6). The aim of this test is to determine the behaviour of a bundle of rope-yarns in transversal and longitudinal shear. This investigation is further developed in chapter 6 of this manuscript.

The capstan grips are mounted on the same testing machine described in section 2.5.4.3. Two wraps around the capstan are done.

A specific "3-rod" device was designed for this study. It consists of one rod and two rollers (Figure 2.20-left). The strand is placed around the rod and rollers such that it will be in diametral compression on the central rod during the tensile test (Figure 2.20-right).

 The central rod has a 20 mm diameter and cannot rotate. The rollers at the top and bottom have a 30 mm diameter and are shaped to align the "3-rod" device to the tensioned strand axis. They are mounted with ball bearings to ensure a homogeneous tension force along the strand. Then, the machine load sensor will measure the strand tension at the centre rod contact. For this study, an angle of 23° between the centre rod axis and the top and bottom roller axes was chosen. This angle produces a significant strand cross-section deformation, easier to measure.

Contact zone
observed

3D Artex spider scanner
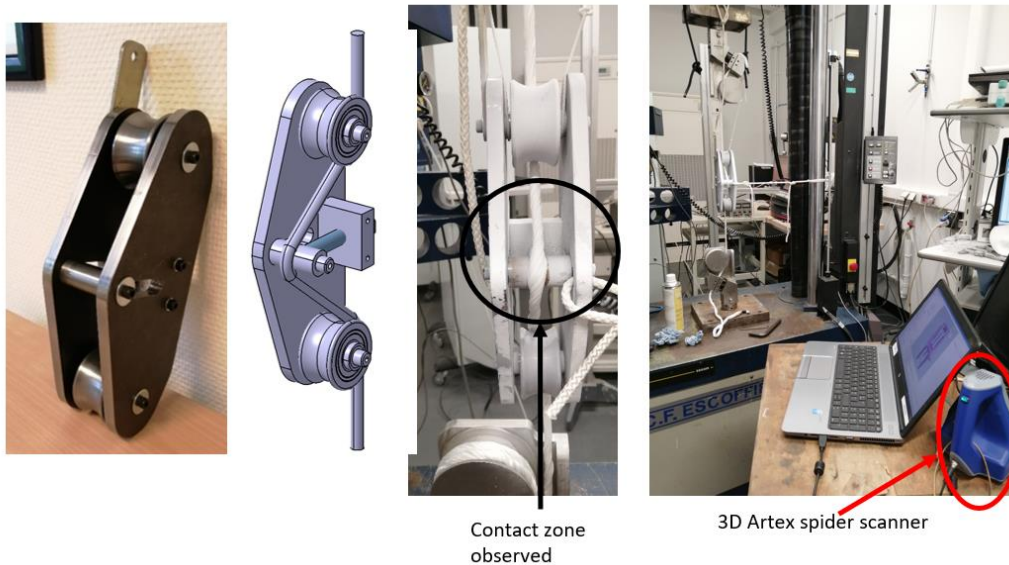
Figure 2.20 - Experimental set-up for the diametral compression of a strand. Left: "3-rod" specific part with one contact rod (middle) and two rollers (top and bottom). Middle: Sample installed on the capstan grips and through the 3-rod part. Right: Closer view of the contact zone inducing a diametral compression.

The test aims to follow the change in the cross-section of the strand during the contact with the central rod during the tensile test. A bedding-in sequence (section 2.4) of two hours was applied before each test. The procedure consisted of a quasi-static tensile test with interruptions from 0 kN to 10 kN, then an unloading with interruptions from 10 kN to 0kN at a loading rate of 50 mm/min.

During each interruption, 3D images of the contact of the strand on the central rod were taken using an Artec Space Spider™ 3D Scanner with a resolution of 0.1 mm and a precision of 0.05 mm (the precision is the accuracy of the numerical copy of the object in comparison with the object; the precision is improved thanks to the calibration performed and can be manually adjusted). One minute was needed to perform a complete 3D scan. Anti-reflection powder was pulverized on the strand and the "3-rod" device to allow the 3D scan measurements.

2.5.5. Additional analyses

2.5.5.1. Microscopy

Scanning Electron Microscopy SEM (JEOL IT 300 LV) was used to assess the main phenomena involved in fatigue failure (chapter 5). We worked in partial vacuum because polyamide is an electrical insulator. Hence, working in total vacuum will disturb the observation. On the contrary, working in partial vacuum allows to deviate the electrons beam and to decrease its power when interacting with the polyamide surface. The pressure in the chamber was 70 Pa. The detector used was a SED detector dedicated to scanning the surface electrons in partial vacuum. The voltage used was 10 kV, the working distance was 14.5mm and the probe current was 45.

2.5.5.2. Tomography

X-ray micro-tomography was used to examine both the details of the rope construction and the development of damage during cycling (chapter 5). This technique involves rotating a sample in an X-ray beam and recording the images. A 3-D reconstruction of the volume is realized with the recorded images. Figure 2.21-c) shows the equipment used (CRT Morlaix, France). The resolution was 20 µm. In order to scan a complete pitch length (50 mm), 3 scans with 2200 images were taken. The total duration was 45 minutes. A specific experimental set-up (Figure 2.21-a, b, c) was developed to allow tomographic analysis on a sub-rope under a small tension (400 N). The attachments of the sub-rope consist of two dead turns around a pin. The sample is placed in a tube is made of polyacetal to avoid filtering the x-ray radiation. The sub-rope is mechanically loaded using mounting bolts. A load sensor placed at the bottom of the set-up allows the tension to be measured before putting it into the tomograph. After applying a tension, the sample was left in relaxation for 20 minutes (constant strain) to assure a stabilization of the load value and of the construction (to limit the viscous movement).
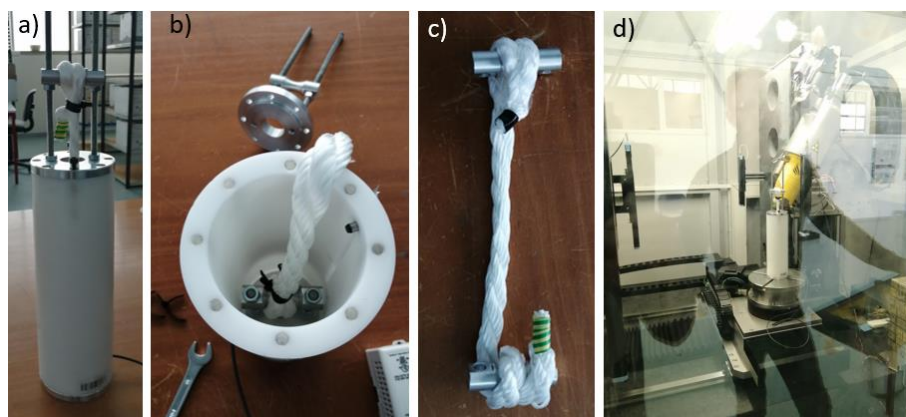
Figure 2.21 – Tomography set-up for 4T sub-rope. a) Whole set-up with sub-rope under tension. b) Set-up with sub-rope attached at the bottom. b) Example of the total attachment with dead turns. b) Set-up inside the X ray tomography chamber

2.6. Conclusions

For this work, a laboratory scale three-stranded twisted sub-rope (minimum breaking load of 4T) and, a higher scale sub-rope (minimum breaking load of 7T), are studied. The experimental methods for testing sub-ropes in water, already present in the laboratory, and developed during Chevillotte work, have been used. The experimental methods to test the smaller scales (rope-yarns and strands) in water have been developed during this study.

Now that the materials and methods are presented, they will be used to study the different scale of polyamide 6 sub-ropes. Next chapter proposes an experimental and modelling study of the constitutive behaviour of polyamide 6 sub-ropes.

Chapter 3. Constitutive behaviour: experiments and modelling

3.1. Introduction

The present chapter is mainly devoted to a study of the POLYAMOOR constitutive law, developed by Chevillotte (Chevillotte, 2020) and based on Flory's proposal. Its development is based on the characterization of a polyamide 6 sub-rope in water and under representative loadings. This phenomenological model aims to describe the complex visco-elasto-plastic behaviour of polyamide 6 lines during loading at sea with (creep-recovery and cycling), considering the history of loading, with one set of parameters and one direct identification method. This model is also implementable in the one-dimensional finite element analyses used in industry (using software such as ®Deeplines, ®Orcaflex, ®Flexcom, ®Sima …).

The beginning of this chapter describes the visco-elasto-plastic characterization method proposed by Chevillotte and the POLYAMOOR constitutive law that was developed based on this characterization. Chevillotte's identification and validation work on virgin 4T sub-rope is briefly recalled and summarized. This first part is an opportunity to investigate the complex response of the studied polyamide sub-rope. A full study on virgin 4T sub-ropes (development, identification and validation) is the subject of a paper under submission (Civier et al., 2023). This study is also presented in chapter 2 of Chevillotte manuscript thesis (Chevillotte, 2020).

After that, a study of a 4T sub-rope after creep. Both, an analysis of the evolution of the mechanical properties, and an identification of the parameters of the POLYAMOOR law following the method described in the first section, are proposed. Finally, an identification of the POLYAMOOR law, on a more representative construction followed by a validation using a more representative in-sea loading sequence, is presented.

The aim of this study is to investigate the ability of the law to describe different constructions and also to determine the sensitivity of the parameters to mechanical aging.

3.2. Elasto-visco-plastic constitutive POLYAMOOR law

First, the visco-elasto-plastic characterization and associated constitutive law proposed by Chevillotte are described. The law requires 11 parameters. Their identification is based on the analysis of the experimental results from multi-relaxation tensile tests (Figure 3.1). An example of the experimental results from this type of test, for a 4T sub-rope sample, is shown in Figure 3.1. This characterization provides the identification of a visco-elasto-plastic behaviour law based on Flory's model.
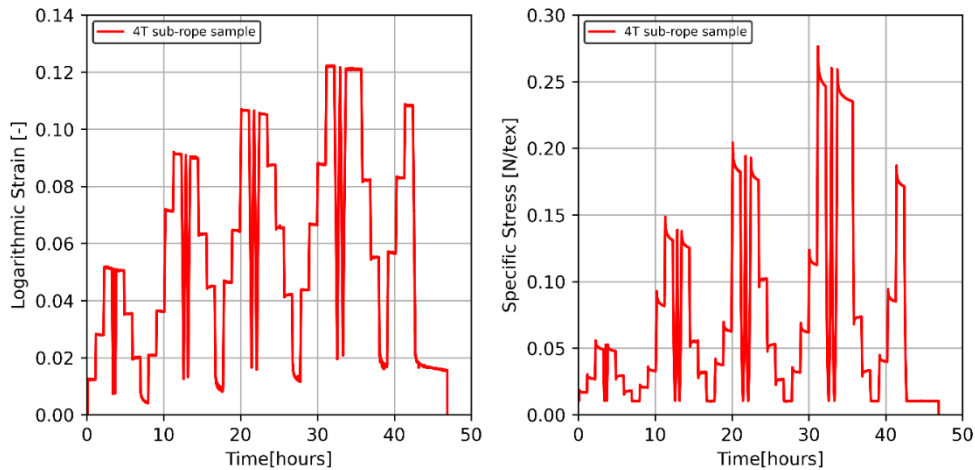
Figure 3.1 - Left: Logarithmic strain versus time of a 4T sub-rope sample during multi-relaxation test. Right: Specific Stress of a 4T sub-rope sample during multi-relaxation test

The one-dimensional spring-dashpot-ratchet law is represented in Figure 3.2 and has the following elements:

- A fast spring describing the dynamic behaviour,
- A dashpot responsible for the viscous response of the polymer,
- A time-independent part consisting of a ratchet element for the plasticity, and a slow spring responsible for the relaxed elasticity.

This proposed law does not represent the construction stretch and the stabilization of the amorphous region, assuming that the bedding-in procedure has been previously applied.
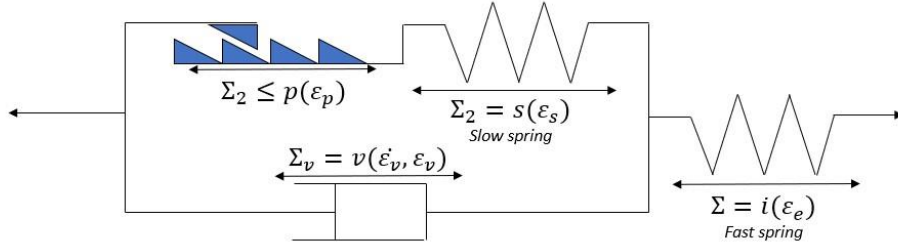
Figure 3.2 - The POLYAMOOR constitutive law

Two major hypotheses led to this model. First, the separate dashpot D$_4$ in Flory's model (Figure 1.19) was removed by considering that a fully relaxed state exists, which means a stabilized state at the end of all creep and relaxation steps (François and Davies assumption (François & Davies, 2008)).

Second, it was observed that the dynamic elasticity modulus is a linear function of stress (see next section 3.2.1). Therefore, it is not affected by the loading history. The dynamic behaviour of Flory's model is revealed by replacing dashpot D$_2$ by a rigid link; the resulting behaviour is not exclusively elastic because of the position of the ratchet element in Flory's model. So, in the proposed law, the ratchet element is put in parallel with the dashpot (Figure 3.2). Therefore, the dynamic behaviour is exclusively given by the elastic spring "i" (fast spring) and is not history dependent.

We can note that this model is similar to the Syrope model presented in chapter 1 section 1.7.1 (Falkenberg et al., 2017) as it can describe the dynamic stiffness thanks to the fast spring and it can also describe both the original curve and the working curve with the fast spring, slow spring and non-linear ratchet elements. The main equations describing this model are the following:

$$\varepsilon = \varepsilon_e + \varepsilon_v \qquad \textit{Eq. 15}$$

$$\varepsilon_v = \varepsilon_p + \varepsilon_s \qquad \textit{Eq. 16}$$

$$\Sigma = \Sigma_v + \Sigma_2 \qquad \textit{Eq. 17}$$

$$\text{with } \Sigma = i(\varepsilon_e) \qquad \textit{Eq. 18}$$

$$\text{and } \Sigma_2 = s(\varepsilon_s) \qquad \textit{Eq. 19}$$

$$\text{and } \Sigma_v = v(\dot{\varepsilon}_v, \varepsilon_v) \qquad \textit{Eq. 20}$$

$$\text{with } \Sigma_2 \leq p(\varepsilon_p) \qquad \textit{Eq. 21}$$

$$\text{and } \dot{\varepsilon}_p \geq 0 \qquad \textit{Eq. 22}$$

$$\text{and } \dot{\varepsilon}_p \cdot [\Sigma_2 - p(\varepsilon_p)] = \dot{\varepsilon}_p \cdot [\Sigma_2 - \dot{p}(\varepsilon_p)] = 0 \qquad \textit{Eq. 23}$$

Where ε and Σ are the strain and the specific stress of the model, respectively. $i(x)$, $s(x)$, $p(x)$ and $v(x, y)$ are non-linear real functions of real variables. $\dot{\varepsilon}_v$ and $\dot{\varepsilon}_p$ are the rates or time derivatives of viscous strain ε_v and plastic strain ε_p. Equations (Eq. 21, Eq. 22, Eq. 23) constitute the classical Kuhn-Tucker conditions for elastoplastic models.

The last three equations are equivalent to the following:

$$\varepsilon_p = p^{-1} \left(\max_{\tau \in [0,t]} (\Sigma_2(\tau)) \right)$$

<div align="right">*Eq. 24*</div>

Where t is the current time, and time 0 describes the time at which the rope was in a virgin state before any mechanical loading.

Each element, and its identification, is described in the following sections. The full identification method and development of model (with associated figures for a 4T virgin sub-rope), proposed in Chevillotte work, is described in a paper currently under submission (Civier et al., 2023). The figures associated with the identifications on a virgin 4T sub-rope are presented in Appendix A (p.201).

3.2.1. Dynamic non-linear elasticity

Short term elasticity can be observed at high frequencies, high strain rates or during sudden changes in the loading. Short term elasticity is occurring at every re-loading after a relaxation, a creep or a recovery. The tangent modulus, just after these stages (named E_{inst} in Figure 3.3) , is considered as a short-term elasticity (Bles *et al* 2009). This modulus is the equivalent of the fast spring in Flory's model during unloading. In the proposed model, this dynamic non-linear elasticity is represented by the fast spring $i(\varepsilon_e)$.

It was observed the dynamic stiffness is linear with respect to the specific stress (an example of an identification for 4T sub-rope after creep is presented in Figure 3.19-left). It confirmed that the dynamic elasticity is not impacted by the history of loading. The function $\Sigma = i(\varepsilon)$ describing this nonlinear elasticity was chosen as follows:

$$\Sigma = i(\varepsilon) = \frac{b}{a} \cdot (e^{a \cdot \varepsilon} - 1)$$

<div align="right">*Eq. 25*</div>

Where a has no units and b is in N/tex.
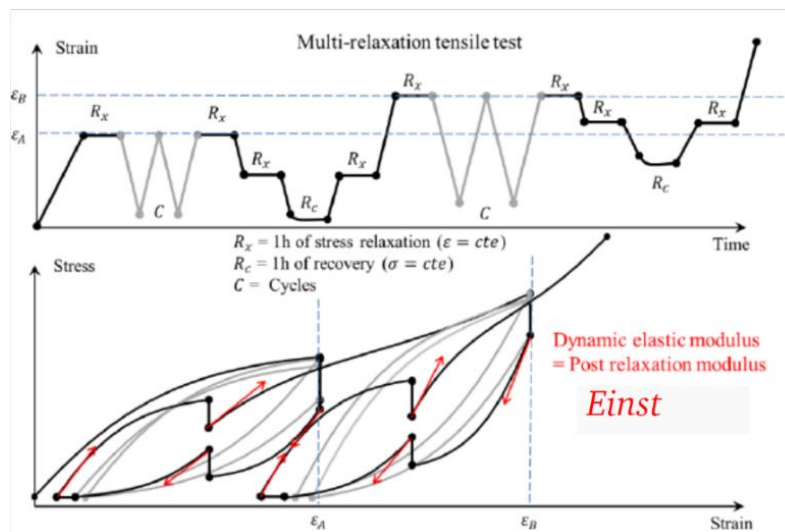
Figure 3.3 - Method for measuring the short-term elastic modulus (Chevillotte, 2020)

This result is in accordance with the work of François and Davies who found the dynamic stiffness to be linear with respect to the mean load for polyester mooring lines (François & Davies, 2008).

3.2.2. Fully relaxed behaviour

François and Davies defined a fully relaxed behaviour (FRB) (François & Davies, 2008). This behaviour should include all the time-independent behaviour contributions, which are: the relaxed nonlinear elasticity and the plasticity. Since it is not possible to obtain a fully relaxed state which, theoretically, would require an infinite relaxation time, the following hypothesis was assumed: at the end of some periods R_x, it was observed that when two relaxations were at the same strain (one during the loading and the other during the unloading), a fully relaxed state could be defined by extending the two time evolutions of the stress relaxation until they meet each other (see scheme on Figure 3.4).
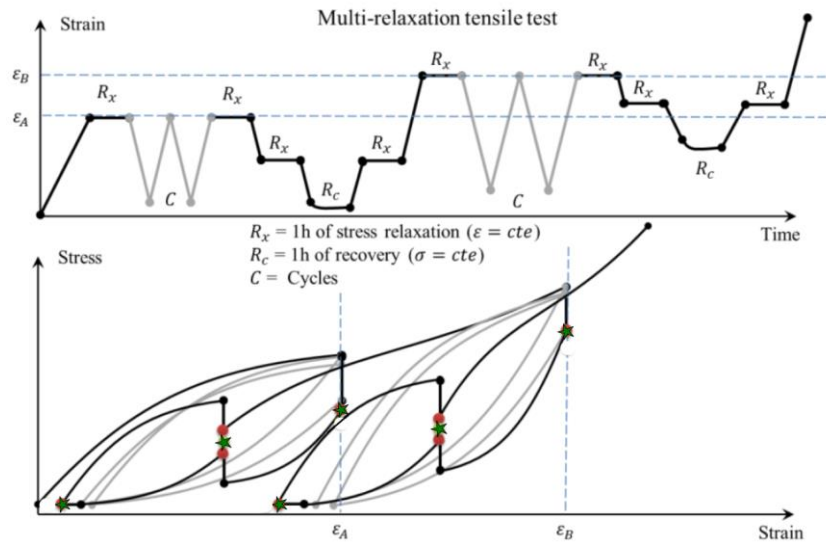
Figure 3.4 - Method for measuring the fully relaxed state (FRB). Green stars: middle points between two relaxations

Hence, a fully relaxed mechanical state can be associated to the stress values at the middle point between two associated relaxations (green stars on Figure 3.4). These fully relaxed strain-stress points were measured for 4T sub-ropes and an example of these fully relaxed strain-stress values, for a virgin 4T sub-rope, is given in Figure 3.5.
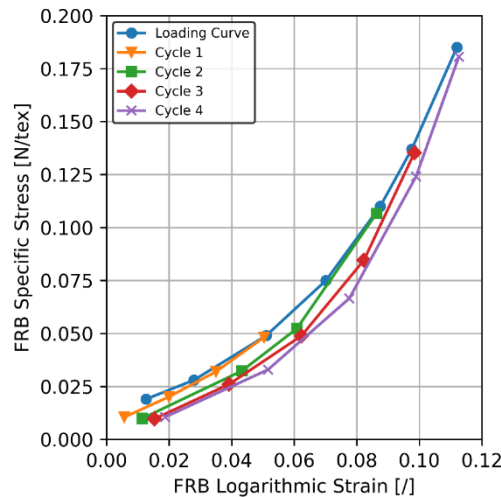
Figure 3.5 - Fully relaxed behaviour (FRB) measured on 4T sub-ropes

On Figure 3.5, we observe that the curves obtained are very similar to the ones of the Syrope model; the original working curve of the Syrope model could be compared to the first loading curve and the working curve corresponds to the FRB curves during cycles (chapter 1 section 1.7.1, Figure 1.18).

This method gives an approximate value of the fully relaxed or time-independent behaviour. Considering the POLYAMOOR model, this behaviour is revealed when the dashpot element is taken out. Only the spring and ratchet elements remain as shown on Figure 3.6.
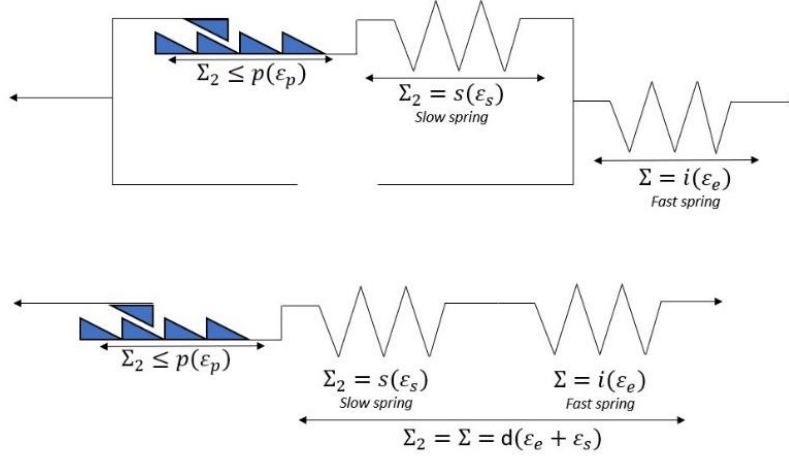
Figure 3.6 - POLYAMOOR model in the case of the fully relaxed behaviour (when the dashpot viscosity is fully relaxed).

For the cycles of the fully relaxed behaviour (not for the loading curve), a tangent modulus $M_{FRB} = \frac{d\Sigma_{FRB}}{d\varepsilon_{FRB}}$ can be determined between two measured relaxed states of the same cycle. It was observed that the measured tangent modulus, M_{FRB}, was linear with respect to the specific stress (an example of an identification for 4T sub-rope after creep is presented in Figure 3.19-right).

A relationship between the stress and the strain $\Sigma_{FRB} = d(\varepsilon_{FRB})$ was therefore found with $d(\varepsilon)$ following:

$$d(\varepsilon) = \frac{g}{c} \cdot (e^{c \cdot \varepsilon} - 1)$$

<div align="right">*Eq. 26*</div>

Parameter c has no units and g is in N/tex.

This is very similar to the quasi-static stiffness introduced by François and Davies who also observed it was linear with the mean load.

As showed in Figure 3.6, the function $d(\varepsilon)$ describes the two springs, ("s" and "i"), in series. So,

$$d^{-1}(\Sigma) = i^{-1}(\Sigma) + s^{-1}(\Sigma)$$

<div align="right">*Eq. 27*</div>

Where $f^{-1}(y)$ denotes the inverse function of a function $f(x)$. Thanks to Eq. 27 and because the function $i(\varepsilon)$ is already identified, the identification of the function $d(\varepsilon)$ provides an identification of the function $s(\varepsilon)$:

$$s^{-1}(\Sigma) = \frac{\ln\left(\frac{c}{g} \cdot \Sigma + 1\right)}{c} - \frac{\ln\left(\frac{a}{b} \cdot \Sigma + 1\right)}{a}$$

<div align="right">*Eq. 28*</div>

This function is inversed numerically using the one-dimensional Newton-Raphson algorithm. So, at this stage, functions $i(\varepsilon)$ and $s(\varepsilon)$ are fully identified. Once the fast elasticity and the slow elasticity are identified, the plastic strain during the experimental test can be deduced.

3.2.3. Plasticity

In the case of the fully relaxed behaviour, the stress of the dashpot element is assumed to be zero:

$$\Sigma_v = 0 \qquad \text{Eq. 29}$$

$$\text{So, } \Sigma_{FRB} = \Sigma_2 \qquad \text{Eq. 30}$$

According to the model definition equations and according to equation Eq. 27 in the FRB case, that is:

$$d^{-1}(\Sigma_{FRB}) = i^{-1}(\Sigma_{FRB}) + s^{-1}(\Sigma_{FRB}) = \varepsilon_{e\,FRB} + \varepsilon_{s\,FRB} = \varepsilon_{FRB} - \varepsilon_p \qquad \text{Eq. 31}$$

we have:

$$\Sigma_{FRB} = d\big(\varepsilon_{FRB} - \varepsilon_p\big) \qquad \text{Eq. 32}$$

For the fully relaxed cyclic behaviour, this leads to the strain-stress $(\varepsilon_{FRB}, \Sigma_{FRB})$, illustrated Figure 3.5, curve being shifted horizontally to the right when the plastic strain ε_p increases.

The plastic strain value increases from one cycle to another as the intersections of the curves with the plastic strain (abscissa axis) are shifted to higher values for each cycle. This identified plastic strain (ε_p) of the model may correspond to the concept of permanent elongation described by François and Davies.

Because the function $d(\varepsilon)$ has been identified previously, we can calculate the plastic strain using:

$$\varepsilon_p = \varepsilon_{FRB} - d^{-1}(\Sigma_{FRB}) \qquad \text{Eq. 33}$$

Therefore, the plastic strain is a function of the maximum stress Σ_{FRB} as illustrated on Figure 3.7.
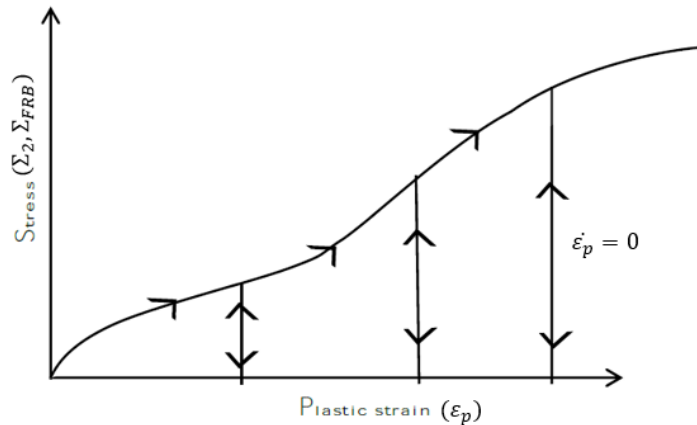
Figure 3.7 - Pattern of the plasticity of the fully relaxed behaviour, resulting from the Kuhn-Tucker conditions as part of the proposed model definition; the plastic strain can increase only when stress $\Sigma_{FRB} = \Sigma_2$ reaches values $p(\varepsilon_p)$.
(Chevillotte, 2020)

A quasi-linear relation between the plastic strain and load, except at the beginning of the curve, was observed. To describe as closely as possible this behaviour, the function was chosen as follows:

$$p(\varepsilon_p) = e \cdot \left(\tanh(f.\varepsilon_p + h) + 1\right) \text{ when } \varepsilon_p \leq \frac{-h}{f}$$

<div align="right">*Eq. 34*</div>

$$p(\varepsilon_p) = e \cdot \left(f \cdot \varepsilon_p + h + 1\right) \text{ when } \varepsilon_p > \frac{-h}{f}$$

<div align="right">*Eq. 35*</div>

Parameters f and h have no units while e is in N/tex (the identifications for a 4T virgin sub-rope and a 4T sub-rope after creep is presented in Figure 3.20).

The only element, that remains to be identified, is the viscosity element.

3.2.4. Viscosity

The viscosity part is described in more details as a simplification of its definition has been made in comparison with Chevillotte's work.

The viscosity is represented by the dashpot, which is in parallel with the slow spring and ratchet element. A nonlinear behaviour of the viscosity element was assumed following the equation below inspired by the work of (François & Davies, 2008):

$$\Sigma_v = v(\dot{\varepsilon}_v, \varepsilon_v) = W_2(\varepsilon_v) \cdot \sinh^{-1}\left(\frac{\dot{\varepsilon}_v}{W_1(\varepsilon_v)}\right)$$

<div align="right">*Eq. 36*</div>

Where Σ_v and $\dot{\varepsilon}_v$ are respectively the stress and the strain rate of the viscosity element. This behaviour leads to an analytical solution that can be approximated by a logarithm of the time for the relaxation. Hence, it is coherent for predicting the stress relaxation and creep strain for polyamide 6 rope which follows a logarithmic time evolution (Civier et al., 2022).

Using the previous identification of the elastic part, the viscous strain during the experimental tests can be deduced using the expression Eq. 15:

$$\varepsilon = \varepsilon_e + \varepsilon_v \iff \varepsilon_v = \varepsilon - \varepsilon_e \iff \varepsilon_v = \varepsilon - i^{-1}(\Sigma)$$

<div align="right">*Eq. 37*</div>

To calculate the viscous stress, the monotonic increasing plastic strain called 'load curve' is used (highlighted in Figure 3.8). This means that only the data from the loadings between the cycles are used. Hence, the obtained identification will include seven relaxations (corresponding to the seven load phases where the load exceeded the previous maximum load).

Along the loading curve, the ratchet element is activated (plasticity) ($\dot{\varepsilon}_p > 0$). According to the equations of the law, the stress Σ_2 and the plastic strain satisfy the limits of relation (Eq. 8):

$$\Sigma_2 = p(\varepsilon_p)$$

<div align="right">*Eq. 38*</div>

The viscous strain is equal to:

$$\varepsilon_v = p^{-1}(\Sigma_2) + s^{-1}(\Sigma_2)$$

<div align="right">*Eq. 39*</div>

We define a function k by its inverse as; $k^{-1}(\Sigma) = p^{-1}(\Sigma) + s^{-1}(\Sigma)$

<div align="center">So, we have: $\varepsilon_v = k^{-1}(\Sigma_2)$</div>

<div align="right">*Eq. 40*</div>

<div align="center">and $\Sigma_2 = k(\varepsilon_v)$.</div>

<div align="right">*Eq. 41*</div>
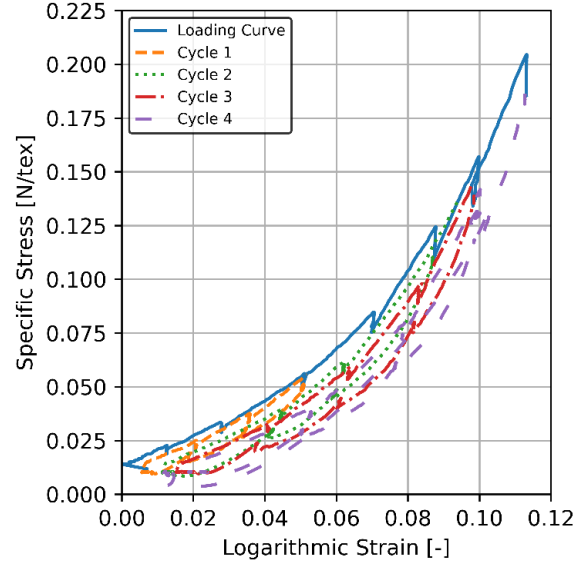
Figure 3.8 - Specific Stress (N/tex) versus logarithmic strain (-) during a multi-relaxation test; the blue continuous line is the loading curve. The dashed lines are the cycles. Case of a 4T subrope.

According to the equations of the model (Eq. 17), the viscous stress can be expressed as:

$$\Sigma_v = \Sigma - \Sigma_2 = \Sigma - k(\varepsilon_v)$$

<div align="right">*Eq. 42*</div>

$$\Leftrightarrow \quad \varepsilon - i^{-1}(\Sigma) - k^{-1}(\Sigma - \Sigma_v) = 0$$

<div align="right">*Eq. 43*</div>

To calculate the viscous stress, we can use the bisection (dichotomy) method to resolve the Eq. 43. This method was applied to the experimental results from multi-relaxation tests on a 4T sub-rope (Figure 3.9).
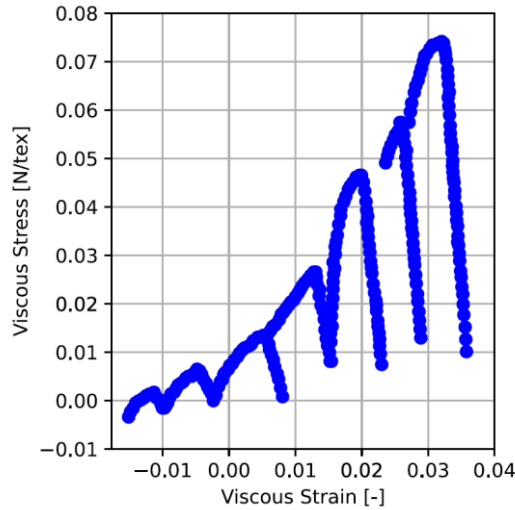
Figure 3.9 - Calculated viscous stress versus the viscous strain during the load curve (no cycle data) for a 4T sub-rope (the straight parts correspond to the relaxation stages of the test where the sub-rope strain is maintained constant)

To identify the parameters of the function $v(\dot{\varepsilon}_v, \varepsilon_v)$, the relaxation stages on Figure 3.9 are used. A linear regression between the viscous stress and the viscous strain for each relaxation stage is used:

$$\Sigma_v = -r \cdot \varepsilon_v + q$$

<div align="right">*Eq. 44*</div>

The chosen viscosity behaviour, added to this linear relation, led to the following differential equation:

$$\dot{\varepsilon}_v = W_1 \cdot \sinh\left(\frac{-r \cdot \varepsilon_v + q}{W_2}\right)$$

Eq. 45

The analytical resolution gives:

$$\Sigma_v(t) = 2 \cdot W_2 \cdot \tanh^{-1}\left[\tanh\left(\frac{\Sigma_v(t_0)}{2 \cdot W_2}\right) \cdot \exp\left(\frac{-r \cdot W_1 \cdot (t - t_0)}{2 \cdot W_2}\right)\right]$$

Eq. 46

In this equation resulting from the behaviour of the model, $\Sigma_v(t)$ is given by the data of Figure 3.9, and the parameter r is given by the linear regression (Eq. 44). The parameters W_1 and W_2 are optimized for a best fit on experimental data of each relaxation stage on Figure 3.9 (7 stages). This optimization was done by a non-linear least-squares Marquardt-Levenberg algorithm applied to Eq. 46. Figure 3.10 presents these values versus the mean value of the viscous strain during the relaxation stages.
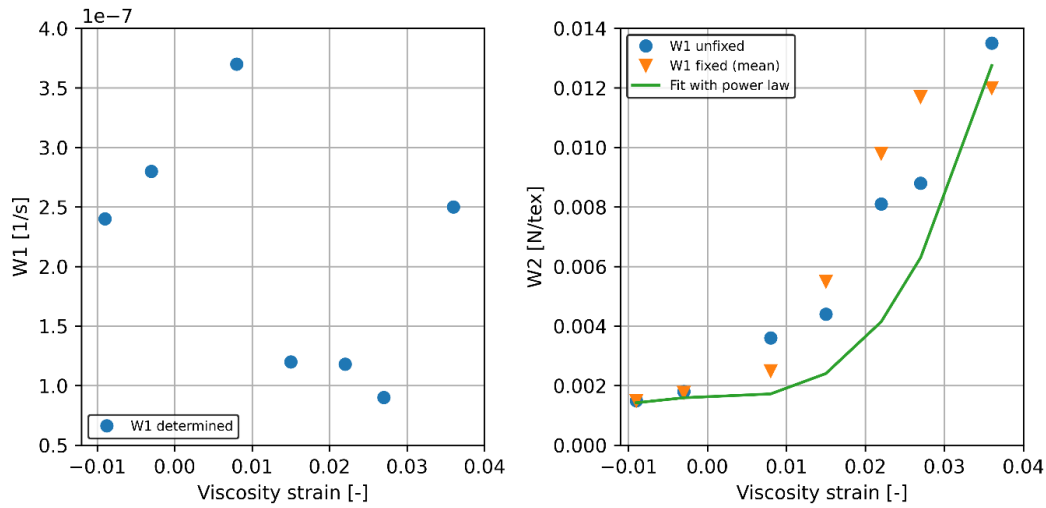
Figure 3.10 - Parameters W1 and W2 calculated from the viscosity behaviour for 4T sub-ropes sample

According to experimental observations (Figure 3.10-left), W1 does not show a simple variation depending on the viscous strain and the variations are small with respect to those of W2, resulting in a low contribution to the overall viscous strain. So, W1 was fixed as a constant (equal to the mean of the obtained values) and not as a function of the viscous strain. Using a fixed value for W1 we can apply the non-linear least-squares Marquardt-Levenberg algorithm again to optimize W2. Figure 3.10-right shows the W2 values obtained both using a fixed value for W1 (triangle) or unfixed values (circle).

The W2 behaviour with respect to the viscous strain can be expressed using a power law:

$$W_2(\varepsilon_v) = a_{w2} \cdot \varepsilon_v^\alpha + b_{w2}$$

Eq. 47

With a_{w2} and b_{w2} expressed in N/tex and α with no units. This is a simpler equation and with less parameters than the POLYAMOOR law proposed in Chevillotte's PhD.

3.2.5. Parameter identification on a virgin 4T sub-rope and experimental validation

Following the identification method, Chevillotte identified the 11 parameters of the POLYAMOOR model using the multi-relaxation data from four multi-relaxation tests on virgin 4T sub-rope samples. For each parameter, the average of the parameters obtained for the four tests was calculated. A new identification of the viscosity, using the simplified definition, was performed during the present work for a virgin 4T sub-rope. These parameters are presented on Table 3.4 and compared to parameters identified for a 4T sub-rope after long creep.

Chevillotte performed a validation of the approach by comparing the simulation of this experimental procedure using these parameters with the measured response. It was checked that the modification of the viscosity proposed in this work did not change the analysis and validity of the law proposed in Chevillotte's work. The behaviour given by the model was found to be very close to the experimental response as shown Figure 3.11-left.
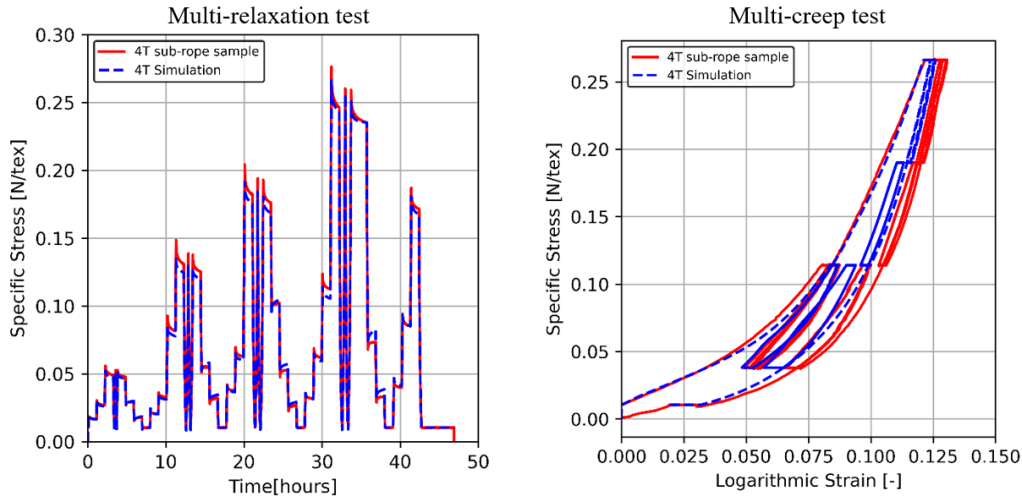
Figure 3.11 - Comparison of the model and the experimental results for the 4T virgin sample Left: experimental result and the model for a multi-relaxation test: logarithmic strain [-] versus time for. Right: experimental result and the model for a multi-creep test: specific stress [N/tex] versus logarithmic strain [-] for

A visible difference in the behaviour during the relaxations at unloading was observed but was expected as the viscous parameters were identified on the first loading sequence of the test and we could expect some differences between the loading and the unloading steps. The choice of equation Eq. 45 to describe the viscosity behaviour could also be questioned and another behaviour might improve the prediction.

Chevillotte also performed a validation of the law by confronting it to a multi-creep test (Figure 3.11-right). The response of the sub-rope to multi-creep appeared to be different to the one during multi-relaxation, the strain value reached for a same applied stress was higher during the multi-creep test than during the relaxation test. Hence the prediction was not as precise but still quite sufficient for the application. It was observed that the simulation was very precise for the first cycles but the strain was underestimated for the last ones; a gap could be seen between the experiment and the model. This additional strain seemed to be due to the combination of creep and cycling. The behaviour during creep steps was well represented. The shapes of the cycles were well predicted by the law. It should be noted that the final strains reached at the end of the simulation were very close to the experimental results. Again, it was checked that the modification of the viscosity proposed in this work did not change the validity of the prediction of the law (Figure 3.11-right).

Overall, the model worked well with cycles and relaxations in the load range of 0.01 to 0.25 N/tex for the 4T sub-rope sample. The differences were not found to be critical for the application. The POLYAMOOR model should allow the behaviour of mooring lines to be determined under normal service loading (cycle 1 reaches 0.1 N/tex around 17%MBL) and under storm conditions (cycle 4 reaches 0.45 N/tex around 77%MBL).

Chevillotte developed and validated the model on a virgin 4T sub-rope. The development of the law for mooring applications requires identification of the changes of the parameters with mechanical ageing of the rope. The next section will investigate the mechanical properties of a 4T sub-rope that has been through one-year creep at 25%MBL followed by 1-year recovery at 2%MBL.

3.3. Study of an aged 4T sub-rope sample

To evaluate both the evolution of the material mechanical behaviour and the sensitivity of the POLYAMOOR law's parameters to ageing, a multi-relaxation test, followed by an identification, was performed on an aged 4T sub-rope. This sample has been creep loaded for one year in water at 25%MBL and then left for one year to recover at 2%MBL (the procedure is described in chapter 2 section 2.4; it is the sample named LC25 in chapter 4 of this manuscript).

The multi-relaxation test was performed following the procedure described in section 2.5.3.4.1 at IFREMER (not the same experimental set-up as the one used by Chevillotte). The specimen was kept wet in a water tank during the transportation from ENSTA Bretagne to IFREMER, Brest. The sample is shown on Figure 3.12, it has a yellow colour due to the ageing in water.

Figure 3.12 - 4T sub-rope sample after creep installed on IFREMER experimental set-up for the multi-relaxation test

A virgin 4T sub-rope sample has also been tested following the programmed procedure on this test bench to be sure that the differences are not due to the sample dimensions or the difference with the experimental set-up (2 meters compared to 1 meter at ENSTA Bretagne for the sample studied in section 3.2.5 by Chevillotte). The construction differences between the two samples are the following:

- *Lay-length:* The 4T and the 4T after creep samples do not have the same lay-lengths at 2% MBL: respectively 50 and 70 mm. The 4T sub-rope loaded in creep has a longer lay-length as it has been loaded at 25%MBL for 1 year; this has caused a modification of the construction and a stabilization of this new construction.
- *Lay angle:* The lay angle α was calculated using Eq. 1 chapter 1. The lay angle is respectively 34° for the virgin 4T and 26° for the sample after creep, considering the same diameter to be 11.5 mm. In fact, the diameter of the sample after creep has certainly decreased, but this change is difficult to measure accurately.

- *Linear density:* the engineering linear density is used to compare the samples (the linear density measured on the virgin sample with a given lay length and diameter); but the 4T after creep might be characterized by a lower linear density due to its changed construction. A lower density would induce a higher measured specific stress for the 4T sample after creep. We will not take this into account in the following comparison as measurements of diameter are difficult to perform accurately. Furthermore, as the linear density varies during the test, choosing which value of linear density to consider is complicated and subjective. Hence, the engineering approach is retained for this study.

3.3.1. Results of the multi-relaxation test

The results of the multi-relaxation tests performed on the 4T sub-rope after long-term creep and on a virgin 4T sub-rope sample are presented on Figure 3.13.
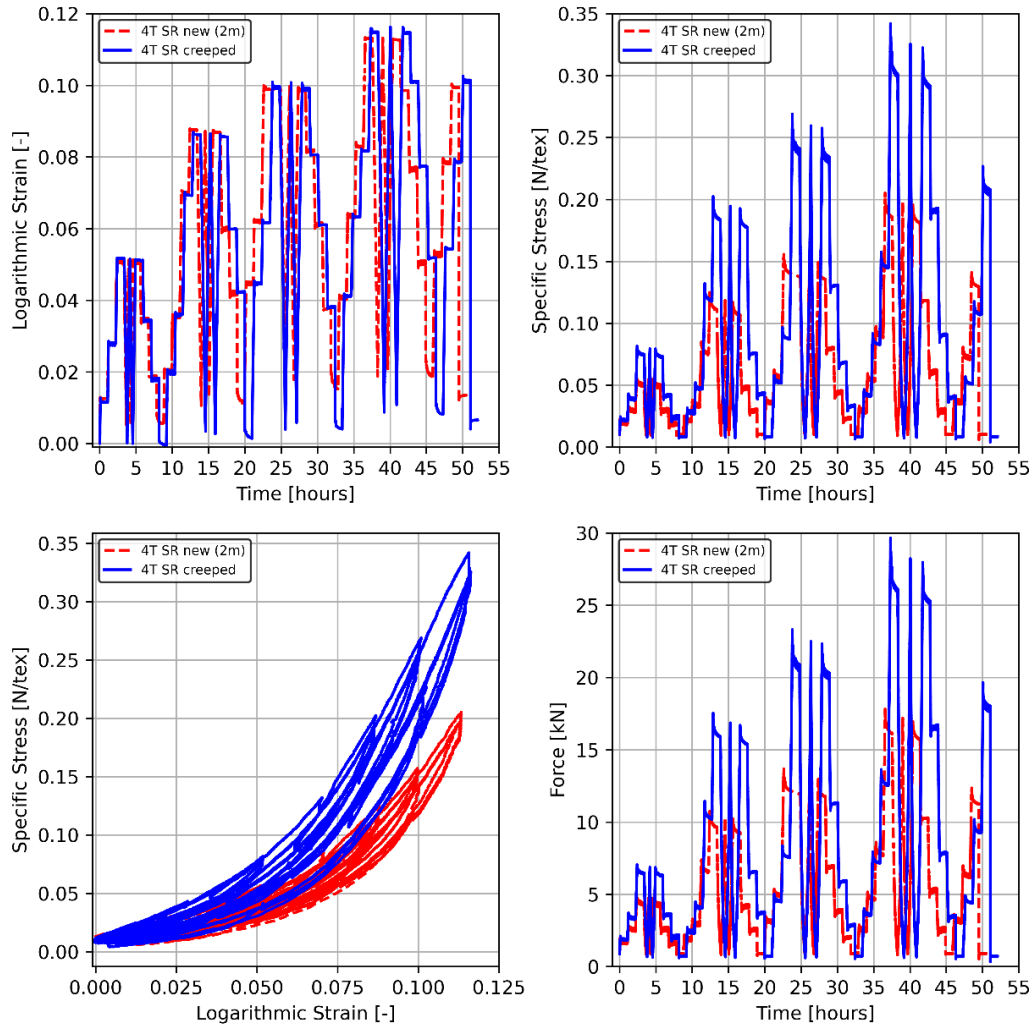
Figure 3.13 - Comparison of the experimental results of a multi-relaxation test for a virgin 4T sample ("new")and the 4T sample after creep LC25 ("creeped"). Top Left: logarithmic strain versus time [-]; Top Right: specific stress [N/tex] versus time; Bottom left: Specific stress [N/tex] versus logarithmic strain [-]; Bottom right: load [kN] versus time

The sample which has undergone creep appears to be stiffer than the virgin sample. On Figure 3.13-top right, we observe that the specific stress reaches higher values for the same strain plateau, reaching around 75% of the MBL of a virgin 4T sub-rope sample during the fourth cycle. As no residual strength test has been performed on the sample after creep, we do not know if it is characterized by the same minimal breaking load. The creep sample also presents

a more important instantaneous reversible strain part as observed on Figure 3.13-top left (the blue curve of the 4T creep reaches smaller strain values during the recovery at 2% of MBL). This could indicate that most of the irreversible strain has already happened, hence the long-term creep appears to have stabilized the construction and the microstructure.

To understand the observed differences, additional tests were performed on the creep samples and are presented in the next section 3.3.2. An identification of the POLYAMOOR law parameters was performed, and is presented section 3.3.3, to quantify the differences using the characterization method associated to the law and to analyse the sensitivity of the parameters.

3.3.2. Additional tests to characterize the 4T sub-rope after creep

This section aims to investigate two reasons that could explain the change in the mechanical properties observed on the 4T sub-rope after creep:

- Changes in the microstructure of the PA6 fibres. More precisely, two mechanisms were investigated: hydrolysis and crystallization. These two mechanisms can take place with water interaction with the PA6 fibres and under stress (coupling).
- Modifications of the construction of the sub-rope sub-components (the rope-yarn lay-angles in the strands or the yarn lay-angles in the rope-yarns).

The samples studied were taken directly from the aged 4T sub rope sample (Figure 3.14) following the method described in section 2.5.4.2 chapter 2.
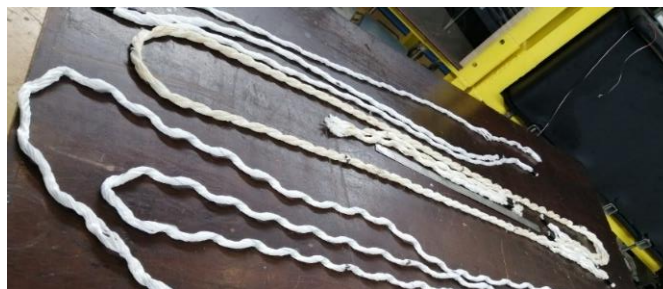
Figure 3.14 - Preparation of the LC25 long term creep samples

3.3.2.1. Crystallinity

DSC analysis was performed to determine the degree of crystallinity, to investigate if microstructural changes are responsible for the change in the mechanical properties.

PA6 fibres are semi-crystalline, hence their mechanical properties are directly linked to their crystallinity content. Two phenomena can modify the microstructure of PA6 fibres that have been subjected to creep in water:

- Previous studies (Deshoulles et al., 2021) of PA6 crystallinity ratio with ageing time in water showed that an increase of this ratio can be associated to hydrolysis of PA6 fibres. This degradation is a chemical reaction between amide and water which leads to chain scissions and formation of acid and amide groups. The chain scission increases the mobility of the macromolecules and some can be integrated in the crystallites, hence increasing the crystalline ratio. This process is referred to as 'chemi-crystallization'.
- Another mechanism is stress-induced crystallization witnessed and studied on rubber (Mitchell J.C & Meier D.J, 1968). This process of 'self-reinforcement' consists of the development of crystallinity on stretching. Strain-induced crystallization has been studied for different materials (Chenal et al., 2007; Gros et al., 2015; Le Gac et al., 2019).

Hence, the increase in stiffness observed at the sub-rope scale could be explained by a higher crystallinity ratio after creep. To characterize the amount of crystalline phase found in PA6 fibres and to determine if some modifications were induced by creep in water, DSC was performed on three samples:

- A virgin 4T sample as a reference;
- A 4T sub-rope sample that was subjected to only one multi-relaxation test (no creep) to separate the effect of the multi-relaxations test from the effect of the long-term creep test;
- The sample LC25 on which a multi-relaxation test was performed after two years under creep in water.

Thermograms for the three samples are presented in Figure 3.15.
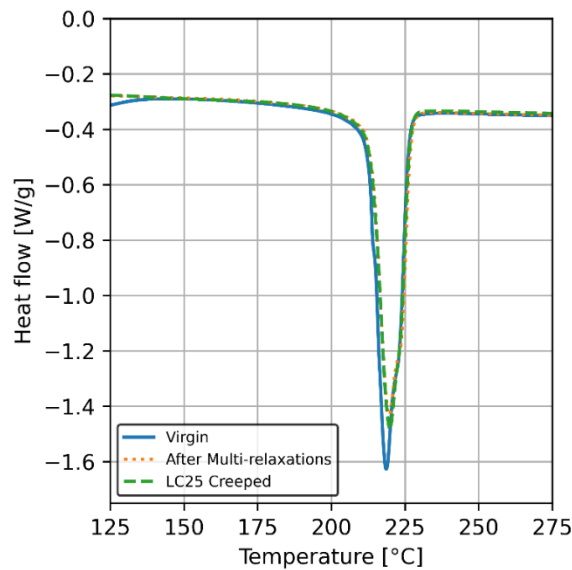
Figure 3.15 - Thermograms obtained with DSC analysis on a virgin 4T sub-rope sample, the 4T sub-rope creep sample LC25 and a 4T sub-rope sample after a multi-relaxation test.

The calculated crystallinity ratios for the three samples are presented in Table 3.1. Three DSC analyses were performed for each sample.

Table 3.1 - Crystallinity ratios calculated for the three samples: a virgin 4T sub-rope sample, the 4T sub-rope sample after creep LC25 and a 4T sub-rope sample after a multi-relaxation test

Sample	Crystallinity ratio (%)			
	Result 1	Result 2	Result 3	Mean
Virgin 4T	36	38	38	37.3
Multi-relaxations 4T	34	33	34	33.6
Creeped and multi-relaxation 4T (LC25)	33	34	34	33.6

A small decrease in crystallinity ratio of less than 4% is observed for samples after multi-relaxation and long-term creep in water. This change is also visible on Figure 3.15 as the enthalpy energy, associated with the fusion of the crystallites, is larger for the virgin sample. This difference is not significant and should not impact the mechanical properties significantly.

3.3.2.2. Quasi-static tests on strands and rope-yarns

To determine if the changes in mechanical properties of the sub-rope are due to changes in the behaviour of its sub-components, we performed quasi-static tensile tests to failure on strands and on rope-yarns taken from three different sub-ropes:

- From a virgin 4T sub-rope called 'Virgin' (a sample which had never been wet)
- From a 4T sub-rope after a bedding-in procedure and a multi-relaxation test in water.
- From the 4T sub-rope after long term creep in water (LC25).
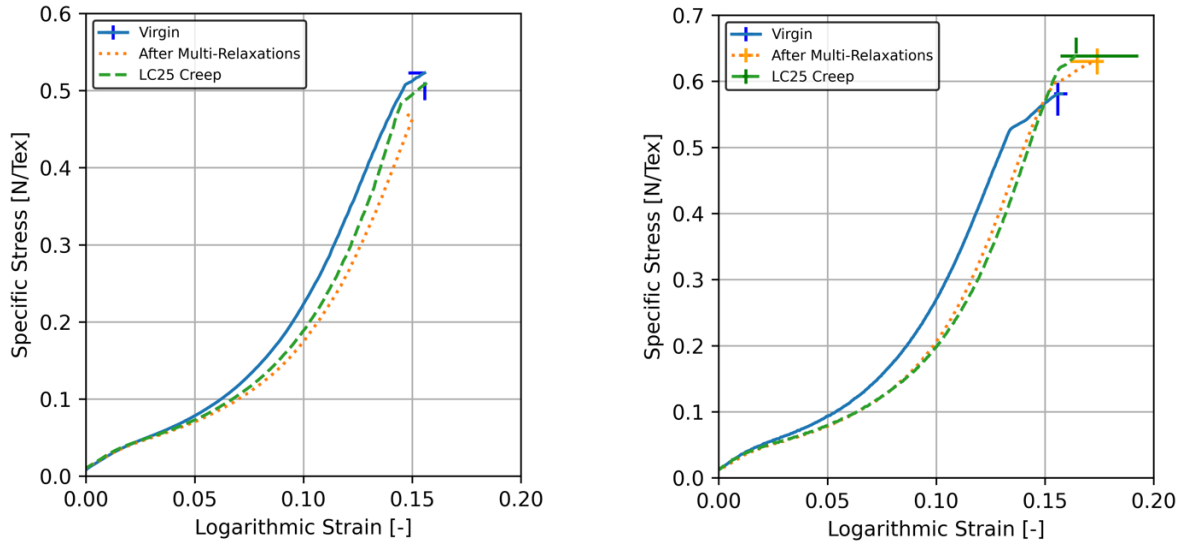
Figure 3.16 - Specific stress [N/tex] versus logarithmic strain [-] obtained for a virgin 4T sub-rope sample, the creeped 4T sub-rope sample LC25 and a 4T sub-rope sample after a multi-relaxation test. Left: performed on strands; Right: performed on rope-yarns

These tests were performed on the dry samples following the method presented in section 2.5.4.3, chapter 2. The results are presented on Figure 3.16-left and Figure 3.16-right respectively for strands and rope-yarns. Some characteristic mechanical properties obtained from these experiments are reported in Table 3.2.

Table 3.2 - Mechanical properties measured on quasi-static tensile tests on strands and rope-yarns scale for three samples: a virgin 4T sub-rope sample, the creeped 4T sub-rope sample LC25 and a 4T sub-rope sample after a multi-relaxation test

Sample	Strands			Rope-yarns		
	Modulus at strain 8% [N/tex]	Break Strength [N/tex]	Break strain [-]	Modulus at strain 8% [N/tex]	Break Strength [N/tex]	Break strain [-]
Virgin 4T	3.3	0.52	0.156	4.18	0.58	0.158
Multi-relaxation	2.3	0.48	0.141	3.02	0.63	0.183
Creeped	2.6	0.51	0.157	2.75	0.63	0.161

The mechanical properties of strands are lower in comparison to the mechanical properties of rope-yarns for all samples. This result is in accordance with literature and experimental observations: higher scales will show reduced moduli due to the construction response (Lechat et al., 2006).

From Figure 3.16, we observe the change in the behaviour for the two scales, strands and rope-yarns, is similar. They both show a slight deviation to the right from the reference behaviour. This is characteristic of reduced mechanical properties which is the opposite of what is observed

at the sub-rope scales when comparing a virgin sample to the creeped sample LC25 (Figure 3.13). The samples after creep or after multi-relaxation show lower modulus and slightly higher strain at rupture for rope-yarns (Table 3.2). This loss of properties can be linked to a plasticization of the material with water and under stress as shown by Humeau *et al.* (Humeau et al. 2018).

The tensile breaking forces do not show the same variation for strands and rope-yarns: a slight decrease is observed at the strand scale while a slight increase is observed at the rope-yarn scale for the aged samples. However, the differences are small and could be due to scatter. Hence, the observed behaviour of the sub-components does not explain the observed behaviour at the sub-rope scale that shows higher moduli after creep.

Nevertheless, the observed loss of properties of the strand and the rope-yarn is in accordance with the observation of a slightly lower crystallinity ratio for these samples (Table 3.1) in comparison with the virgin sample. These changes are suspected to be caused by water. As the changes in behaviour are very close for a sample after long term creep and for a sample after a multi-relaxation test, we can deduce that the changes are due to short-term mechanisms and not to long-term mechanisms associated with the long-term creep in water.

We can conclude that the stiffer behaviour of the sub-rope after creep, observed during multi-relaxation tests, is not due to a change in behaviour of its sub-components: it not due to changes of construction of its sub-components and it is not due to changes in the fibre material properties.

The remaining explanation is that the change in lay-length of the 4T sub-rope after long-term creep is responsible for the change in behaviour; indeed, it was observed that the 4T creep sub-rope is characterized by a higher lay-length at 2%MBL: 70mm instead of 50mm for a virgin 4T sub-rope.

3.3.2.3. Impact of the lay-length on the mechanical behaviour of a 4T sub-rope

In this section, we investigate the impact of the lay-length on the mechanical properties of a sub-rope. The 4T sub-rope after long-term creep is characterized by a higher lay-length of 70 mm in comparison with the virgin 4T sub-rope. To be able to estimate if the lay-length can be responsible for the changes in mechanical properties observed, we un-stranded a 4T virgin sample manually. To do so, we take a 1-meter long 4T sub-rope sample with splices (sample dimensions used for fatigue test) and we change its lay-length, from 50 mm to 70 mm, by turning its two terminations while it is under a low tension. We appreciate that, this procedure to obtain a different construction, is not comparable to having a sample designed to have a 70mm lay-length and manufactured on an industrial machine. However, but we could not get a sample with a different construction during the time of the PhD.

We performed fours quasi-static tensile tests: two tests on a virgin 4T sub-rope and two tests on an un-stranded virgin 4T sub-rope (called here 'new lay-length') following the method described in section 2.5.3.2 chapter 2 (after the 2-hour bedding-in procedure). The results are presented on Figure 3.17-left and all the mechanical properties are presented in Table 3.3.

For the comparison to be as close as possible to the study on the multi-relaxation test, we consider the same linear density for both samples even if the sub-rope with a new lay-length should be characterized by a lower linear density, hence higher specific stress. Figure 3.17-right presents the calculated modulus (using linear regressions) variations versus the logarithmic strain.
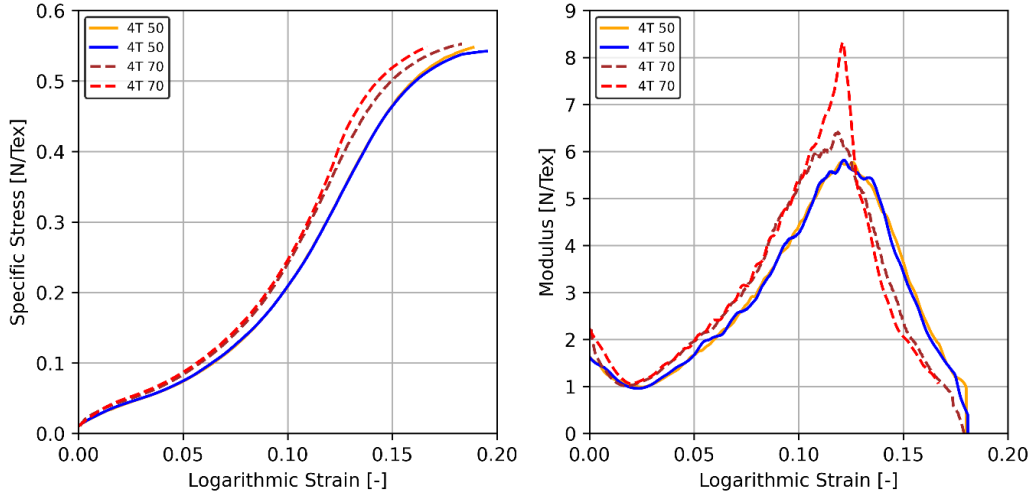
Figure 3.17 - Comparison of the response of virgin 4T sub-ropes with a 50-mm lay-length and of virgin 4T sub-ropes with a 70-mm lay-length during a quasi-static tensile test. Left: Specific stress [N/tex] versus logarithmic strain [-]. Right: Tangent modulus [N/tex] versus logarithmic strain [-].

Table 3.3 – Mechanical properties obtained during quasi-static tensile tests for virgin 4T sub-ropes with 50-mm lay-length and for virgin 4T sub-ropes with 70-mm lay-length

Sample	Lay angle (degrees)	Modulus at strain 8% [N/tex]	Break Strength [N/tex]	Break strain [-]
50mm 4T	34°	3.0	0.54	0.19
70mm 4T	26°	3.5	0.55	0.18

The characteristic S-shape of the stress-strain curve is observed for both lay-lengths. The sub-ropes characterized by higher lay-length present a slight deviation to the left from the reference 4T sub-rope samples. This indicates higher mechanical properties which is highlighted by a higher modulus versus strain during the test until the second part of the S-shape.

Between the two 4T sub-ropes samples, the ratio of lay angle $\frac{\alpha_{70mm}}{\alpha_{50mm}}$ is 1.3 and the ratio of modulus, $\frac{E_{70mm}}{E_{50mm}}$, at a strain of 8%, is around 1.2 during the first part of the S-shape. Closer to failure, the ratio of mechanical properties is inversed and the reference sub-ropes are stiffer than the ones with higher lay angle.

A study by Ghoreishi *et al.* (Ghoreishi, Cartraud, et al., 2007) showed that the mechanical properties evolve linearly with the lay angle. Those authors developed an analytical model of synthetic fibre ropes, characterized by an assembly of a large number of twisted elements, and subjected to axial load. In that study, a continuum model formed by a set of coaxial helixes was proposed. The material was assumed to show a linear elastic behaviour ($\sigma_{tt} = E \cdot \varepsilon_{tt}$). The dimensionless stiffness matrix components were expressed as a function of only the extension ratio of the structure and the lay angle of the outer layer of the structure in the initial state. Among other things, Ghoreishi showed that, for lay angles close to the ones of the 4T sub-ropes tested in our study (between 15° and 30°), the predicted dimensionless stiffness matrices showed a linear variation with the lay angle.

We observe the same trend with our comparison but we could only compare two lay-lengths because of the experimental constraints. In fact, for the 4T sub-rope sample with a 70-mm lay-length, there are only three full twists in the gauge length. For a higher lay-length, a 1-meter

long sample is too short and longer samples should be tested. Further studies are required using the higher scale test bench that is better suited to testing longer samples.

This study demonstrates that the observed mechanical properties of the sub-rope after a creep test lasting 2 years are caused by changes in construction during long-term creep. The identification of the POLYAMOOR law in the next section will investigate if the identified parameters highlight these new properties and can allow us to quantify the changes in behaviour.

3.3.3. Identification of the 4T sub-rope sample parameters after creep, comparison and analysis

The aim of this part of the study is to evaluate the impact of the long-term creep on the constitutive law parameters for a 4T sub-rope. Following the identification method described in section 3.2, the parameters of the aged sample LC25 are determined. The values obtained are shown in Table 3.4 along with the parameters identified on a virgin sub-rope sample at IFREMER. As a validation, the multi-relaxation test on the 4T creep sample is simulated with the identified law and the prediction is compared with the experimental data on Figure 3.18.

Table 3.4 - Identified parameters using a multi-relaxation test on the creeped 4T sub-rope sample LC25

	Virgin 4T	Creep 4T	Element of the POLYAMOOR model
a [-]	33.	47.8	$i(\varepsilon) = \dfrac{b}{a} \cdot (e^{a \cdot \varepsilon} - 1)$
b [N/tex]	0.49	0.67	
c [-]	26	28	$d(\varepsilon) = \dfrac{g}{c} \cdot (e^{c \cdot \varepsilon} - 1)$
g [N/tex]	0.090	0.12	
e [N/tex]	0.072	0.065	$p(\varepsilon_p) = e \cdot \left(\tanh(f \cdot \varepsilon_p + h) + 1\right)$ if $\varepsilon_p \leq \dfrac{-h}{f}$
f [-]	150	300	
h [-]	7.8	15.95	$p(\varepsilon_p) = e \cdot \left(f \cdot \varepsilon_p + h + 1\right)$ if $\varepsilon_p > \dfrac{-h}{f}$
W_1 (s^{-1})	$2.0 \cdot 10^{-7}$	$3.0 \cdot 10^{-8}$	$\Sigma_v = v(\dot{\varepsilon}_v, \varepsilon_v) = W_2(\varepsilon_v) \cdot \sinh^{-1}\left(\dfrac{\dot{\varepsilon}_v}{W_1}\right)$
α [-]	3	3	$W_2(\varepsilon_v) = a_{w2} \cdot \varepsilon_v^{\alpha} + b_{w2}$
a_{W2} [N/tex]	239.	100.	
b_{w2} [N/tex]	0.0016	0.0017	
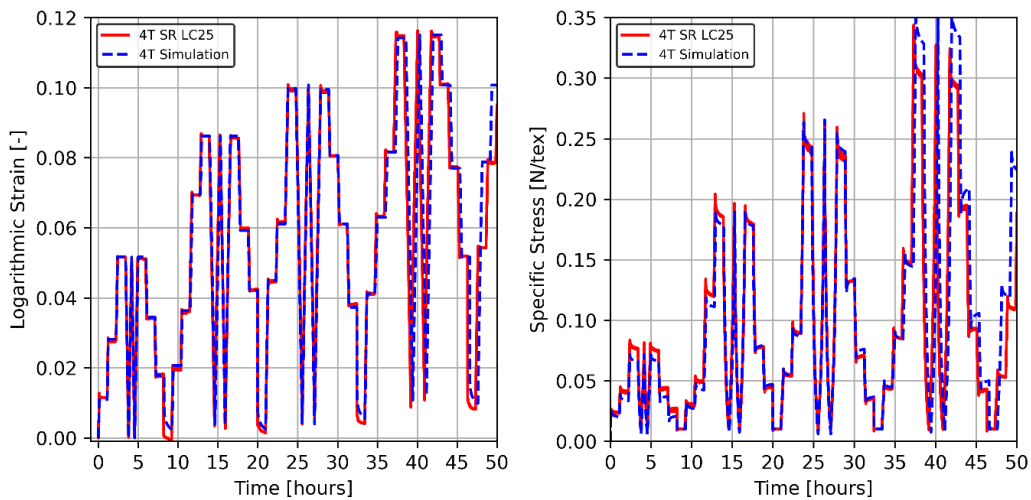
Figure 3.18 - Comparison of the model and the experimental results for the 4T creep sample Left: logarithmic strain versus time [-] for the experimental result and the model; Right: specific stress versus time [N/tex]

The differences observed between the simulation and the experimental data are not critical, as observed on Figure 3.18. The differences are more important in the first and last cycles. The recovered strain during the recoveries in Figure 3.18-left is underestimated and a shift is visible for all cycles. However, the prediction remains in good agreement with experimental data. The identified parameters are compared to the one identified on a virgin sample and an analysis is proposed.

3.3.3.1. Comparisons and proposal of an analysis

The non-linear function used to describe the different behaviours (elastic, time-independent and viscous) cannot be compared using simple ratios. Hence, we will compare the modulus associated with the different functions. The instantaneous modulus and the FRB modulus obtained, with the associated identifications, are presented in Figure 3.19. They are compared to the identification on 4T virgin sub-ropes (dashed lines).
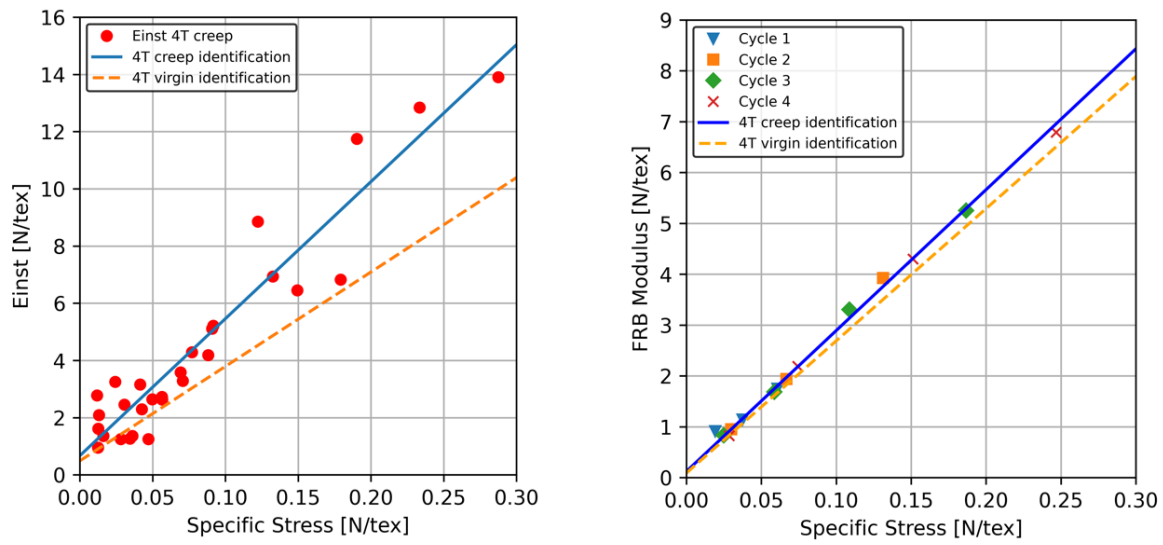
Figure 3.19 - Left: Short-term elasticity modulus (E_{inst}) versus the specific stress at the beginning of the sudden change for a 4T sub-rope after creep. Right: Fully relaxed behaviour modulus [N/tex] versus specific stress [N/tex] for a 4T sub-rope after creep

The instantaneous modulus is consequently higher for the creep sample than for a virgin sample. The ratios obtained are comparable to the ratio obtained in section 3.3.2.3 when comparing an un-stranded sub-rope. They are close to a linear evolution of the mechanical properties with the lay angle. The ratio between the lay angles is 1.4 and the ratio of the parameter a [-], characteristic of the instantaneous modulus versus specific stress, is 1.44.

The FRB modulus of the creep sample is higher but the ratio between the parameter c [-] associated with the fully relaxed behaviour is 1.06 which remains close to 1. This result is in accordance with the hypothesis of a time-independent behaviour. It means the fully relaxed behaviour did not change during the long-term creep test, and so, did not change with time.

Figure 3.20 compares the plastic behaviour of both samples and the same conclusions can be made as the plastic behaviours are very similar.
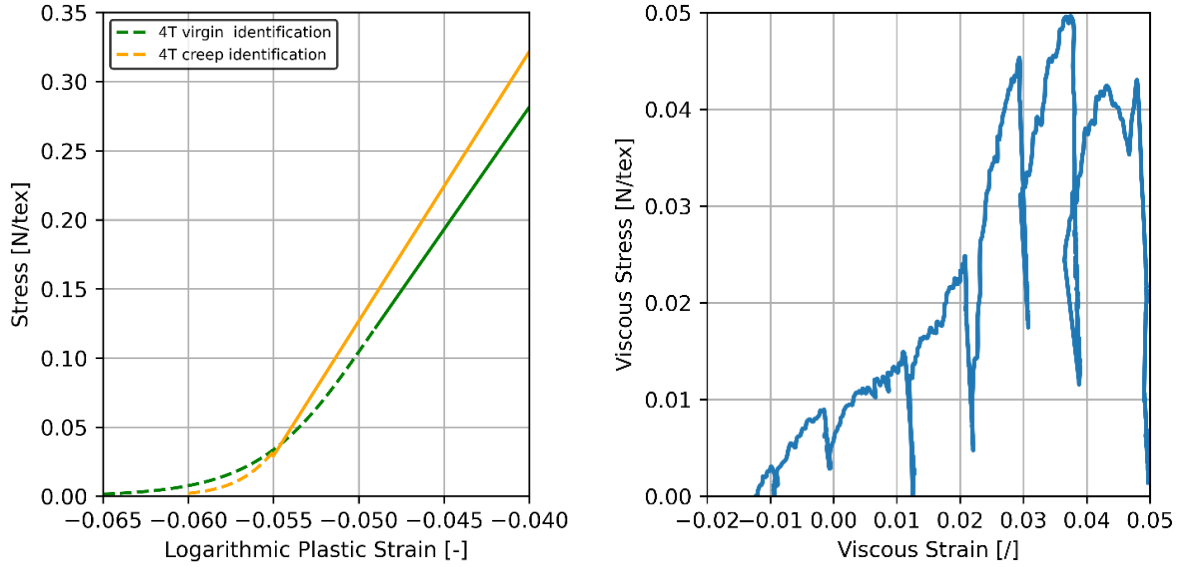
Figure 3.20 – Left: Plastic behaviour for a virgin and a 4T sub-rope after creep. Specific Stress [N/tex] versus logarithmic strain [-]. Right: Viscous stress [N/tex] versus viscous strain [-] in the dashpot for a 4T sample after creep

The viscous behaviour is harder to identify on the creeped 4T sub-rope after creep as shown on Figure 3.20-right and Figure 3.21. Parameter W1 presents considerable variations which cannot be described by simple functions. The mean value for W1 was calculated without considering the two extreme values (black cross on Figure 3.21) that are associated with more complicated experimental data and that disturb the identification for all the other relaxations. Taking a fixed W1 value induces a description of the relaxation with poor precision for some plateaux (the two plateaux with the black cross not taken for the identification). This difficulty can be due to the more severe relaxations at higher stresses that are not well monitored by the displacement sensors. However, the identification still allows an acceptable description of the relaxations but improvements could be added to the viscosity expression of the law.
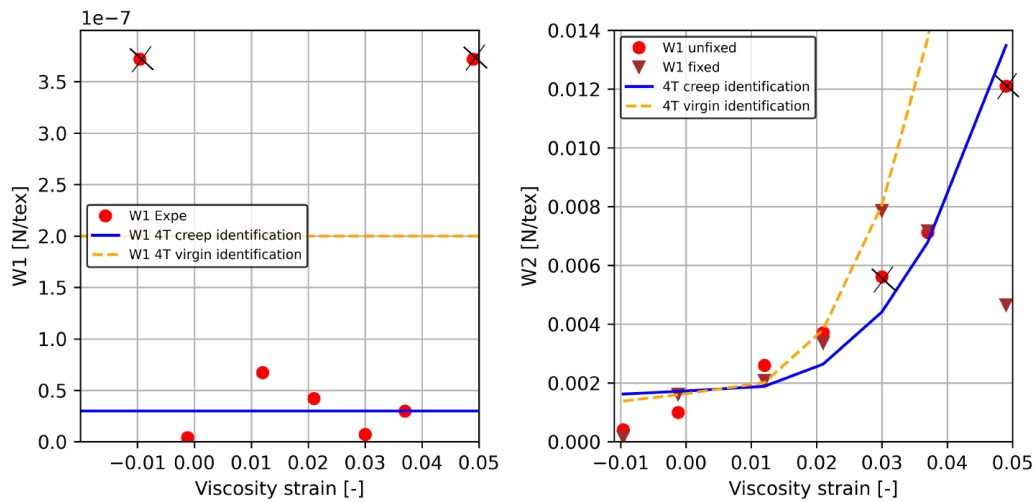
Figure 3.21 - W1 [N/tex] and W2 [N/tex] parameters identified on Figure 3.20-right for a 4T sub-rope sample after creep

As the development of the law was made on 4T sub-rope samples, an identification of the law at a higher scale is presented in the following section. The aim is to investigate if larger scale ropes, composed of the same fibres but with a different construction, show a similar response to the one identified on the 4T sub-rope.

3.4. Parameter identification on a 7T sub-rope, comparison, analysis and experimental validation

A third identification of the parameters was made following the same identification method on the 7T sub-rope. Only one test could be performed (following the procedure described in chapter 2 section 2.5.3.4.1). The aim of this identification is to investigate if a larger scale rope, composed of the same fibres but with a different construction and diameter, shows a response similar to the one identified on the 4T sub-rope. The POLYAMOOR law should be applicable to describe any rope scale provided that the identification is performed at that scale.

The 7T sub-rope sub-components do not have the same composition and lay-angle as the 4T. The number of rope-yarns and their lay-angle in the strands are not the same; also, the number of yarns and lay-angle are not the same in the rope-yarns. Hence, no direct comparison and analysis between the virgin 4T sub-rope and the 7T sub-rope can be made as too many parameters are changing. However, parameters identified by Chevillotte using 3 multi-relaxation tests on virgin 4T sub-rope sample are given in Table 3.5 with the identified parameters of the 7T sub-rope sample to allow a quick comparison.

3.4.1. Identification and analysis

The 11 parameters were identified following the procedure described in section 3.2 and are presented in Table 3.5. A first validation of the identification is made with the comparison between the results obtained from an FE simulation and the experimental results which are presented in Figure 3.22.

All the figures associated with the identification of the 7T sample are presented in appendix B (p.204).

Table 3.5 - Identified parameters using a multi-relaxation test on a 7T sub-rope sample

	Virgin 4T sub-rope	Virgin 7T sub-rope	Element of the POLYAMOOR model
a [-]	33.5	44.67	$i(\varepsilon) = \dfrac{b}{a} \cdot (e^{a \cdot \varepsilon} - 1)$
b [N/tex]	0.49	0.89	
c [-]	26	30	$d(\varepsilon) = \dfrac{g}{c} \cdot (e^{c \cdot \varepsilon} - 1)$
g [N/tex]	0.090	0.10	
e [N/tex]	0.072	0.078	$p(\varepsilon_p) = e \cdot \left(\tanh(f \cdot \varepsilon_p + h) + 1\right)$ if $\varepsilon_p \leq \dfrac{-h}{f}$
f [-]	150	200	
h [-]	7.8	10.3	$p(\varepsilon_p) = e \cdot (f \cdot \varepsilon_p + h + 1)$ if $\varepsilon_p > \dfrac{-h}{f}$
$W_1 \ (s^{-1})$	$2.0 \cdot 10^{-7}$	$5.0 \cdot 10^{-7}$	$\Sigma_v = v(\dot{\varepsilon}_v, \varepsilon_v) = W_2(\varepsilon_v) \cdot \sinh^{-1}\left(\dfrac{\dot{\varepsilon}_v}{W_1}\right)$
α [-]	3	3	$W_2(\varepsilon_v) = a_{w2} \cdot \varepsilon_v^{\alpha} + b_{w2}$
a_{W2} [N/tex]	239.	126.	
b_{w2} [N/tex]	0.0016	0.0026	

On Figure 3.22, we observe similar differences for the 7T sub-rope sample to those previously observed and explained for the virgin 4T sub-rope sample (section 3.2.5). The specific stress is slightly under or overestimated for some cycles and the relaxations during unloading show differences with the experimental data. The recoveries are well represented and the evolution of the plastic strain is accurate. These differences are not critical for the application. The POLYAMOOR model should allow the behaviour of the mooring lines under normal service loading (cycle 1 reaches 0.1 N/tex around 17%MBL) and under storm conditions (cycle 4 reaches 0.45 N/tex around 77%MBL) to be determined.
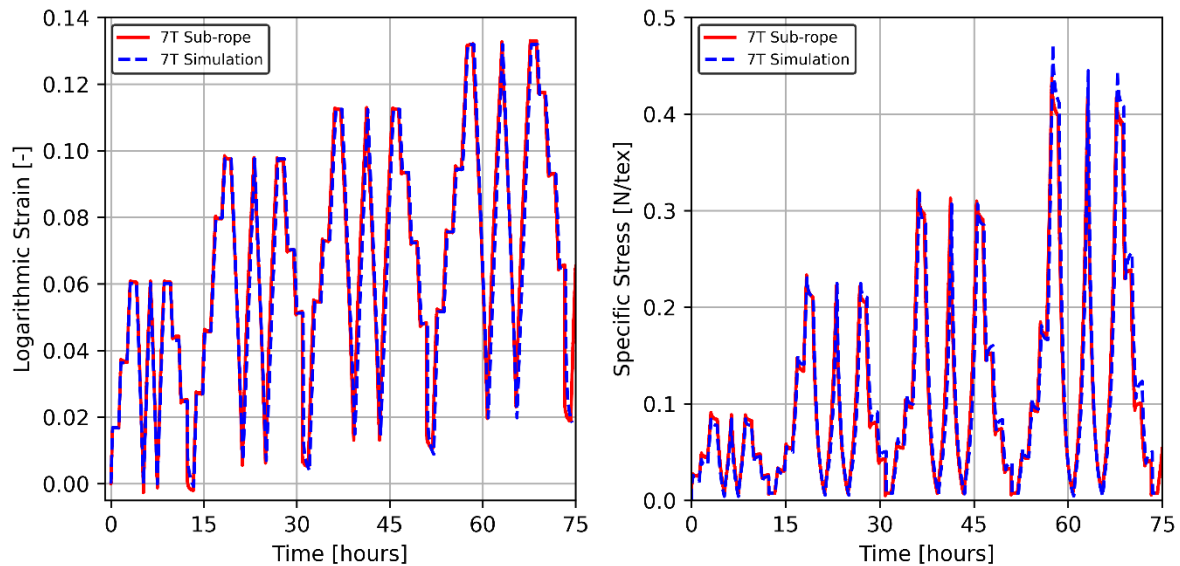
Figure 3.22 - Comparison of the model and the experimental results for a 7T sample Left: logarithmic strain [-] versus time for the experimental result and the model. Right: specific stress [N/tex] versus time

The comparison of a virgin 4T sub-rope and a 4T sub-rope after creep in section 3.3.3 showed that the change in lay-length could be responsible for an increase in the mechanical properties. Even though the construction of the 7T sub-rope sample is very different, a first comparison was made but no linear trend between the lay-length and the modulus was observed. However, the tendency remains accurate with an increase of the modulus. The parameters associated with the dashpot were also more difficult to identify than for the virgin 4T sample (appendix B). However, the model still allows a good prediction of the relaxations and recoveries as shown in Figure 3.22.

3.4.2. Validation of the law on a stochastic test for 7T sub-rope

To be useful the POLYAMOOR law should be predictive. A first validation was made by Chevillotte, at the 4T scale, with the comparison of experimental results from a multi-creep test using an FE simulation (summarized section 3.2.5). As the law was developed for mooring line applications, a validation on a higher scale and for more representative in-service conditions should be performed. The objective is to describe the response of a polyamide 6 line to dynamic tension loads (wave and wind induced) considering the non-linearities of the response observed in cycling tests. Hence, in this section, the law will be used to simulate a stochastic loading test, which consists of a random amplitude cycling around a chosen mean tension value. The experimental data used are from a stochastic test performed on a 7T sub-rope.

As explained in chapter 2 section 2.5.3.4.2, the 7T sub-rope sample had a complicated history before the stochastic sequence was performed. So, the first sequence simulated was chosen to be representative of this history of loading. The entire simulated loading is the following and is represented in Figure 3.23:

- A loading at 40kN followed by a 1-hour creep
- An unloading at 1.4 kN followed by a 2-hour recovery
- The bedding-in procedure (100 cycles over the range 14-17kN)
- The associated stochastic sequence (described in chapter 2 section 2.5.3.4.2)
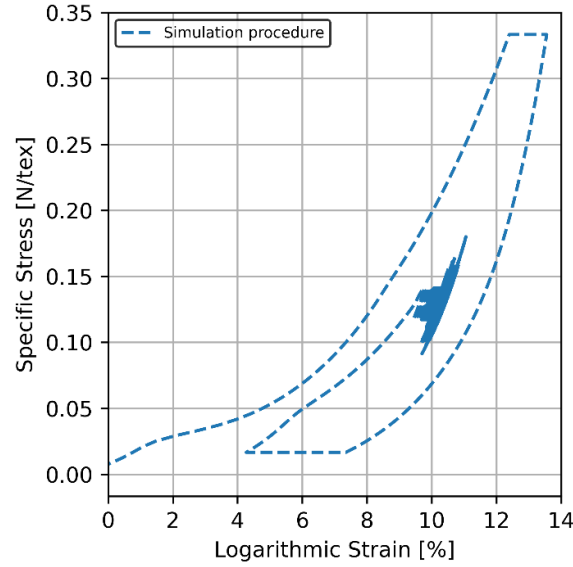
Figure 3.23 - Loading procedure simulated on Abaqus software using the POLYAMOOR law and the identified parameters on the 7T sub-rope
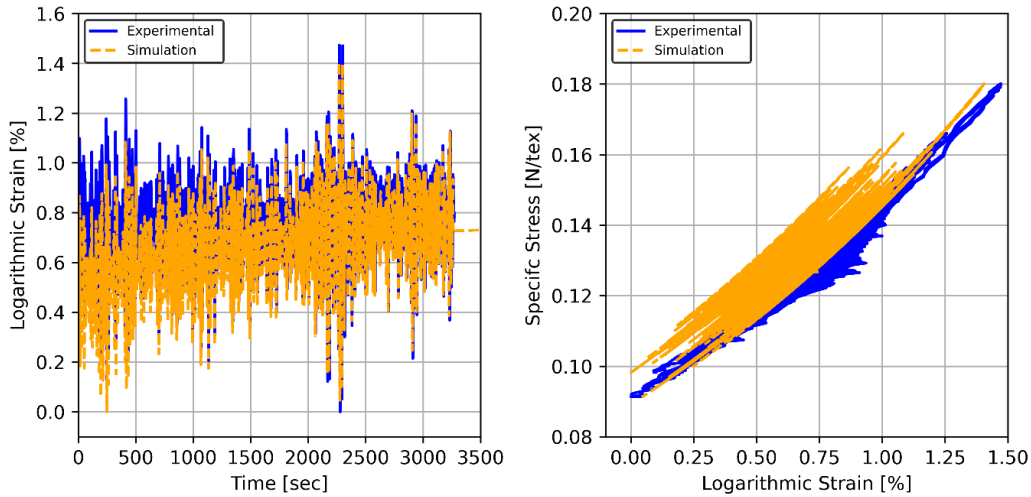
Figure 3.24 - Comparison of the experimental results with a FE simulation using the POLYAMOOR law for load spectrum of a stochastic test. Left: Evolution of the logarithmic strain [%] with time [sec]. Right: Specific Stress [N/tex] versus logarithmic strain [%]

The POLYAMOOR law was used with the parameters identified for the 7T sub-rope scale. The comparison between the simulation and the experimental result is shown in Figure 3.24. The zero strain, or reference length, was measured under a 15 kN tension just before the bedding-in.

We can observe on the experimental data (blue curve) that all the stress-strain values appear to fall around a single curve. On the contrary, the POLYAMOOR law predicts some static creep during the stochastic sequence. This difference might be due to the history of loading of the 7T sub-rope sample. This experimental behaviour can be interpreted by a stabilized viscous behaviour. The POLYAMOOR law, after a 2-hour recovery, predicts creep during the sequence, due to the characteristic time identified. This is expected, as the law was identified on 1-hour relaxation and creep sequences, hence the characteristic time associated to longer time mechanisms are not represented by the law.
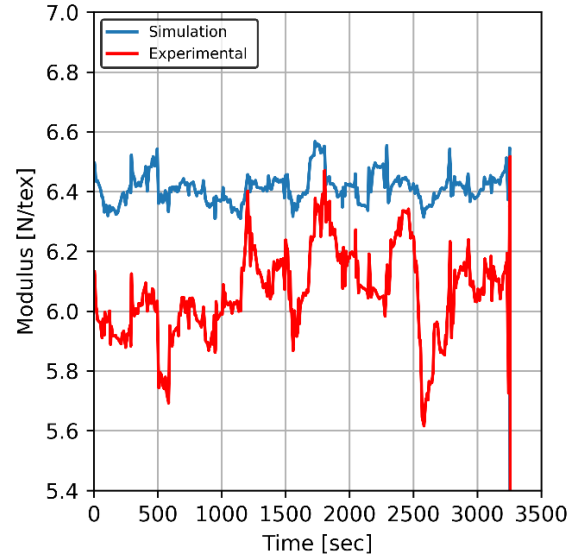
Figure 3.25 - Comparison of the experimental and simulated dynamic stiffness [N/tex] evolution with time [sec] during the stochastic test

The dynamic stiffness predicted by the law is compared to the one observed experimentally. It is calculated for each loading and unloading using a linear regression. The comparison is presented in Figure 3.25. The dynamic stiffness predicted by the law is accurate. Also, a good agreement is observed between the cyclic maximal and minimal strains obtained from the model and measured.

This first simulation suggests that the law is sensitive to the applied bedding-in procedure before the sequence. To improve our understanding of the POLYAMOOR law, another procedure with a different bedding-in (more adapted to the identified characteristic time) was simulated using the law, it consisted of:

- A bedding-in sequence with 100 cycles between 11 kN and 21 kN followed by a creep of 2 minutes at 20 kN.
- The stochastic sequence, with no bedding-in.

The comparisons of the results with the stochastic test are presented in Figure 3.26.
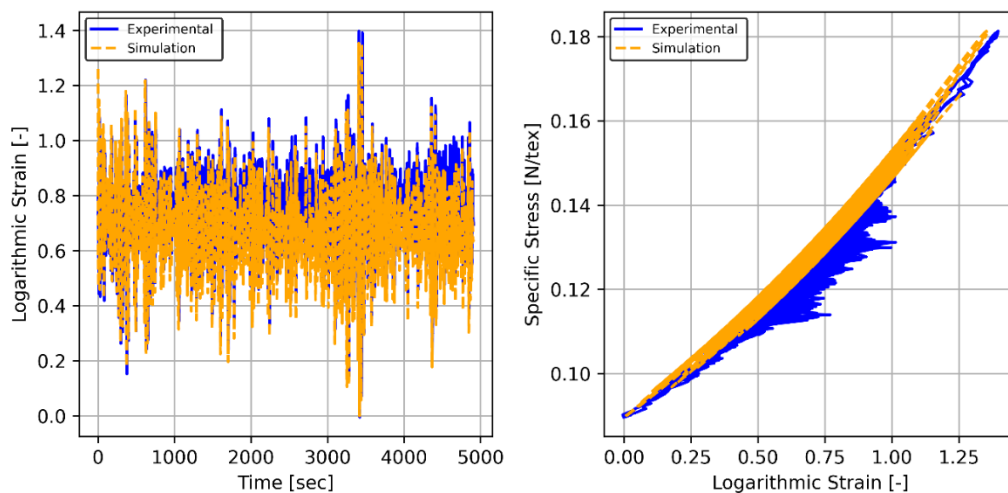
Figure 3.26 - Comparison of the experimental results with a FE simulation using the POLYAMOOR law for load spectrum of a stochastic test. Left: logarithmic strain [%] versus time [sec]. Right: Specific Stress [N/tex] versus logarithmic strain [%]

In Figure 3.26, a slight recovery is noted during the load spectrum for the simulated result. Following this bedding-in procedure, we have a response shape closer to the shape observed experimentally but the reasons are not the same:

- Experimentally, we witness a stabilized viscous behaviour during the stochastic sequence.
- With the law, a recovery occurs during the sequence leading to an equivalent shape.

We can conclude that the POLYAMOOR law will be relevant to predict short-term behaviour of polyamide 6 ropes. The longer duration induces long-term mechanisms that are not represented by the law. This conclusion will be enhanced in Chapter 4 in which long-term creep is simulated using the POLYAMOOR law.

3.5. Conclusion

A constitutive model based on Flory's proposal and its identification method was proposed by Chevillotte (Chevillotte, 2020). It does not require any inverse identification and allows good control over the model. This model identification was developed using a cyclic multi-relaxation test which can be applied to the prediction of the mechanical behaviour of polyamide 6 fibre ropes under representative loading. It has the following elements:

- A fast spring describing the dynamic behaviour,
- A dashpot responsible for the viscous response of the polymer,
- A time-independent part consisting of a ratchet element for the plasticity, and a slow spring responsible for the relaxed elasticity.

We proposed a simplification of the parameter W_2 as a function of the viscous strain. A first validation was made by Chevillotte on a 4T virgin sub-rope and it was checked that the proposed simplification hadn't changed the previous observations. The first validation was made by comparing the model results to the experimental data used for the identification. The model predicted some small differences as it under- or overestimated the specific stress during some cycles. Also, some differences on the recovery stages were visible but remained small. The viscous expression is suspected to be the source of differences and further work may allow optimization of this component. It was concluded that the differences were not critical for the application and that further optimization of the parameters could allow a correction of the model if needed. Another validation was made by Chevillotte using a multi-creep test on a 4T sub-rope sample. The law presented a shift to the left of the specific stress-strain behaviour. This underestimation of the strain seemed to be due to the difference in the response of polyamide 6 to combined creep and cycling in comparison to relaxations and cycling. Nevertheless, the law still provides a good prediction of the shape of the cycles as well as the strain at the end of the loading sequences.

The mechanical properties of a 4T sub-rope after creep were studied (2-year creep). The post-creep sample was characterized by a stiffer behaviour. The sub-rope sub-components (strands and rope-yarns) were characterized with a quasi-static tensile test. Contrary to what was observed at the sub-rope scale, a small decrease in mechanical properties was noted. The crystallinity ratio showed a very small decrease that was in accordance with the decrease of the mechanical properties of the sub-components scale (rope-yarns and strands). It was concluded that, after long-term creep, the main factor influencing the evolution of the mechanical properties is the lay-length at the sub-rope scale (lay-angle of the twisted strands).

The 11 parameters of the POLYAMOOR law were identified at this scale and comparison with the virgin sample parameters was proposed. The short-term elasticity behaviour and the time-dependent behaviours are more strongly impacted by ageing than the time-independent response. This agrees with our hypothesis the fully relaxed behaviour (FRB) is not time dependent. Furthermore, it was shown that the evolution of the short-term parameter 'a' is in accordance with a linear evolution of the short-term stiffness with the lay-angle.

As the development of the law was made on 4T sub-rope samples, an identification of the law at a higher scale, on a 7T sub-rope sample, was also performed. It was observed that the model fitted the experimental data well. It was shown that the differences between the identified parameters for the 4T and the 7T sub-ropes were in accordance with experimental observations and previous studies. The 7T sub-rope is characterized by parameters highlighting its stiffer behaviour due to its smaller lay angle. The viscous behaviour was harder to identify and an alternative expression associated with another identification method could be proposed.

Chapter 4. Short and long term creep behaviour

4.1. Introduction

The present chapter describes a study of the long term creep behaviour of polyamide 6 sub-rope in water and examines the use of a simple model to fit the data. A specific experimental set-up has been designed to test 4T sub-rope samples in water for long term creep tests. It was developed in a previous study (Chevillotte, 2020) and is described in chapter 2 section 2.5.3.5.1. A repeated creep test was also performed to investigate if long-term creep at low loads (in-service tension) is more critical than short term creep at higher loads (e.g. during a storm).

The present chapter is divided into two parts: a first part contains a comparison between creep and recovery kinetics (from section 4.2 to section 4.6). Short term creep tests were performed in order to conclude on the need to perform long term creep tests. The experimental data are used to compare the predictions of the POLYAMOOR law presented in chapter 3 to long term creep data, and to conclude on its ability to predict long term viscous behaviour of polyamide 6 mooring lines. This first part corresponds to a published article in Ocean Engineering: 'Short and long term creep behaviour of polyamide ropes for mooring applications' (Civier et al., 2022).

The second part examines the continuation of this long term creep study, but it was chosen to not combine both parts of the study for clarity, as some tests were extended, others stopped and other questions were raised (section 4.7).

4.2. Bedding-in first investigation

For many synthetic fibres ropes, a bedding-in protocol is applied in order to settle and stabilize the fibres and their geometry (Bain et al., 2020; Lian et al., 2018; Weller et al., 2014). Such procedures can be difficult and expensive for large ropes but can ensure a better durability and control of the mooring lines. It is important to determine whether such a protocol will be needed for polyamide 6, and if so, which loading sequence would be suitable. Figure 4.1 presents the superposition of two creep tests at 45% MBL. One was performed with no bedding-in (LC45$_A$) and the other was preloaded and is referred to as LC45$_B$ in Table 1.
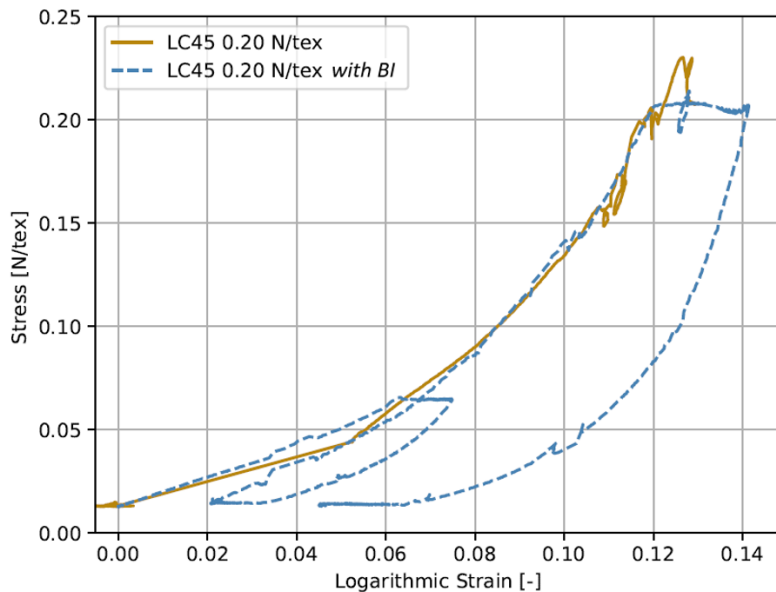
Figure 4.1 - Stress in N/tex versus logarithmic strain for two tests at 45% MBL. The first one (continuous lines) being without a bedding-in procedure and the second one (dashed line) with a bedding-in procedure

The bedding-in procedure is detailed in chapter 2 section 2.4. It does not appear to have an impact during the subsequent loading phase of the sample. The plots are superposed even after the bedding-in. These results justify not applying a bedding-in procedure in the following comparison. However, other bedding-in protocols with higher loads might have an effect in the stabilization of the rope structure, and are being examined in current work. Hence, the long term creep tests studied in the next section were performed with no bedding-in before the loading except for this test at 45%MBL.

4.3. Long term creep: Influence of the load

Long term creep tests were conducted in water on polyamide 6 sub-ropes for a two-year period. The experimental data are presented in Figure 4.2 and Figure 4.3.
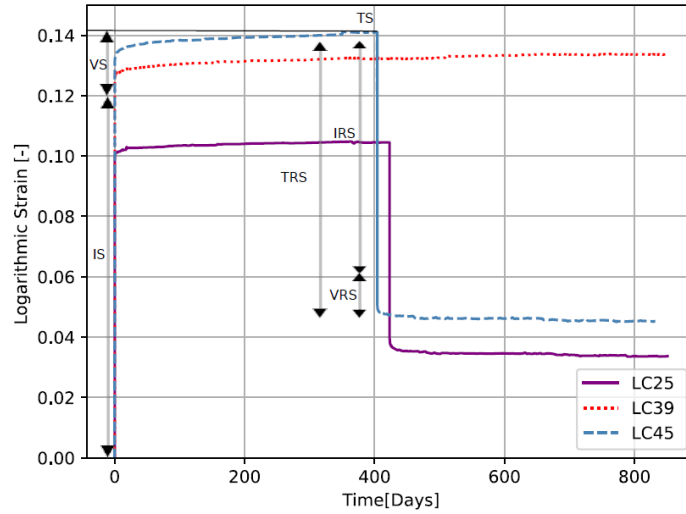
Figure 4.2 - Long term creep and recovery results for three different loadings respectively 25%, 39% and 45% MBL

The small peak we observe on the red dotted line curve LC39 on Figure 4.3 corresponds to a local instability of the loading and did not impact the results (no corresponding peak on the strain results).
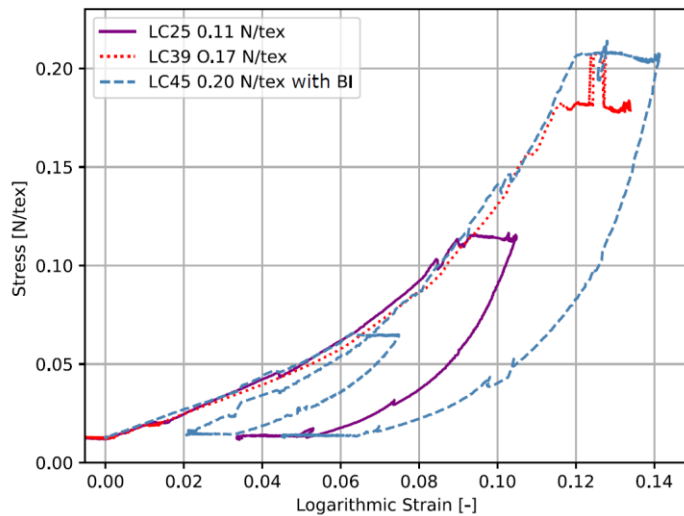
Figure 4.3 - Stress [N/tex] versus logarithmic strain [/] of long term creep tests for three different loadings respectively 25%, 39% and 45% MBL

Table 4.1 summarizes the measured instantaneous strain (IS), time-dependent strain (VS) and total strain (TS) during the loading (creep) and unloading (recovery) phases.

The load level has a clear effect. The creep and elastic strains increase with applied stress. The instantaneous strain values are around 85% to 90% of TS for all loads, the time-dependent values are around 10% to 15% of TS.

Table 4.1 - Results of long and short Creep and Recovery Tests

Test	Loading phase				Recovery phase			
	Total duration (days)	TS (/)	IS (/)	VS (/)	Total duration (days)	TRS (/)	IRS (/)	VRS (/)
$LC25$	424	0.104	0.093	0.011	414	0.070	0.052	0.018
$LC39$	838	0.134	0.116	0.018	/	/	/	/
$LC45_B$	405	0.141	0.120	0.021	433	0.096	0.077	0.019
$SC25$	0.125	0.101	0.094	0.006	0.125	0.063	0.057	0.006
$SC39$	0.125	0.124	0.116	0.008	0.125	0.099	0.066	0.033
$SC45$	0.125	0.138	0.131	0.007	0.125	0.105	0.064	0.041

TS is the total strain; IS is the instantaneous strain, VS is the viscous strain
TRS, IRS and VRS are the same for recovery

The samples at 25% and 45 %MBL recovered around 67% of TS, so 33% of TS after creep has not been recovered. For LC25 and LC45$_B$, the instantaneous recovery is respectively 74% and 80% of the TRS and the time-dependent recovery is around respectively 26% and 20% of the TRS. The instantaneous creep strain is higher than the instantaneous recovery strain, meaning we may have modified the material during the loading phase leading to a permanent strain.

4.4. Kinetic study of creep and recovery

The curves in Figure 4.4 confirm that polyamide 6 shows a logarithmic visco-elasto-plastic creep behaviour (Hunt & Darlington, 1978, 1979). The creep presents two phases. The primary phase goes from t_0 (beginning of the creep) to 10^{-2} days. From 10^{-2} days (around 15 minutes), we observe a stabilization of the creep rate. It becomes nearly linear as a function of the logarithm of time, which could indicate the beginning of the secondary phase. The recovery presents three phases (Figure 4.5): the first two phases are comparable to those of creep with a secondary phase following a linear evolution of the strain as a function of the logarithm of time. However, recovery rates seem to stabilize at the end of the test (Figure 4.5).

We can fit the relationship between creep (and recovery) strain and time by a logarithmic law (for t > t_0):

$$\varepsilon_c = A \, log_{10} \, (t - t_0) + \, \varepsilon_0$$

<div align="right">*Eq. 48*</div>

With A the logarithmic creep rate, t_0 the beginning of the creep (in days) taken when the load has reached a constant creep value and ε_0 the strain after one day of creep (at t_0 + 1day). This expression has the disadvantage of not being accurate for times close to t_0 but can be used for all other practical times. The logarithmic fits presented on Figure 4.4 are determined using Eq. 48 identified on the data from 10^{-2} days up to the end of the experiment. The parameters t_0 and ε_0 are identified beforehand using the stress versus strain curve (Figure 4.3) to determine when the load becomes constant (beginning of creep). The parameter A is the slope of the logarithmic fit. Therefore, it is possible to model the creep over this strain range using a single linear logarithmic law following Eq. 48 (Figure 4.4).
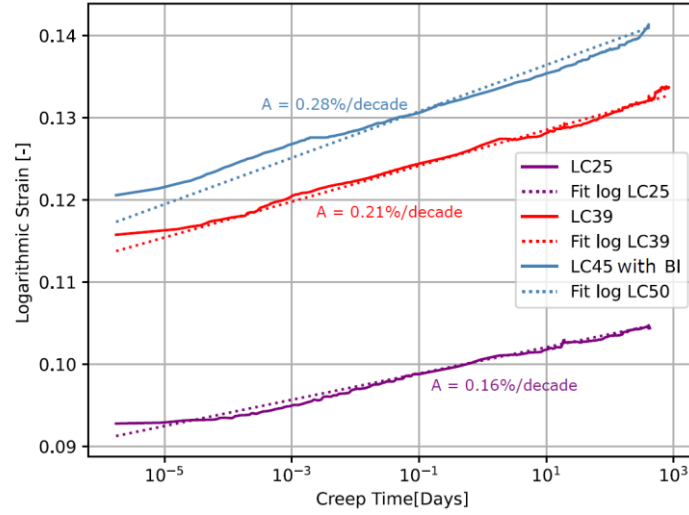
Figure 4.4 - Long term creep strain versus logarithm of creep time for three different loadings respectively 25%, 39% and 45% MBL

Hence, we use a logarithmic identification for the creep rate:

$$A = \frac{\Delta\varepsilon}{\Delta log_{10}(t - t_0)}$$

Eq. 49

To analyse the different phases in more detail, the creep rate was calculated for each decade of days and then smaller intervals were added for the last decade as it represents most of the creep duration. These measured creep and recovery rates are presented in Figure 4.6.
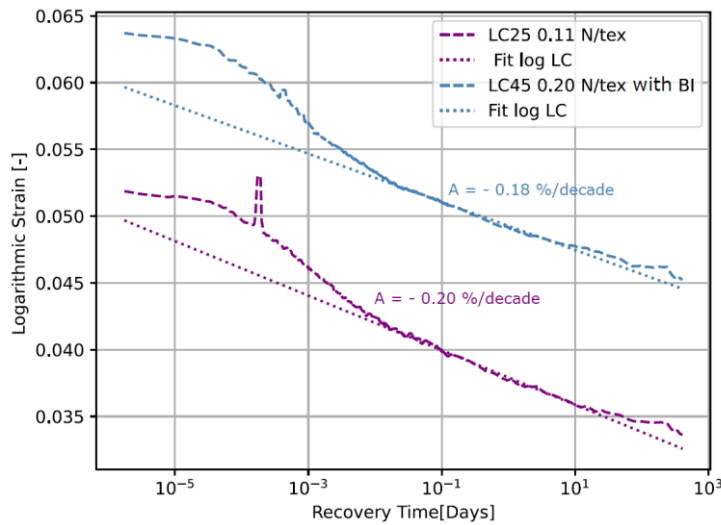
Figure 4.5 - Recovery of the long term creep at 25% and 45% MBL

The creep and recovery rates are not smooth. This could be explained by the influence in the creep calculation of the instabilities of the measurements; these are especially likely to happen for long term experiments which are characterized by more frequent occurrence of perturbing events. Another explanation is that this may be due to damage inside the sub-rope or a sudden change in the construction of the rope. For example, increases in the creep rate values might be due to a "stick-slip" mechanism: the fibres creep slowly until they rearrange in a position that induces resistance (stick part). They then rearrange and produce a "slip" effect. The creep rate is sensitive to these types of variations because they can induce, locally, large increases in strain. The creep rate plot highlights the two phases mentioned above. There is a primary phase, between 0 and 10^{-2} days, where the creep rate is increasing. The second phase is located

between 10^{-2} days and 100 days. This phase should present a stabilized logarithmic creep rate but is characterized by instabilities. If we note the creep scale, these variations remain small. Beyond 100 days of creep, the effect of the load is more visible with respectively for 25%, 39% and 45%, calculated rates of 0.2 %/decade, 0.3 %/decade and 0.35 %/decade. The creep rate values are almost proportional to the tension values.
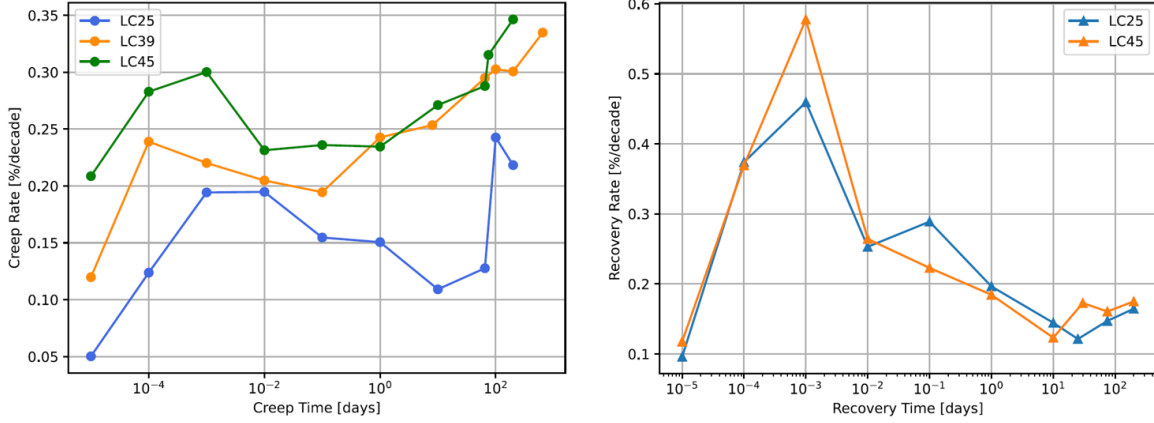
Figure 4.6 - Right: Creep rate in %/decade for the long term creep tests. Left: Absolute value of recovery rate in %/decade for the long term creep tests

The recovery rates also present three phases: the first one, between 0 and 10^{-2} days, is characterized by a fast recovery rate. It is followed by a decrease between 10^{-2} and 10^1 days and maybe a stabilization from 10^1 days to the end. Nonetheless, the recovery is still on-going and we did not reach a stable value of permanent strain. Comparing the initial values of creep and recovery rates (Figure 4.6), the recovery is faster than the creep at the beginning.

4.5. Comparison of long and short term creep tests

Given the logarithmic evolution of the creep strain, it might be questioned whether long tests are necessary. The results obtained during an independent series of short term creep tests (3 hours) were therefore compared to those. The aim was to determine if we can predict long term creep strain with short term experiments. Figure 4.7 shows the results and Figure 4.8 presents a superposition of the long and short term creep test results on a logarithmic time scale.
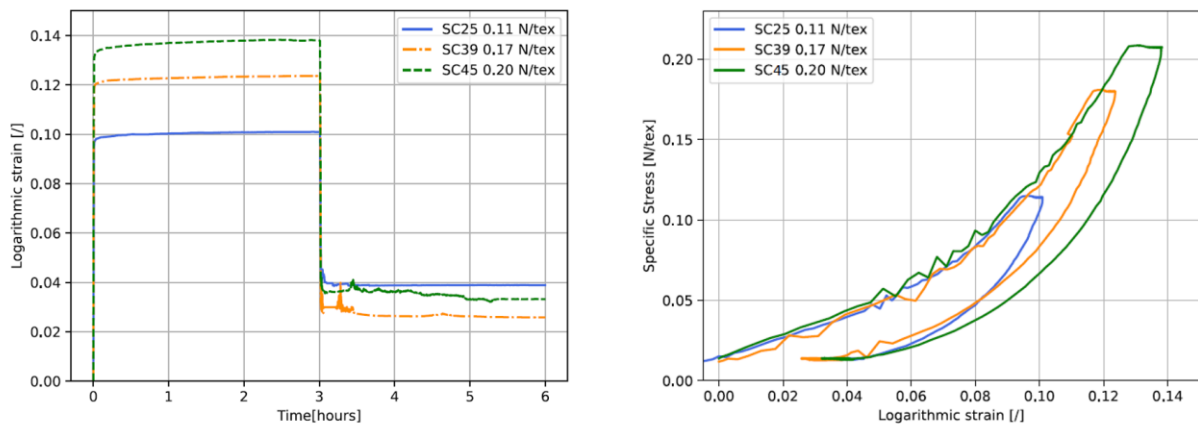
Figure 4.7 – Left: Short term creep and recovery results for three different loadings respectively 25%, 39% and 45% MBL. Right: Stress [N/tex] versus logarithmic strain [/] of short term creep tests for three different loadings respectively 25%, 39% and 45% MBL

On Figure 4.7-right, we can observe some small irregularities during recovery. Unfortunately, these appear to be caused by instabilities of the wire sensors when the sub-rope recovers. They may vibrate which gives a poor-quality signal. As the main aim of the study was to compare long and short-term creep, it was decided not to process this signal and to not use the first part of the short-term creep test recovery curve (SC25, SC39, SC45). Hence, the recovery analysis was only based on the final stabilized values obtained after 3 hours of recovery. These final values are not affected by the noise recorded between 3 and 4 hours. Efforts are being made to improve the measurement set up for future tests.

The total creep strains for short and long term creep are very similar (Figure 4.8). The small gap between the two seems to be due to the instantaneous response. These gaps could be explained by the variability between the samples (e.g. small differences in the splicing, which is a manual operation). It is observed from Table 4.1, that the instantaneous strain values (IS) are around ~ 93% of TS and the viscous strain (VS) are ~ 7% of TS for short term creep tests. As expected, the long term creep tests are characterized by a larger creep strains (around 10% to 15%). The instantaneous strain (IS) is not completely recovered by the instantaneous recovery strain (IRS).
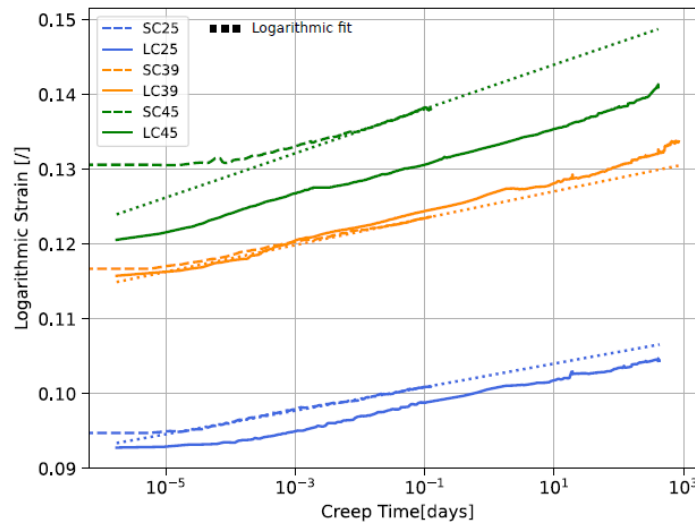
Figure 4.8 - Superposition of long and short term creep strain in function of the logarithm of time with extrapolated short term creep logarithmic fit

The creep secondary phase reached at 10^{-2} days is visible on the short term creep tests (figure 14). Table 4.2 compares the values of creep rate 'A' for a single logarithmic law fitted from 10^{-2} days to the end of the creep test. Extrapolation of the law identified on short term creep test indicates that a short term creep test of 3 hours could provide a good prediction of the creep after two years using a logarithmic linear law. For longer times, the creep rate may increase as a function of the load.

Table 4.2 - Creep Rates from 10^{-2} days to the end of the creep test

	$LC25$	$LC39$	$LC45_B$	$SC25$	$SC39$	$SC45$
Rate %/decade	0.16	0.21	0.28	0.16	0.18	0.29

4.6. Model predictions

4.6.1. Empirical model

An approach by Fancey (Fancey, 2005) suggested that the viscoelastic changes occur through incremental jumps, and this was used to describe primary and secondary creep regimes. The model is based on the Weibull distribution function. It was identified with a fit of experimental data on dry polyamide 6,6 fibres. The molecular mechanism envisaged was segments of molecules jumping between positions of relative stability. The expression for creep under applied load is:

$$\varepsilon_c tot(t) = \varepsilon_i + \varepsilon_c \left[1 - \exp\left(-\left(\frac{t}{\eta_c}\right)^{\beta_c}\right)\right]$$

Eq. 50

Where ε_i is the initial instantaneous strain from application of the load and the ε_c function represents creep strain, which is determined by the characteristic life (η_c) and shape (β_c) as a function of the duration of loading, t. The unloading phase is also characterized by an elastic instantaneous strain recovery followed by time-dependent recovery:

$$\varepsilon_r vis(t) = \varepsilon_r \left[\exp\left(-\left(\frac{t}{\eta_r}\right)^{\beta_r}\right)\right] + \varepsilon_f$$

Eq. 51

where the ε_r function for viscoelastic strain recovery is determined by parameters similar to the creep function, ε_c, and ε_f the permanent strain from viscous flow.

Fitting Eq. 50 and Eq. 51 to the data gives the results presented in Table 4.3 and results are displayed, for creep, for the sample at 39 % MBL on Figure 4.9-left and, for recovery, for the sample at 25% MBL on Figure 4.9-right.
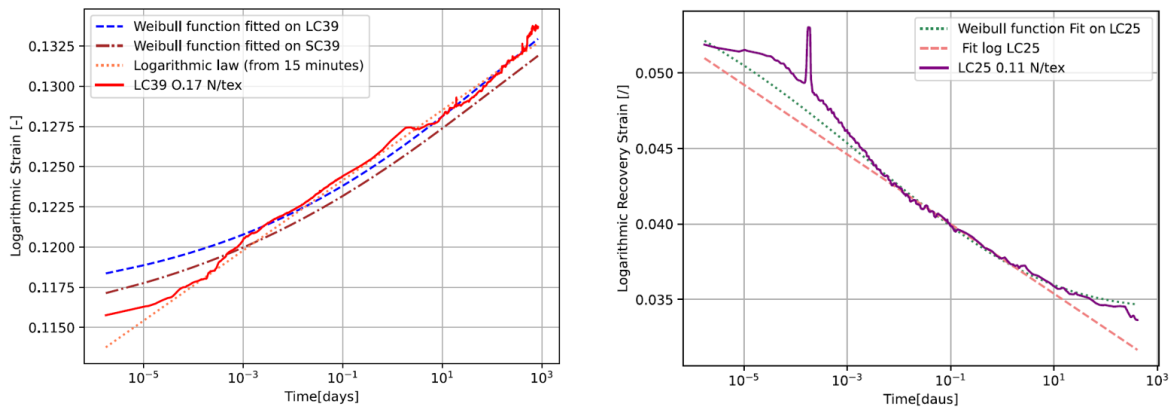
Figure 4.9 – Left: - Weibull model fitted to the long term creep data LC39 at 39% MBL and to the short term creep SC39 at 39% MBL and comparison to a logarithmic law. Right: Weibull model fitted to the long term recovery data at 25% MBL and comparison to a logarithmic law

We observe that the Weibull function is not accurate to represent the beginning of creep. It may underestimate the importance of the reorganization of the structure in the primary phase. The result given by the Weibull model is close to the result obtained using a single logarithmic law identified from data between 10^{-2} days up to the end of creep. Looking at the values of ε_c, both predict the creep contribution to be around 2% to 3%.

The short term creep tests were fitted using the Weibull function to conclude on its ability to predict long term creep strain using short term creep tests. The obtained total strain after extrapolation is close to the long term creep value but does not take into account the strong increase at the end of the creep test. It was shown that a logarithmic linear law can accurately predict long term creep strain using short term creep tests (Figure 4.8). The use of the Weibull function does not show any advantage for creep prediction.

Table 4.3 - Parameters obtained for Weibull model (equations (Eq. 50) and (Eq. 51))

Test name	$LC25$	$LC39$	$LC45_B$	$SC25$	$SC39$	$SC45$
Creep						
$\varepsilon_i \; [-]$	0.089	0.16	0.117	0.091	0.114	0.127
$\varepsilon_c \; [-]$	0.023	0.023	0.0346	0.024	0.025	0.037
$\eta_c \; [hours]$	2000	3000	2303	2169	2588	3120
$\beta_c \; [-]$	0.097	0.130	0.102	0.097	0.112	0.144
$r \; [-]$	0.992	0.998	0.999	0.989	0.993	0.986
Recovery						
$\varepsilon_r \; [-]$	0.026	-	0.034	-	-	-
$\eta_r \; [hours]$	0.066	-	0.004	-	-	-
$\beta_c \; [-]$	0.13	-	0.11	-	-	-
$\varepsilon_f \; [-]$	0.035	-	0.046	-	-	-
$r \; [-]$	0.981	-	0.978	-	-	-

However, the Weibull function fitted on the recovery data provides a better fit than the logarithmic law (Figure 4.9-right) as it considers the decrease in the recovery rate with a shape parameter below unity. The viscous flow ε_f is predicted to be around 3% to 4% which would indicate we reached the permanent strain value expected by the model. However, the measured experimental recovery rate is not zero (Figure 4.9-right) and so the permanent strain does not seem to have been reached in the experimental data.

In service, the load is not always constant and the moorings may be subjected to cyclic amplitude variations due to waves or storms. Therefore, the identification of a model that considers the elasto-visco-plastic behaviour of the polyamide is needed.

4.6.2. Predictions using the POLYAMOOR law

The POLYAMOOR law developed by Chevillotte (Chevillotte, 2020) and presented in chapter 3 section 3.2 of this manuscript was confronted to a long term creep result. The prediction from this model is now compared to the experimental data. Figure 4.10-left shows the specific stress versus logarithmic strain and Figure 4.10-right plots the evolution of the logarithmic strain with time for the experimental data and for the POLYAMOOR model. As the law was identified after a bedding-in procedure, we shifted the stress-strain curve origin of the prediction to a higher strain to confront the simulation to the loading phase after the bedding-in on the experimental data (Figure 4.10-left).
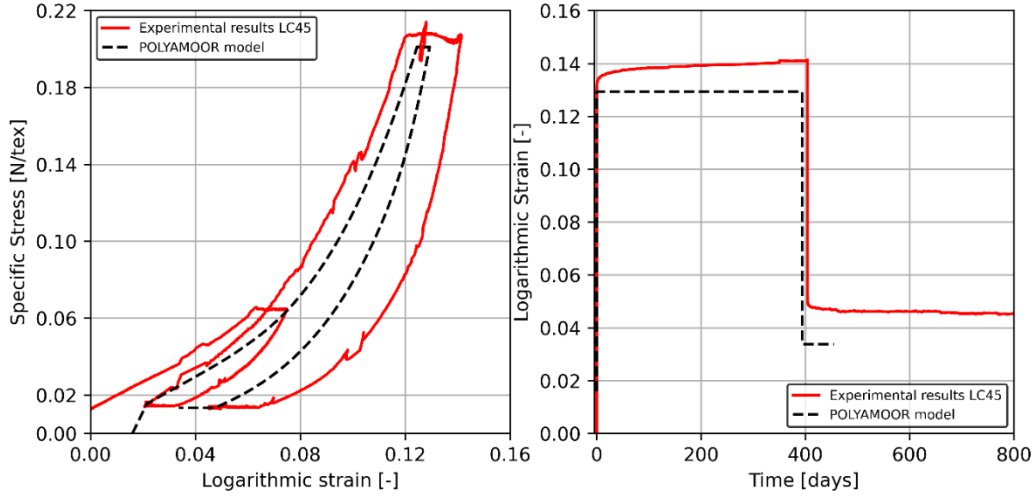
Figure 4.10 – Comparison of the POLYAMOOR law prediction and the experimental results for test LC45. Left: Specific Stress [N/tex] versus logarithmic strain [-]. Right: Logarithmic Strain versus time [days]

Figure 4.11 is a zoom of Figure 4.10-right. It highlights the stabilization of the creep strain predicted by the law at a constant value after 0.1 day. The creep strain calculated by the model is around 4% of the total strain. The experimental creep strain was around 15% of total strain. In fact, for test LC45, the creep rate is 0.35 %/decade at the end of the creep while the model creep rate becomes zero between 0.2 and 0.4 day. This model was identified on multi-relaxation tests with one-hour relaxations. Hence, we can conclude that the model lacks relaxation times. Figure 4.11-right presents the identified viscous specific stress predicted by the model and supports this conclusion, as it reaches zero between 0.2 and 0.4 day. This indicates the viscosity contribution is no longer acting in the model beyond this duration.
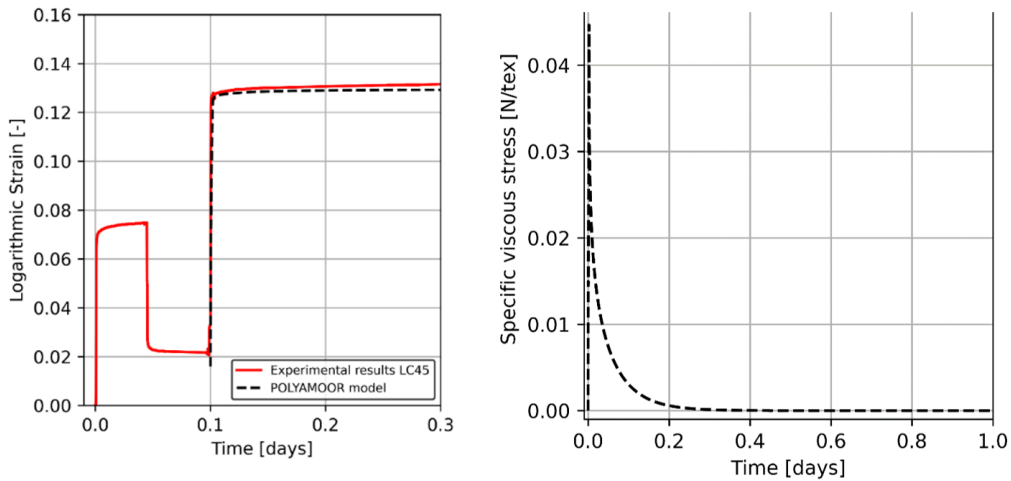
Figure 4.11 – Left: Logarithmic Strain [-] evolution with time [days] for the experimental test LC45 and the POLYAMOOR model. Zoom of the first hours. Right: Viscous specific stress [N/tex] evolution with time [days] in the dashpot of the POLYAMOOR law during the simulation of test LC45

It is observed that the model overestimates the instantaneous strain, reaching 0.124 compared with only 0.120 for the experimental data. This difference might be due to the loading rate. In fact, as explained in chapter 2 section 2.5.3.5.1, the weights are placed using a forklift that does not allow a precise control of the loading and unloading speeds. The rate of loading for the long term creep LC45 was calculated at $0.007 \ N.tex.s^{-1}$ which is nearly four times faster than during the multi-relaxations tests with a speed of $0.002 \ N.tex.s^{-1}$. A study of the strain rate influence (Chevillotte, 2020) on the sub-rope response concluded that the higher the strain rate,

the higher the specific stress at a given strain. This is usual with polymeric materials. We can suppose that with a higher loading speed, the strains reached are smaller. This could explain the difference between the stress-strain curve predicted by the model and the experimental one. Also, the model predicts that 73% of the total strain will be recovered by the sub-rope while only 67% of the total strain was recovered for the test LC45.

We can conclude that the model is not adapted to describe long term creep and recovery phenomena because of its identification on short-term relaxations. Also, the loading rate has an influence on the response of the rope. An underestimation of the load rate will induce error in predicted instantaneous strain.

This first part of the study is published in Ocean Engineering (Civier et al., 2022). It was chosen to extend this study and to investigate other questions about long term creep. This extension is presented in the next sections.

4.7. Extended study

As explained in chapter 2 section 2.5.3.5.1, three tests can be performed at the same time on the test frame. Four decisions were taken to pursue the study of long term creep behaviour of polyamide 6 mooring lines (see table Table 2.5 chapter 2):

- The test LC25 was stopped. A multi-relaxation test was performed on this sample and is presented in chapter 3 section 3.3. The 11 parameters of the POLYAMOOR law were identified on this sample and an investigation of its properties after ageing and long-term creep was carried out.
- The sample 'LC39' was maintained under creep at 39%MBL. Hence, the investigation of long term creep behaviour was extended.
- The sample 'LC45', that had been under creep at 45%MBL for 404 days, and under recovery at 2%MBL during 672 days, was reloaded at 45%MBL to evaluate the evolution of its behaviour and whether the recovery was long enough to recover its initial properties.
- A repeated creep test was launched after the test 'LC25' was stopped. The repeated creep test was performed following the procedure presented in Table 2.6 chapter 2 section 2.5.3.5.1. The aim of this repeated creep is to investigate if long term creep at lower loads is more critical than short term creep at higher loads (storm effect).

In this second part of the study, the temperature was no longer controlled due to an issue with the water circulation. The temperature was recorded during the totality of the long term creep tests for 'LC39' and 'LC45' and is presented on Figure 4.12-left. We observe, after 800 days, that the temperature is no longer controlled and varies considerably. The results of the extended long term creep test LC45 and LC39 are presented on Figure 4.12-right. They will be discussed respectively in section 4.7.1 and section 4.7.2.
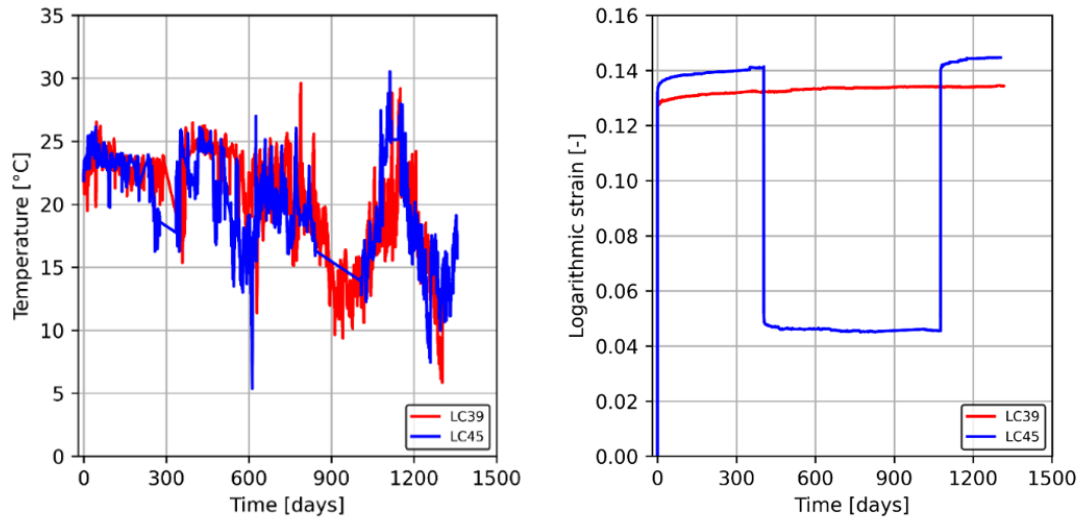
Figure 4.12 – Left: Temperature [°C] evolution with time [days] for long term creep test LC45 and LC39 that has been extended. Right: Logarithmic strain [-] evolution with time [days] for extended long term creep test LC45 and LC39

4.7.1. Extended study: latest results for long term creep test at 39%MBL

The first part of the study included the first 838 days for test LC39. The test duration has now reached 1316 days. Hence, the 4T polyamide 6 sub-rope has been loaded for 478 additional days under creep at 39%MBL. The measured instantaneous strain (IS), time-dependent (VS) strain, total strain (TS) and logarithmic creep rate calculated using Eq. 48 and Eq. 49 (on all of the data from 10^{-2} days to the end of the experiment) are presented in Table 4.4:

Table 4.4 - Measured instantaneous strain (IS), time-dependent (VS) strain, total strain (TS) and logarithmic creep rate for test LC39

Test	Total duration (days)	TS (/)	IS (/)	VS (/)	Logarithmic creep rate (%/decade)
LC39_PartA	838	0.13436	0.116	0.018	0.21
LC39_PartB	1316	0.13437	0.116	0.0187	0.21

We observe that the increase in strain during the last 478 days is not apparent with only 3 significant digits. In fact, the difference can be detected using 5 significant digits. The calculated creep rate using a single logarithmic fit is the same after 478 days. Therefore, the creep rate is still stabilized. To support this conclusion, a local creep rate was calculated between 838 days and 1316 days (during the last 478 days of the experiment) using the same method as presented in chapter 4 section 4.4. This new creep rate is of 0.35%/decade and could be added to Figure 4.6-right. This new value is close to the creep rate calculated previously.

To conclude, the pursuit of this creep study showed that, after 1316 days, the stabilization of the creep behaviour is maintained. No tertiary regime is reached and the conclusion that a short-term creep test could predict long term creep is therefore still valid for this duration.

4.7.2. Extended study: reloading of long term creep LC45 at 45%MBL

The test LC45 was under creep at 45%MBL during 404 days, under recovery at 2%MBL during 672 days, it was reloaded at 45%MBL and it has now been under creep for 281 days.

The first part of this chapter presented the first creep and recovery until 434 days. Hence, the polyamide 6 4T sub-rope has been through 238 days more in recovery followed by another creep at 45%MBL. Figure 4.13-left presents the specific stress versus logarithmic strain. It can be observed, on Figure 4.12-right, that the recovery has remained stable during the last 238 days with a stabilized low rate.

This section will focus on the study of the second loading and creep at 45%MBL plotted as a dashed line in Figure 4.13-left. The different phases of the test are distinguished by different colours.
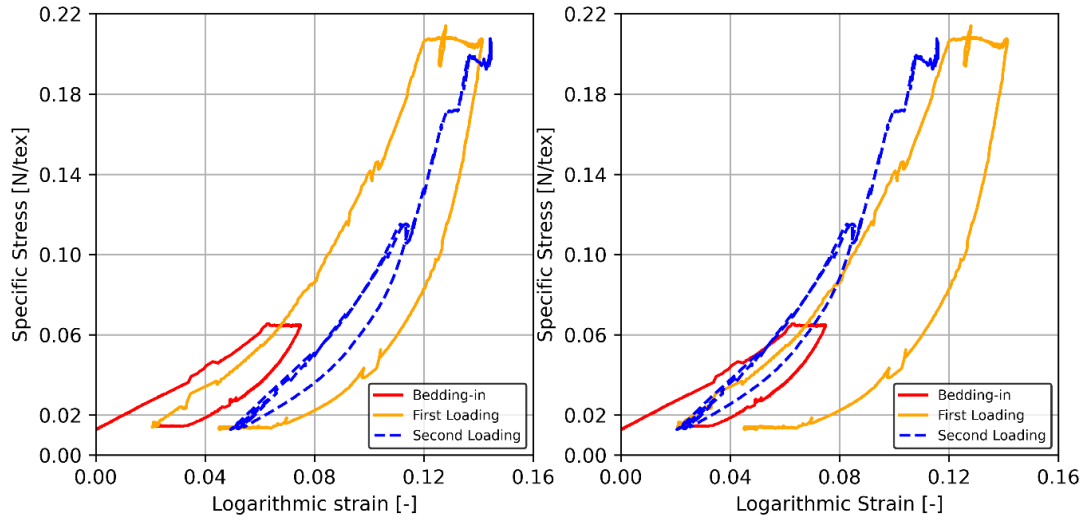
Figure 4.13 – __Left:__ specific stress [N/tex] versus logarithmic strain for LC45 test during the bedding-in [red solid line], the first creep and recovery (yellow solid line) and the second creep (dashed blue line). __Right:__ specific stress [N/tex] versus logarithmic strain for LC45 test with a shift of the second creep (dashed blue line) to match the first creep (yellow solid line)

In chapter 3 section 3.3, it was shown that the behaviour of the sample LC25 (after one-year creep at 25%MBL and one-year recovery at 2%MBL) was characterized by higher mechanical properties and higher instantaneous stiffnesses. To check if this observation can also be made on this sample, we first investigate the stiffness of the sub-rope during the re-loading. Figure 4.13-right presents a shift of the stress-strain curve to match the first loading phase. It indicates that the second loading presents a higher stiffness with lower strains reached for the same specific stresses. The modulus at 9% strain was calculated for the first and second loading phases and values are respectively 2.8 N/tex and 4.6 N/tex. The ratio $\frac{E_{SecondLoading}}{E_{FirstLoading}}$ is 1.63. Hence, this result is in accordance with the results presented previously. In chapter 3 section 3.3.3.1, the ratio of the a parameter (characteristic of the instantaneous behaviour in the POLYAMOOR law) between a virgin sample and the LC25 sample was 1.44.

We can conclude that long term creep and recovery will increase the stiffness of polyamide 6 4T sub-rope. For mooring lines, it could be important to consider this evolution of properties when dimensioning mooring of offshore floating wind platforms.

Table 4.5 summarizes the measured instantaneous strain (IS), time-dependent (VS) strain, total strain (TS) and logarithmic creep rate calculated using Eq. 48 and Eq. 49 on all the data from 10^{-2} days to the end:

Table 4.5 – Comparison of the measured instantaneous strain (IS), time-dependent (VS) strain, total strain (TS) and logarithmic creep rate for test LC45 first and second creep

Test	Total duration (days)	TS (/)	IS (/)	VS (/)	Logarithmic creep rate (%/decade)
$LC45_B$ first creep	405	0.141	0.120	0.021	0.21
$LC45_B$ second creep	281	0.144	0.137	0.008	0.16

The acquisition system was adapted for LC45 between the two loadings to change the acquisition frequency with more ease and some small loadings were applied but were not recorded to check if the sensors calibration. That is why we observe a shift on Figure 4.13-left between the end of the recovery phase (yellow solid curve) and the beginning of the second loading phase (blue dashed curve). The total strain reached is higher during the second creep than during the first but this could be explained by these experimental events.

However, the calculated creep rate using a single logarithmic fit from 10^{-2} days to the end is lower for the second creep phase with 0.16%/decade versus 0.21%/decade during the first creep. To validate this first observation, the evolution of the creep rate during this second loading phase was also studied following the same procedure as in section 4.4. The logarithmic creep rate was evaluated every decade using Eq. 49. Figure 4.14 plots the creep rates versus time for the first and the second creep phase.
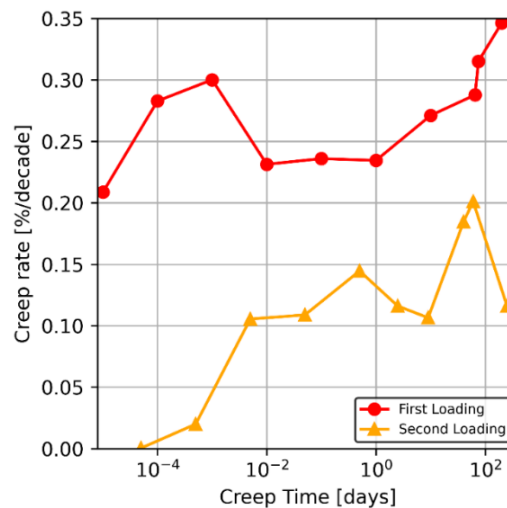
Figure 4.14 – Creep rated [%/decade] versus the creep time [days] for the first creep of LC45 (red circles) and for the second creep (yellow triangles)

We observe the creep rate during the second creep phase is below the one during the first creep phase throughout the creep duration. The explanation could be a stabilization of the viscous behaviour during the first creep and recovery phase. This also means the long recovery did not lead to a complete recovery of the initial state. Furthermore, the kinetics of creep might be less important after long recovery phases. The material microstructure and construction might stabilize with time.

4.7.3. Repeated creep test

The test presented in this section focuses on the characterization of short-term creep at high loads versus long term creep at low loads on the same sub-rope. This study aims to determine how much creep we need to consider over the lifetime of a project. Also, this test should help evaluate if most creep is generated during a few short storm events (higher loads) or during long periods at pre-tension (lower loads). The test presented here includes a storm event lasting 1 hour and a recovery during, at least, 3 months at a pre-tension level of 25%MBL. The procedure is repeated two times. The procedure is described in table Table 2.6 chapter 2 section 2.5.3.5.1.

Figure 4.15-left plots the logarithmic strain evolution with time and Figure 4.15-right presents the specific stress versus logarithmic strain. Figure 4.16-left and Figure 4.16-right are respectively zooming of the first and the second storm events lasting 1 hour. Table 4.6 summarizes the strains and the logarithmic creep rates measured for this test.
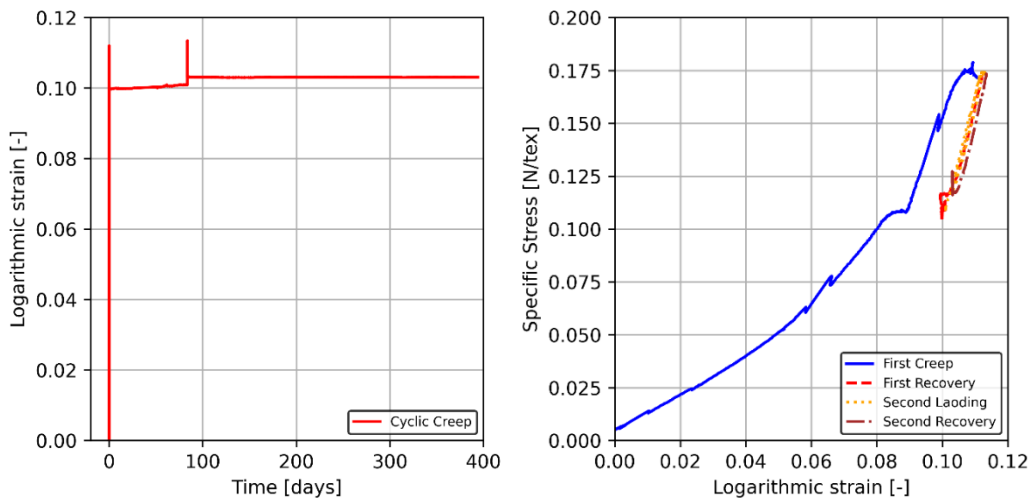
Figure 4.15 – __Left:__ Logarithmic strain [-] versus time [days] for the repeated creep test. __Right:__ Specific stress [N/tex] versus logarithmic strain [-] for repeated creep test with the first creep (blue solid line); first recovery (red dashed line); second loading creep (yellow dotted line); second recovery (brown dashed-dotted line)

Table 4.6 - Measured instantaneous strain (IS) and recovered instantaneous strain (IRS), time-dependent (VS) strain and time-dependent recovered strain (VRS), total strain (TS) and total recovered strain (TRS) and logarithmic creep rate

Step	Duration	TS (/)	IS (/)	VS (/)	Logarithmic creep rate (%/decade)	TRS (/)	IRS (/)	VRS (/)
39%MBL	1 hour	0.112	0.107	0.0050	0.21	-	-	-
25%MBL	83 days	0.101	-	0.0016	0.14	0.0126	0.0098	0.0028
39%MBL	1 hour	0.113	0.112	0.0009	0.031	-	-	-
25%MBL	393 days	-	-	-	-	0.011	0.0022	0.0081

The values in Table 4.6 highlight that the behaviour of the sub-rope is significantly different during the first two steps (39%MBL followed by 25%MBL) and during the last two steps (repeat of the same sequence). The kinetics of creep and recovery are much lower during the second phase of the procedure. The first phase at 39%MBL leads to around 0.5% creep strain (4.5% of the total strain) while only 0.09% creep strain is observed for the second phase at 39%MBL (0.8% of the total strain). The second storm event presents a creep rate of only 0.031 %/decade against 0.21%/decade for the first.

Also, during the first pre-tension at 25%MBL, a recovery is first observed but it is followed by creep. This creep at lower tension is characterized by a creep rate of 0.14%/decade (Table 4.6). Hence, this creep at lower tension shows higher kinetics than the second creep at 39%MBL (0.031<0.14). On the contrary, during the second pre-tension event at 25%MBL, no creep phenomenon is observed before the recovery. The sub-rope continues to recover very slowly after 393 days, hence more than one year. Bles (Bles & Kadiri, 2020) performed a study at the rope-yarns scale with similar procedures; creep tests at different loads. The observations were that the rope-yarn will creep after recovery if the test duration in pre-tension is long enough. Depending on the ratio $F_{max}/F_{pre-tension}$, the time of recovery before creep changes. The duration of these tests was around 1 day. We may suppose that, if we wait longer, creep might follow recovery.

This difference between the first and last steps could indicate that the loads applied have stabilized the construction and/or the microstructure of polyamide 6 material. Hence, the history of loading is important for polyamide 6 sub-ropes. This is in accordance with the observations made when re-loading the test LC45 described in chapter 4 section Part B.4.7.2.

We can conclude that the short-term storm events generate most creep. During the first two steps: the short loading at 39%MBL has generated more creep than the long one at 25%MBL. The same observation can be made during the repeat of the procedure. However, the first recovery at 25%MBL is characterized by more creep than the second creep at 39%MBL, but this seems to be due to stabilization of the sub-rope viscous properties. Therefore, after stabilization, we observe the short period at higher load presents more creep than the longer time at low loads.
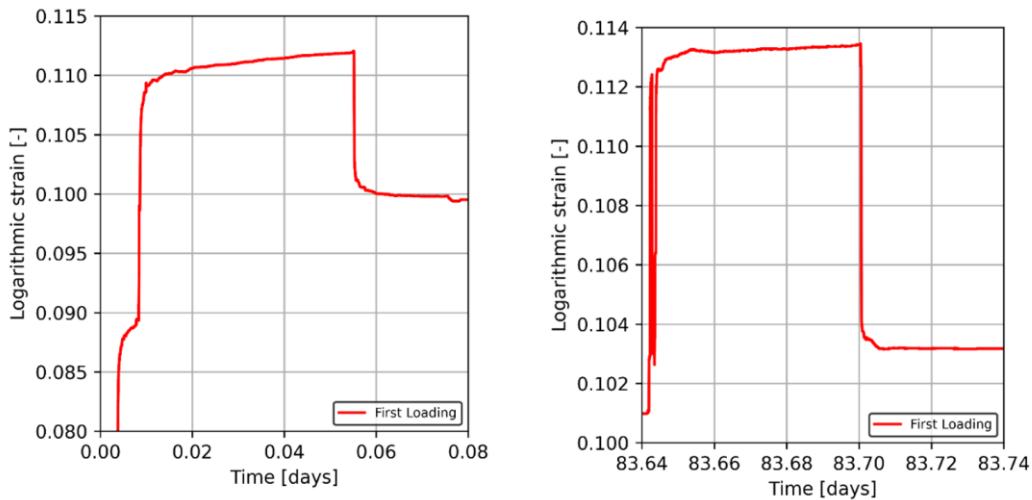
Figure 4.16 – Left: zoom of the logarithmic strain [-] evolution with time [days] for the first storm event. Right: zoom of the logarithmic strain [-] evolution with time [days] for the second storm event.

Conclusions from this test are that a sub-rope that has not been loaded will show higher viscous kinetics during its first months of use. Also, storm events could be followed by a stabilization of the rope viscous kinetics as the second pre-tension is characterized by a nearly constant strain value (no creep and nearly no recovery). This experiment suggests that a bedding-in sequence at higher loads consisting of creep and recoveries would help stabilize the sub-rope and decrease the viscosity kinetics. Also, we can conclude that short tests (only storm loads) could be used to predict the total creep strain over the lifetime of a project.

4.8. Conclusion

This chapter presented experimental results to evaluate the long term creep properties of polyamide 6 mooring lines and to examine the necessity of running long term creep experiments. The main findings are:

- The load level affects the creep behaviour. Higher loads will increase the creep strain values and the creep rate almost proportionally.
- Both creep and recovery kinetics show three phases. The third phase of creep is characterized by an increase of the rate whereas for recovery, it is a stabilization of the rate. The recovery in the primary phase is faster than the creep.
- Short term creep tests of up to 3 hours can provide a good prediction of long term creep behaviour using a logarithmic-linear law up to 2 years.
- A simple creep law can be used to describe the creep behaviour of polyamide 6 sub-ropes. A single logarithmic law identified using the data from the beginning of the secondary phases is accurate enough for creep but less for recovery. An approach using the Weibull function is more accurate for recovery and acceptable for creep though the beginning of the creep is not well described. Further work will examine bedding-in procedures applying different loading sequences before creep. The influence of rope construction is also being evaluated, through tests on yarns, rope-yarns and strands.
- Short events at higher load will generate most of the creep while longer creep at lower loads will be characterized by slower creep rate. Therefore, we can use short term storm events to characterize the creep over the lifetime of a mooring project.
- The POLYAMOOR law is not adapted to predicting long term creep as it lacks relaxation times. Also, it has been identified on a strain rate controlled multi-relaxation (corresponding to $0.002 \ N.tex.s^{-1}$), hence when the load rate studied is considerably different (ie, faster) than the load rate used during the identification test, this can induce errors in the prediction.
- Long term creep and recovery will have an effect on the behaviour of a polyamide 6 4T sub-rope resulting in an increased stiffness. After long term creep and recovery, a sub-rope will show slower creep and recovery kinetics, as was observed for the re-loading of sample LC45 and during the repeated creep test.

Chapter 5. Fatigue investigations: from mechanisms to heat build-up prediction

5.1. Introduction

As presented in Chapter 1, fatigue durability is a key aspect for the use of polyamide ropes as mooring lines. In contrast to polyester, polyamide fibres are sensitive to abrasion damage so this mechanism must be clearly understood. The study presented here is the continuation of the work performed by Chevillotte (Chevillotte, 2020) and presented in chapter 1 section 1.6. Hence, this section proposes an experimental study that aims to complete the work started during that previous project.

This fatigue study is performed on 4T scale sub-ropes described in chapter 2 section 2.3. As noted previously this construction was developed by the rope-maker for the first research performed by Chevillotte. It is characterized by a shorter lay-length than usual constructions. This allows fatigue tests to be performed on more standard laboratory test equipment such as the SERVOTEST presented in chapter 2 section 2.5.3.3. The difficulties when performing fatigue tests on twisted polyamide sub-ropes are the following:

- The control of the failure zone is complicated. It must not be in the terminations, which is often the case when testing sub-rope in fatigue. Hence, splices are used for the terminations. However, to increase control on the failure, the splices must present a minimal length and number of tucks. The splices used for the 4T tests are the minimum length required, with 6 tucks. The sub-ropes will be subjected to a torque when loaded in tension and they must balance this torque to stabilize the construction. Longer splices would have been preferable but were not possible on the SERVOTEST machine (stroke limitations).
- The machine used must have a long stroke because of the displacement amplitudes associated with the long sub-rope samples tested (with the splices). Also, polyamide 6 sub-ropes extend much more than polyester with a strain at failure reaching 20%. The SERVOTEST machine has a stroke of 700 mm. Hence, even with this laboratory scale sub-rope, the stroke required is considerable and the machines that can provide it are rare.
- Another difficulty is the duration of the test that depends on the loading frequency that can be achieved. The frequency must be chosen in regard to the final application. For mooring lines, the wave swell frequency is around 0.1 Hz. This very low frequency was therefore used for our fatigue campaign. Hence, the tests lasted several days with a maximum duration reaching one month. The availability of the test machine for such a campaign is limited. Moreover, the machine must run continuously (no electricity power cuts nor cooling water issues). Also, the machine used is hydraulic and there may be issues with the oil pressure (leaks). Therefore, the test campaigns realized during this project (both by the research assistant and the PhD) were complicated, requiring several repairs to the test machine.
- Also, polyamide sub-ropes are sensitive to water and, for this mooring line application, the tests have to be performed in water.
- Finally, polyamide sub-rope fatigue lifetime is caused by two main mechanisms: creep and abrasion. The chosen load ratio has an influence on the mechanism that will cause failure. Chevillotte showed that, for a load ratio around 0.04 (heat build-up test) and 0.15, the results were close. We performed our test campaign to extend Chevillotte results, therefore we worked with a fixed minimum value at 2%MBL and changing the maximum value, similar to what is performed during heat-build up test. Hence, the amplitudes of the fatigue loadings were important.

To deal with these difficulties, and to ensure that the required results would be obtained, it was chosen, at the beginning of the project, to also have a post-doctoral researcher working on this time consuming, fatigue study.
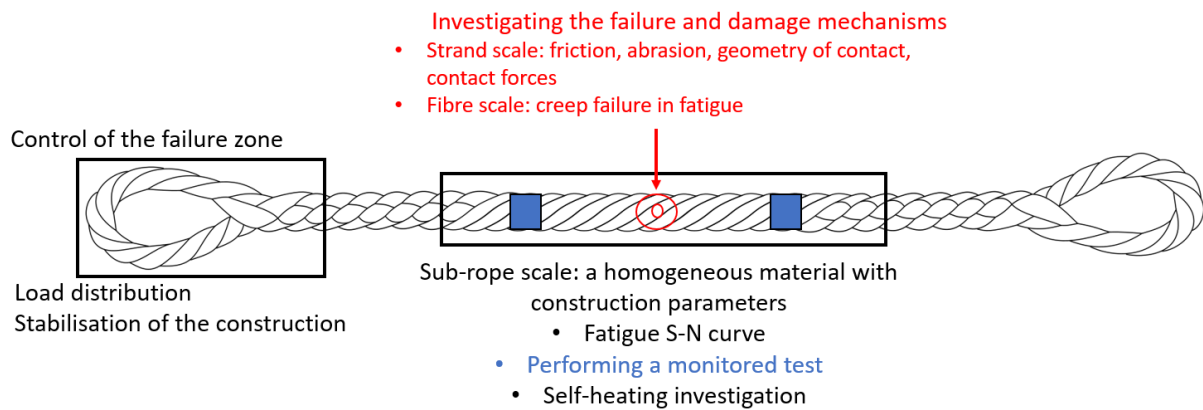
Figure 5.1 – Scheme of the fatigue study objectives and difficulties proposed in this chapter

The study is schematized in Figure 5.1 and the objectives are the following:

- First, the results of fatigue tests on 4T sub-rope samples at low maximum loads for long lifetimes were needed. This study is presented in section 5.2. The fatigue curve in the traditional S-N format, with cycles to failure plotted versus maximum load normalized by the nominal wet break load, is extended with these new experimental results. The failure mechanisms are further investigated using X-ray tomography scans and SEM images in section 5.3.2.
- A test with strain monitoring was needed to have first responses on the mechanical response and hysteresis of sub-ropes during cyclic loading. This was not done in the previous work where only cycles to failure were recorded. One experimental fatigue test with strain measurement was therefore performed during this project and will be presented in section 5.4. The calculation of the dynamic stiffness and the measurement of creep and hysteresis during this test are described. These results are also used to compare with model results, using the 1D constitutive POLYAMOOR law presented in chapter 3 section 3.2, and to conclude on its ability to describe the dynamic behaviour of polyamide 6 sub-ropes. They serve as a basis to propose future work.
- The heat build-up protocol developed by Chevillotte needed to be validated by other operators. In fact, the analysis of these experimental tests, described in chapter 2 section 2.5.3.3.1, is complicated and the results could be operator dependent. Hence, a validation of the repeatability by different operators was necessary. The prediction proposed by Chevillotte also needed to be validated with more experimental fatigue tests and the analysis to be clarified based on an enriched self-heating curve. This study is presented in section 5.5.

5.2. Fatigue tests on sub-ropes

Twenty-one 4T sub-rope specimens were tested wet in fatigue, following the procedure described in chapter 2 section 2.5.3.3.2. These twenty-one new fatigue results were added to the results obtained previously by Chevillotte (blue diamonds called 'POLYAMOOR' in Figure 5.2). The completed S-N curve with the maximal load (%MBL) plotted versus the number of cycles to failure is presented in Figure 5.2.
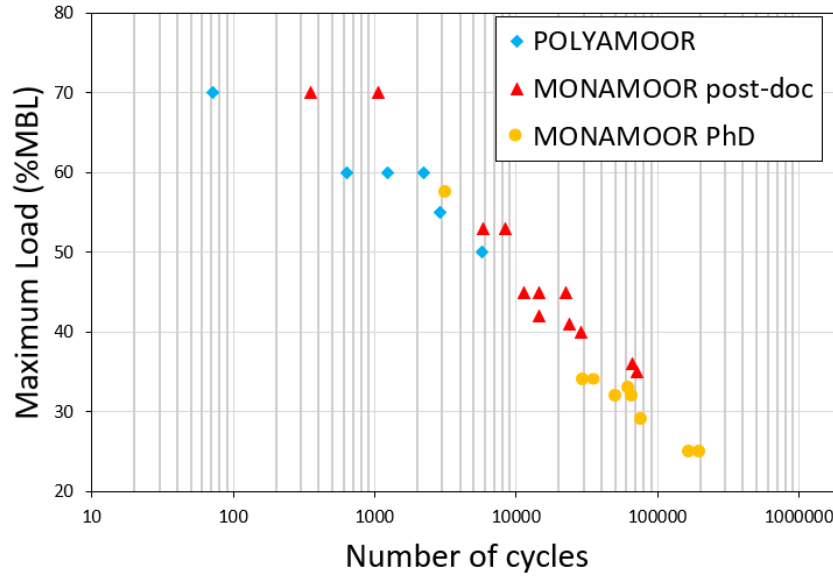
Figure 5.2 - Results of the fatigue tests on 4T sub-rope samples obtained during POLYAMOOR and MONAMOOR post-doct and PhD. Maximal load (%MBL) versus the number of cycles to failure

Twelve specimens taken from the same batch of polyamide 6 sub-rope as Chevillotte (orange triangle markers named "POLYAMOOR") were tested and nine specimens were tested from a new batch (yellow circle markers). We observe that the points corresponding to specimens from the new batch, are shifted slightly to the left in comparison with the rest of the data. This indicates that the sub-rope taken from the new spool (new sub-rope) presents a reduced fatigue lifetime compared to the sub-ropes taken from an aged spool (three years aged spool). A similar finding was made in Chevillotte's study (Chevillotte et al., 2018) on 7T sub-rope samples. In their study, they showed that, an older sample batch (a more aged one), had a higher fatigue lifetime time and a lower variability than a newer batch. The main suspected reason for this difference between batches is the coating. Indeed, the coating (for which we do not know the formulation) may continue to evolve with time until it reaches a stable state. Hence, aged sub-ropes might be characterized by a different coating state. As internal abrasion has been identified as one of the main degradation mechanisms (Mandell 1987), a change in the coating can have a visible and significant impact on fatigue lifetime. As the gap between the curves is not higher than the scatter, the shift could also simply be due to the data spread. However, the twenty-one new fatigue test results confirm the linear trend observed and no endurance plateau has been reached.

Figure 5.3 shows a summary of the results from all the fatigue tests on the 4T sub-rope scale and compares them to the results previously obtained on the 7T sub-rope sample (Chevillotte et al., 2018), and to recently published results for polyamide 6 parallel twisted sub-ropes by Banfield *et al.* (Banfield & Ridge, 2017). The load range, normalized by the minimal breaking load (MBL) is plotted versus the number of cycles to failure. The experimental results for the 7T sub-rope sample are from fatigue tests performed with the same load ratio LR (cycling from 2% of MBL to a maximal value). The data from Banfield *et al.* are from fatigue tests to failure, conducted with a mean load of 40%MBL with load ranges between 70%MBL and 40%MBL. There are two results from Banfield 2017 associated with two different constructions.
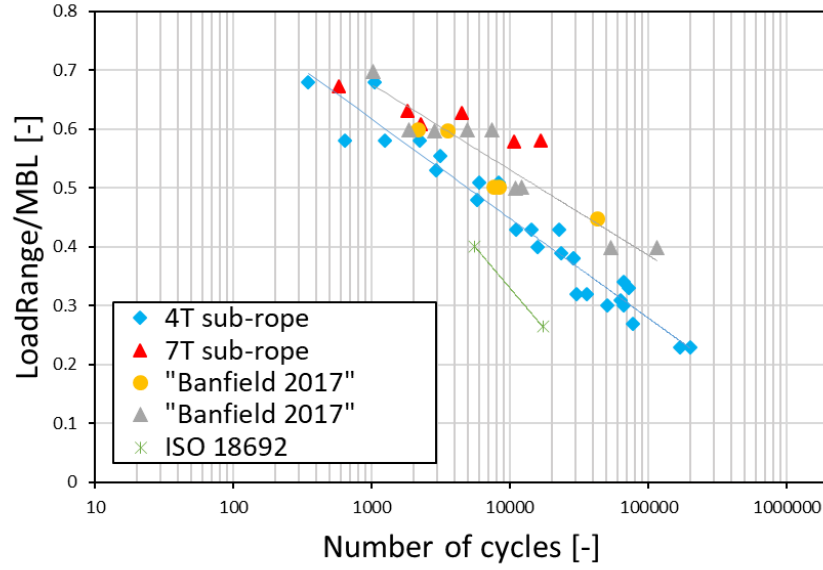
Figure 5.3 – Load range/MBL plotted versus number of cycles to failure. Comparison of the complete fatigue curve of 4T sub-rope samples obtained (blue diamond) to data obtained on 7T sub-rope sample (red triangles (Chevillotte et al., 2018)) and to data obtained on two higher scale twisted polyamide constructions (orange circles and grey triangles (Banfield & Ridge, 2017)).

We chose to plot a semi-logarithmic scale because it allows to appreciate the differences in behaviour. Indeed, we often see plotted log-log scale but it will reduce the differences in fatigue lifetime between samples and might lead to incorrect conclusions. Also, using a log-log scale to propose a best fit can lead to an overestimation of the lifetime. Here, we will use a best fit of the form Eq. 52 to allow easier comparison with literature results.

$$K \cdot (LR/MBL)^{-m} = N$$

Eq. 52

Where N is the number of cycles, LR is the load ratio and m and K are constants for the rope. The parameters N and K obtained for the 4T sub-rope are presented in Table 5.1 and compared to other parameters from literature for polyamide and polyester.

Table 5.1 - Fatigue properties of the polyamide 4T sub-rope scale of this study, of polyamide rope from Banfield et al. (Banfield & Ridge, 2017), of polyester (Flory et al., 2016) of and steel chain from DNV (DNV, 2021). The fibre rope properties for tension ranges normalized by MBL, while the chain data are given for stress ranges in MPa

	PA 4T sub-rope (this study)	PA	PET	Steel Chain
K	76	25.3	1.2×10^4	6.0×10^{10}
m	13.3	7.5	5.15	3.0

On Figure 5.3, we observe a slight shift of the 4T sub-rope to the left compared to the 7T sub-rope, attesting a reduced fatigue lifetime. This is in accordance with the difference of construction between the samples. Indeed, the 4T sub-rope has a construction specifically made for laboratory experiments. It is characterized by a smaller number of components in the strands, rope-yarns and yarns as well as a higher twist angle (shorter lay-length). The twist angle will impact the amount of sliding of the strand during tensile loading and unloading, hence it will impact the inter-abrasion. On Figure 5.3, we observe an apparent difference for lower load ranges (from a load range of around 0.5 to 0.2) while the data at high load ranges, for the different specimens, seem to converge. This result could be interpreted by a change in the dominant failure mechanism for the 4T sub-rope samples. Mandell *et al.* (Mandell, 1987) showed that creep is responsible for the fatigue failure at high loads while, at higher cycles and

lower loads, inter-abrasion will dominate. The inter-abrasion mechanism is dependent on the construction of the rope. We can therefore expect to observe more differences in fatigue lifetime between samples with different constructions at lower loads. The fatigue tests performed on the 4T sub-ropes have a changing mean load. The points between 0.2 and 0.45 have mean loads between 11% MBL and 21%MBL while between 0.5 and 0.7, the mean load is between 25%MBL and 45%MBL. For the lower mean loads, the inter-abrasion might be more active while for the higher mean loads, the creep will dominate, leading to a less significant impact of the lay length and construction on the failure. On the contrary, all the fatigue tests from Banfield *et al.* were carried out at a mean load of 40%MBL and only the load range is changing. Hence, for low ranges with 40%MBL mean load, we could suppose that the inter-abrasion is less active and the creep will dominate. That would explain the divergence of the fatigue lifetimes, at lower load ranges, between the 4T scale polyamide sub-rope and the polyamide sub-ropes from Banfield *et al.* on Figure 5.3.

Also, as mentioned in chapter 2 section 2.5.3.1, the splices are made manually for the 4T sub-rope and are the minimal length required to perform a fatigue test. Longer splices would have secured the rupture in the gauge length and the load distribution. Indeed, Figure 5.4 shows the different types of failure obtained in this campaign for different samples. There are three types of failure: failure in the gauge length; failure in the splice (end); failure of one strand. The failure of only one strand was only observed for the sample loaded with a maximal load of 25%MBL. This specific failure profile can be the result of inter-abrasion at lower loads. Inter-abrasion can lead to a loss of material associated with a non-uniform distribution of the stress inside the three strands. Hence, one strand might break first due a to stress concentration and reduced mechanical properties, but, as the load is not too high, the two other strands can continue to hold it without breaking. At higher loads, it might also be one strand that first breaks, but as the redistributed load is too high, the remaining strands will break immediately after the first.

Figure 5.4 - 4T sub-rope samples after fatigue failure obtained during the MONAMOOR project

In comparison, the 7T sub-rope's splices, tested by Chevillotte, were prepared by the supplier, with a higher length in comparison to the gauge length studied, and all failed between the splices. Hence, it was expected that the 7T sub-rope would present a higher fatigue lifetime in comparison with the 4T sub-rope.

The difference observed between the 4T, the 7T and Banfield's 2017 results can therefore be explained by differences in the construction and also by differences in the coating. However, the 4T sub-rope construction is interesting as it allows to have a curve that is comparable to Banfield's result, that is conservative and that is easier to study in the laboratory.

The next section proposes a study of the damage and failure mechanisms on 4T sub-rope samples after fatigue testing to investigate if some mechanisms can be identified.

5.3. Investigation of damage and failure mechanisms

Figure 5.5 is a picture of a rope after fatigue failure in the eye. We can observe its shape after fatigue as the gauge length was not broken. This picture reveals significant abrasion in the contact area between the rope strands. The inner surfaces in contact also reveal broken fibres. This first global observation requires some further analysis using dedicated experimental means.

Figure 5.5 - Damaged 4T sub-rope after fatigue testing

As noted previously, two failure mechanisms dominate cyclic response of polyamide ropes. At high loads, creep rupture, at the fibre scale, is the main mechanism leading to rupture. It is associated with a failure morphology of the fibre close to the one observed during tensile test to rupture. At lower loads, it was shown by Bunsell (Bunsell & Hearle, 1971) that another failure morphology of fibre could be observed, characterized by a tail on the fibre. Hence, an investigation of the failure morphology of the fibres was performed on our broken samples. Also, the internal abrasion, that is suggested to be the failure mechanisms dominating at lower loads (Mandell, 1987), is observed at the rope-yarn and strand scales. Tomography analysis can therefore be used to investigate this damage mechanism.

Hence, this section will present an optical study of the damage and failure mechanisms of 4T sub-ropes during fatigue testing, using optical microscopy, SEM and X-ray tomography analysis.

5.3.1. Failure morphology

SEM observations were performed (following the procedure described in chapter 2 section 2.5.5.1) on samples after fatigue failure to determine the failure morphology at the fibre scale. The morphology is compared to results from other studies. Figure 5.6 shows examples of the failure morphology obtained after fatigue tests between 2%MBL and 34%MBL.

On Figure 5.6-a and b, we observe a strip shapes comparable to what has been observed in other studies (Bunsell & Hearle, 1971; Ramirez et al., 2006). This morphology is typical of fatigue failure with a crack propagating in the axial direction of the fibre before propagating in the radial direction until failure. On Figure 5.6-c, we observe a melted fibre end after failure. Herrera also observed this phenomenon and explained it by the speed of failure which does not allow the heat to be evacuated and leads to melting of material. Finally, Figure 5.6-d highlights a failure with a propagation of the crack radially and no peeled strip, that could be associated with a simple tensile loading failure.
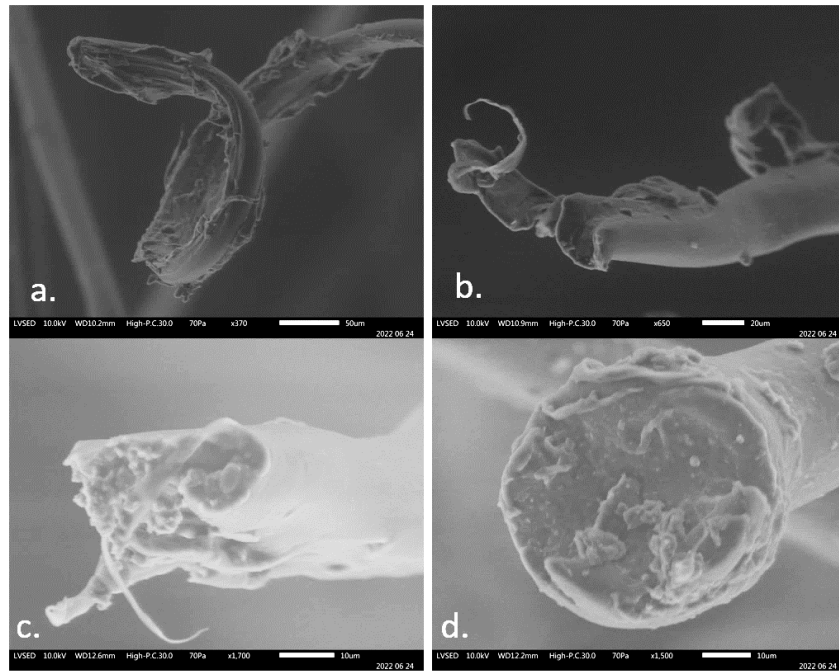
Figure 5.6 - Failure morphology of fibres taken on failed sample in the gauge length

The presence of distinct mechanisms in the same broken sample highlights that, while one phenomenon will dominate the rupture, other phenomena can occur at the fibre scale when failure happens (fibres at different locations in the cross-section undergo different loads, resulting in different failure mechanisms).

5.3.2. Damage mechanisms

5.3.2.1. X-ray tomography

The gauge length of a 4T sub-rope sample that broke in fatigue (cyclic loading between 2%MBL and 29%MBL) in the eye-splice has been analysed with X-ray tomography to investigate the damage mechanisms. A comparison of the tomography scans of this sample after fatigue with scans of a virgin sample is proposed. The two samples (virgin and after fatigue) are presented on Figure 5.7. The procedure and parameters of the tomography scans are presented in chapter 2 section 2.5.5.2.

Figure 5.7 - Image of the samples analysed with X-ray tomography. a) Virgin sample. b) Sample after fatigue testing and failure in the eye-splice

Two scans were performed on each sample (virgin and after fatigue): one scan with no tension and one with a low tension of 400 N to observe a construction closer to a configuration during fatigue loading. Figure 5.8 and Figure 5.9 present the scans of the transverse section for the

virgin and the fatigued sample respectively with tension and without tension; Figure 5.10 and Figure 5.11 present the tomography scans of the axial section of the virgin and the after fatigue sample respectively with tension and without tension. The blue lines on each image of the transverse section in Figure 5.8 delimit one strand (bigger outlines) and the red lines define one rope-yarn (smaller outlines) of the sub-rope. These allow the trajectory of these components along the sub-rope to be followed. Only one rope-yarn is indicated in Figure 5.9 for the scans under tension.
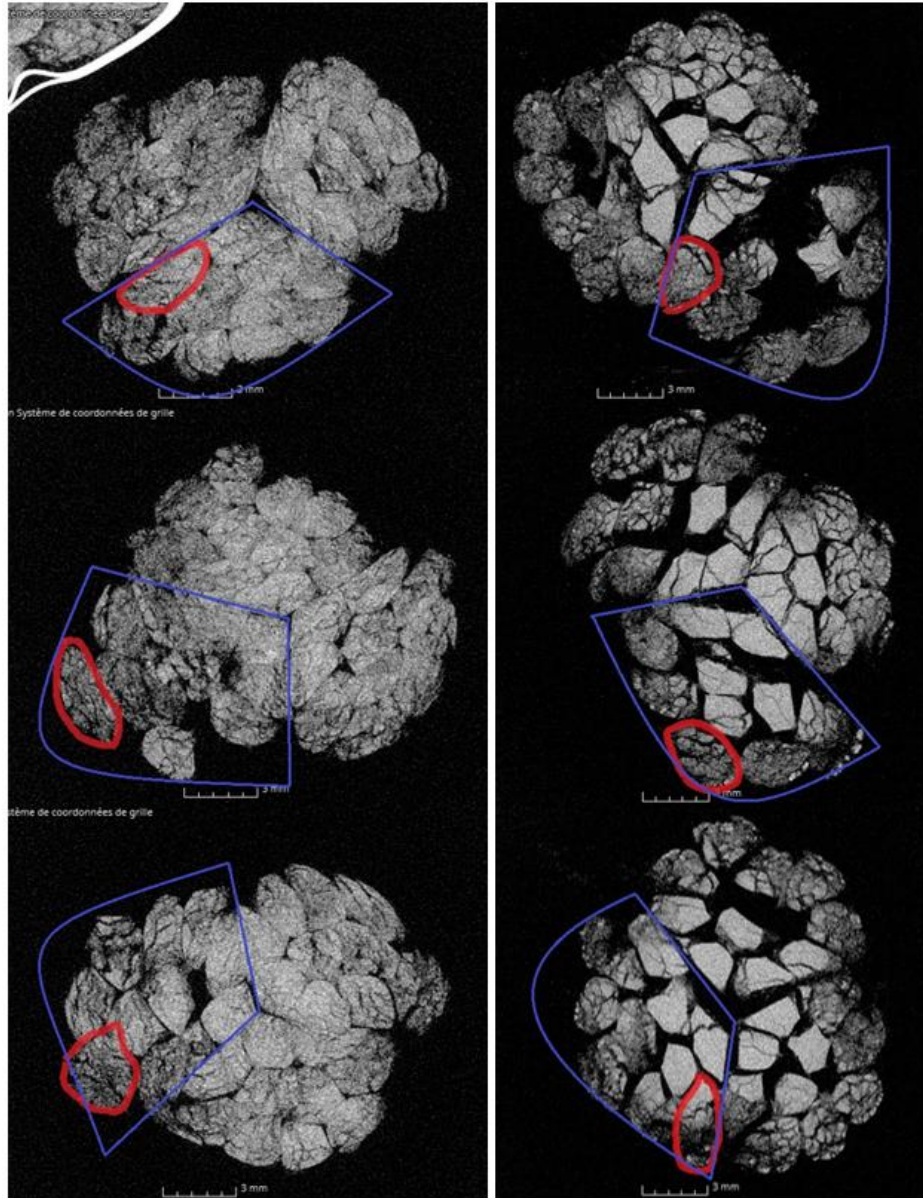
Figure 5.8 – Tomography scans of the radial section of a 4T sub-rope without tension. Left: Virgin sample. Right: fatigued sample (after a fatigue test at 29%MBL). Red small circles: rope-yarn. Blue big circles: Strand.

Several observations can be made on these tomography scans. First, we can appreciate the helicoidal trajectory of the strand along the sub-rope from scan to scan. In the same way, the helicoidal trajectory of a rope-yarn inside a strand can be followed. We observe that, depending on the position along the axial direction, the rope-yarns will alternate between being inside the sub-rope, in the contact region between strands, and outside the sub-rope. The rope-yarns will remain at the same radial distance from the helix axis of the strand. This is in agreement with the description of the twisted packing proposed by Leech (Leech, 2002).

The shape of the rope-yarns and strands is also consistent with the truncated wedges shape described by Leech for transversely soft components.

The angle between the rope-yarns and the helix axis changes along the radial direction. On the axial section scans (Figure 5.10 and Figure 5.11), the rope-yarn radial sections are not cut following the same angle. This is also in accordance with the description of Leech. Such a construction and trajectories will induce different loading conditions for a rope-yarn along its length. It will be subjected to more tension at the inner part of the sub-rope; in contrast it will go through more flexion and shearing when at the outer surface of the sub-rope.
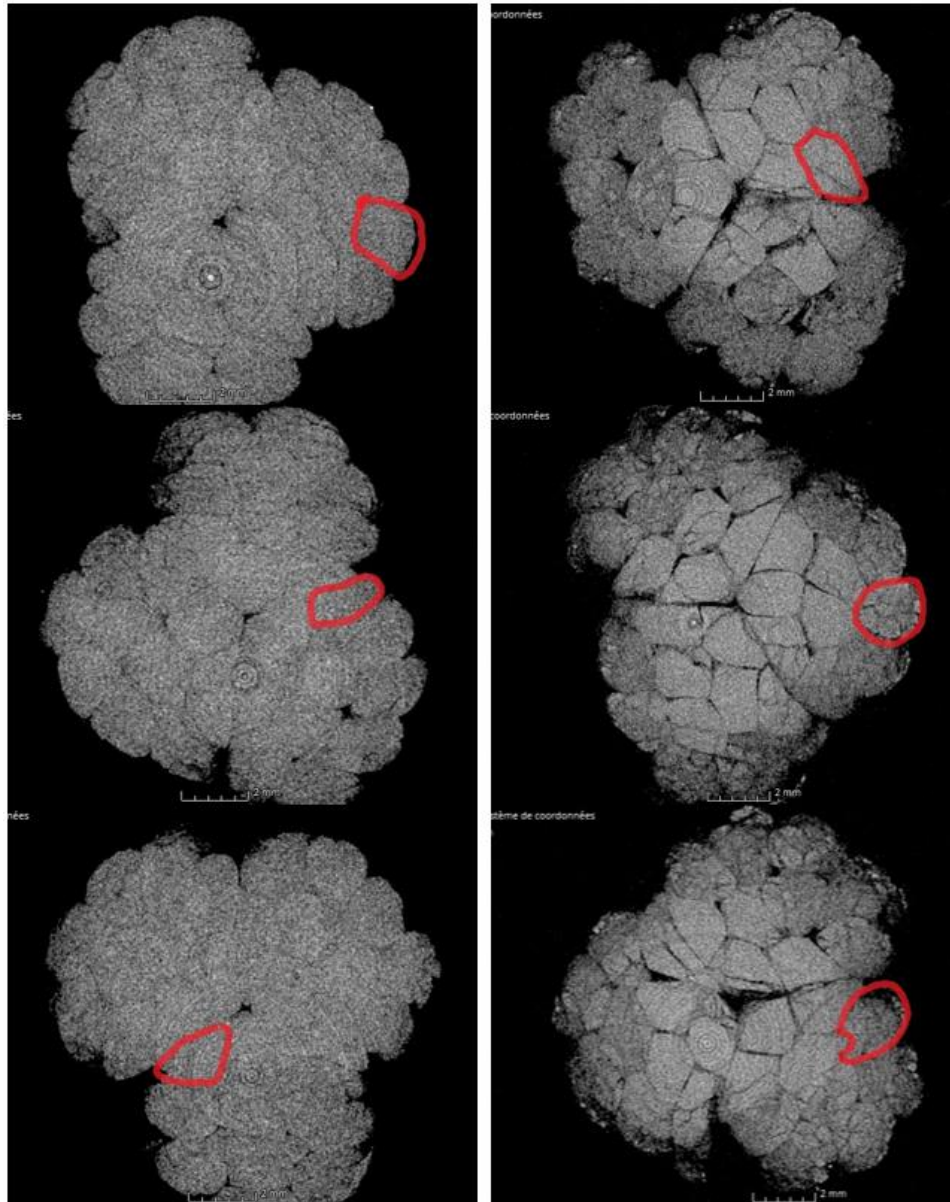
Figure 5.9 - Tomography scans of the radial section of a 4T sub-rope under 300N tension. Left: Virgin sample. Right: fatigued sample (after a fatigue test at 29%MBL). Red small circles: rope-yarn.

Also, a compaction of the rope-yarns is visible on the after-fatigue sample scans. On Figure 5.8 and Figure 5.9, at the inner surface of the after-fatigue sample, the rope-yarns are denser and more compact due to radial compression resulting in transverse compaction. Their shape is very angular both under tension and without tension.

On Figure 5.9 and Figure 5.11, we also observe that the contact areas between the three strands, at 120°, are more visible on the fatigued sub-rope. These contact areas (inner surfaces) are subjected to radial compression and compaction that is associated with a change in the optical aspects of the contact area on the tomography scans. This difference between the fatigued and virgin sub-rope is even more visible in tension. In fact, it becomes difficult to detect the contact areas for the virgin sample. Bain observed these types of changes, due to lustering, in the contact area between HMPE textile ropes and a pulley ring (Bain, 2020; Bain, Marco, et al., 2022). Additional SEM scans were performed and are presented in the next section 5.3.2.2 to investigate this phenomenon.
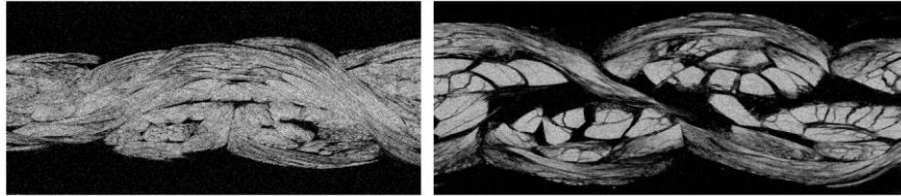
Figure 5.10 – Tomography scans of the transversal section of a 4T sub-rope without tension. Left: Virgin sample. Right: fatigued sample (after a fatigue test at 29%MBL).
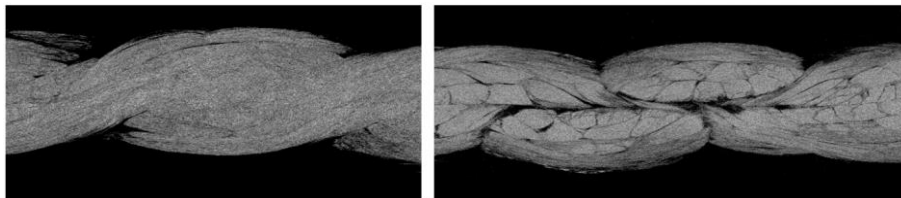
Figure 5.11 - Tomography scans of the transversal section of a 4T sub-rope under 300N tension. Left: Virgin sample. Right: fatigued sample (after a fatigue test at 29%MBL).

5.3.2.2. Additional SEM analysis: study of the material at the filament scale

X-ray scans highlighted that the rope-yarns were more rigid for the fatigued sample than for the virgin sample. Additional SEM observations were performed (following the procedure described in chapter 2 section 2.5.5.1) on the fatigued sample (Figure 5.7.b) after fatigue failure to investigate the state of the material at the filament scale. Figure 5.12 presents SEM pictures at different magnifications (left: virgin material and right: fatigued material). We observe the fibres composing the rope-yarns and yarns are more compacted for the fatigued sample. The new positioning and organisation of the fibres is associated with a smoother, more compact and more rigid surface of contact, even without tension. No melting of fibres was observed; hence, the new state of the rope-yarns seems to only be due to the rearrangement of the fibres under tension. This new state of the surface at the contact area might be associated with a lower friction coefficient and so, an improved fatigue durability. These observations are similar to the studies made by Bain on other textile fibres ropes (Bain, Marco, et al., 2022).

Moreover, we observe on the fatigued sample, on Figure 5.12.b (magnification x50) a zone that makes a specific angle with the fibre direction. This zone is suspected to be due to the friction of the fibres composing this strand with the fibres composing the other strand in contact with them.
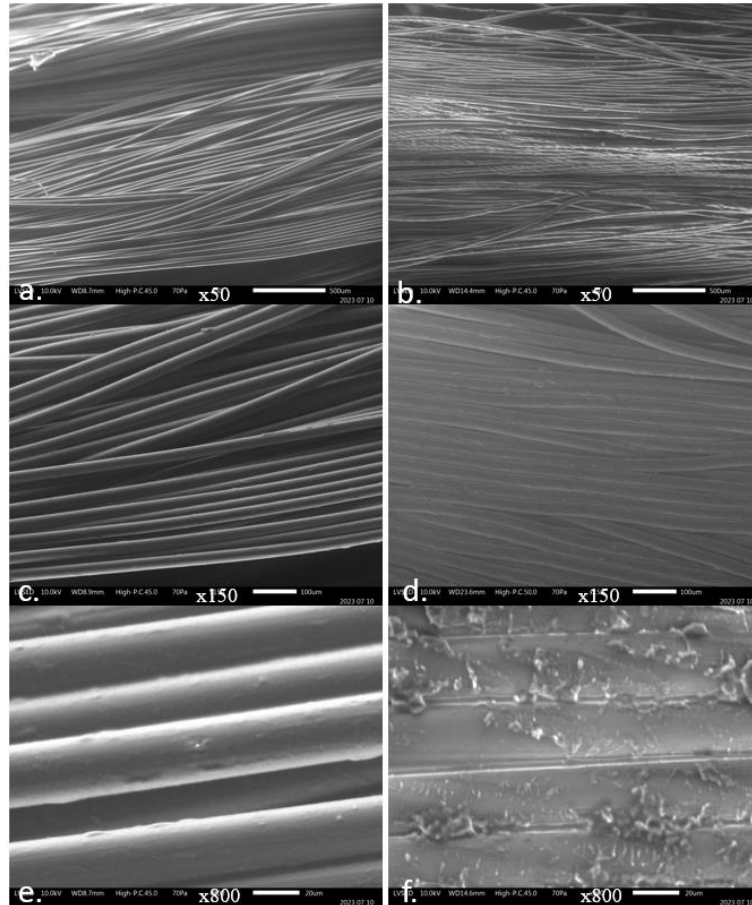
Figure 5.12 – SEM pictures: organisation of the material at the fibres scale for different magnifications: a) and b): x50. c) and d): x150 e) and f): x800. Left: virgin material. Right: Fatigued material

A zoom of this region was performed to allow a better observation and is presented in Figure 5.13. This confirms that it is similar to the mark made by the pull-out, or melting, of the material, or of the coating, during the contact and friction between the fibres. This highlights that the friction coefficient will depend on the orientation of the fibres with respect to the loading direction. The friction will cause a pull-out of the material under a specific angle. This is in accordance with the work of Bain *et al.* on the main parameters influencing the friction between polyamide rope-yarns that showed the friction coefficient was dependent on the angle between the fibres (Bain, Davies, et al., 2022).
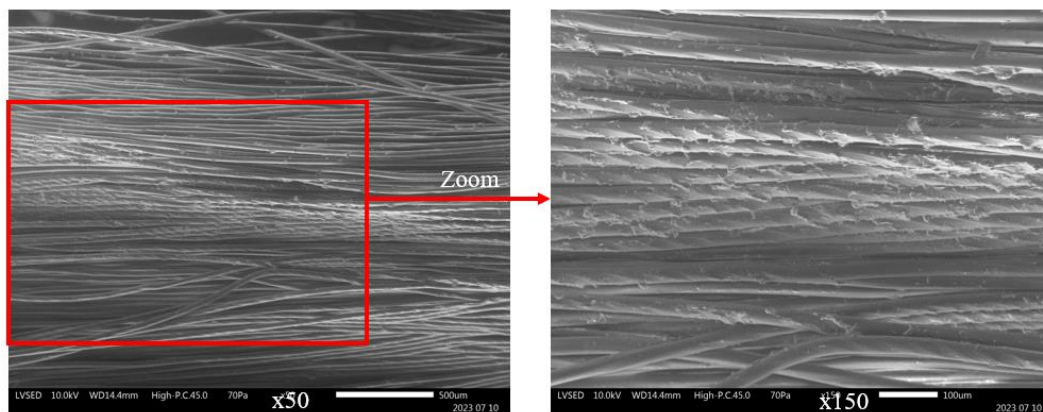
Figure 5.13 – Zoom of figure Figure 5.12-b). Magnification x150. Organisation and aspect of the fibres.

5.3.3. Conclusions on the damage and failure mechanisms investigation

These observations highlight the complexity of the mechanical response of twisted ropes, due to their hierarchical multi-scale construction. We first showed that the loading conditions evolve along the length on the rope-yarn, depending on its position in the sub-rope; the density of the sub-ropes also evolves due to the compaction and radial compression of the rope-yarns inside the strand; the surface of contact is also changing with the loading: from elliptic to prismatic.

Hence, a fatigue test changes significantly the 3 main parameters influencing the fatigue lifetime and the mechanical response of the sub-rope, which are: the geometry of contact, the friction coefficient and the organization of the sub-components. Depending of the loading level, these parameters will change differently. These modifications seem rather beneficial, as the smoothing of the contact area might decrease the friction coefficient and the compaction induces a rigidification of the material (rope-yarns). This type of evolution was also observed and validated on other type of textiles fibre ropes (Bain, 2020; Bain, Davies, et al., 2022).

An improved understanding of the mechanical phenomena at the scale of the elements of synthetic ropes is required. With this objective an approach using a 3D mesoscopic scale model will be proposed in chapter 6 of this manuscript. This model aims at transcribing the construction response, the friction between the components and the visco-elasto-plastic response of polyamide 6 sub-ropes.

This section has investigated the damage and failure mechanisms during a fatigue test. Next section proposes an investigation on the mechanical strain response under fatigue load and on the evolution of this response.

5.4. Mechanical strain response under fatigue load

One fatigue test was performed with continuous strain measurement, following the procedure described in chapter 2 section 2.5.3.3.2. A 4T sub-rope was cycled between 2%MBL and 45%MBL for 830 cycles. A maximal load of 45%MBL was chosen so that we could compare the creep during fatigue to a 4T sub-rope loaded under creep at 45%MBL for one year, studied in chapter 4. The specific stress plotted versus strain is presented in Figure 5.14.
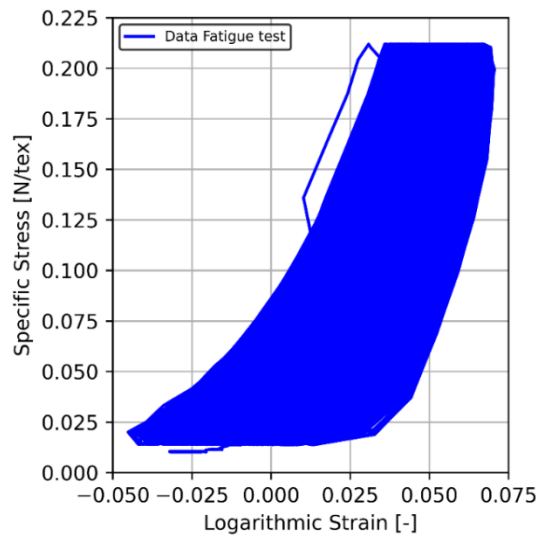
Figure 5.14 - Specific stress [N/tex] versus logarithmic strain [-] during a cyclic test on a 4T sub-rope sample.

The fatigue behaviour will be investigated using four thermomechanical quantities:

- Two secant moduli estimated classically as follows for the load and unload responses:

$$E_s = \frac{\Delta \Sigma}{\Delta \varepsilon}$$

Eq. 53

The secant modulus during loading was calculated on the loading phase of a cycle using a linear regression from 0.03 N/tex to 0.22 N/tex. The secant modulus calculated on the unloading phase of a cycle used a linear regression from 0.03 N/tex to 0.22 N/tex (illustrated of Figure 5.16).

- Cyclic mean logarithmic strain rate defined as:

$$A = \frac{\Delta \varepsilon}{\Delta log_{10}(t - t_0)} = \frac{\Delta \varepsilon}{\Delta log_{10}((N - N_0) \times 10)}$$

Eq. 54

- The hysteresis energy density was calculated using the trapeze method:

$$W_h = \int \sigma d\varepsilon$$

Eq. 55

5.4.1. Evolution of the behaviour with time

Figure 5.15 presents the strain versus the number of cycles for five chosen cycles at different times during the test.
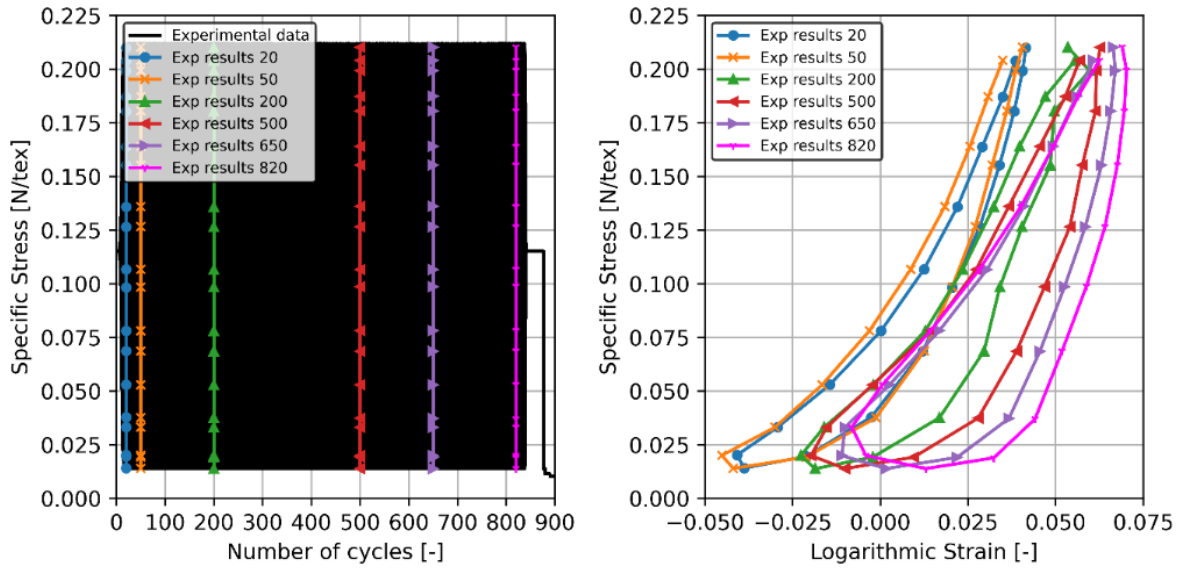
Figure 5.15 - Left: Specific Stress [N/tex] versus number of cycles. Right: Specific Stress [N/tex] versus logarithmic strain [-] during the fatigue test with strain monitoring.

We can divide this response into three zones illustrated in Figure 5.16:

- Zone 1 is the loading; the sub-rope is characterized by an initial construction with an associated rigidity and modulus at loading. During the loading, the sub-rope components change orientation under the loading. They rearrange and align with the loading direction. Hence, the construction evolves during the loading and, at the end of the loading, a new construction is installed.
- Zone 2 is the beginning of the unloading; it corresponds to the new construction, developed during the cyclic loading. This construction is stiffer than the initial construction which explains the higher modulus at unloading.
- Zone 3 is happening at a zero-stress level: during this phase, the strain decreases at constant stress. This can be explained by the low loading frequency, 0.1 Hz. Due to this low frequency, the sub-rope has enough time to continue to rearrange before the new loading phase begins. This indicates that its current configuration is not stable.
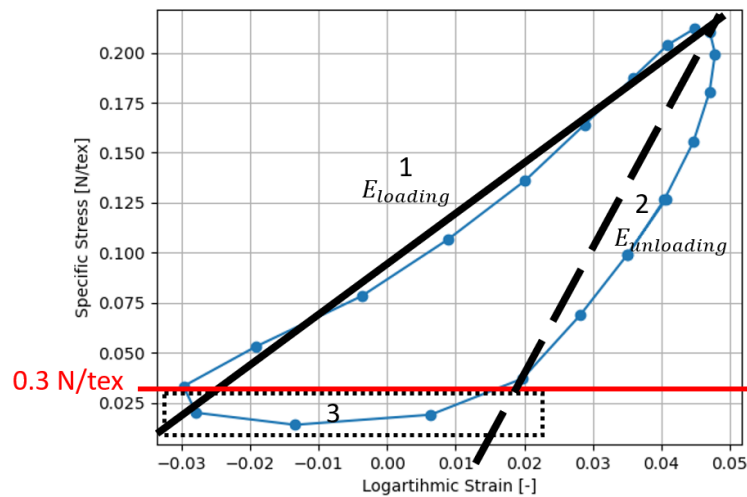
Figure 5.16 – Illustration of the three phases of the response of a 4T sub-rope during a fatigue cycle. The modulus are calculated using Eq. 53

The hysteresis loop characterizes a conversion of mechanical energy. The first phenomena responsible for this conversion, in the case of a polyamide 6 sub-rope, is the dissipative behaviour of the polymer macromolecule.

Figure 5.17-a) shows the calculated hysteresis energy versus the number of cycles, calculated using Eq. 55. A substantial evolution of the hysteresis is observed. The hysteresis energy has increased from 0.0015 to 0.0040 (increase of 166%). Herrera studied fatigue of individual polyamide 6 fibres and showed that the hysteresis during cycling did not change during the fatigue test (Herrera-Ramirez, 2004). Hence, the evolution of the hysteresis observed during the fatigue test on 4T sub-rope (Figure 5.15) is mainly the result of the geometric effect associated with the change in construction during one cycle (phase 1, 2 and 3). The evolution of the shape of the hysteresis suggests that, during phase 3, the sub-rope does not recover its initial construction which leads to an evolution of the hysteresis area and a "plasticity".

The plastic strain is plotted in Figure 5.17 – b). A total plastic strain of 4% is measured during the test. This plastic strain is due to both irreversible changes to the material microstructure and to the changes in construction.
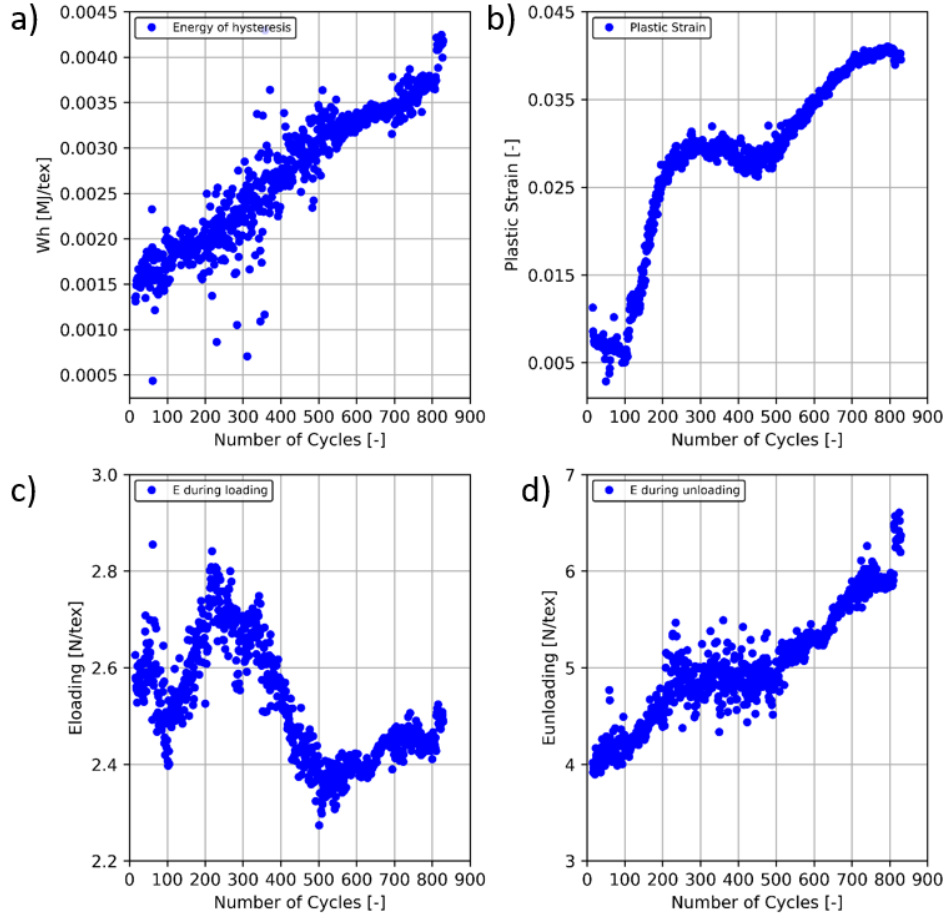
Figure 5.17 – a) Energy of hysteresis calculated during the fatigue test versus the number of cycles. b) Plastic strain versus the number of cycles. c) Modulus during loading versus the number of cycles. d) Modulus at unloading versus the number of cycles.

Observations (pictures taken by the camera for the image correlation analysis) of the sub-rope during the test are presented in Figure 5.18 to evaluate the change in construction. Figure 5.18 -a) presents respectively: images of the sub-rope, at the beginning and at the end, of the cycle number 10 (beginning of the test); it corresponds to a hysteresis close to the behaviour of the blue cycle on Figure 5.15. Figure 5.18 – b) presents images of the sub-rope, at the beginning and at the end, of the cycle number 820 (end of the test); it corresponds to a hysteresis close to the behaviour of the red cycle on Figure 5.15.

The change in construction, between cycle number 10 and cycle number 820, is highlighted by the evolution of the black line on the sub-rope, observed between Figure 5.18.a and Figure 5.18.b. This black line is used, during the splicing process, to indicate the lay-length of the sub-rope. In Figure 5.18-a), the line is straight and corresponds to the initial lay-length (50 mm). In Figure 5.18-b) (end of test), it is curved around the sub-rope which indicates the lay-length has changed (has increased in this case). We also observe that the splices have slipped between Figure 5.18 -a) and b) (a marker has been uncovered). Hence, the change in construction is allowed by the slippage of the splice.

Therefore, the torsion of the sub-rope is evolving during the test. The slippage of the splice is due to the low number of tucks in the splices (only 6 versus 30 for longer samples). The balance between the splice and the gauge length is leading to a torque and allows a significant change in construction. We can conclude that the evolution of hysteresis is mainly due to the change in construction of the sub-rope during the test.
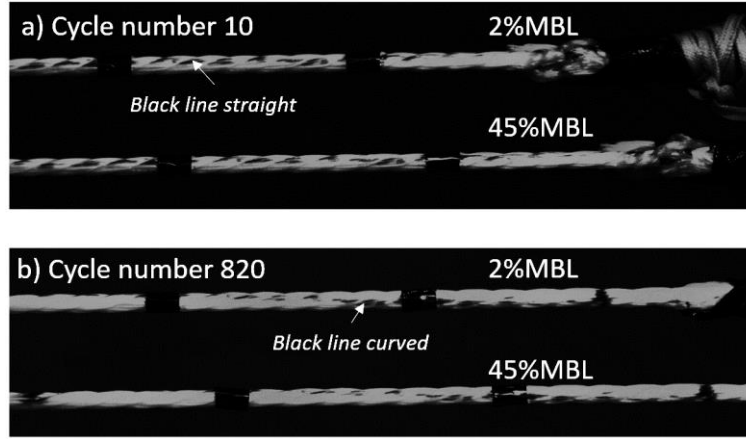
Figure 5.18 - Picture of the sample during the fatigue test with strain monitoring. a) Beginning and end of cycle number 10. b) Beginning and end of cycle number 820.

The evolution of the modulus at loading and unloading are plotted versus the number of cycles in Figure 5.17-a) and b). We observe that the modulus during loading tends to decrease but the variation is not large (decrease of 7%). On the contrary, the modulus during unloading increases from 4 N/tex to around 6.5 N/tex (an increase of 62.5%). This increase can be explained by the change in material state observed in section 5.3.2. In fact, it was shown that a compaction and rigidification of the rope-yarns are observed after a fatigue test (Figure 5.12). The increase in modulus during the fatigue test suggests that the compaction is increasing during the loading.

This study highlights the importance of the terminations and more specifically, of the length of the splices and also on their tightness at the end of the splicing process. These observations pose the question of the validity of the fatigue results on 4T sub-ropes. The contribution of the rotation and torque could increase the abrasion and lead to a reduced fatigue lifetime. But the observed changes in compaction and rigidity of the material could balance this negative effect.

5.4.2. Creep during cycling

Figure 5.19 presents the strain versus time during the test. The first two hundred cycles are not considered in the fatigue response as they are characteristic of the transient regime. Hence, we investigated the creep between 200 cycles and 830 cycles.
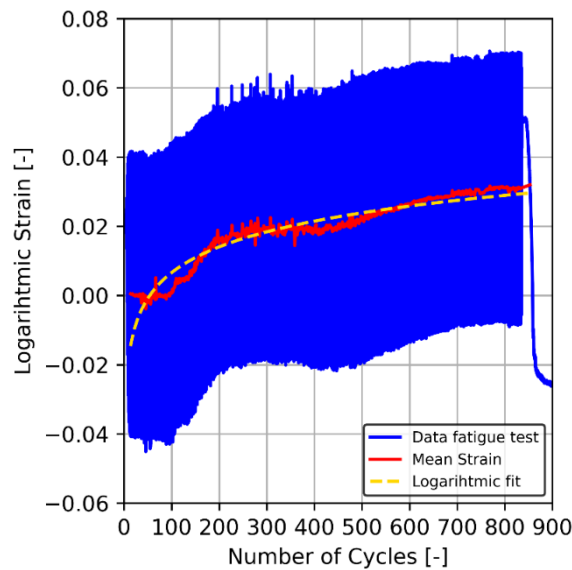
Figure 5.19 - Logarithmic strain [-] versus number of cycles] during a cyclic test between 2%MBL and 45%MBL.

It was shown, in chapter 4 section 4.5, that polyamide 6 follows a logarithmic creep strain response with time during long term creep loading. To compare the creep during a dynamic test and the creep during a static test, a logarithmic fit of the form Eq. 49 was applied to the mean strain between 200 cycles and 830 cycles to calculate the logarithmic creep rate. The fit is the dotted line on Figure 5.19 named 'fit'. The measured creep rate is 1.05 %/decade versus 0.28%/decade measured in chapter 4 for a creep test at 45%MBL. The creep kinetics are four times faster during this fatigue test than during the long-term creep test. This result is only for one test and this significant difference between the rates might also be explained by the changes in the sub-rope construction or by the slippage of the splice as showed in the previous section. Also, it was shown, in section 5.3.2, that fatigue loading changes important parameters such as the construction of the sub-rope, the geometry of contact and the friction coefficient.

Nevertheless, this first strain monitored fatigue test shows that it is interesting and necessary to characterize the creep resistance under a given static load. The load ratio will also have an important impact on the cyclic creep. Hence, further work should investigate the load ratio influence on the mechanical response of the sub-rope during fatigue.

Next section proposes to confront a simulation, using the POLYAMOOR law, of this strain monitored fatigue test to the experimental results.

5.4.3. Comparison with the POLYAMOOR law

A comparison between the POLYAMOOR law and this monitored fatigue test is proposed in this section. The identification of the parameters of the law on a 4T sub-rope was realized and is presented in chapter 3 section 3.2. The eleven parameters used are detailed in chapter 3 Table 3.4 for a virgin 4T sub-rope.

A simulation using the POLYAMOOR law of the monitored fatigue test, presented in section 5.4.1, with strain measurement was performed. A cyclic loading at a mean tension of 21.5%MBL and a load range of 43%MBL was simulated. The specific stress versus strain obtained experimentally is compared to the simulated results in Figure 5.20. Table 5.2 presents a comparison between the mechanical properties predicted by the law and the ones measured on the experimental data.
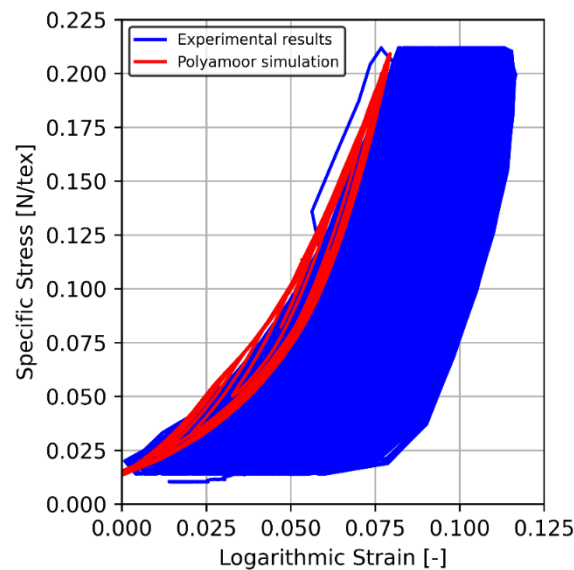
Figure 5.20 - Specific Stress [N/tex] versus logarithmic strain [-] during fatigue test. Confrontation of a simulation using the POLYAMOOR law with the experimental data.

It can be seen the shape of the cycles predicted are in accordance with the shape of the first cycles observed experimentally. The predicted hysteresis energy of the law is of 0.0013 MJ/tex and remains constant during the simulation. This value is close to the one calculated on the first cycles on the experimental data as seen in Table 5.2. Also, the modulus at loading is well predicted by the law during the test and it does not evolve significantly with the number of cycles. Hence, this law is adapted to simulate cyclic loading for the first cycles.
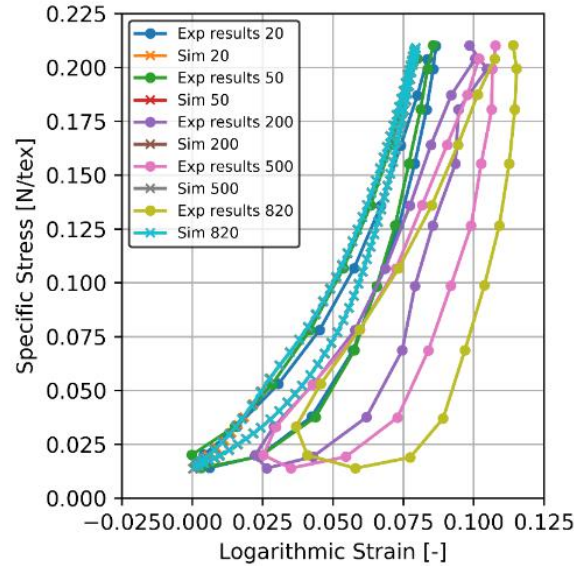
Figure 5.21 - Specific Stress [N/tex] versus logarithmic strain [-] during fatigue test for chosen cycles. Comparison between simulation using the POLYAMOOR law and the experimental data.

Figure 5.21 presents the comparison of some selected cycles from the experiment and the corresponding cycles from the simulation. The change in shape and the observed increase of hysteresis energy is not predicted by the law. In fact, we observed in section 5.4.1 that this evolution was mainly caused by a geometric effect. Also, we observe in section 5.3.2 that fatigue loads change important parameters such as the construction and the friction coefficient. No significant change of construction was observed during the short multi-relaxation tests used to identify the law. Hence, it is not surprising that the model is not able to predict the mechanical properties associated with this change of construction.

It appears that the POLYAMOOR law does not predict the ratcheting strain observed experimentally. The total strain obtained with the law is around 0.3%. The absence of ratcheting during this simulation is due to the load range and the minimal load reached during the loading. For large amplitude and low load, the dashpot will stabilize its strain at a zero value. Therefore, no accumulated strain is considered.

Table 5.2 – Comparison between the mechanical properties calculated and measured

	$E_{loading}$ [N/tex]	$E_{unloading}$ [N/tex]	Hysteresis energy [MJ/tex]
POLYAMOOR Law	2.8	3.3	0.0013
Start of test	2.6	4	0.0013
End of test	2.5	6.7	0.0043

We can conclude that this law is adapted to simulate cyclic loading for the first cycles. The predicted hysteresis and moduli (loading and unloading) are in accordance with the behaviour at the beginning of the test. For longer durations, the law is not adapted to describe the hysteresis as no geometric effect was observed during the identification. Also, the characteristic times are more adapted to small amplitude loadings to describe the creep strain.

Some comparison of the POLYAMOOR law with experimental data from longer samples (length of the splice sufficient) would be closer to the application. Also, it is necessary to confirm this behaviour by repeating this test. There was not sufficient time to perform the required repeatability tests here.

The difficulty to perform fatigue tests and to extend S-N curves on sub-ropes was showed in previous sections. Hence, next section investigates the self-heating method for fast fatigue prediction.

5.5. Self-heating for fast fatigue prediction

The self-heating prediction method consists of the use of thermal measurements to determine the fatigue properties and to estimate lifetime of a material. A cyclic dissipated energy per cycle can be estimated from the thermal measurements and can provide an energy criterion to predict the Wöhler curve. The method was developed on 4T and 8T sub-rope samples by Chevillotte (Chevillotte, 2020, 2020).

This study will, first, assess the repeatability and robustness of the self-heating experimental protocol on 4T sub-ropes when the operator changes. This will also allow the self-heating curve to be extended with more data points. The additional fatigue tests performed on 4T sub-ropes, presented in section 5.2, will be used to validate the first self-heating prediction proposed. Finally, an improvement of the prediction will be proposed, based on the new experimental campaign of self-heating tests.

5.5.1. Self-heating: hypothesis and method

This first section will explain the method and the assumptions made to identify the thermal sources from the temperature measurements. The heat-equation can be written following Eq. 56 (Doudard et al., 2005; Jegou et al., 2013; Rosa & Risitano, 2000):

$$\rho c \dot{T} + div(\vec{q}) = \rho c S_t = \Delta + r + \rho T \cdot \frac{\partial^2 \Psi}{\partial v_k \partial T} \cdot \dot{V}_k + \rho T \cdot \frac{\partial^2 \Psi}{\partial \varepsilon^e \partial T} \cdot \dot{\varepsilon}^e \qquad \textit{Eq. 56}$$

With ρ the density, c the specific heat capacity considering the internal variables V_k as constant, T the temperature, q the mass density, S_t the thermal sources, Δ the intrinsic dissipation, r the external heat supply, Ψ the Helmholtz free energy and ε^e the elastic strain tensor.

Some classical hypotheses can be applied: the external heat sources are supposed not to be time-dependent and the temperature variations are supposed to be low enough (estimated under 10°C according to Chevillotte's study on 7T sub-rope samples). Hence, we can neglect the variations of ρc and the couplings between the temperature and the internal variables (other than elastic variables). We define κ as the thermoelastic tensor (considered isotropic $\kappa = \kappa_1$) and λ the conductivity tensor. Using Fourier's law, the heat equation in Eq. 56 can be written:

$$\rho c \dot{T} - \lambda \Delta T = \Delta + r + \rho T \cdot \dot{\varepsilon}^e \qquad \textit{Eq. 57}$$

We consider only cyclic tests in this study. During such tests, the external heat supply is supposed constant and the thermo-elastic term cancels itself out over a mechanical cycle. Hence, solving the heat equation reduces to Eq. 58:

$$\rho c \dot{T} - \lambda \Delta T = \Delta \qquad \textit{Eq. 58}$$

It is convenient to use the intrinsic dissipation over a cycle Δ^* and the frequency f_r to express the heat equation as:

$$\rho c \dot{T} - \lambda \Delta T = \Delta^* \cdot f_r \qquad \textit{Eq. 59}$$

Our sub-rope sample is a multi-scale material and the dissipation field is likely to be heterogenous. However, consistent with the fact that the stress and the strain are averaged, we consider an average temperature over our sample. The thermal measurements made during this study are represented on Figure 5.22:
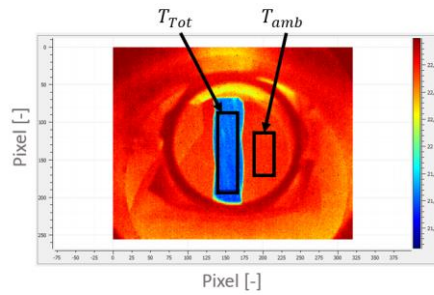
Figure 5.22 - Temperature map obtained from infrared radiation measurements during a self-heating test. The blue part is the sub-rope.

The mean temperature variation $\theta \ (= T - T_0)$ is measured on one zone of the sub-rope. A measurement of the ambient temperature is also performed to correct the temperature drift due to the environment (T_{amb} in Figure 5.22). Experimentally, the infrared camera measures a flux of infrared radiations. A radiation balance is applied and we convert the measured radiations into temperatures. In a first approximation, as Chevillotte did in his work (Chevillotte, 2020), we did not correct the impact of water on the radiation balance.

As we did not correct for the water in the radiation balance, we are not measuring the temperature of the sub-rope but of the sub-rope and of the water surrounding it. Hence, we could not calculate the intrinsic dissipation of the sub-rope. However, we suppose that the total measured dissipation will be related to the intrinsic dissipation of the sub-rope. For simplicity, we will note Δ^*, the global dissipation per cycle.

Under this assumption, it can be written that:

$$\rho c \dot{\theta} - \frac{\theta}{\tau_{eq}} = \Delta^* \cdot f_r \qquad \textit{Eq. 60}$$

With τ_{eq} the characteristic time which is dependent on the thermal boundary conditions and the sample geometry. To calculate the equivalent dissipation from the average temperature, we have to determine the characteristic time. Figure 5.23 is a plot of the temperature versus time during one block of self-heating.
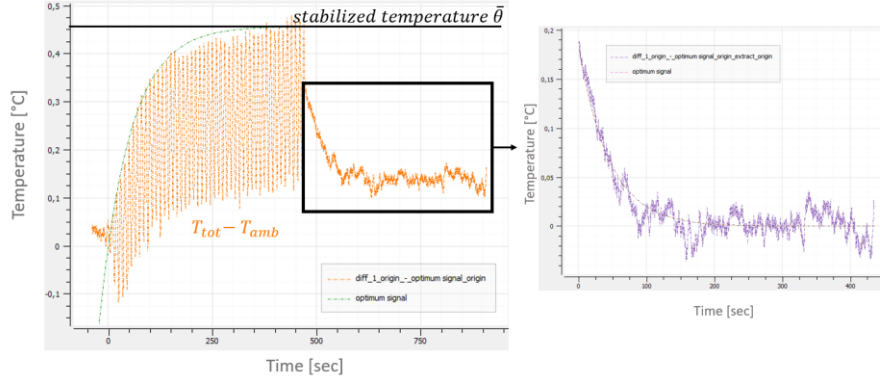
Figure 5.23 - Average temperature [°C] versus time [sec] during one block of self-heating. Method to identify τ_{eq} and $\overline{\theta_{MAX}}$ using Eq. 61 and Eq. 62

The temperature change during the heating and the cooling period can respectively be fitted using Eq. 61 and Eq. 62:

$$\theta(t) = (\overline{\theta_{MAX}}) \times \left(1 - e^{-t/\tau_m}\right)$$ *Eq. 61*

$$\theta(t) = \overline{\theta_{moy}} \times e^{-t/\tau_d}$$ *Eq. 62*

The characteristic time is considered during the cooling phase for several reasons. First, it is harder to measure it on the loading as there is some thermo-elastic coupling. Also, the PID is hard to adjust because of this coupling and the first cycles of the loading are often not respecting the expected shape. Hence, we have $\tau_d = \tau_{eq}$. Knowing τ_{eq}, the next step is to solve Eq. 60 for the cyclic loading block which leads to the following expression:

$$\theta(t) = \frac{f_r \tau_{eq} \Delta^*}{\rho c} \times \left(1 - e^{-t/\tau_{eq}}\right)$$ *Eq. 63*

Finally, the equivalent cyclic dissipation can be written as:

$$\Delta^* = \frac{\rho c \bar{\theta}}{f_r \cdot \tau_{eq}}$$ *Eq. 64*

This expression enables the heat-build up to be plotted, such as the one that was proposed by Chevillotte and presented in Figure 5.24.
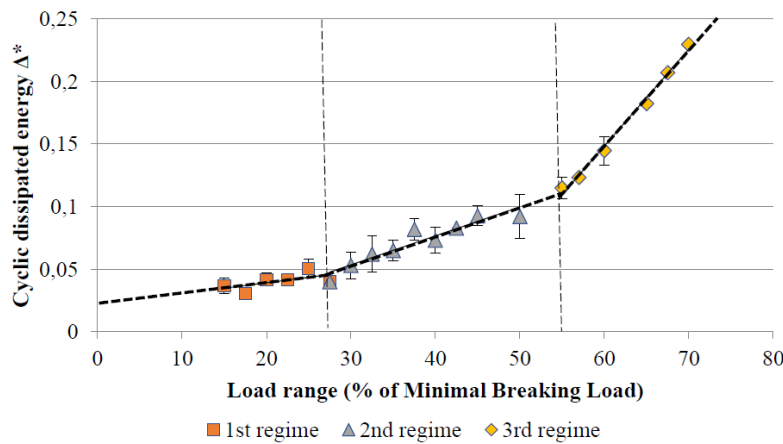
Figure 5.24 - Heat build-up curve for 4T sub-ropes and linear fit of three regimes (dashed lines) proposed by Chevillotte (Chevillotte, 2020)

Chevillotte proposed an empirical analysis of the heat build-up curve. This graphical and empirical approach has been performed on numerous materials previously (Doudard et al., 2005; Marco et al., 2017) with success. It is based on the analysis of the shape of the curve. More precisely, changes in the shape of the curve are related to dissipation mechanism changes and so, to fatigue lifetime at a given load. For some materials, it has been observed empirically that the first change of slope is related to a fatigue lifetime of 10^6 cycles (Abello et al., 2013; Le Saux et al., 2010; Leveuf et al., 2018). Chevillotte used this empirical assumption during his work, which led him to a prediction of a 10^6 cycles lifetime for a fatigue test with a maximal load of 29% MBL (first change of slope at 29% MBL on Figure 5.24).

The energy criterion chosen enables the number of cycles leading to failure N to be related to the equivalent dissipated energy during the stabilized cycle Δ^*. This relation is usually written:

$$\Delta^* N^b = C$$

<div align="right">*Eq. 65*</div>

With b and C the model parameters to identify. The energy criterion has been applied with success on metallic material (Doudard et al., 2005), elastomers (Marco et al., 2017) and composites (Jegou et al., 2013). The identification of the two parameters requires two equations with known N and Δ^*. A first couple can be identified using the fatigue test results at high loads that are associated with fatigue measurements. The second pair is chosen empirically and is associated with the first change of slope of the heat build-up curve. Chevillotte proposed a fatigue prediction, using the arbitrary (empirical) value of 10^6 for the transition from the first to the second regime, shown in Figure 5.25.

5.5.2. Self-heating prediction

Chevillotte lacked experimental fatigue data at high numbers of cycles to validate the proposed prediction. Hence, in the current study additional fatigue tests were performed for higher numbers of cycles and the S-N fatigue curve was extended (chapter 5 section 5.2). The final curve is compared to Chevillotte's prediction on Figure 5.25.
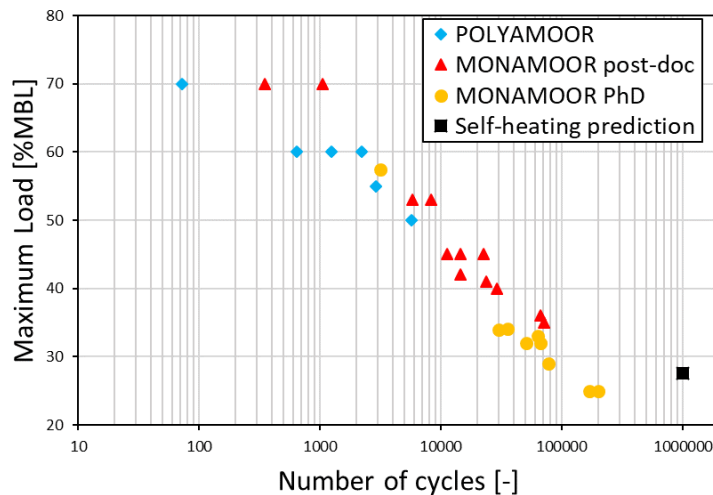
Figure 5.25 - Results of the fatigue tests on 4T sub-rope samples confronted to Chevillotte self-heating prediction (black rectangle). Maximal load (%MBL) versus the number of cycles to failure

The prediction overestimates the fatigue lifetime. This prediction was graphically determined. The self-heating curve obtained by Chevillotte, Figure 5.24, did not present a lot of points which complicated an accurate description of the change of shape and, more specifically, the first change of slope. Also, it was specified at the time that further understanding of the dissipation phenomena was needed to analyse the self-heating data and improve the prediction.

5.5.3. Proposition of a new prediction

This section is devoted to fatigue lifetime prediction based on a more complete self-heating curve for 4T sub-ropes. Following the procedure described in section 2.5.3.3.1, self-heating measurements were performed. A global dissipation per cycle was measured and calculated on the surface of the sub-rope. The self-heating curve is presented in Figure 5.26. The results obtained during POLYAMOOR and those obtained during the MONAMOOR project, by two different operators, are superposed to attest the repeatability of the measurements.
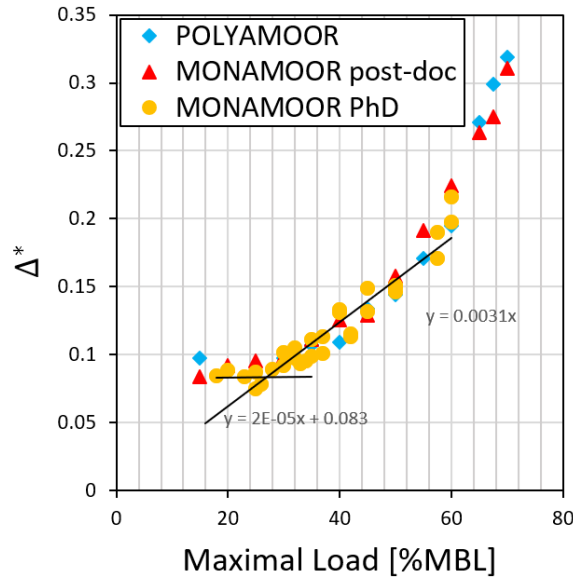
Figure 5.26 - Heat build-up curve for 4T sub-ropes and linear fit of two regimes (black continue lines). Results from self-heating tests performed by three operators

On Figure 5.26, we can first confirm the good repeatability of this complex experimental procedure; from the experimental set-up, to the data treatment leading to the self-heating curve.

The new self-heating curves obtained during MONAMOOR (yellow circles and red triangles) allow a more complete description of the equivalent dissipation changes between 15%MBL and 30%MBL. Graphically, the first change of slope (associated to a change of dissipation regime) now appears to be at 25%MBL rather than 29%MBL. In this study, we will also consider that this first change of slope is associated to a lifetime of 10^5 cycles to be more conservative.

This graphical and empirical approach, which involves determining graphically the first change of slope and then relating this change to a fatigue lifetime, would require a deeper understanding of the dissipative mechanisms. As noted previously, up to five main mechanisms are contributing to the heat-build-up (Parsey, 1983). These have been detailed in chapter 1 section 1.6.2 and are related to the dissipative behaviour of the material and to the friction at several scales within the rope construction. It was shown, in section 5.4.1, that the construction was changing during the loading and the unloading of one cycle, leading to a hysteresis due to geometric effect. Also, the contact surfaces are changing during a fatigue test (rearrangement of a rope-yarns inside a strand) which induces changes in the friction coefficient. More detailed investigations would be required to replace the graphical approach by models of the physical mechanisms along the self-heating curve.

However, using only the experimental data obtained during MONAMOOR, we can propose an adapted prediction using the global dissipated energy per cycles as an energy criterion following Eq. 65. Figure 5.27 plots the global dissipation per cycle measured versus the maximum load

(%MBL) of the fatigue test. The two red points on the curve are the points used to identify the parameters b and C of the model. The experimental data correspond to self-heating measurements performed at the beginning of fatigue tests (following the procedure described in chapter 2 section 2.5.3.3.2) and not during a self-heating protocol. Hence, these points were not used for the identification of the energy criterion and can be used to validate our model and criterion.
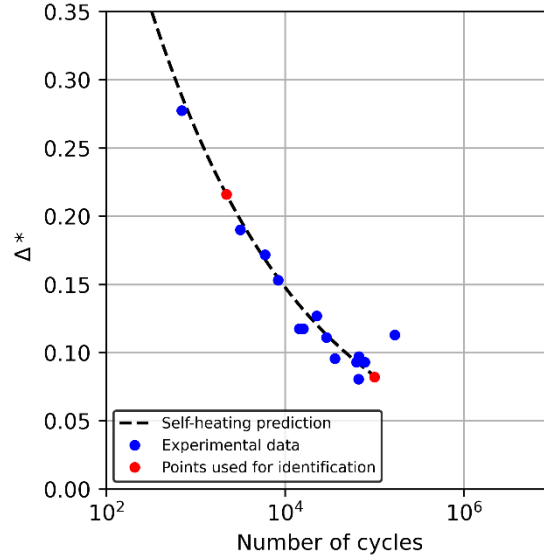
Figure 5.27 - Equivalent dissipation of the sub-rope and the water versus the number of cycles. Comparison between the model prediction of the energy criterion following Eq. 65 and the measured equivalent dissipation at the beginning of fatigue tests

We have a relation between the number of cycles and the energy criterion. Using a fit of the heat build-up curve with a 3-order polynomial, we also have a relationship between the equivalent cyclic dissipation energy and the maximal load of a fatigue test. Hence, it is possible to predict the mean fatigue S-N curve.

Figure 5.28 presents a comparison between the self-heating prediction (curve with blue circles) and the experimental fatigue curve (yellow circles). The red triangle is the fatigue lifetime empirically associated with the first change of slope observed on the self-heating curve (Figure 5.26).
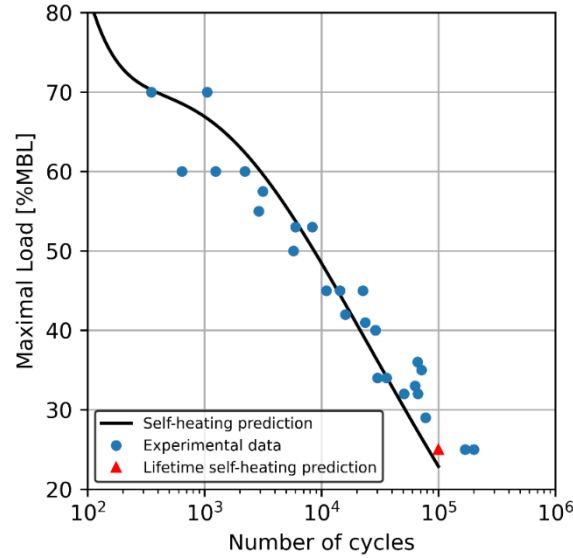
Figure 5.28 - Predicted fatigue plots using the self-heating prediction method on a 4T sub-rope scale based on the energy criteriion (black continuous line and red triangle). Comparison with the experimental S-N curve obtained on a 4T sub-rope scale (blue circles)

We observe the prediction self-heating prediction is in accordance with the experimental results. It is a conservative prediction that may underestimates the lifetime of the sub-rope.

This study showed that, using a heat build-up test of a duration of only half a day, we can propose an accurate description of the S-N fatigue curve. This method would allow considerable experimental time savings. To obtain this fatigue curve for a 4t sub-rope, several fatigue test campaigns over 6 years were required. Moreover, the importance of the construction parameters on the fatigue response of the sub-rope was shown in this chapter. Using the self-heating method could allow the fatigue durability of several constructions to be investigated in a reduced amount of time.

The main objective in the future is to have a better understanding of the physical mechanisms and to be able to replace the graphical approach. Two main possibilities to investigate the heat build-up are:

- To use an infrared camera with a higher spatial resolution and to distinguish zones with higher dissipation (due to friction at the contact zone of the strand). This method would require a more complex geometric analysis.
- To use a 3D model describing the complex anisotropic behaviour of the sub-rope and use it to understand and describe the mechanisms related to the degradation and dissipation.

We propose, in chapter 6, the development of a mesoscopic model, at the rope-yarn scale, to help understand the complex nonlinear behaviour of polyamide 6 twisted sub-rope.

5.6. Conclusion

The fatigue study on 4T sub-rope samples allowed the work of Chevillotte (Chevillotte, 2020) during the POLYAMOOR project to be extended; the S-N curve reached a failure at 10^5 cycles for 25% MBL. The 4T sub-rope construction was proven to be interesting as it allows to have a curve that is comparable to results obtained on higher scale sub-ropes, that is conservative and that is easier to study in the laboratory.

A study of degradation mechanisms highlighted that fatigue failure could be observed for the sample tested for lower load range and maximal load (between 25% and 35% MBL). The failure morphology was the same as the one observed by (Ramirez et al., 2006). Also, tomography scans were performed on an after-fatigue sample and a virgin sample. The scans show a new state of material at the rope-yarn scale for the fatigued samples. The material is denser and the rope-yarn contours are sharp. The contact area between the strands is visible on the fatigued sub-rope. This new state of material was investigated using SEM observations. It was shown the rope-yarns are more compact, more aligned. Also, a damaged area due to the inter-strand friction was observed. The observations also revealed a lustering effect similar to observations made on other types of textile ropes (Bain, Marco, et al., 2022).

A strain monitored fatigue test was performed on a 4T sub-rope sample. The stress-strain curve obtained displayed a change in the hysteresis loop associated with a 4% permanent strain. The response of the sub-rope could be divided into three zones: the loading, the unloading, and the strain recovery at constant load. It was shown that the construction was evolving significantly during the cyclic loading. The new construction at the beginning of the unloading was more rigid. Finally, because of the low frequency of the test, a third zone during which the sub-rope continues to recover its initial construction is present. This change in construction was also recorded during the test for the image correlation analysis and allowed this construction changes to be visualized. The splices also slipped because of the torsion, allowing some permanent construction changes. Only one test with strain monitoring could be performed and the repeatability of these measurements should be validated in future work.

Finally, the extended S-N curve updated the self-heating prediction proposed by Chevillotte. New self-heating tests were performed and allowed the repeatability of the complicated experimental protocol to be validated. An adapted prediction based on the enriched self-heating curve and clarified analysis was proposed. This prediction is conservative (it may underestimate the fatigue lifetime) and is in accordance with the fatigue results obtained on the 4T sub-rope. The self-heating method seems to be a powerful solution to avoid the complexity and long testing times required for the fatigue studies on synthetic sub-ropes characterized by different constructions. However, there is a need to deepen our understanding of the dissipation mechanisms to improve on the graphical approaches.

Chapter 6. Multiscale rope modelling

6.1. Objectives and motivation for the modelling

A key scientific challenge is to understand the construction influence on the mechanical response of polyamide ropes. These ropes are made of polymer filaments, twisted together to form yarns, that themselves are braided, or twisted, to form the higher scales. The mechanics include sliding between the yarns and between the strands, the associated friction, and also a transverse compression, due to the overall rope tension and the helix-shaped paths of the components (Leaf, 1995, Leech, 2022).

The fatigue damage due to numerous cyclic loadings was studied in chapter 5 of this manuscript. In that study, the comparison of the fatigue lifetimes for different sub-ropes suggested that fatigue lifetime differences could be at least partly explained by different constructions. The importance of the role of friction in the fatigue damage mechanisms and fatigue lifetime was also highlighted. Moreover, tomography scans and SEM images revealed the changes in strand and rope-yarn organisation and compactness during cyclic loading, and also, the change in the contact surface geometry. Fatigue studies being very time-consuming, a fast method to predict fatigue lifetime, based on self-heating measurements, was investigated. This method relies on the analysis of the stress evolution of the mean dissipation of the sub-rope during cyclic loadings. The improvement of this method requires a focus on the dissipation produced by the frictions between the rope components (strands, rope-yarns). Indeed, at least two mechanisms are contributing to dissipation: the visco-elasto-plasticity of the material and the friction between the sub-elements of the rope (Eq. 66):

$$\Delta^* = \Delta^*_{material} + \Delta^*_{friction}$$

<div align="right">*Eq. 66*</div>

The friction is directly link to the construction of the sub-rope as it depends on the geometry, the surfaces in contact and the contact forces. Bain *et al.* showed the friction coefficient was dependent on the angle between the rope-yarns and, an investigation in chapter 5, shows it could evolve during fatigue loading (change in surface roughness due to reorganisation and lustrage at the fibres scale). To quantify the contribution of the friction to the dissipation, a possible approach is to develop a model to determine the geometry of the contact surfaces, the contact forces and the friction at scales playing an important role in the rope response. The model should also describe the non-linear visco-elasto-plastic behaviour of the material. Such a model could allow the dissipation due to the frictions at the different modelled scales to be distinguished from the dissipation due to the visco-elasto-plasticity of the material (Figure 6.1).
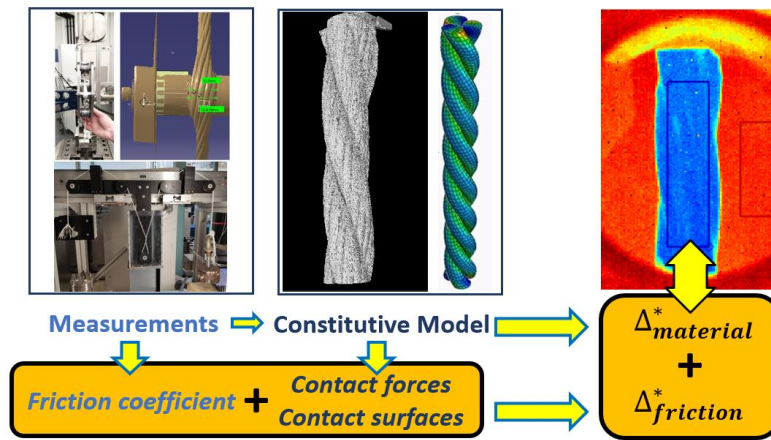
Figure 6.1 – Scheme of the objectives for the development of a mesoscopic scale model to improve understanding of self-heating tests
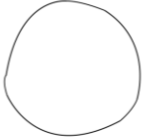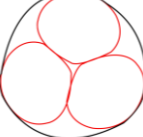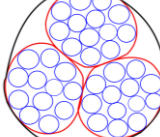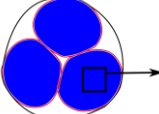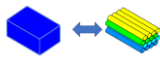
This chapter describes a 3D modelling approach of a rope structure, called a meso-scale model, to understand the interaction and displacement of the components of the rope. The main objective is to be able to separate the dissipation due to the friction, from the dissipation due to the material, during a tensile cyclic loading. More specifically, the first objective is to simulate a self-heating test procedure (several cyclic loading blocks), to improve the reliability of the self-heating method for fatigue prediction.

A second objective of the model is to study the influence of the construction parameters (lay-length, twist angle, diameters of sub-components) on the mechanical response. Previous chapters highlighted the importance of the construction on the complex non-linear mechanical behaviour of polyamide 6 mooring lines. Chapter 3 of this manuscript presented the identification of a 1D constitutive law (POLYAMOOR law), at two scales, characterized by different constructions. It allowed the changes of the mechanical properties with the construction to be quantified. However, no tendency could be drawn since only two different constructions were tested. The use of a model to numerically compare different constructions, in order to optimise rope construction, could save a lot of experimental working time.

6.2. Bibliography and choice of an approach

Because of the multi-scale hierarchical construction of synthetic ropes, the modelling approach has to choose which and how many scales have to be described. Table 6.1 gives some possible approaches.

Table 6.1 - Different FEM modelling approaches for a sub-rope. Outlined in red: models used during this study.

	Sub-rope	Strands	Rope-yarns	Yarns	Filaments
Scale level	1	2	3	4	5
Scheme				…	…
POLYAMOOR Modelling (Chapter 3)	1D constitutive law	/	/	/	/
Modelling method A	Contact between scale 2 elements	Contact between scale 3 elements	Contact between scale 4 elements	Contact between scale 5 elements	1 chain of beam elements per filaments with elastic properties
Modelling method B	Contact between scale 2 elements	Contact between scale 3 elements	1 chain of beam elements per rope-yarns with elastic properties	/	/
Modelling method C (presented in this chapter 6)	Contact between scale 2 elements	Mesh of 3D solid elements with scale 3 properties (bundle of rope-yarns) as a homogeneous material	Bundle of rope-yarns considered as a homogeneous material defined by a non-linear hyperelastic transverse-isotropic law	/	/

Method A does not assume any simplification. The lowest scale, hence the filaments, are modelled by a 1D chain of beam elements. Thus, this model has to deal with the numerous contact possibilities between scale 5 up to scale 1. In this type of model, the contact-pair management is one of the difficult key points (Durville, 2012; Wang et al., 2022; Wielhorski & Durville, 2015). So, method A is very complicated to use. In fact, in the literature, some authors used a simplification of method A, called Method B in Table 6.1, with a modelling stopping at a higher scale: the rope-yarn scale. Each rope-yarn is described by one chain of beam elements. Some authors, like Durville and Wang, succeeded in dealing with this type of model, but, the contact-interaction management remains a challenge. In these types of model, the tensile behaviour of the components is limited in order to focus on the contact detection and modelling.

Another modelling approach, that avoids the numerous contact interaction management, is possible. By releasing this difficult point, we aim to be able to implement more realistic behaviour laws for the components of synthetic ropes. Indeed, polymer filaments (polyester, polyamide), that constitute mooring synthetic ropes, often have a complex visco-elasto-plastic behavior. We propose to focus on method C in Table 6.1, as Charmetant, Vidal-Sallé and Boisse did in the case of a woven fabric, using a hyperelastic law (Charmetant et al., 2011). Each strand will be meshed with three-dimensional solid finite elements. We consider the strand to be made of a homogeneous material. This homogeneous material has to be defined by a behaviour law that models accurately the complex transverse-isotropic behaviour of the rope-yarn bundles which compose the strand. This reduces greatly the number of contact interactions. We could have chosen a smaller scale to define the behaviour law (i.e. the yarns or the fibres), but it would have added many contacts to model in the simulation and hence, it would have complicated the study.

6.2.1. Chosen approach
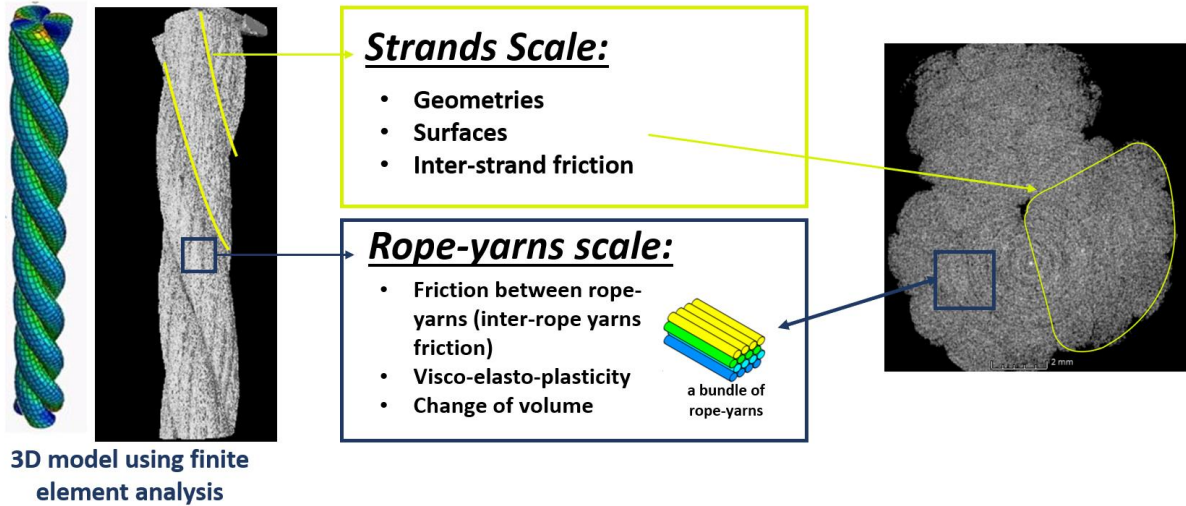
Figure 6.2 – Choice of a mesoscopic scale

In our proposed approach, the three strands will be modelized as 3 cylinders in contact. The contacts and frictions at the strand scale (inter-strands friction) will be described by the contact law used between the three cylinders in the finite element analysis software. Each cylinder will be meshed with three-dimensional solid finite elements (Figure 6.2).

Then, our chosen approach requires to define a law for the transverse-isotropic behaviour of the bundle of rope-yarns composing the strand. This law has to describe the shear strain modes between the rope-yarns that are associated with friction (inter-rope-yarns friction). It also has to describe the visco-elasto-plasticity of the polyamide material inside the rope-yarns.

Polyamide 6 is a material with a high strain to rupture (20%). Hence, we chose to use a hyperelastic law to define its behaviour. The classical hyperelastic and hypoelastic laws for transverse-isotropic materials are associated with complex behaviour at large strains. These laws are difficult to interpret and are difficult to control for the analyst (Bles, 2023; Charmetant, 2011). Also, these laws do not provide accurate geometries for synthetic fibre ropes (Bain, 2020).

Charmetant *et al.* proposed an approach using a hyperelastic law, based on physically motivated invariants. Each invariant describes a strain mode of the studied material. In their approach, a dedicated behaviour law can be defined for each strain mode. They managed to perform accurate predictions of the response of woven fabrics (Naouar et al., 2016).

Hence, the work presented in this manuscript will follow the procedure proposed by Charmetant *et al*. A hyperelastic law for defining the behaviour of a bundle of rope-yarns, based on physically motivated invariants, will be developed. However, different invariants (or variables) to those of Charmetant will be proposed to allow a complete description of the shear strain modes where the frictions take place. The development of this model is driven by one main final goal: to quantify and distinguish the dissipation due to the friction between the sub-components (inter-strands and inter-rope-yarns friction) from polyamide intrinsic dissipation, also called *material dissipation* in the following.

However, this final goal will not be reached in this study as it requires considerable time and effort. The goal we aim at is to perform a feasibility study of this approach for polyamide 6 sub-rope, both numerically (first simulations of a sub-rope) and experimentally (dedicated experimental tests developed for the identification). Hence, it has been chosen to first define the law as hyperelastic, without any dissipation in the strain mode inducing friction (we only represent the sliding), and without visco-elasto-plasticity. Therefore, this study will not allow the inter-rope-yarns friction and the material dissipation to be quantified. It will provide: a description of the hyperelastic response of the material and a description of the inter-rope-yarns sliding. This first development should enable a first simulation of a sub-rope during cyclic loading to be performed, which should allow the advantages of the new choice of invariants to be evaluated. We will check if the law gives realistic geometries at the strands scale, and a consistent behaviour at the rope-yarns scale, in comparison with the observations made in previous chapters and in the literature.

This is exploratory work: the results will show if this approach is interesting and justifies spending more time to improve the different parts (identification, simulation) and adding dissipation in the shear strain modes and visco-elasto-plasticity.

The next sub-section contains some theoretical basics of finite transformation theory and hyperelasticity (Forest, 2022). Then, an analysis is performed to determine why, and how, the proposal of new invariants is of interest in order to study the friction in the case of a 3-strand polyamide 6 sub-rope. A more detailed description of the hyperelastic model developed by Charmetant *et al.* for a woven fabric is proposed in appendix C (p.207).

6.2.2. Finite transformation theory and hyperelasticity

Let $\vec{X}$ be the initial position of a material point in the initial configuration Ω_0 and $\vec{x}$ its position in the current configuration Ω_t. The deformation gradient tensor, $\tilde{F}$, is then:

$$d\vec{x} = \tilde{F} \cdot d\vec{X}$$

Eq. 67

This tensor allows the transformation of any material fibre, described by a vector $\vec{A}$ in the initial configuration into a vector $\vec{a}$ in the current (deformed) configuration.

$\tilde{F}$ can be decomposed into two elementary deformations: a pure strain followed by a rotation (or the other way around). This is called the polar decomposition and can be written:

$$\tilde{F} = \tilde{R} \cdot \tilde{U}$$

Eq. 68

$\tilde{R}$ is the proper rotation of the matter and $\tilde{U}$ is a pure strain.

Several strain measures can be used. In our study, we will use:

- $\tilde{U}$ the pure right strain tensor
- $\widetilde{LnU}$ the right tensor of the logarithmic strain (also called Hencky right or Hill right)

Two formalisms exist to describe the strain: the Lagrangian formalism and the Eulerian formalism. The "right" strain tensors are Lagrangian because they give the information of the strain from the point of view of a reference frame (proper rotation) that follows the matter movement (translation and rotation). The left tensors of strain measures give the information of the strain from reference frames that does not follow the matter in its movement.

The change of volume between configurations Ω_0 and Ω_t, usually noted J, is and defined as:

$$J = \det \tilde{F}$$

Eq. 69

We define the gradient of the velocity of the deformation $\tilde{L}$ such that the temporal derivative of $\tilde{F}$, noted $\dot{\tilde{F}}$, is related to $\tilde{L}$ following:

$$\dot{\tilde{F}} = \tilde{L} \cdot \tilde{F}$$

Eq. 70

The tensor of the rate of strain $\tilde{D}$, also called *stretching tensor*, is the symmetric part of tensor $\tilde{L}$:

$$\tilde{D} = \frac{1}{2}(\tilde{L} + \tilde{L}^T)$$

Eq. 71

An important property is $\tilde{D}^T = \tilde{D}$.

Relationships exist between $\tilde{D}$ and the time derivatives of strains. For example, we have the following property:

$$\dot{J} = J.Tr(\tilde{D})$$

Eq. 72

In our study, we will use the Cauchy stress tensor $\tilde{T}$ that represents the stress state of the material. We define $d\vec{s}$ as a surface constituting the material and $d\vec{f}$ the force applied from the exterior on the interior of the material through $d\vec{s}$. $\tilde{T}$ can be defined by the linear application:

$$\forall \, d\vec{s} \quad d\vec{f} = \tilde{T} \cdot d\vec{s}$$

Eq. 73

We will also use the specific Cauchy stress defined as follows:

$$\tilde{\Sigma} = \frac{\tilde{T}}{\rho_t}$$

Eq. 74

With ρ_t, the density of the material in configuration Ω_t.

Finally, we will use the second stress tensor of Piola-Kirchhoff $\tilde{S}$:

$$\tilde{S} = (\det \tilde{F}) \cdot (\tilde{F}^{-1} \cdot \tilde{T} \cdot \tilde{F}^{-T})$$

<div align="right">*Eq. 75*</div>

A hyperelastic material may be defined as follows: a material that undergoes very large deformations without any dissipation. Hence, the intrinsic dissipation is null. Its behaviour is reversible and only depends on the current strain state (Forest, 2022).

To establish a hyperelastic material model, a general procedure is to start from a scalar strain energy density function ψ, called also *hyperelastic potential*, which is constructed from experiments. This strain energy density represents the energy stored in the material due to a deformation. It is formulated as a function of strain variables and the temperature. Once this energy density function is constructed, it is differentiated with respect to the chosen strain variables and results in stress variables. It can be expressed using different strain variables. The chosen strain variables will define the law obtained after the differentiation.

If e is the specific internal energy and s the specific entropy. Then, the specific free energy is equal to:

$$\psi = e - \theta \cdot s$$

<div align="right">*Eq. 76*</div>

θ is the temperature. According to the thermodynamics of deformable solids (Germain, 1973):

$$\forall \left(\theta, \tilde{F}, \dot{\theta}, \dot{\tilde{F}} \right)$$

$$\dot{\psi} = -p_{int} - s \cdot \dot{\theta} - \varphi_1$$

<div align="right">*Eq. 77*</div>

$$\dot{\psi} = Tr(\tilde{\Sigma} \cdot \tilde{D}) - s \cdot \dot{\theta} - \varphi_1$$

<div align="right">*Eq. 78*</div>

$$\Leftrightarrow \dot{\psi} = \tilde{\Sigma} : \tilde{D} - s \cdot \dot{\theta} - \varphi_1$$

<div align="right">*Eq. 79*</div>

Where φ_1 is the intrinsic dissipation per unit of mass. In the case of hyperelastic materials, this dissipation is always null:

$$\forall \left(\theta, \tilde{F}, \dot{\theta}, \dot{\tilde{F}} \right) \qquad \dot{\psi} = \tilde{\Sigma} : \tilde{D} - s \cdot \dot{\theta}$$

If we assume the hyperelastic potential, for example with $\tilde{E}$, the Green-Lagrange strain tensor, as strain variable,

$$\psi(\theta, \tilde{E})$$

Then the second Piola Kirchhoff stress tensor is given by

$$\tilde{S} = \frac{\partial \rho_0 \psi(\theta, \tilde{E})}{\partial \tilde{E}}$$

<div align="right">*Eq. 80*</div>

Where ρ_0 is the initial density, and ψ the specific free energy (per unit of mass), so $\rho_0 \psi$ is the free energy per unit of initial volume.

Appendix C proposes a more detailed description of Charmetant *et al.*'s hyperelastic model for a woven fabric. The next sub-section proposes an analysis to allow an adaptation of this model to another type of material: a 3-strand polyamide 6 sub-rope.

The next sub-section provides an analysis and an explanation of the need to propose different strain invariants than the one proposed by Charmetant *et al.* for the study of friction.

6.2.3. Charmetant's invariants limitation

Charmetant *et al.* (Charmetant et al., 2011) proposed and validated an anisotropic hyperelastic model for the mechanical behaviour of textile composite reinforcements. Fabrics are materials that consist of yarns combined together following textile architecture: woven, knitted, braided or non-crimped fabrics. Their approach is based on a decomposition of the deformation gradient to determine strain physically-based invariants.

Since Charmetant's model is hyperelastic, it is not relevant for any friction dissipation. However, we can develop this model to introduce some irreversibility and to be able to model the frictions between the rope-yarns of the polyamide sub-rope. But we will see below that, both the hyperelastic type of the model and Charmetant's strain invariants, have to be changed to be able to model the frictions of the sub-rope properly.

To understand the limitation of Charmetant's strain invariants for our study, let us propose a complete decomposition of the total strain of a material, in the case of small displacements. Any strain tensor $\tilde{\varepsilon}$ can be expressed by a linear combination of the six following deformation modes:

$$\widetilde{D_1} = \frac{1}{\sqrt{2}}\begin{bmatrix} 1 & 0 & 0 \\ 0 & 1 & 0 \\ 0 & 0 & 0 \end{bmatrix}_{(\overrightarrow{e_{a0}},\overrightarrow{e_{b0}},\overrightarrow{e_{c0}})} \qquad \widetilde{D_2} = \frac{1}{\sqrt{2}}\begin{bmatrix} 1 & 0 & 0 \\ 0 & -1 & 0 \\ 0 & 0 & 0 \end{bmatrix}_{(\overrightarrow{e_{a0}},\overrightarrow{e_{b0}},\overrightarrow{e_{c0}})}$$

$$\widetilde{D_3} = \begin{bmatrix} 0 & 0 & 0 \\ 0 & 0 & 0 \\ 0 & 0 & 1 \end{bmatrix}_{(\overrightarrow{e_{a0}},\overrightarrow{e_{b0}},\overrightarrow{e_{c0}})} \qquad \widetilde{D_4} = \frac{1}{\sqrt{2}}\begin{bmatrix} 0 & 1 & 0 \\ 1 & 0 & 0 \\ 0 & 0 & 0 \end{bmatrix}_{(\overrightarrow{e_{a0}},\overrightarrow{e_{b0}},\overrightarrow{e_{c0}})} \qquad \textit{Eq. 81}$$

$$\widetilde{D_5} = \frac{1}{\sqrt{2}}\begin{bmatrix} 0 & 0 & 1 \\ 0 & 0 & 0 \\ 1 & 0 & 0 \end{bmatrix}_{(\overrightarrow{e_{a0}},\overrightarrow{e_{b0}},\overrightarrow{e_{c0}})} \qquad \widetilde{D_6} = \frac{1}{\sqrt{2}}\begin{bmatrix} 0 & 0 & 0 \\ 0 & 0 & 1 \\ 0 & 1 & 0 \end{bmatrix}_{(\overrightarrow{e_{a0}},\overrightarrow{e_{b0}},\overrightarrow{e_{c0}})}$$
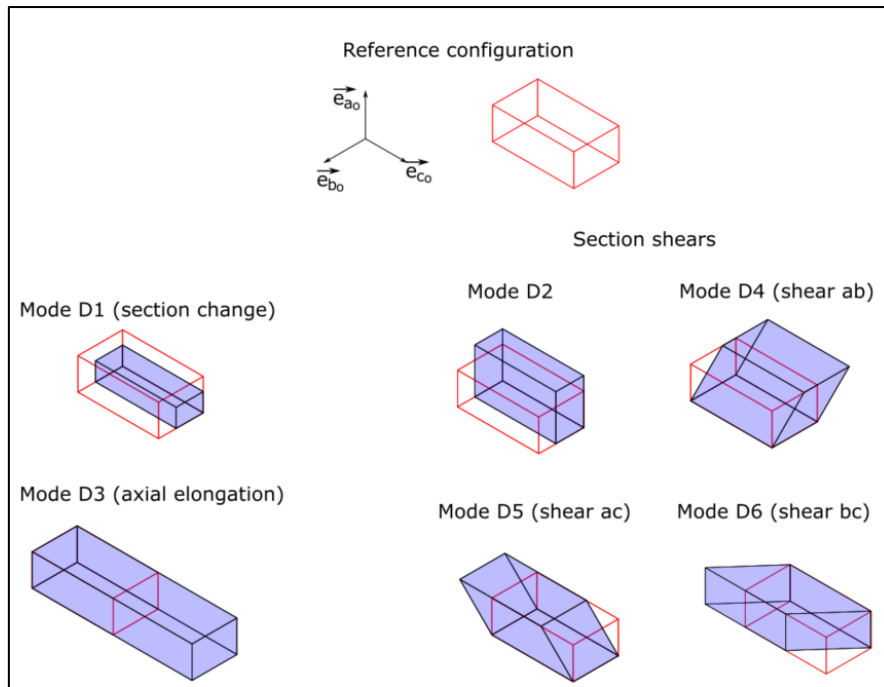
Figure 6.3 – Strain decomposition into 6 strain modes for a bulk material

The set of these tensors (Eq. 81) is an orthonormal basis of the vector space of the second-order symmetric tensors. We can give a physical interpretation of these strain modes (Figure 6.3 illustrates these modes):

- $\widetilde{D_1}$ is the change of the transversal section area.
- $\widetilde{D_2}$ is the shear strain in the transverse section (principal direction $\vec{a}, \vec{b}$).
- $\widetilde{D_3}$ is the axial elongation.
- $\widetilde{D_4}$ is the shear ab. It is identical to $\widetilde{D_2}$ but in a different direction
- $\widetilde{D_5}$ is the shear ac.
- $\widetilde{D_6}$ is the shear bc.

Therefore, we can decompose any strain in the tensor basis $(\widetilde{D_1}, \dots, \widetilde{D_6})$ (Eq. 81):

$$\tilde{\varepsilon} = \varepsilon_1 \widetilde{D_1} + \varepsilon_2 \widetilde{D_2} + \varepsilon_3 \widetilde{D_3} + \varepsilon_4 \widetilde{D_4} + \varepsilon_5 \widetilde{D_5} + \varepsilon_6 \widetilde{D_6} \qquad \text{Eq. 82}$$

Hence, the shear strains, where the friction could occur for a bundle of rope-yarns, are in the two following strain modes:

- The longitudinal shears: $\widetilde{D_5}$ and $\widetilde{D_6}$ which happens in a two-dimensional space:
$$(\varepsilon_5 \widetilde{D_5} + \varepsilon_6 \widetilde{D_6})$$
- The transversal shears: $\widetilde{D_2}$ and $\widetilde{D_4}$ which happens in a two-dimensional space:
$$(\varepsilon_2 \widetilde{D_2} + \varepsilon_4 \widetilde{D_4})$$

In their work, Charmetant *et al.* proposed a dedicated scalar invariant for: the axial elongation, the compaction, the shear and the distortion; and defined each invariant as a function of the classical invariants of the Cauchy-Green deformation tensor $\tilde{C}$ (see appendix C):

$$I_{elong} = \frac{1}{2}\ln(I_4)$$
$$I_{comp} = \frac{1}{4}\ln\left(\frac{I_3}{I_4}\right)$$
$$I_{shear} = \sqrt{\frac{I_5}{I_4^2} - 1} \qquad \text{Eq. 83}$$
$$I_{dist} = \frac{1}{2}\ln\left(\frac{I_1 I_4 - I_5}{2\sqrt{I_3 I_4}} + \sqrt{\left(\frac{I_1 I_4 - I_5}{2\sqrt{I_3 I_4}}\right)^2 - 1}\right)$$

Hence, only one scalar invariant, I_{shear}, describes the evolution of the longitudinal shears, $\widetilde{D_5}$ and $\widetilde{D_6}$, and another scalar invariant, I_{dist}, describes the transversal shears, $\widetilde{D_2}$ and $\widetilde{D_4}$. Hence, each 2D space is described with only one scalar invariant. This choice of invariant leads to a limited description of the strains where the friction will occur.

The following section proposes a decomposition of the deformation similar to that of Charmetant *et al.,* but with a new choice of invariants to replace I_{dist} and I_{shear}. The objective is to overcome the identified limitation and to propose a complete description of the shear strains.

6.3. Anisotropic law for a bundle of rope-yarns

In order to establish the anisotropic law for a bundle of rope-yarns, we will follow this procedure:

- Define the scale we aim to describe (section 6.3.1).
- Propose a decomposition of the deformation gradient tensor $\tilde{F}$ (sections from 6.3.2 to 6.3.8).
- Choose specific strain invariants or variables, physically motivated, to describe each mode of strain. The specific free energy density ψ, will be expressed as a function of them (section 6.3.8).
- Calculate the time derivative of each strain variable (in a form of a linear function of $\tilde{D}$), in order to solve: $\dot{\psi} = \tilde{\Sigma} : \tilde{D} - s \cdot \dot{\theta} - \varphi_1$ (section 6.3.10).
- Solve the equation to obtain a stress-strain relation (section 6.3.11).

6.3.1. Choice of the mesoscopic scale

The chosen mesoscopic scale is a bundle of rope-yarns. In our proposed model, the strands will be modelled as 3 cylinders in contact, each made of a homogeneous material described by the proposed anisotropic law (Figure 6.4). The anisotropic law should describe the complex anisotropic behaviour of a bundle of rope-yarns. We consider that the rope-yarns are parallel with no space between them (Figure 6.4-Reference configuration). The preferred direction of the homogenized material is following the rope-yarns direction $\overrightarrow{c_0}$. The material corresponding to a "bundle of rope-yarns" is considered transversely isotropic.
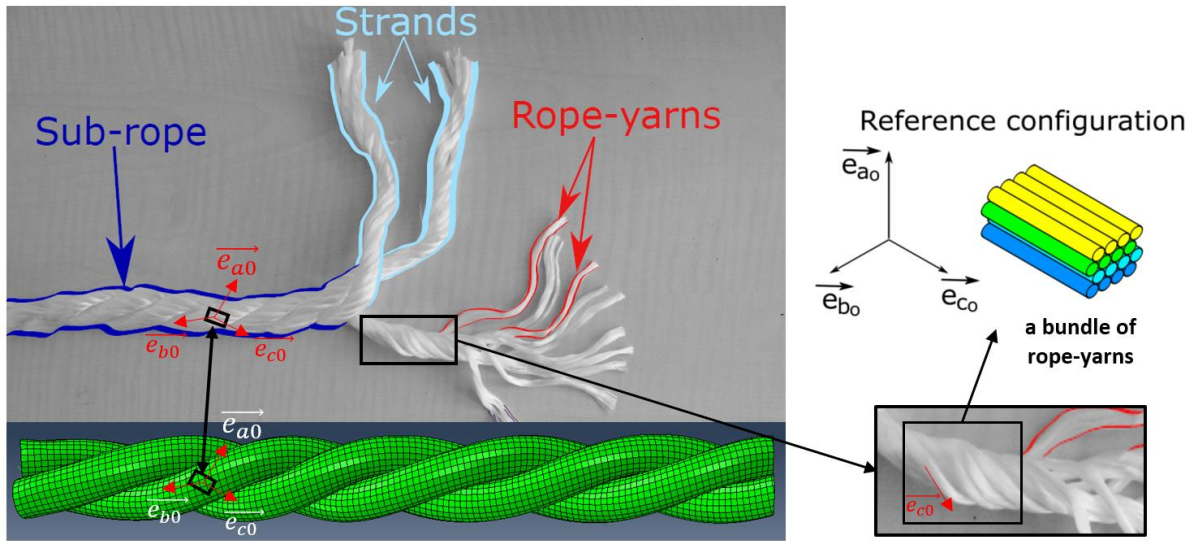
Figure 6.4 - Different scales of a 4T sub-rope and choice of a mesoscopic scale and modelling approach

We approximate the construction of the rope-yarns inside the strand by helices. The law should represent the helical geometry of the bundle of rope-yarns inside the strands. To do so, we use the description proposed by Leech and validated by the tomography scans presented in chapter 5 section 5.3.2.1 (Figure 6.5).
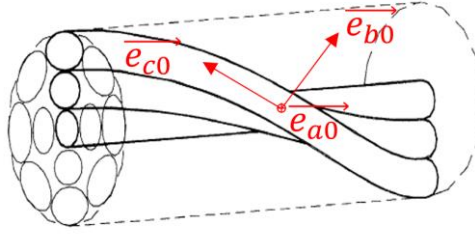
Figure 6.5 - Rope-yarns geometry inside a strand as described by Leech (Leech, 2002)

We consider n rope-yarns, each with a diameter d, located at a radius r_{RY} from the strand axis and each rope-yarns follows a helix about the structure axis with p the pitch (turns/unit length). The rope-yarn attitude or direction cosine is related to the pitch and the helix geometry by the following equation (Leech, 2002):

$$\cos \alpha_{RY} = \frac{1}{\sqrt{1 + (2 \cdot \pi \cdot p \cdot r_{RY})^2}}$$

Eq. 84

With α_{RY} the twist angle of a rope-yarn located at a radius r_{RY} from the centre of the helix and p the pitch of the helix (related the twist angle by chapter 1 Eq. 1).

Hence, using the twist angle at the outer diameter or surface of the strands, the orientation of one rope-yarn can be calculated as a function of its radial position inside the strand.

6.3.2. Deformation decomposition

The decomposition of the deformation gradient allows the strain modes to be isolated and thus to define adapted behaviour law for each of them. Because we expect large shear strains (friction modes), this decomposition has to be made according to the finite deformation theory (Forest, 2022). For each of these strain modes, a dedicated invariant (or strain variable) will be chosen, by following the way paved by the work of Charmetant *et al*.

The reference configuration Ω_0 is chosen and represented on Figure 6.4. The deformation gradient tensor $\tilde{F}$ allows the transformation of the reference configuration Ω_0 to the deformed configuration Ω_t. Three material vectors are chosen:

- The vector $\vec{c}$ is chosen to be parallel to the rope-yarns in all configurations
- The three vectors $\vec{a}, \vec{b}, \vec{c}$ are orthogonal in the reference configuration Ω_0 (the $\overrightarrow{a_0}, \overrightarrow{b_0}, \overrightarrow{c_0}$, in the reference configuration, illustrated on Figure 6.4)
- The three vectors $\vec{a}, \vec{b}, \vec{c}$ are direct in all configurations

Hence, we have:

$$\vec{a} = \tilde{F} \cdot \overrightarrow{a_0}$$
$$\vec{b} = \tilde{F} \cdot \overrightarrow{b_0}$$
$$\vec{c} = \tilde{F} \cdot \overrightarrow{c_0}$$

Eq. 85

The three vectors $(\vec{a}, \vec{b}, \vec{c})$ are a basis of $\mathcal{P}$ (the vector space) in all configurations, not necessarily orthonormal. We define its dual basis $(\overrightarrow{a^*}, \overrightarrow{b^*}, \overrightarrow{c^*})$ to respect the following equations:

$$\vec{a} \cdot \overrightarrow{a^*} = 1 \qquad \vec{b} \cdot \overrightarrow{b^*} = 1 \qquad \vec{c} \cdot \overrightarrow{c^*} = 1$$
$$\vec{a} \cdot \overrightarrow{b^*} = 0 \qquad \vec{b} \cdot \overrightarrow{a^*} = 0 \qquad \vec{c} \cdot \overrightarrow{a^*} = 0$$
$$\vec{a} \cdot \overrightarrow{c^*} = 0 \qquad \vec{b} \cdot \overrightarrow{c^*} = 0 \qquad \vec{c} \cdot \overrightarrow{b^*} = 0$$

Eq. 86

For a vector $\vec{x}$, we call the scalar x, its norm, and the vector $\overrightarrow{e_x}$, its unit vector.

We define the projection tensors parallel to the rope-yarns (symmetric and non-invertible) following:

$$\widetilde{P_c} = \tilde{I} - (\overrightarrow{e_c} \otimes \overrightarrow{e_c})$$
$$\widetilde{P_{c0}} = \tilde{I} - (\overrightarrow{e_{c0}} \otimes \overrightarrow{e_{c0}})$$

<div align="right">Eq. 87</div>

And:

$$\overrightarrow{a_\pi} = \widetilde{P_c} \cdot \vec{a}$$
$$\overrightarrow{b_\pi} = \widetilde{P_c} \cdot \vec{b}$$

<div align="right">Eq. 88</div>

With the following properties:

$$\vec{0} = \widetilde{P_c} \cdot \vec{c}$$
$$\vec{0} = \overrightarrow{b_\pi} \cdot \vec{c} = \overrightarrow{a_\pi} \cdot \vec{c}$$

<div align="right">Eq. 89</div>

6.3.3. Shear strain along the rope-yarns direction

We first define the deformation $\widetilde{G_\pi}$ such that:

$$\overrightarrow{a_\pi} = \widetilde{G_\pi} \cdot \vec{a}$$
$$\overrightarrow{b_\pi} = \widetilde{G_\pi} \cdot \vec{b}$$
$$\vec{c} = \widetilde{G_\pi} \cdot \vec{c}$$

<div align="right">Eq. 90</div>

Hence,

$$\widetilde{G_\pi} = \widetilde{P_c} + \vec{c} \otimes \overrightarrow{c^*}$$

<div align="right">Eq. 91</div>

With $\overrightarrow{c^*}$ a vector of the dual basis defined by Eq. 86.

The inverse of $\widetilde{G_\pi}$, noted $\widetilde{G_\pi}^{-1}$, represents the sliding of the rope-yarns on one another along the rope-yarns direction. This mode of deformation is associated with shear strains (Figure 6.6).
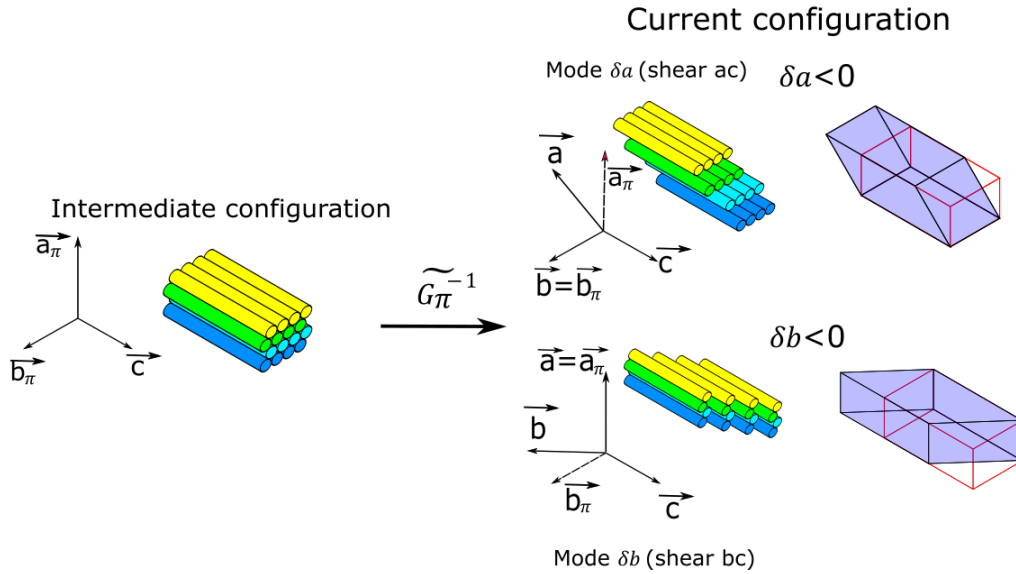
Figure 6.6 – Shear strain deformation of a bundle of rope-yarns along the rope-yarns direction

This deformation has to be at a constant volume. Indeed, if we call $vol(\vec{a}, \vec{b}, \vec{c})$, the volume of the parallelepiped constituted by the three vectors $(\vec{a}, \vec{b}, \vec{c})$, then:

$$vol\left(\overrightarrow{a_\pi}, \overrightarrow{b_\pi}, \vec{c}\right) = vol\left(\vec{a} - (\vec{a} \cdot \overrightarrow{e_c})\overrightarrow{e_c}, \overrightarrow{b_\pi}, \vec{c}\right) = vol(\vec{a}, \overrightarrow{b_\pi}, \vec{c}) = vol(\vec{a}, \vec{b}, \vec{c})$$

<div align="right">Eq. 92</div>

Hence, this deformation is at a constant volume and:

$$\det \widetilde{G_\pi} = 1$$

Eq. 93

So the deformation tensor $\widetilde{G_\pi}$ is invertible. We can define the deformation tensor $\widetilde{F_\pi}$ such that:

$$\widetilde{F_\pi} = \widetilde{G_\pi} \cdot \tilde{F}$$

Eq. 94

Also equal to (using Eq. 91):

$$\widetilde{F_\pi} = \widetilde{P_c} \cdot \tilde{F} + \left(\frac{c}{c_0}\right)(\vec{e_c} \otimes \vec{e_{c0}})$$

Eq. 95

Because:

$$\tilde{F}^T . \vec{c^*} = \frac{\vec{c_0}}{c_0{}^2}$$

Eq. 96

Hence, $\widetilde{F_\pi}$ defines a deformation that contains all the deformations happening other than the sliding of the rope-yarns on one another along the rope-yarns direction.

The next step is to decompose this deformation $\widetilde{F_\pi}$ to define the other deformation modes.

6.3.4. Polar decomposition of $\widetilde{F_\pi}$

The polar decomposition of $\widetilde{F_\pi}$ can be written:

$$\widetilde{F_\pi} = \widetilde{V_\pi} \cdot \widetilde{R_\pi} = \widetilde{R_\pi} \cdot \widetilde{U_\pi}$$

Eq. 97

With $\widetilde{R_\pi}$, the rotation of $\widetilde{F_\pi}$ and $\widetilde{U_\pi}$ the pure strain of $\widetilde{F_\pi}$. Hence, the strain tensor $\widetilde{U_\pi}$ describes the remaining strain modes without the sliding of the rope-yarns on one another along the rope-yarns direction.

Using Eq. 95 and Eq. 97, we obtain:

$$\widetilde{U_\pi}^2 = \widetilde{F^T} \cdot \widetilde{P_c} \cdot \tilde{F} + (\frac{c}{c_0})^2 \, (\vec{e_{c0}} \otimes \vec{e_{c0}})$$

Eq. 98

With:

$$\widetilde{F^T} \cdot \widetilde{P_c} \cdot \tilde{F} \cdot \vec{e_{c0}} = \vec{0}$$

Eq. 99

Hence:

$$\widetilde{U_\pi}^2 \cdot \vec{e_{c0}} = \left(\frac{c}{c_0}\right)^2 \vec{e_{c0}}$$

Eq. 100

Therefore, $\vec{e_{c0}}$ is an eigenvector of the matrices $\widetilde{U_\pi}^2$ *and* $\widetilde{U_\pi}$, with the following eigenvalues $\left(\frac{c}{c_0}\right)^2$ and $\left(\frac{c}{c_0}\right)$, respectively. We can write $\widetilde{U_\pi}$ following:

$$\widetilde{U_\pi} = \begin{bmatrix} U_{\pi 11} & U_{\pi 12} & 0 \\ U_{\pi 12} & U_{\pi 22} & 0 \\ 0 & 0 & \left(\frac{c}{c_0}\right) \end{bmatrix}_{(\vec{e_{a0}}, \vec{e_{b0}}, \vec{e_{c0}})}$$

Eq. 101

Using Eq. 94, we also have:

$$\det \widetilde{U_\pi} = \det \tilde{F} = J$$

Eq. 102

6.3.5. Change of volume

The pure strain tensor of change of volume of the deformation gradient tensor $\tilde{F}$ is:

$$\widetilde{U_{vol}} = \sqrt[3]{J}\, \tilde{I}$$

<div align="right">*Eq. 103*</div>

With

$$\det \widetilde{U_{vol}} = J = \det \tilde{F}$$

<div align="right">*Eq. 104*</div>

Its logarithm is equal to:

$$\ln \widetilde{U_{vol}} = \frac{\ln J}{3}\, \tilde{I}$$

<div align="right">*Eq. 105*</div>

This strain mode is represented in Figure 6.7.
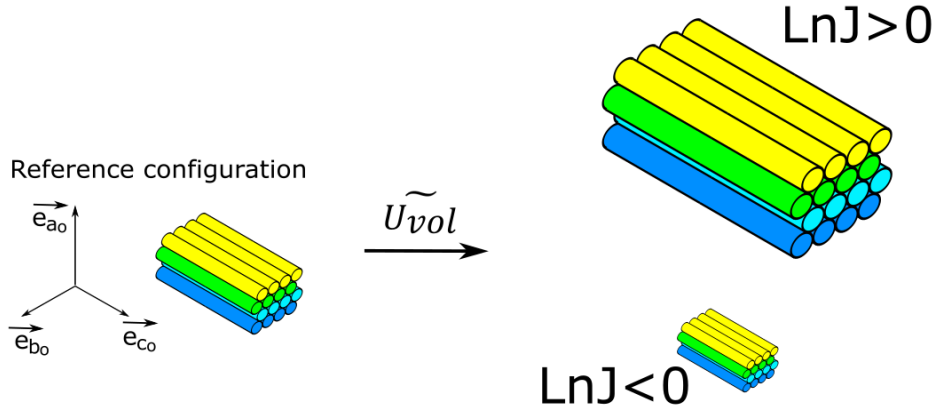
Figure 6.7 – Change-of-volume strain mode for a bundle of rope-yarns

We aim to separate all the deformation modes. Therefore, we remove the change of volume from the pure strain $\widetilde{U_{\pi}}$ defined above. We call $\widetilde{U_{\bar{\pi}}}$ this new deformation without change of volume:

$$\widetilde{U_{\bar{\pi}}} = \widetilde{U_{vol}}^{-1} \cdot \widetilde{U_{\pi}} = \frac{1}{\sqrt[3]{J}} \begin{bmatrix} U_{\pi 11} & U_{\pi 12} & 0 \\ U_{\pi 12} & U_{\pi 22} & 0 \\ 0 & 0 & \left(\dfrac{c}{c_0}\right) \end{bmatrix}_{(\overrightarrow{e_{a0}}, \overrightarrow{e_{b0}}, \overrightarrow{e_{c0}})}$$

<div align="right">*Eq. 106*</div>

Hence, we have:

$$\det \widetilde{U_{\bar{\pi}}} = 1$$

<div align="right">*Eq. 107*</div>

At this stage, we have separated:

- $\widetilde{G_{\pi}}^{-1}$ the sliding of the rope-yarns on one another along the rope-yarns direction (deformation without change of volume) (Figure 6.6).
- $\widetilde{U_{vol}}$ the change of volume contained in $\widetilde{U_{\pi}}$ and in $\tilde{F}$ (Figure 6.7)
- $\widetilde{U_{\bar{\pi}}}$ containing the remaining deformation modes to establish (without change of volume).

6.3.6. Axial Elongation

We recall that the vectors $\vec{c_0}$ and $\vec{c}$ are respectively the vectors in the direction of the rope-yarns in the reference configuration and in the deformed configuration. Hence, following our notation, the scalars c_0 and c are their norms. Thus, the axial elongation in the rope-yarns axis direction (without change of volume), $\widetilde{U_c}$, can be expressed:

$$\widetilde{U_c} = \frac{1}{\sqrt[3]{J}} \begin{bmatrix} \sqrt{J\left(\frac{c_0}{c}\right)} & 0 & 0 \\ 0 & \sqrt{J\left(\frac{c_0}{c}\right)} & 0 \\ 0 & 0 & \left(\frac{c}{c_0}\right) \end{bmatrix}_{(\vec{e_{a0}},\vec{e_{b0}},\vec{e_{c0}})} = \begin{bmatrix} [\frac{1}{\sqrt[3]{J}}\frac{c}{c_0}]^{-\frac{1}{2}} & 0 & 0 \\ 0 & [\frac{1}{\sqrt[3]{J}}\frac{c}{c_0}]^{-\frac{1}{2}} & 0 \\ 0 & 0 & \frac{1}{\sqrt[3]{J}}\frac{c}{c_0} \end{bmatrix}_{(\vec{e_{a0}},\vec{e_{b0}},\vec{e_{c0}})}$$

Eq. 108

Its determinant is equal to:

$$\det \widetilde{U_c} = 1$$

Eq. 109

Its logarithm is equal to:

Eq. 110

$$\widetilde{LnU_c} = \ln\left(\frac{1}{\sqrt[3]{J}}\frac{c}{c_0}\right) \begin{bmatrix} -\frac{1}{2} & 0 & 0 \\ 0 & -\frac{1}{2} & 0 \\ 0 & 0 & 1 \end{bmatrix}_{\vec{e_{a0}},\vec{e_{b0}},\vec{e_{c0}}} = \ln\left(\frac{1}{\sqrt[3]{J}}\frac{c}{c_0}\right)(\tilde{I} - \frac{3}{2}\widetilde{P_{c0}})$$

The pure strain $\widetilde{U_c}$ represents the axial elongation of the rope-yarns without any change of volume. This deformation mode is represented in Figure 6.8.
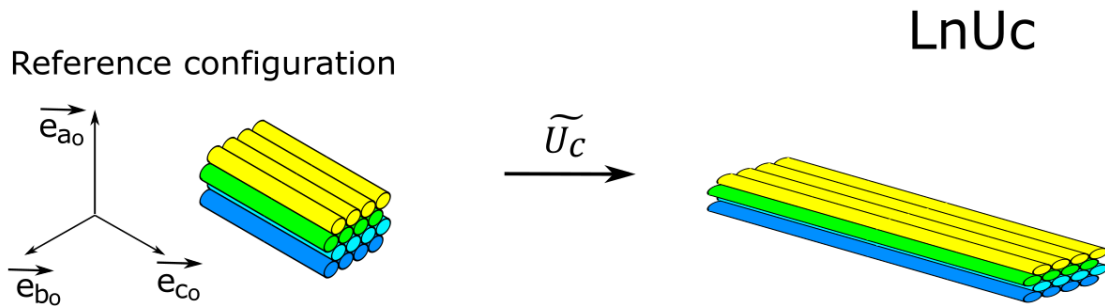
Figure 6.8 – Axial elongation strain mode at constant volume for a bundle of rope-yarns

This deformation mode is contained in the pure strain tensor $\widetilde{U_{\overline{\pi}}}$. Note that $\widetilde{U_c}$ and $\widetilde{U_{\overline{\pi}}}$ can commute:

$$\widetilde{U_c} \cdot \widetilde{U_{\overline{\pi}}} = \widetilde{U_{\overline{\pi}}} \cdot \widetilde{U_c} \text{ and } \widetilde{U_c} \cdot \widetilde{U_\pi} = \widetilde{U_\pi} \cdot \widetilde{U_c}$$

Eq. 111

6.3.7. Deformation of the rope-yarns in the transverse section of the rope-yarn

We define the last deformation mode, $\widetilde{U_{ab}}$ contained in $\widetilde{U_{\overline{\pi}}}$, by removing the deformation mode $\widetilde{U_c}$ such that:

$$\widetilde{U_{ab}} = \widetilde{U_{\overline{\pi}}} \cdot \widetilde{U_c}^{-1} = \widetilde{U_c}^{-1} \cdot \widetilde{U_{\overline{\pi}}}$$

Eq. 112

Therefore, using Eq. 106 and Eq. 108:

$$\widetilde{U_{ab}} = \begin{bmatrix} U_{\pi 11}\sqrt{\dfrac{c}{Jc_0}} & U_{\pi 12}\sqrt{\dfrac{c}{Jc_0}} & 0 \\ U_{\pi 12}\sqrt{\dfrac{c}{Jc_0}} & U_{\pi 22}\sqrt{\dfrac{c}{Jc_0}} & 0 \\ 0 & 0 & 1 \end{bmatrix}_{(\overrightarrow{e_{a0}},\overrightarrow{e_{b0}},\overrightarrow{e_{c0}})} \qquad \text{Eq. 113}$$

Its determinant is equal to:

$$\det \widetilde{U_{ab}} = 1 \qquad \text{Eq. 114}$$

And its logarithm is equal to:

$$\widetilde{LnU_{ab}} = \begin{bmatrix} \ln U_{ab11} & \ln U_{ab12} & 0 \\ \ln U_{ab12} & -\ln U_{ab11} & 0 \\ 0 & 0 & 0 \end{bmatrix}_{(\overrightarrow{e_{a0}},\overrightarrow{e_{b0}},\overrightarrow{e_{c0}})} \qquad \text{Eq. 115}$$

Also:

$$Tr\left(\widetilde{LnU_{ab}}\right) = Ln\left(\det \widetilde{U_{ab}}\right) = 0 \qquad \text{Eq. 116}$$

The deformation $\widetilde{U_{ab}}$ is the deformation of the rope-yarns in their transverse section, without any change of volume. This strain mode is represented in Figure 6.9.
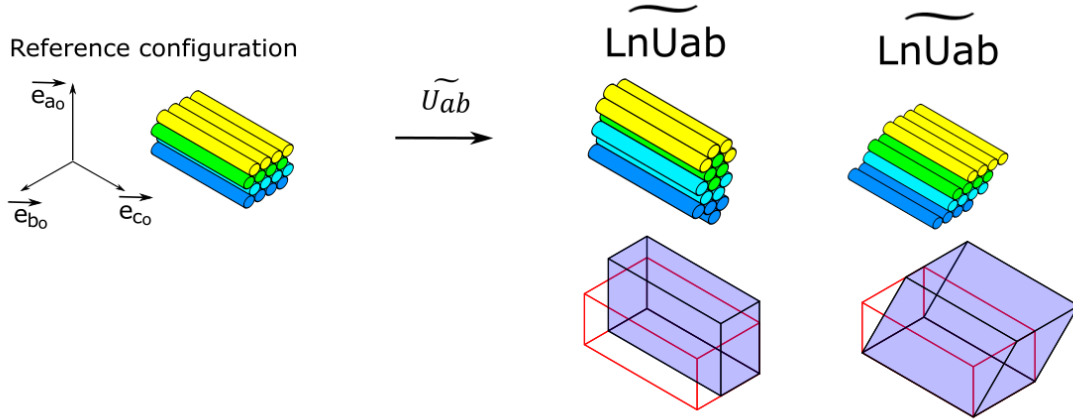
Figure 6.9 – Transversal shear strain mode for a bundle of rope-yarns

6.3.8. Final decomposition of the deformation $\widetilde{F}$

We have decomposed the deformation gradient $\widetilde{F}$ into four strain modes and the associated rotation of the matter, such that:

$$\widetilde{F} = \widetilde{G_\pi}^{-1} \cdot \widetilde{R_\pi} \cdot \widetilde{U_{vol}} \cdot \widetilde{U_c} \cdot \widetilde{U_{ab}} \qquad \text{Eq. 117}$$

To have a decomposition in the Lagrangian formalisation, we define $\widetilde{K_\pi}$ to respect:

$$\widetilde{F} = \widetilde{G_\pi}^{-1} \cdot \left(\widetilde{R_\pi} \cdot \widetilde{U_{vol}} \cdot \widetilde{U_c} \cdot \widetilde{U_{ab}}\right) = \left(\widetilde{R_\pi} \cdot \widetilde{U_{vol}} \cdot \widetilde{U_c} \cdot \widetilde{U_{ab}}\right) \cdot \widetilde{K_\pi}^{-1} \qquad \text{Eq. 118}$$

We also have:

$$\widetilde{F} = \widetilde{G_\pi}^{-1} \cdot \widetilde{F_\pi} = \widetilde{F_\pi} \cdot \widetilde{K_\pi}^{-1} \qquad \text{Eq. 119}$$

And:

$$\widetilde{F_\pi} = \widetilde{G_\pi} \cdot \tilde{F} = \tilde{F} \cdot \widetilde{K_\pi} \qquad \text{Eq. 120}$$

Hence, using Eq. 95,

$$\widetilde{K_\pi} = \tilde{F}^{-1} \cdot \widetilde{G_\pi} \cdot \tilde{F}$$
$$\widetilde{K_\pi} = \tilde{F}^{-1} \cdot \tilde{P}_c \cdot \tilde{F} + (\overrightarrow{e_{c0}} \otimes \overrightarrow{e_{c0}})$$
$$\widetilde{K_\pi} = \tilde{I} - \overrightarrow{e_{c0}} \otimes [\frac{c_0}{c^2} \tilde{F}^T \cdot \vec{c}] + (\overrightarrow{e_{c0}} \otimes \overrightarrow{e_{c0}}) \qquad \text{Eq. 121}$$

We know that:

$$\left[\frac{c_0}{c^2} \tilde{F}^T \cdot \vec{c}\right] = \begin{pmatrix} \dfrac{c_0}{c} \dfrac{\vec{a} \cdot \overrightarrow{e_c}}{a_0} \\[2mm] \dfrac{c_0}{c} \dfrac{\vec{b} \cdot \overrightarrow{e_c}}{b_0} \\[2mm] 1 \end{pmatrix}_{(\overrightarrow{e_{a0}}, \overrightarrow{e_{b0}}, \overrightarrow{e_{c0}})} \qquad \text{Eq. 122}$$

Because

$$\overrightarrow{a_0} \cdot [\tilde{F}^T \cdot \vec{c}] = \vec{a} \cdot \vec{c}$$

$$\overrightarrow{b_0} \cdot [\tilde{F}^T \cdot \vec{c}] = \vec{b} \cdot \vec{c}$$

$$\overrightarrow{c_0} \cdot [\tilde{F}^T \cdot \vec{c}] = \vec{c} \cdot \vec{c}$$

We define the vector $\vec{\delta}$ such that:

$$\vec{\delta} = \begin{pmatrix} \delta_a \\ \delta_b \\ 0 \end{pmatrix}_{(\overrightarrow{e_{a0}}, \overrightarrow{e_{b0}}, \overrightarrow{e_{c0}})} \qquad \text{Eq. 123}$$

$$\text{With } \delta_a = \frac{c_0}{c} \frac{\vec{a} \cdot \overrightarrow{e_c}}{a_0} \text{ and } \delta_b = \frac{c_0}{c} \frac{\vec{b} \cdot \overrightarrow{e_c}}{b_0} \qquad \text{Eq. 124}$$

Therefore,

$$\widetilde{K_\pi} = \tilde{I} - \overrightarrow{e_{c0}} \otimes (\vec{\delta} + \overrightarrow{e_{c0}}) + (\overrightarrow{e_{c0}} \otimes \overrightarrow{e_{c0}}) = \tilde{I} - \overrightarrow{e_{c0}} \otimes \vec{\delta} \qquad \text{Eq. 125}$$

We can write the matrix $\widetilde{K_\pi}$:

$$\widetilde{K_\pi} = \begin{bmatrix} 1 & 0 & 0 \\ 0 & 1 & 0 \\ -\delta_a & -\delta_b & 1 \end{bmatrix}_{(\overrightarrow{e_{a0}}, \overrightarrow{e_{b0}}, \overrightarrow{e_{c0}})} \quad \text{and} \quad \widetilde{K_\pi}^{-1} = \begin{bmatrix} 1 & 0 & 0 \\ 0 & 1 & 0 \\ \delta_a & \delta_b & 1 \end{bmatrix}_{(\overrightarrow{e_{a0}}, \overrightarrow{e_{b0}}, \overrightarrow{e_{c0}})} \qquad \text{Eq. 126}$$

Its determinant is equal to:

$$\det \widetilde{K_\pi} = \det \widetilde{K_\pi}^{-1} = 1 \qquad \text{Eq. 127}$$

This deformation is at constant volume and describes two shears in the planes (ac) and (bc). Therefore, they are the longitudinal shear strain modes.

The final expression of the deformation $\tilde{F}$ following our decomposition is:

$$\tilde{F} = \widetilde{R_\pi} \cdot \widetilde{U_{vol}} \cdot \widetilde{U_c} \cdot \widetilde{U_{ab}} \cdot \widetilde{K_\pi}^{-1} \qquad \text{Eq. 128}$$

6.3.9. Choice of physically motivated invariants and advantages

We should choose invariants that describes the strain modes presented above. The following invariants or strain variables are chosen for each deformation mode (illustrated on Figure 6.10):

For the change of volume: $\ln J = \ln(\det \tilde{F})$

Eq. 129

For the axial elongation: $LnU_c = \ln(\frac{1}{\sqrt[3]{J}} \frac{c}{c_0})$

Eq. 130

For the deformation in the transverse section of the rope-yarns:

$$\widetilde{LnU_{ab}} = \begin{bmatrix} \ln U_{ab11} & \ln U_{ab12} & 0 \\ \ln U_{ab12} & -\ln U_{ab11} & 0 \\ 0 & 0 & 0 \end{bmatrix}_{(\overrightarrow{e_{a0}},\overrightarrow{e_{b0}},\overrightarrow{e_{c0}})}$$

Eq. 131

Finally, for the sliding of the rope-yarns on one another along their axis;

$$\tilde{\varepsilon}_\delta = \begin{bmatrix} 0 & 0 & \dfrac{\delta_a}{2} \\ 0 & 0 & \dfrac{\delta_b}{2} \\ \dfrac{\delta_a}{2} & \dfrac{\delta_b}{2} & 0 \end{bmatrix}_{(\overrightarrow{e_{a0}},\overrightarrow{e_{b0}},\overrightarrow{e_{c0}})}$$

Eq. 132

With Eq. 124: $\delta_a = \frac{c_0}{c} \frac{\vec{a} \cdot \overrightarrow{e_c}}{a_0}$ and $\delta_b = \frac{c_0}{c} \frac{\vec{b} \cdot \overrightarrow{e_c}}{b_0}$

And: $\tilde{\varepsilon}_\delta = \frac{1}{2}\left(\widetilde{K_\pi}^{-1} + \widetilde{K_\pi}^{-T}\right) - \tilde{I} = \widetilde{P_{c0}} - \frac{1}{2}(\tilde{F}^{-1} \cdot \widetilde{P_c} \cdot \tilde{F} + \tilde{F}^T \cdot \widetilde{P_c} \cdot \tilde{F}^{-T})$

Eq. 133
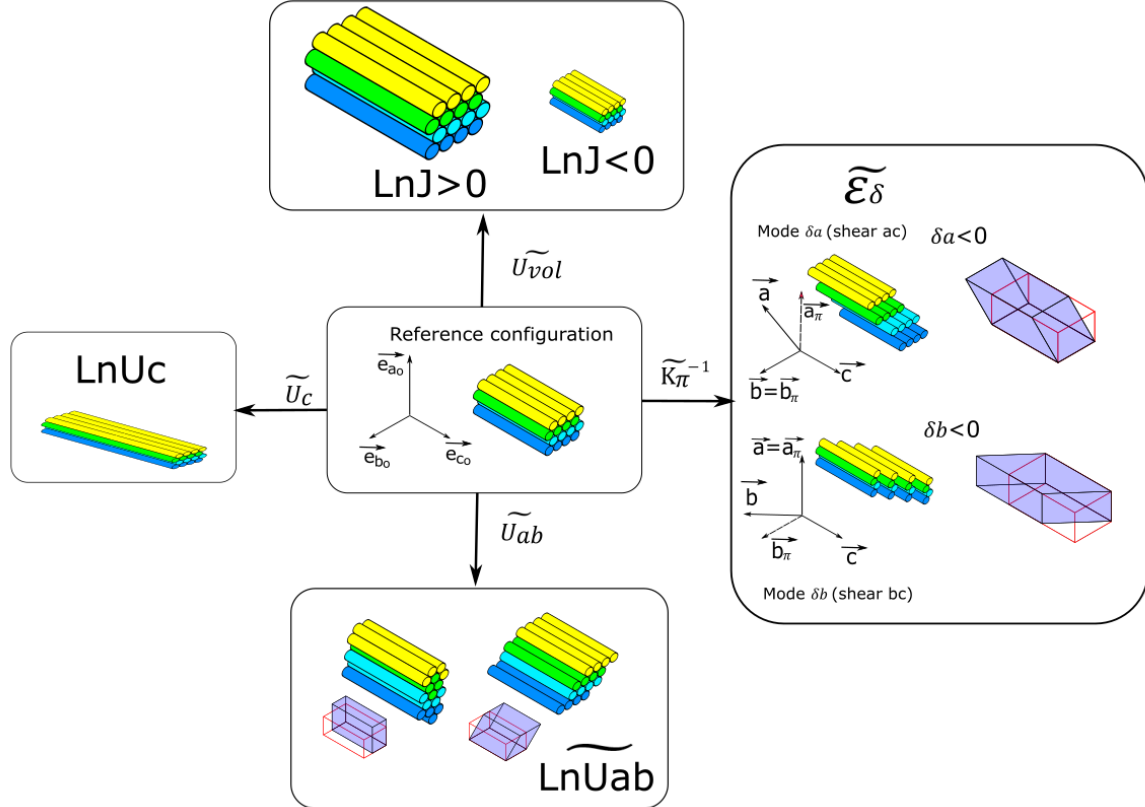
Figure 6.10 – Final decomposition of the deformation for a bundle of rope-yarns. Choice of physically motivated invariants or strain variables to describe these strain modes

These invariants describe completely the shear strain modes, where all the friction events are happening during a deformation. We propose to highlight the relationships, and differences, between the invariants chosen by Charmetant *et al.* and our invariants. To do so, we will express the invariants chosen by Charmetant as a function of our proposed invariants.

Charmetant *et al.* expressed their invariants as a function of the classical invariants of the Cauchy-Green tensor (appendix C). These classical invariants can be expressed, using our deformation decomposition:

$$I_3 = J^2$$
$$I_4 = \left(\frac{c}{c_0}\right)^2$$
$$I_5 = \left(\frac{c}{c_0}\right)^4 (\delta_a^2 + \delta_b^2 + 1)$$

<div align="right">*Eq. 134*</div>

Hence, we can demonstrate that:

$$I_{comp} = \frac{1}{2}\ln\left(\frac{Jc_0}{c}\right)$$
$$I_{elong} = \ln\left(\frac{c}{c_0}\right)$$

Hence: $\begin{pmatrix} I_{comp} \\ I_{elong} \end{pmatrix} = \begin{bmatrix} \frac{1}{3} & -\frac{1}{2} \\ \frac{1}{3} & 1 \end{bmatrix} \cdot \begin{pmatrix} Ln\,J \\ Ln\,U_c \end{pmatrix}$

And:

<div align="right">*Eq. 135*</div>

$$I_{shear} = \sqrt{\delta_a^2 + \delta_b^2} = \|\tilde{\varepsilon}_\delta\| . \sqrt{2}$$
$$I_{dist} = \frac{\|\widetilde{LnU_{ab}}\|}{\sqrt{2}}$$

The use of our proposed invariants has only consequences for the friction as Eq. 135 shows that:

- For the invariants (I_{comp}, I_{elong}), we only performed a linear change of variables to obtain $Ln\,J$ and LnU_c.
- The invariants I_{dist} and I_{shear} of Charmetant are proportional to the norms $\|\widetilde{LnU_{ab}}\|$ and $\|\tilde{\varepsilon}_\delta\|$. Hence, using the new invariants, $\widetilde{LnU_{ab}}$ and $\tilde{\varepsilon}_\delta$, leads to a more complete description of the shear strains.

If we recall the decomposition of a transformation (Figure 6.3) proposed in section 6.2.3, the shear strain modes were happening in two dimensional spaces following Eq. 82:

- The longitudinal shears: $\widetilde{D_5}$ and $\widetilde{D_6}$ which happens in the two-dimensional space:
$$(\varepsilon_5 \widetilde{D_5} + \varepsilon_6 \widetilde{D_6})$$
- The transversal shears: $\widetilde{D_2}$ and $\widetilde{D_4}$ which happens in the two-dimensional space:
$$(\varepsilon_2 \widetilde{D_2} + \varepsilon_4 \widetilde{D_4})$$

Using our new proposed strain variables, we have:

$$\tilde{\varepsilon}_\delta = \begin{bmatrix} 0 & 0 & \frac{\delta_a}{2} \\ 0 & 0 & \frac{\delta_b}{2} \\ \frac{\delta_a}{2} & \frac{\delta_b}{2} & 0 \end{bmatrix}_{(\overrightarrow{e_{a0}},\overrightarrow{e_{b0}},\overrightarrow{e_{c0}})} = (\frac{\delta_a}{\sqrt{2}}\widetilde{D_5} + \frac{\delta_b}{\sqrt{2}}\widetilde{D_6})$$

<div align="right">*Eq. 136*</div>

$$LnU_{ab} = \begin{bmatrix} \ln U_{ab11} & \ln U_{ab12} & 0 \\ \ln U_{ab12} & -\ln U_{ab11} & 0 \\ 0 & 0 & 0 \end{bmatrix}_{(\overrightarrow{e_{a0}}, \overrightarrow{e_{b0}}, \overrightarrow{e_{c0}})} = (\ln U_{ab11}\sqrt{2}\,\widetilde{D_2} + \ln U_{ab12}\,\sqrt{2}\widetilde{D_4})$$

Eq. 137

Hence these strain variables also evolve in two-dimensional spaces, allowing a complete description of the friction happening during a deformation. When the invariants $\widetilde{LnU_{ab}}$ and $\tilde{\varepsilon}_\delta$ evolve in their two-dimensional spaces, frictions occur between the rope-yarns. When using I_{dist} and I_{shear}, the description of the frictions is limited.

To conclude on the differences and advantages of these new invariants in comparison to Charmetant's invariants:

- The invariants describing the change of volume and axial elongation, $Ln\,J$ and LnU_c, are similar. We only performed a linear change of variables.
- The invariants describing the shear strains allow a complete description of the frictions happening during a deformation as show Eq. 136 and Eq. 137.

6.3.10. Derivation of the invariants

The time derivatives of the invariants and strain variables, in the form of a linear function of $\widetilde{D}$, are necessary to define the stress-strain law as explained in section 6.2.2. The final objective is to solve Eq. 79.

Let us recall, with $\widetilde{D}$ the strain rate tensor, that:

$$Tr(\tilde{X} \cdot \widetilde{D}) = \tilde{X} : \widetilde{D}^T = \tilde{X} : \widetilde{D}$$

Eq. 138

We will also use the fourth-order tensors $\tilde{\tilde{Q}}_{(\tilde{A})}$, $\tilde{\tilde{\gamma}}_{(\tilde{A})}$ defined as follows:

$$\forall \tilde{X} \ \ and \ \ \forall \tilde{B}, \ \ \tilde{\tilde{Q}}_{(\tilde{B})} : \tilde{X} = \tilde{B} \cdot \tilde{X} \cdot \tilde{B}^T$$

And if $\tilde{A}$ is a symmetric second-order tensor with positive eigen values (never null),

$$\forall \tilde{A} \ \ and \ \ \forall \dot{\tilde{A}}, \ \ \ \dot{\widetilde{LnA}} = \frac{1}{2}\tilde{\tilde{\gamma}}_{(\tilde{A})} : (\dot{\tilde{A}} \cdot \tilde{A}^{-1} + \tilde{A}^{-1} \cdot \dot{\tilde{A}})$$

Eq. 139

In fact, tensor $\tilde{\tilde{\gamma}}_{(\tilde{A})}$ may also be defined by the following relation:

$$\widetilde{\overset{\circ}{LnV}} = \tilde{\tilde{\gamma}}_{(\tilde{V})} : \widetilde{D}$$

Eq. 140

Where $\tilde{V}$ is the left pure strain tensor and $\widetilde{\overset{\circ}{LnV}}$ is the Green-Naghdi objective rate of the left logarithmic strain tensor. According to (Hoger, 1986) the matrix of this tensor in the Voigt-Mandel notation from eigenvectors $(\overrightarrow{a_1}, \overrightarrow{a_2}, \overrightarrow{a_3})$ of tensor $\tilde{A}$, is as follows:

$$\tilde{\tilde{\gamma}}_{(\tilde{A})} = \begin{bmatrix} 1 & 0 & 0 & 0 & 0 & 0 \\ 0 & 1 & 0 & 0 & 0 & 0 \\ 0 & 0 & 1 & 0 & 0 & 0 \\ 0 & 0 & 0 & g(a_1, a_2) & 0 & 0 \\ 0 & 0 & 0 & 0 & g(a_1, a_3) & 0 \\ 0 & 0 & 0 & 0 & 0 & g(a_2, a_3) \end{bmatrix}_{VM(\overrightarrow{a_i})}$$

Eq. 141

Where (a_1, a_2, a_3) are eigenvalues of tensor $\tilde{A}$ (symmetric with positive eigenvalues) and

$$g(x, y) = g(y, x) = \frac{2xy\,ln\left(\frac{x}{y}\right)}{(x^2 - y^2)} \ and \ g(x, x) = 1.$$

Note that:

$$\tilde{\tilde{\gamma}}_{(\tilde{A})}: (\vec{a_i} \otimes \vec{a_i}) = (\vec{a_i} \otimes \vec{a_i}) \quad \forall i = 1,2,3$$

We first derivate the change of volume invariant:

$$\dot{\ln} J = \frac{\dot{J}}{J} = Tr(\widetilde{D}) = \tilde{I} : \widetilde{D}$$

<div align="right">Eq. 142</div>

The derivative of the invariant describing the axial elongation is equal to:

$$Ln\dot{U}_c = \frac{\dot{c}}{c} - \frac{\dot{J}}{3J} = (\vec{e_c} \otimes \vec{e_c}): \widetilde{D} - \frac{1}{3}\tilde{I}:\widetilde{D}$$

<div align="right">Eq. 143</div>

$$Ln\dot{U}_c = \left(\vec{e_c} \otimes \vec{e_c} - \frac{1}{3}\tilde{I}\right): \widetilde{D}$$

$$Ln\dot{U}_c = \left(\frac{2}{3}\tilde{I} - \widetilde{P}_c\right): \widetilde{D}$$

To determine $\dot{\widetilde{LnU}}_{ab}$, we need to derivate $\widetilde{U}_\pi$. Starting from Eq. 98, we have:

$$\overline{\dot{\widetilde{U}_\pi}^2} = \overline{\dot{\widetilde{F^T} \cdot \widetilde{P}_c \cdot \tilde{F}}} + 2\frac{c}{c_0}\left(\frac{\dot{c}}{c_0}\right)(\vec{e_{c0}} \otimes \vec{e_{c0}})$$

<div align="right">Eq. 144</div>

With:

$$\overline{\dot{\widetilde{F^T} \cdot \widetilde{P}_c \cdot \tilde{F}}} = 2\widetilde{F^T} \cdot \widetilde{P}_c \cdot \widetilde{D} \cdot \widetilde{P}_c \cdot \tilde{F}$$

<div align="right">Eq. 145</div>

Hence,

$$\overline{\dot{\widetilde{U}_\pi}^2} = 2\widetilde{F^T} \cdot \widetilde{P}_c \cdot \widetilde{D} \cdot \widetilde{P}_c \cdot \tilde{F} + 2\left(\frac{c}{c_0}\right)^2 (\vec{e_{c0}} \otimes \vec{e_{c0}}) \otimes (\vec{e_c} \otimes \vec{e_c}) : \widetilde{D}$$

<div align="right">Eq. 146</div>

To obtain an expression following form Eq. 139, we write:

$$\widetilde{U}_\pi^{-1} \cdot \overline{\dot{\widetilde{U}_\pi}^2} \cdot \widetilde{U}_\pi^{-1} = 2\widetilde{U}_\pi^{-1} \cdot \widetilde{F^T} \cdot \widetilde{P}_c \cdot \widetilde{D} \cdot \widetilde{P}_c \cdot \tilde{F} \cdot \widetilde{U}_\pi^{-1} + 2\left(\frac{c}{c_0}\right)^2 \cdot [(\widetilde{U}_\pi^{-1} \cdot \vec{e_{c0}}) \otimes (\widetilde{U}_\pi^{-1} \cdot \vec{e_{c0}})] \otimes (\vec{e_c} \otimes \vec{e_c})$$
$$: \widetilde{D}$$

$$\Leftrightarrow \dot{\widetilde{U}}_\pi \cdot \widetilde{U}_\pi^{-1} + \widetilde{U}_\pi^{-1} \cdot \dot{\widetilde{U}}_\pi = 2\widetilde{R}_\pi^T \cdot \widetilde{P}_c \cdot \widetilde{D} \cdot \widetilde{P}_c \cdot \widetilde{R}_\pi + 2(\vec{e_{c0}} \otimes \vec{e_{c0}}) \otimes (\vec{e_c} \otimes \vec{e_c}) : \widetilde{D}$$

$$\Leftrightarrow \dot{\widetilde{U}}_\pi \cdot \widetilde{U}_\pi^{-1} + \widetilde{U}_\pi^{-1} \cdot \dot{\widetilde{U}}_\pi = 2\left[\widetilde{\widetilde{Q}}_{(\widetilde{R}_\pi^T \cdot \widetilde{P}_c)} + (\vec{e_{c0}} \otimes \vec{e_{c0}}) \otimes (\vec{e_c} \otimes \vec{e_c})\right] : \widetilde{D}$$

$$\Leftrightarrow \dot{\widetilde{LnU}}_\pi = \left[\widetilde{\tilde{\gamma}}_{(\widetilde{U}_\pi)} : \widetilde{\widetilde{Q}}_{(\widetilde{R}_\pi^T \cdot \widetilde{P}_c)} + (\vec{e_{c0}} \otimes \vec{e_{c0}}) \otimes (\vec{e_c} \otimes \vec{e_c})\right] : \widetilde{D}$$

<div align="right">Eq. 147</div>

Using Eq. 128, the decomposition of the deformation proposed section 6.3.8 defined $\widetilde{U}_\pi$ as:

$$\widetilde{U}_\pi = \widetilde{U_{vol}} \cdot \widetilde{U_c} \cdot \widetilde{U_{ab}}$$
$$\Leftrightarrow \widetilde{LnU}_\pi = \widetilde{LnU}_{vol} + \widetilde{LnU}_c + \widetilde{LnU}_{ab}$$
$$\Leftrightarrow \widetilde{LnU}_\pi = \frac{\ln J}{3}\tilde{I} + LnU_c\left(\tilde{I} - \frac{3}{2}\widetilde{P_{c0}}\right) + \widetilde{LnU}_{ab}$$
$$\Rightarrow \dot{\widetilde{LnU}}_\pi = \frac{\dot{\ln} J}{3}\tilde{I} + Ln\dot{U}_c\left(\tilde{I} - \frac{3}{2}\widetilde{P_{c0}}\right) + \dot{\widetilde{LnU}}_{ab}$$

<div align="right">Eq. 148</div>

Therefore, we can deduce $\dot{\widetilde{LnU}}_{ab}$ from Eq. 142, Eq. 143 and Eq. 147:

$$\dot{\widetilde{LnU}}_{ab} = \left[\widetilde{\tilde{\gamma}}_{(\widetilde{U}_\pi)} : \widetilde{\widetilde{Q}}_{(\widetilde{R}_\pi^T \cdot \widetilde{P}_c)} - \frac{1}{2}(\widetilde{P_{c0}} \otimes \widetilde{P}_c)\right] : \widetilde{D}$$

<div align="right">Eq. 149</div>

The derivative of the invariant $\dot{\tilde{\varepsilon}}_\delta$ can be obtain using the derivative $\dot{\delta}_a$ and $\dot{\delta}_b$:

$$\dot{\delta}_a = \sqrt{2}\left(\frac{c_0}{c}\right)^2 \left[\tilde{\tilde{Q}}_{(\widetilde{F_\pi})}:\widetilde{D_5}\right]:\tilde{D} = \sqrt{2}\left(\frac{c_0}{c}\right)^2 \left[\tilde{\tilde{Q}}_{(\widetilde{F_\pi})}^{\ T}:\tilde{D}\right]:\widetilde{D_5}$$

<div align="right">Eq. 150</div>

$$\dot{\delta}_b = \sqrt{2}\left(\frac{c_0}{c}\right)^2 \left[\tilde{\tilde{Q}}_{(\widetilde{F_\pi})}:\widetilde{D_6}\right]:\tilde{D} = \sqrt{2}\left(\frac{c_0}{c}\right)^2 \left[\tilde{\tilde{Q}}_{(\widetilde{F_\pi})}^{\ T}:\tilde{D}\right]:\widetilde{D_6}$$

<div align="right">Eq. 151</div>

See appendix D (p.209) for the proof of these relations.

Hence, as $\tilde{\tilde{Q}}_{(\tilde{A})}^{\ T} = \tilde{\tilde{Q}}_{(\tilde{A}^T)}$, we obtain:

$$\dot{\tilde{\varepsilon}}_\delta = \dot{\delta}_a \frac{\widetilde{D_5}}{\sqrt{2}} + \dot{\delta}_b \frac{\widetilde{D_6}}{\sqrt{2}}$$

<div align="right">Eq. 152</div>

$$\dot{\tilde{\varepsilon}}_\delta = \left(\frac{c_0}{c}\right)^2 \left(\widetilde{D_5}\otimes\widetilde{D_5} + \widetilde{D_6}\otimes\widetilde{D_6}\right): \tilde{\tilde{Q}}_{(\widetilde{F_\pi}^T)}:\tilde{D}$$

6.3.11. Free energy and hyperelastic law

The obtained specific free energy is expressed as a function of the chosen invariants and strain variables:

$$\forall(\theta,\tilde{F})\quad \psi\left(\theta,\ln J, LnU_c, \widetilde{LnU_{ab}}, \tilde{\varepsilon}_\delta\right) = W_{Jc}(\theta, \ln J,\ LnUc) + W_{ab}\left(\theta, \widetilde{LnU_{ab}}\right) + W_\delta(\theta, \tilde{\varepsilon}_\delta)$$

<div align="right">Eq. 153</div>

The change of volume and the axial elongation strain modes are considered coupled and are described by one potential W_{Jc}.

We also have the thermodynamic fundamental relation Eq. 79:

$$\forall(\theta,\tilde{F}, d\theta, d\tilde{F})\quad \dot{\psi} = \tilde{\Sigma}:\tilde{D} - s\cdot\dot{\theta} - \varphi_1$$

Because of the hyperelasticity assumption, the intrinsic dissipation is null: $\varphi_1 = 0$

We consider a constant configuration, $\tilde{D} = \tilde{0}$, hence:

$$-s = \frac{\partial\psi}{\partial\theta}$$

Therefore, we obtain the equality:

$$\forall(\theta,\tilde{F},\tilde{D})$$

$$\tilde{\Sigma}:\tilde{D} = W'^J{}_{Jc}\cdot l\dot{n}J + W'^c{}_{Jc}\cdot Ln\dot{U}c + \widetilde{W'_{ab}}:\widetilde{Ln\dot{U}_{ab}} + \widetilde{W'}_\delta:\dot{\tilde{\varepsilon}}_\delta$$

<div align="right">Eq. 154</div>

Where $\quad \widetilde{W'}_a = \frac{\partial\widetilde{W_a}}{\partial\tilde{X}}(\theta,\tilde{X}); W'^x_a = \frac{\partial W_a}{\partial x}(\theta,x,y)\ and\ W'^y_a = \frac{\partial W_a}{\partial y}(\theta,x,y)$

Using Eq. 142, Eq. 143, Eq. 149 and Eq. 152, we derive:

$$\tilde{\Sigma}:\tilde{D} = \left\{W'^J{}_{Jc}\cdot\tilde{I} + W'^c{}_{Jc}\cdot\left(\frac{2}{3}\tilde{I} - \tilde{P}_c\right) + \widetilde{W'_{ab}}\right.$$

$$: \left[\tilde{\tilde{\gamma}}_{(\widetilde{U_\pi})}:\tilde{\tilde{Q}}_{(\widetilde{R_\pi}^T\cdot\widetilde{P_c})} - \frac{1}{2}(\widetilde{P_{c0}}\otimes\tilde{P}_c)\right] + \left(\frac{c_0}{c}\right)^2\widetilde{W'}_\delta$$

<div align="right">Eq. 155</div>

$$\left.: \left[(\widetilde{D_5}\otimes\widetilde{D_5} + \widetilde{D_6}\otimes\widetilde{D_6}):\tilde{\tilde{Q}}_{(\widetilde{F_\pi}^T)}\right]\right\}:\tilde{D}$$

$$\Leftrightarrow \tilde{\Sigma}:\tilde{D} = \left\{ W'^{J}{}_{Jc} \cdot \tilde{I} + W'^{c}{}_{Jc} \cdot \left((\overrightarrow{e_c} \otimes \overrightarrow{e_c}) - \frac{1}{3}\tilde{I}\right)\right.$$
$$+ \left[\tilde{\tilde{Q}}_{(\widetilde{P_c}.\widetilde{R_\pi})}:\tilde{\tilde{\gamma}}_{(\widetilde{U_\pi})} - \frac{1}{2}(\widetilde{P_c} \otimes \widetilde{P_{c0}})\right]:\widetilde{W'}_{ab}$$
$$\left. + \left(\frac{c_0}{c}\right)^2 \tilde{\tilde{Q}}_{(\widetilde{F_\pi})}:(\widetilde{D_5} \otimes \widetilde{D_5} + \widetilde{D_6} \otimes \widetilde{D_6}):\widetilde{W'}_\delta\right\}:\tilde{D}$$

Eq. 156

Because of their definitions, we assume that:

$$\widetilde{W'}_{ab} = \begin{bmatrix} W'_{ab11} & W'_{ab12} & 0 \\ W'_{ab12} & -W'_{ab11} & 0 \\ 0 & 0 & 0 \end{bmatrix}_{(\overrightarrow{e_{a0}},\overrightarrow{e_{b0}},\overrightarrow{e_{c0}})} = W'_{ab11}\sqrt{2}.\widetilde{D_2} + W'_{ab12}\sqrt{2}.\widetilde{D_4}$$

Eq. 157

$$\widetilde{W'}_\delta = \begin{bmatrix} 0 & 0 & W'_{\delta a} \\ 0 & 0 & W'_{\delta b} \\ W'_{\delta a} & W'_{\delta b} & 0 \end{bmatrix}_{(\overrightarrow{e_{a0}},\overrightarrow{e_{b0}},\overrightarrow{e_{c0}})} = W'_{\delta b}\sqrt{2}.\widetilde{D_5} + W'_{\delta b}\sqrt{2}.\widetilde{D_6}$$

Eq. 158

So,

$$(\widetilde{D_5} \otimes \widetilde{D_5} + \widetilde{D_6} \otimes \widetilde{D_6}):\widetilde{W'}_\delta = \widetilde{W'}_\delta$$

Eq. 159

And:

$$\left[\tilde{\tilde{Q}}_{(\widetilde{P_c}.\widetilde{R_\pi})}:\tilde{\tilde{\gamma}}_{(\widetilde{U_\pi})} - \frac{1}{2}(\widetilde{P_c} \otimes \widetilde{P_{c0}})\right]:\widetilde{W'}_{ab} = \tilde{\tilde{Q}}_{(\widetilde{R_\pi})}:\tilde{\tilde{\gamma}}_{(\widetilde{U_\pi})}:\widetilde{W'}_{ab}$$

Eq. 160

See appendix E (p.210) for the proof of this last equation.

Then,

$$\tilde{\Sigma}:\tilde{D} = \left\{ W'^{J}{}_{Jc} \cdot \tilde{I} + W'^{c}{}_{Jc} \cdot \left((\overrightarrow{e_c} \otimes \overrightarrow{e_c}) - \frac{1}{3}\tilde{I}\right) + \tilde{\tilde{Q}}_{(\widetilde{R_\pi})}:\tilde{\tilde{\gamma}}_{(\widetilde{U_\pi})}:\widetilde{W'}_{ab}\right.$$
$$\left. + \left(\frac{c_0}{c}\right)^2 \tilde{\tilde{Q}}_{(\widetilde{F_\pi})}:\widetilde{W'}_\delta\right\}:\tilde{D}$$

Eq. 161

$\forall \tilde{D}$ *symmetric*,

$$\left\{\tilde{\Sigma} - W'^{J}{}_{Jc} \cdot \tilde{I} - W'^{c}{}_{Jc} \cdot \left((\overrightarrow{e_c} \otimes \overrightarrow{e_c}) - \frac{1}{3}\tilde{I}\right) - \tilde{\tilde{Q}}_{(\widetilde{R_\pi})}:\tilde{\tilde{\gamma}}_{(\widetilde{U_\pi})}:\widetilde{W'}_{ab}\right.$$
$$\left. - \left(\frac{c_0}{c}\right)^2 \tilde{\tilde{Q}}_{(\widetilde{F_\pi})}:\widetilde{W'}_\delta\right\}:\tilde{D} = 0$$

Eq. 162

So, the following second-order tensor:

$$\tilde{\Sigma} - W'^{J}{}_{Jc} \cdot \tilde{I} - W'^{c}{}_{Jc} \cdot \left((\overrightarrow{e_c} \otimes \overrightarrow{e_c}) - \frac{1}{3}\tilde{I}\right) - \tilde{\tilde{Q}}_{(\widetilde{R_\pi})}:\tilde{\tilde{\gamma}}_{(\widetilde{U_\pi})}:\widetilde{W'}_{ab}$$
$$- \left(\frac{c_0}{c}\right)^2 \tilde{\tilde{Q}}_{(\widetilde{F_\pi})}:\widetilde{W'}_\delta$$

Eq. 163

is skew-symmetric; because all tensors in this expression are also symmetric, this leads to

$$\tilde{\Sigma} - W'^{J}{}_{Jc} \cdot \tilde{I} - W'^{c}{}_{Jc} \cdot \left((\overrightarrow{e_c} \otimes \overrightarrow{e_c}) - \frac{1}{3}\tilde{I}\right) - \tilde{\tilde{Q}}_{(\widetilde{R_\pi})}:\tilde{\tilde{\gamma}}_{(\widetilde{U_\pi})}:\widetilde{W'}_{ab}$$
$$- \left(\frac{c_0}{c}\right)^2 \tilde{\tilde{Q}}_{(\widetilde{F_\pi})}:\widetilde{W'}_\delta = \tilde{0}$$

Eq. 164

Finally, we obtain:

$$\widetilde{\Sigma} = W'^J{}_{Jc}\tilde{I} + W'^c{}_{Jc}\left((\overrightarrow{e_c} \otimes \overrightarrow{e_c}) - \frac{1}{3}\tilde{I}\right) + \widetilde{R_\pi} \cdot \left(\tilde{\gamma}_{(\widetilde{U_\pi})} : \widetilde{W'}_{ab}\right) \cdot \widetilde{R_\pi}{}^T + \left(\frac{c_0}{c}\right)^2 \widetilde{F_\pi} \cdot \widetilde{W'}_\delta \cdot \widetilde{F_\pi}{}^T \qquad \textit{Eq. 165}$$

In function of the Cauchy stress, this expression becomes:

$$\widetilde{R_\pi}{}^T \cdot \tilde{T} \cdot \widetilde{R_\pi} = \frac{1}{J}[\rho_0 W'^J{}_{Jc}\tilde{I} + \rho_0 W'^c{}_{Jc}\left((\overrightarrow{e_{c0}} \otimes \overrightarrow{e_{c0}}) - \frac{1}{3}\tilde{I}\right)$$

$$+ \tilde{\gamma}_{(\widetilde{U_{ab}})} : \rho_0\widetilde{W'}_{ab} + \left(\frac{c_0}{c}\right)^2 \widetilde{U_\pi} \cdot \rho_0 \widetilde{W'}_\delta \cdot \widetilde{U_\pi}] \qquad \textit{Eq. 166}$$

The expressions of the potential associated to each strain mode: $W_{Jc}(\theta, \ln J, LnUc)$, $W_{ab}(\theta, \widetilde{LnU_{ab}})$, $W_\delta(\theta, \widetilde{\varepsilon_\delta})$ have to be identified using dedicated experimental tests.

6.4. Implementation and verification (Appendix F)

The implementation of a constitutive behaviour law on Abaqus/Standard (Implicit algorithm) was performed by using a sub-routine called UMAT, written in FORTRAN. This sub-routine must allow the stress state of the material to be determined as a function of the imposed strain.

This sub-routine must contain the linear application or fourth-order tensor $\tilde{J}$ defined, for any strain rate tensor $\widetilde{D}$ as Eq. 166 was calculated.

$$\overset{\circ}{J \cdot \tilde{T}} = J \cdot \tilde{J} : \widetilde{D} \qquad \textit{Eq. 167}$$

The notation $\overset{\circ}{J \cdot \tilde{T}}$ represents the Jaumann objective rate of the Kirchhoff stress tensor, i.e. the volume change times the Cauchy stress tensor. Hence, the Jaumann rate of the stress-strain law Eq. 166 was calculated.

During this PhD, considerable time has been devoted to writing this sub-routine in FORTRAN. The first implementation aimed at validating the law with simple potentials and a first set of parameters, before adding the potential identified experimentally on polyamide 6 rope-yarns and the associated parameters. Hence, the first implementation of the law was done by using linear functions for the conjugated stresses $W'^J{}_{Jc}$, $W'^c{}_{Jc}$, $\widetilde{W'}_{ab}$ and $\widetilde{W'}_\delta$. Hence, the associated potentials were chosen to be quadratic.

To check that the implementation was correct, simulations using only one three-dimensional solid (C3D8) cubic element were performed. Each deformation mode was tested by using a dedicated loading. This work is presented in appendix F (p.212).

Once the implementation of the law is validated with simple linear potentials, we can define more complex potential for each strain mode.

6.5. Strain energy potential for each strain mode

The proposed anisotropic law, Eq. 166, is defined by three different potentials $W_{Jc}(\theta, \ln J, LnUc)$, $W_{ab}(\theta, \widetilde{LnU_{ab}})$, $W_\delta(\theta, \widetilde{\varepsilon_\delta})$. The next sub-section described the chosen hyperelastic potentials for this study. These potentials should be changed in future work to add dissipation in the shear strain modes and to add visco-elasto-plasticity.

6.5.1. Axial elongation and change-of volume strain modes

The change of volume and the axial elongation strain modes are considered coupled and are described by one potential W_{Jc}. We have to choose a function to define the W_{Jc} potential. This potential has to be convex, for that we will try to respect the following condition: its hessian matrix has to be positive.

The hessian matrix is defined as:

$$\rho_0 \begin{bmatrix} W''^J & W''^{Jc} \\ W''^{Jc} & W''^c \end{bmatrix}$$

Eq. 168

It is positive if: $W''^J > 0$ and $W''^J W''^c - (W''^{Jc})^2 > 0$

Eq. 169

We will consider: $W'^J_{Jc}(0,0) = 0$ and $W'^c_{Jc}(0,0) = 0$.

We propose the following definition for W_{Jc} potential:

$$\rho_0 W_{Jc}(\ln J, LnU_c) = a \cdot (\ln J)^2 + b \cdot \ln J \cdot LnU_c + f(LnU_c)$$

Eq. 170

Hence,

$$W'^J_{Jc} = \frac{\partial W_{Jc}}{\partial \ln J} = 2 \cdot a \cdot \ln J + b \cdot LnU_c$$

Eq. 171

$$W'^c_{Jc} = \frac{\partial W_{Jc}}{\partial LnU_c} = b \cdot \ln J + f'(LnU_c)$$

Eq. 172

In this potential,

- $a \cdot \ln J^2$: describes the behaviour for the change of volume. It seems difficult to propose change-of-volume experimental tests for identifying this behaviour for this type of multi-scale material. It would require to develop a hydrostatic test that allows to isolate the rope-yarns from the environment as it is not a bulk material; hence the surrounding environment may penetrate the rope-yarns and modify its change-of-volume behaviour during the test.
  Hence, we propose a simple linear behaviour for this deformation mode characterized by a constant modulus a. A bulk modulus K may be defined as:

$$K = \frac{Tr(\tilde{T})}{3 \ln J}$$

Eq. 173

  Then, it is related to the parameter a following:

$$Tr(\tilde{T}) = \frac{3}{J} \rho_0 W'^J_{Jc}(\ln J, LnU_c = 0) \quad \text{hence } K = \frac{2a}{J} \sim 2a$$

The bulk modulus K is the slope of the curve $Tr(\tilde{T}) - 3 \ln J$ for small strains. At small strains, the change of volume is small and $J \sim 1$. Hence, we assume: $K = \frac{2a}{J} \sim 2a$.

As the bulk modulus is complicated to measure, we considered the bulk modulus of a bundle of rope-yarns is equal to the bulk modulus of polyamide 6 bulk material in the present work. The bulk modulus of polyamide 6 and polyamide 66 bulk material have been measured between 3GPa and 6GPa (Kanzenbach et al., 2017; Péron et al., 2018). We first considered a bulk modulus of $K_{PA6} = 6000\ MPa$ hence, we took $a = 3000\ MPa$. In the future, more time should be taken to test the impact of the bulk modulus value taken as it might not be the same for the fibres bundles and the bulk material.

- $b \cdot \ln J \cdot LnU_c$: describes the coupling between the change of volume and the axial elongation strain modes. It is characterized by a constant modulus b.
- $f(LnU_c)$: describes the axial elongation behaviour. Several functions were tested. Finally, the following definition was chosen to fit the tensile experimental results:

$$f(LnU_c) = c \cdot LnU_c^2 + d \cdot LnU_c^3 \qquad \textit{Eq. 174}$$

Four parameters (a, b, c and d) are needed to define the behaviour in axial elongation and change of volume. We already have fixed a. Thus, three parameters have to be identified using an experimental campaign.

In the next section the definition for the potential defining the shear strain modes will be selected.

6.5.2. Longitudinal and transversal shear strain modes

A direct experimental characterization of the longitudinal and transversal shear strain parameters, defined respectively by the two energy potentials $W_\delta(\theta, \widetilde{\varepsilon_\delta})$ and $W_{ab}(\theta, \widetilde{LnU_{ab}})$, is difficult to perform. Hence, for simplicity, it has been assumed that the axial and transversal shear stiffnesses are constant which leads to the following quadratic strain energy functions:

$$\rho_0 W_{ab}(\theta, \widetilde{LnU_{ab}}) = G_{ab} \cdot \left(\widetilde{LnU_{ab}} : \widetilde{LnU_{ab}}\right) \qquad \textit{Eq. 175}$$

$$\rho_0 W_\delta(\theta, \widetilde{\varepsilon_\delta}) = G_\delta \cdot (\widetilde{\varepsilon_\delta} : \widetilde{\varepsilon_\delta}) \qquad \textit{Eq. 176}$$

We have defined the hyperelastic potentials we will use for this study. Next section summarizes the key aspects of the proposed law and the chosen potentials.

6.5.3. Conclusion of the proposed anisotropic law: the FiBuLa law

This section summarizes the proposed anisotropic law for a bundle of rope-yarns. This law will be called the "FiBuLa law" hereafter (for Fibre Bundle Law). We adopted the following model choices:

- A bundle of rope-yarns is considered as a homogenous continuum
- It is a hyperelastic material; the intrinsic dissipation is supposed null
- A complete system of variables is;
  - The temperature θ
  - The change of volume, $\ln J$, defined by Eq. 129
  - The axial deformation of the rope-yarns, LnU_c, defined by Eq. 130
  - The transversal shear of the rope-yarns, $\widetilde{Ln\,U_{ab}}$, defined by Eq. 131
  - The longitudinal shear of the rope-yarns defined, $\widetilde{\varepsilon_\delta}$, by Eq. 132
- The specific free energy is defined by Eq. 153:

$$\forall(\theta, \tilde{F})$$
$$\psi(\theta, \ln J, LnU_c, \widetilde{LnU_{ab}}, \widetilde{\varepsilon_\delta}) = W_{Jc}(\theta, \ln J, LnUc) + W_{ab}(\theta, \widetilde{LnU_{ab}}) + W_\delta(\theta, \widetilde{\varepsilon_\delta})$$

The stress-strain law relation is defined following Eq. 166:

$$\widetilde{R_\pi}^T \cdot \tilde{T} \cdot \widetilde{R_\pi} = \frac{1}{J}[\rho_0 W'^J{}_{Jc}\tilde{I} + \rho_0 W'^c{}_{Jc}\left((\overrightarrow{e_{c0}} \otimes \overrightarrow{e_{c0}}) - \frac{1}{3}\tilde{I}\right) + \widetilde{\tilde{\gamma}}_{(\widetilde{U_{ab}})}$$
$$: \rho_0 \widetilde{W'_{ab}} + \left(\frac{c_0}{c}\right)^2 \widetilde{U_\pi} \cdot \rho_0 \widetilde{W'}_\delta \cdot \widetilde{U_\pi}]$$

The chosen potentials for the first study are defined by Eq. 170, Eq. 174, Eq. 175 and Eq. 176:

$$\rho_0 W_{Jc}(\ln J, LnU_c) = a \cdot \ln J^2 + b \cdot \ln J \cdot LnU_c + c \cdot LnU_c^2 + d \cdot LnU_c{}^3$$

$$\rho_0 W_{ab}(\theta, \widetilde{LnU_{ab}}) = G_{ab} \cdot (\widetilde{LnU_{ab}} : \widetilde{LnU_{ab}})$$

$$\rho_0 W_\delta(\theta, \widetilde{\varepsilon_\delta}) = G_\delta \cdot (\widetilde{\varepsilon_\delta} : \widetilde{\varepsilon_\delta})$$

We use the Cauchy Stress for the expression of the stress-strain relation of this law, and not the specific stress in N/tex, because we consider that the bundle of rope-yarns is a homogeneous material. Hence, we don't need the specific stress that considers the construction effect. Also, the model proposed in this study aims at describing the section's geometries. Hence, in our experimental work of identification, we will have to measure the section of the rope-yarns. Therefore, the advantage of the specific stress, that consists in not measuring the section in tensile loading, is lost. Therefore, working with the Cauchy stress is easier in this case and also has the advantage of being more usual in material engineering.

Next section presents the identification of the parameters of the chosen potentials.

6.6. Identification of the FiBuLa law

The proposed anisotropic law, Eq. 166, is defined by three different potentials $W_{Jc}(\theta, \ln J, LnUc)$, $W_{ab}(\theta, \widetilde{LnU_{ab}})$, $W_\delta(\theta, \widetilde{\varepsilon_\delta})$ defined by Eq. 170, Eq. 174, Eq. 175 and Eq. 176. These potentials must be identified using dedicated experimental tests for each strain modes (Table 6.2). We aim at understanding the behaviour of a wet (or immersed) polyamide 6 sub-rope during a cyclic loading, similar to a self-heating test procedure. Hence, if possible, these tests should be done in water. The scale we chose to model is a bundle of rope-yarns. Hence, the experimental tests must be done on rope-yarn and bundles of rope-yarns (for example, on strands).

The next section presents two different experimental tests designed during this PhD. The first one aims at identifying the rope-yarns behaviour for an axial elongation coupled with a change of volume (similar to a "Poisson effect"). The second one aims at identifying their behaviour for the shear strain modes.

Table 6.2 – Final expression of the potential to identify and proposed method of identification

Potential	Expression	Number of parameters to identify	Identification method	Experimental test	Experiment measures
$W_{Jc}(\theta, \ln J, LnUc)$	$a \cdot \ln J^2 + b \cdot \ln J \cdot LnU_c + c \cdot LnU_c^2 + d \cdot LnU_c{}^3$	4	Direct	Tensile cyclic test on a rope-yarn in water (Chap 2 section 2.5.4.5)	Axial and diametral strains
$W_{ab}(\theta, \widetilde{LnU_{ab}})$	$G_{ab} \cdot (\widetilde{LnU_{ab}} : \widetilde{LnU_{ab}})$	1	Indirect	Diametral compression test on strand (Chap 2 section 2.5.4.6)	Geometric properties of the contact section
$W_\delta(\theta, \widetilde{\varepsilon_\delta})$	$G_\delta \cdot (\widetilde{\varepsilon_\delta} : \widetilde{\varepsilon_\delta})$	1	Indirect	Diametral compression test on strand (Chap 2 section 2.5.4.6)	Geometric properties of the contact section

6.6.1. Identification of the behaviour in axial elongation

To perform this identification, we first need to express the stress-strain law during a uniaxial test. Then, uniaxial tensile tests on rope-yarn will be performed and the equations obtained in the first section will be used for the identification.

6.6.1.1. Expression of the law in a uniaxial tensile test

We first express the stress-strain law, Eq. 166, during a uniaxial tensile test. In a tensile test, we can demonstrate that $\widetilde{G_\pi} = \tilde{I}$ and $\widetilde{U_{ab}} = \tilde{I}$.

We will consider the stresses are null at null strains, which can be expressed as:

$$\widetilde{W'_{ab}}\left(\widetilde{LnU_{ab}} = \tilde{0}\right) = \tilde{0} \text{ and } \widetilde{W'}_\delta(\tilde{\varepsilon}_\delta = \tilde{0}) = \tilde{0}$$

Hence, using Eq. 166, the stress-strain law can be written, during a tensile test:

$$\widetilde{R_\pi}^T \cdot \tilde{T} \cdot \widetilde{R_\pi} = \frac{1}{J}[\rho_0 W'^J{}_{Jc}\tilde{I} + \rho_0 W'^c{}_{Jc}\left((\overrightarrow{e_{c0}} \otimes \overrightarrow{e_{c0}}) - \frac{1}{3}\tilde{I}\right)]$$

<div align="right">Eq. 177</div>

We use the Kirchhoff stress:

$$J\tilde{T} = \rho_0 W'^J{}_{Jc}\tilde{I} + \rho_0 W'^c{}_{Jc}\left((\overrightarrow{e_c} \otimes \overrightarrow{e_c}) - \frac{1}{3}\tilde{I}\right)$$

<div align="right">Eq. 178</div>

Note that, in this case, vector $\overrightarrow{e_{c0}}$ is equal to vector $\overrightarrow{e_c}$.

<div align="right">Eq. 179</div>

We define the section of a rope-yarn at a time t by: $S_t = \frac{\pi D^2}{4}$

Then, T is the applied Cauchy stress equal to: $T = \frac{F}{S_t}$

<div align="right">Eq. 180</div>

Eq. 178 can therefore be written based on $(\overrightarrow{e_{a0}}, \overrightarrow{e_{b0}}, \overrightarrow{e_{c0}})$:

$$J\begin{bmatrix} 0 & 0 & 0 \\ 0 & 0 & 0 \\ 0 & 0 & T \end{bmatrix}_{(\overrightarrow{e_{a0}},\overrightarrow{e_{b0}},\overrightarrow{e_{c0}})} = \rho_0 \begin{bmatrix} W'^J{}_{Jc} - \dfrac{W'^c{}_{Jc}}{3} & 0 & 0 \\ 0 & W'^J{}_{Jc} - \dfrac{W'^c{}_{Jc}}{3} & 0 \\ 0 & 0 & W'^J{}_{Jc} + \dfrac{2 \cdot W'^c{}_{Jc}}{3} \end{bmatrix}_{(\overrightarrow{e_{a0}},\overrightarrow{e_{b0}},\overrightarrow{e_{c0}})}$$

<div align="right">Eq. 181</div>

Hence, we have to resolve the two following equations:

$$3 \cdot W'^J{}_{Jc}(\ln J, LnU_c) = W'^c{}_{Jc}(\ln J, LnU_c)$$

<div align="right">Eq. 182</div>

$$JT = \rho_0 W'^c{}_{Jc}(\ln J, LnU_c)$$

<div align="right">Eq. 183</div>

Using Eq. 171 and Eq. 172, Eq. 182 and Eq. 183 respectively become:

$$\ln J = \frac{f'(LnU_c) - 3bLnU_c}{6a - b} = g_1(LnU_c)$$

<div align="right">Eq. 184</div>

$$JT = \frac{6a}{6a - b}f'(LnU_c) - \frac{3b^2}{6a - b}LnU_c = g_2(LnU_c)$$

<div align="right">Eq. 185</div>

Four parameters (a, b, c and d) are needed to define the behaviour in axial elongation and change of volume. We have already fixed a. Thus, three parameters have to be identified using the experimental results. The function to minimize is the following:

$$\sqrt{\frac{\Sigma_i(JT_{exp}[i] - g_1(LnU_{c\,exp}[i]))^2}{(JT_{exp})^2} + \frac{\Sigma_i(\ln J_{exp}[i] - g_2(LnU_{c\,exp}[i]))^2}{(\ln J_{exp})^2}}$$

<div align="right">Eq. 186</div>

6.6.1.2. Experimental results and identification of the potential for the axial elongation and change of volume invariants

An experimental set-up has been developed to perform tensile cyclic tests on rope-yarn in water. Three cyclic tensile tests on rope-yarns were performed in water, following the experimental procedure described in chapter 2 section 2.5.4.5. These cyclic tests were performed after the bedding-in procedure also described in chapter 2 section 2.5.4.5. The initial state of the rope-yarn is taken after the bedding-in, under a tension of 2%MBL. The loading path chosen is similar to the loading path of a self-heating test (several blocks with increasing maximal load) as we want to improve our understanding of self-heating tests (presented in chapter 5 section 5.5). An example of the loading procedure is presented in Figure 6.11.
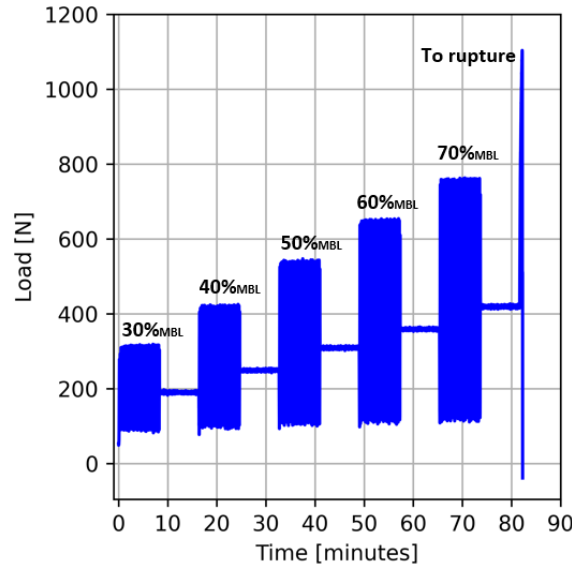
Figure 6.11 - Loading path of the tensile cyclic test on rope-yarns in water. Load [N] versus time [minutes]

During these tests, two strains were measured: the axial strain (in the rope-yarns axis direction) and the transversal strain (in the transverse section) (Figure 6.12).

These tensile tests allow the stress-strain state to be defined by Eq. 181. Hence, we have to minimize Eq. 186, which depends on the change-of-volume invariant and the axial elongation invariant, to identify the free energy potential $W_{Jc}(\theta, \ln J, LnUc)$ parameters. Therefore, we need to relate these invariants to the measured axial and diametral logarithm strains.
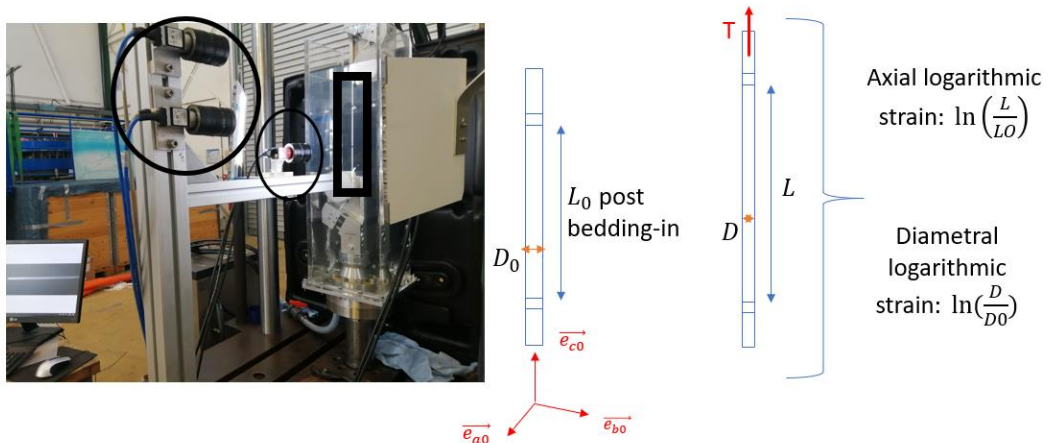
Figure 6.12 - Experimental set-up for cyclic tests in water with a plane-diopter tank and three cameras: two cameras for axial strain measurement; one camera for transversal strain measurement. Scheme of the measurements

During a tensile test, the transformation $\tilde{F}$ is defined, in the basis $(\overrightarrow{e_{a0}}, \overrightarrow{e_{b0}}, \overrightarrow{e_{c0}})$ of the rope-yarn, by:

$$\tilde{F} = \begin{bmatrix} \dfrac{D}{D_0} & 0 & 0 \\ 0 & \dfrac{D}{D_0} & 0 \\ 0 & 0 & \dfrac{L}{L_0} \end{bmatrix}_{(\overrightarrow{e_{a0}}, \overrightarrow{e_{b0}}, \overrightarrow{e_{c0}})} = \begin{bmatrix} \dfrac{a}{a_0} & 0 & 0 \\ 0 & \dfrac{b}{b_0} & 0 \\ 0 & 0 & \dfrac{c}{c_0} \end{bmatrix}_{(\overrightarrow{e_{a0}}, \overrightarrow{e_{b0}}, \overrightarrow{e_{c0}})} \qquad \textit{Eq. 187}$$

The change of volume invariant is defined by Eq. 129 which leads to:

$$\ln J = \ln(\det \tilde{F}) \Leftrightarrow \ln J = \ln(\frac{L \cdot D^2}{L_0 \cdot D_0^{\;2}}) = 2 \cdot \ln\left(\frac{D}{D_0}\right) + \ln(\frac{L}{L_0}) \qquad \textit{Eq. 188}$$

The axial elongation invariant is defined by Eq. 130 which leads to:

$$\mathrm{Ln}U_c = \ln(\frac{1}{\sqrt[3]{J}}\frac{c}{c_0}) \Leftrightarrow \mathrm{Ln}U_c = \frac{2}{3}[\ln\left(\frac{L}{L_0}\right) - \ln(\frac{D}{D_0})] \qquad \textit{Eq. 189}$$

The mean results of the three performed tests were calculated and used for the identification. The Kirchhoff stress versus the axial elongation invariant for the stabilized cycles is plotted on Figure 6.13-left (using Eq. 180 and Eq. 189). The change of volume invariant is plotted versus the axial elongation invariant for the stabilized cycles on Figure 6.13-right (using Eq. 188 and Eq. 189). The measurement of the transversal strain directly depends on the resolution of the camera used (number of pixels). We observe, in Figure 6.13-right, that the measurement is not as precise as desired, because of the camera used, but it is sufficient for a first identification. We optimize the function Eq. 186 using a Sequential Least Squares Programming in python and the parameters obtained are:

$a = 3000\ MPa, b = 3459\ MPa, c = 1371\ MPa\ and\ d = 3878\ MPa$

Figure 6.13-left, and right, also plots the fits obtained using this set of parameters for Eq. 184 and Eq. 185.
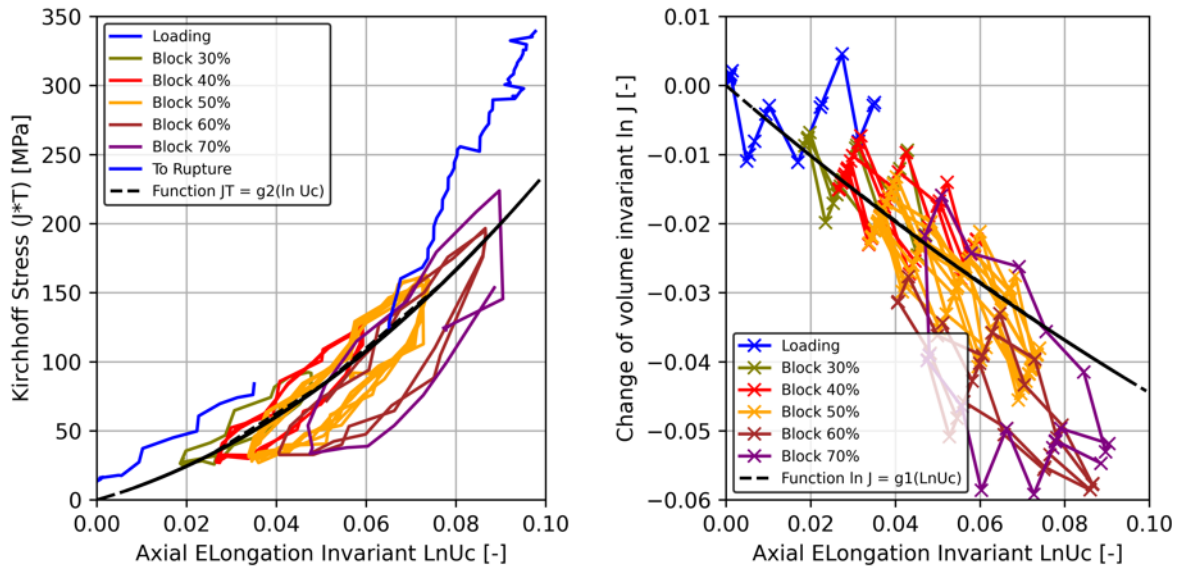
Figure 6.13 – Comparison of the modelled and the experimental results of a tensile cyclic test on rope-yarns in water for the stabilized cycles. Left: Kirchhoff Stress [MPa] versus axial elongation invariant [-]. Right: Change of volume invariant [-] versus axial elongation invariant [-]

In Figure 6.13-left, the fit obtained of the Kirchhoff stress versus LnU_c is compared to the stabilized cycles of each block. This fit provides a good fit of the tendency for the stabilized cycles. The hysteresis is not represented as the chosen law is hyperelastic. The last load to rupture is not accurately described. Also, the reference state in the experimental test is taken after the bedding-in procedure at 2%MBL. Hence, the experimental test starts at a null axial elongation strain for a load around 10 MPa (2%MBL). On the contrary, the simulated stress is null for a null axial elongation because of the hypothesis of null stresses for null strains considered for the modelling.

In Figure 6.13-right, the fit of the volume change invariant versus the axial elongation invariant is compared to the stabilized cycles of each block. We observe the volume decreases when the tension elongation increases. This change is opposite to the one in the classical case of bulk materials (metallic, polymer), where the volume increases in tension, i.e. a Poisson ratio below 0.5. This unusual volume behaviour in tension is probably due to the particular fibre arrangement of these rope-yarns and strands; there are a lot of air gaps between the fibres at zero tension and these will probably be closed when the tension force increases. This unusual behaviour is difficult to model and partly explains the need to develop adapted model for this type of materials.

In Figure 6.13-right, we observe the second fit is more approximate. The last cycles are not well described by the fit. We did not find any definition of the potential that allowed a better fit and respected the constraint for the Hessian matrix to be positive. However, the tendency predicted by the simulation remains acceptable for a first identification.

Two main aspects of this identification could be improved in future work:

- The measurement of the transversal strain could be improved by the use of a camera with a higher resolution.
- Irreversibility should be added to this hyperelastic law to allow a description of the history of loading effect. Hence a hyperelastic potential is too limited. We could choose a rheological law (such as the POLYAMOOR law, described chapter 3), that includes time-dependent parameters to describe the axial elongation and the change of volume strain modes. This would add a dissipation due to the material at the rope-yarns scale for these strain modes.

The parameters of the axial elongation and change-of-volume behaviours have been identified for the chosen hyperelastic potential. The next section proposes an identification of the shear strain modes.

6.6.2. Identification of the shear strain modes

For this identification, an indirect method has been used. For this exploratory study, both an original experimental test and a simulation of this test have been set-up.

6.6.2.1. Experimental results

For this identification, an original experimental test, described in chapter 2 section 2.5.4.6, has been designed. The strand is placed around a rod and rollers such that it will be in diametral compression on the central rod during a tensile test. A tension is applied in the strand axis direction (Figure 6.14). The tensile test is performed after a bedding-in procedure. The aim is to induce large deformations in the two shear modes (transversal and longitudinal). This tensile test around a "3-rod" device leads to crushing of the strand cross-section, hence it led to an important deformation in the transverse section of the strand ($\widetilde{LnU_{ab}}$).

This crush, added to the tensile loading, is characterized by some changes in orientation of the rope-yarns and therefore by some sliding of the rope-yarns on one another along their axis direction ($\widetilde{\varepsilon}_\delta$).

We used a 3D scanner to obtain 3D images of the external surface of the cross-section of the strand during the contact with the central rod (Figure 6.14). For each scan, we used the CAD software tool CATIA to measure the width of the contact area and the height of the contact cross-section of the strand (Figure 6.14).
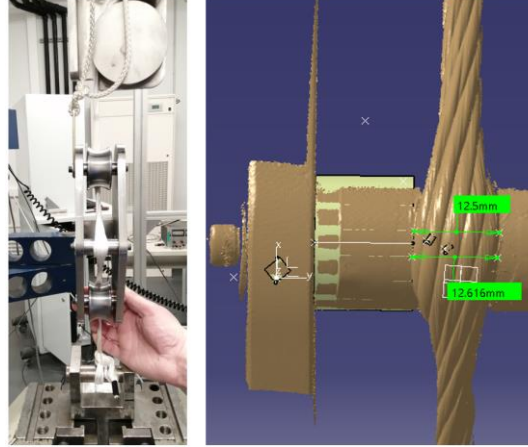
Figure 6.14 – Left: Experimental set-up for the diametral compression of a strand. Right: 3D scan of the contact area and treatment with CATIA software

The obtained width and height versus tensile load (force measured by the load cell) are plotted on Figure 6.15-right and left.
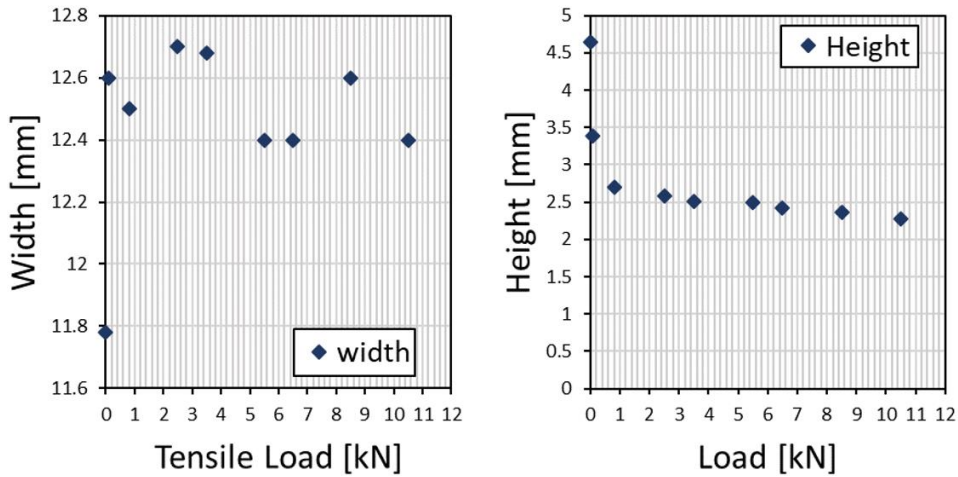
Figure 6.15 – Experimental result of the diametral compression test. Left: Measured width [mm] versus tensile load [kN]. Right: Measured height [mm] versus tensile load [kN]

We observe that a stable cross-section is reached rapidly at the contact area. The variation of the width (Figure 6.15-left) highlights the difficulty to have a precise measure on the 3D image. We will consider a stabilized width and height respectively of 12.5 mm and 2.3 mm.

For this exploratory study, we will keep these first experimental results. However, this experimental work, and the procedure used for the measurements, could be improved to increase the reliability of the results. Also, this experiment could be adapted to allow a wet strand to be tested.

6.6.2.2. Simulation and inverse identification

For the identification of the longitudinal and transversal shear strain parameters, an inverse method is set-up using finite element analysis. We perform a quasi-static analysis using *Abaqus*™ software and the proposed FiBuLa law. In the initial step of the simulation, the strand is represented by a straight axisymmetric cylinder. The initial state of the strand is taken after the bedding-in, under 2%MBL tension. The initial diameter, measured in the reference state is $D_0 = 6.36mm$. The length of the strand is $L = 500\ mm$ (Figure 6.16). The twist angle of the rope-yarns at the surface of the strand, after the bedding-in, is $\alpha = 22°$. The twist angle of the rope-yarns inside the strand can be calculated using the measured rope-yarns twist angle at the surface of the strand (Eq. 84). The rope-yarns are Z-twisted to form the strand. The initial configuration of the vectors $\overrightarrow{e_{a0}}, \overrightarrow{e_{b0}}$ and $\overrightarrow{e_{c0}}$ is represented in Figure 6.16 ($\overrightarrow{e_{c0}}$ follows the direction of the rope-yarns axis in the initial configuration).
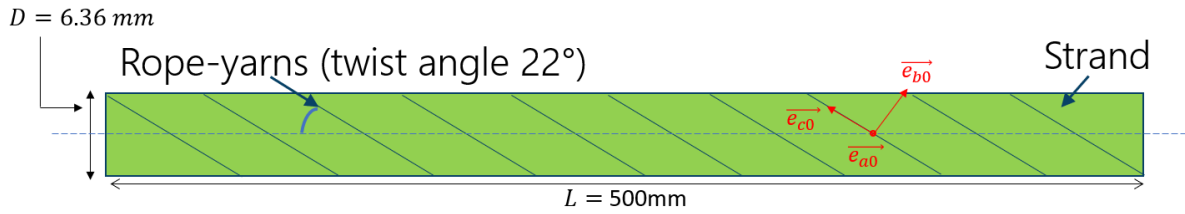
Figure 6.16 – Reference state of the strand, taken after the bedding-in, for the initial step of the calculation.

The "3-rod" device is modelled by three analytical surfaces that are fixed during the simulation. The potential W_{Jc}, defined by Eq. 170 and Eq. 174, and the parameters a, b, c and d identified in section 6.6.1, are used. The mesh was chosen to allow several simulations to be done without being too time-consuming. The mesh was composed of 22 000 8-node linear brick (cubic) C3D8 elements.
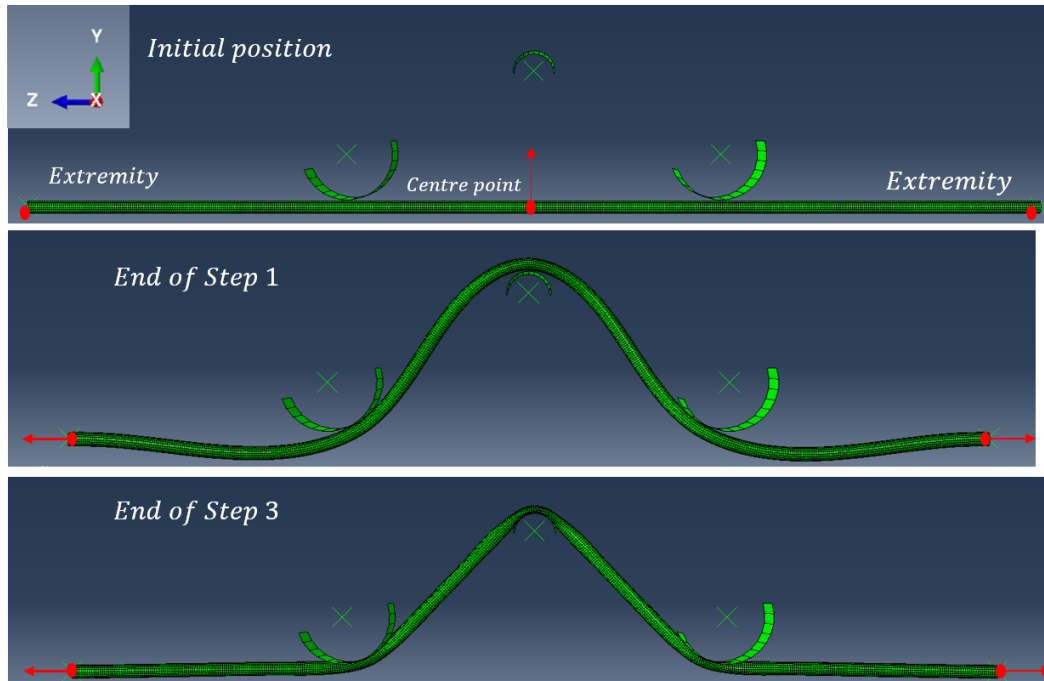
Figure 6.17 – Simulation of the diametral compression test: three steps

The simulation is performed using *Abaqus*/Static with a classical quasi-static analysis. It is divided into three steps (Figure 6.17):

- Step 1: The strand is placed around the "3-rod" device. This step is controlled by displacement. The centre point of the strand is piloted in the $\vec{y}$ direction and fixed for the other degrees of freedom. The two extremities are free along the $\vec{z}$ axis and fixed for the other degrees of freedom. Contacts between the two rollers (bottom part of the "3-rod") and the strand are activated in this step but no contact is defined between the centre rod and the strand.
- Step 2: The contact between the centre rod and the strand is added. A contact stabilization is used to allow the convergence. A contact stabilization is a viscous damping that is applied between the contact pairs. This stabilization is only for the nodes defined in the contact surfaces. A contact stabilization allows the instabilities to be overcome and helps to get a converged simulation. A displacement along $\vec{z}$ is imposed on both extremities of the strand to simulate a tension on the strand. All the other degrees of freedom of the extremities are fixed.
- Step 3: The stabilization of the contact is removed. The displacement imposed on both sides of the strand is increased. The other boundary conditions are kept identical.

Unfortunately, we did not manage to get a converged simulation above a calculated tensile load of 400N at the extremities. More time would have been needed to improve the simulation and increase the convergence. However, it is difficult to obtain realistic results for the simulation of synthetic fibre rope material during this type of test (Bain, 2020). The results are, qualitatively, in accordance with the experimental results as illustrated in Figure 6.18. It is already a success to manage to obtain this satisfactory geometry in this first simulation.
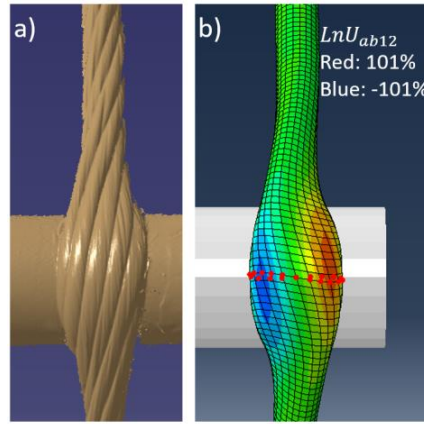
Figure 6.18 – Comparison of the obtained experimental cross-section and simulated cross-section. The aim is to obtain the same cross-sections.

Figure 6.19 presents colour maps of the cross section during the final increment of time of the simulation. These colour maps represent the transversal and longitudinal shear strain invariants. We observe that the transverse shear strain reached 100% and -100% (Figure 6.19-a and b). The axial shear strain in the plane bc reached 64%, and the axial shear strain in the plane ac reached 34% (Figure 6.19-c and d). Hence, we managed to reach high shear strain values even if we did not exceed 400N tensile load. Experimentally, at 400N, the geometry of the cross-section is already very close to the final stable cross-section.

For these reasons, we chose to work with this first simulation to identify G_{ab} and G_{δ}. As we aimed to describe accurately the stable cross-section, it was chosen, in the present study, to only measure the width and height of the cross-section in the simulation for the last increment of time (400 N tensile load) and to compare those values with the experimental results at 400N.
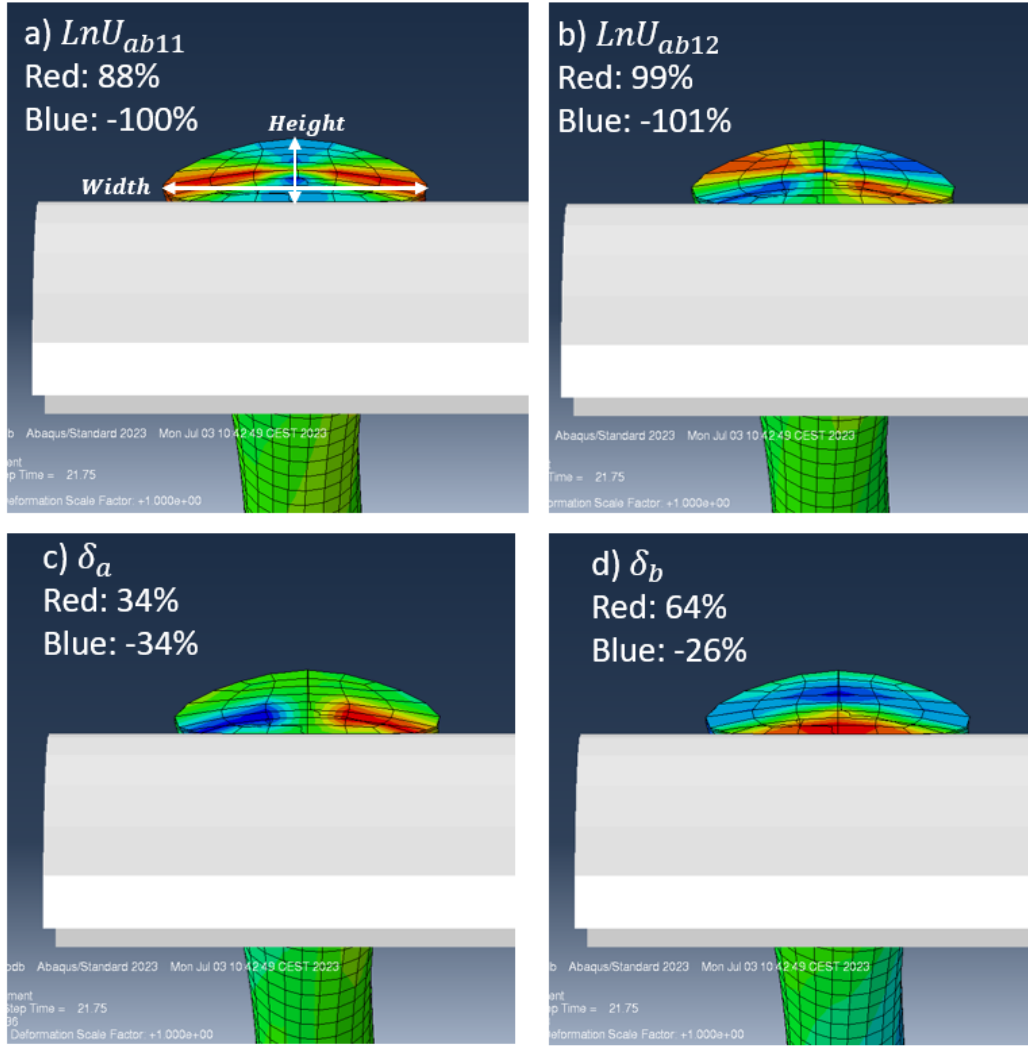
Figure 6.19 - Colour maps of the cross section during the final increment of time. a) Transversal shear strain invariant LnU_{ab11}***; measurement of the height and width; b) Transversal shear strain invariant*** LnU_{ab12}***; c) longitudinal shear strain invariant (ac plane); d) longitudinal shear strain invariant (bc plan)***

We chose to perform a manual optimization, of the parameters G_{ab} and G_δ, in order to better understand the model response and its sensitivity to the parameters. The function chosen to optimise the parameters was based on the shape factor of the final section defined by the ratio of the height over the width. The function to minimize has the following expression:

$$abs\left[\left(\frac{height}{width}\right)_{num} - \left(\frac{height}{width}\right)_{exp}\right] \qquad \textit{Eq. 190}$$

We chose a scan interval, for the parameters G_{ab} and G_δ, between [0.0015 MPa; 10 MPa]. The initial values taken for the parameters were the extrema. Then, we fixed one parameter and changed the other and the other way around.

In future work, the simulation should be improved to get a better convergence using an automatic optimization.

The comparison of the geometrical properties obtained experimentally and numerically are presented in Table 6.3. The value of the experimental shape factor $\left(\frac{height}{width}\right)_{exp}$ is 0.208. The best shape factor $\left(\frac{height}{width}\right)_{num}$ obtained numerically is 0.239 for $G_{ab} = 0.06\ MPa$ and $G_\delta = 2\ MPa$.

Table 6.3 – Area of the transverse section of the strand obtained experimentally and in the simulation at the beginning and the end of diametral compression test

	Initial cross-section (mm²) (Circle)	Width (mm)	Height (mm)	$\dfrac{height}{width}$	Final Cross-section (mm²) (Ellipse Eq. 191)
Experimental (at 400 N)	31.6	12.5	2.6	0.208	22.6
Simulation (last increment at 400N)	31.6	13	3.11	0.239	31.8

The limitation, which explains why we do not succeed in describing perfectly the final shape of the cross-section, is the change of surface area. Table 6.3 summarizes the approximate areas of the cross-sections. The initial cross-section is approximated by the area of a circle of radius 6.36mm (reference state of the strand after the bedding-in). The final cross-section is approximated by the area of an ellipse related to the height and the width, illustrated in Figure 6.19 following:

$$EllipseArea = \pi \cdot \frac{Height}{2} \cdot \frac{Width}{2}$$

<div align="right">*Eq. 191*</div>

The simulation predicts a constant area (the difference in the value might be due to the approximation of an ellipse area) while, experimentally, we observe a loss of 28.5% of the initial area. This limitation may be due to our choice for the change-of-volume behaviour. We chose a value of the bulk modulus found in literature for a bulk polyamide. Hence, this value might not be appropriate to describe the behaviour of a bundle of rope-yarns. In Charmetant *et al.*'s work, it was considered that the yarn compaction stiffness never reaches the bulk stiffness of glass, hence, the voids in the yarns did not collapse altogether (Charmetant et al., 2011). Also, our definition for the free energy potential does not consider any coupling between the shear deformation modes and the change of volume. Under the hypothesis of a constant volume strain, it can be difficult to obtain a cross-section characterized by radii (width and height) as small as those measured experimentally.

To improve the description of the shear strain modes, future work could:

- Perform this experiment on a wet strand;
- Improve the treatment of the 3D scans;
- Get a converged simulation above 400N by changing the simulation (for example, not representing the two rollers at the extremities);
- Propose a new identification for the bulk modulus, for instance by adding it to the searched parameters during the '3-rod' identification process.
- Improve the hyperelastic law by including dissipation and thus, that allows to quantify the friction associated to these shear modes. For example, by changing the current 2D elastic law for a 2D elasto-plastic law of the Saint-Venant type; an elastic spring in series with a plastic element.

The six parameters that define the law for a bundle of rope-yarns have been identified. The following section proposes a first validation of the identified behaviour law at the upper scale. The parameters identified and used for the following sections are given in Table 6.4:

Table 6.4 – Identified parameters for the FiBuLa law for a 4T polyamide sub-rope's bundle of rope-yarns

a (MPa)	b (MPa)	c (MPa)	d (MPa)	G_{ab} (MPa)	G_{δ} (MPa)
3000	3459	1371	3878	0.06	2

6.7. Validation of the law on a stand-alone strand

In the previous identification section, six parameters have been identified to define the anisotropic constitutive law for a bundle of rope-yarns (Table 6.4). Some parameters were identified using tensile cyclic tests on rope-yarns. The aim of the following section is to validate the behaviour law by performing a simulation of a tensile cyclic test on a strand and comparing it to the experimental results of tensile cyclic tests on strand in water.

An analysis of the invariant results will allow an assessment of the consistency of the predicted behaviour of the rope-yarns composing the strands in comparison with literature and regarding their helicoidal geometry inside the strand.

6.7.1. Experimental results

Three tensile cyclic tests on strands in water have been performed following the procedure described in chapter 2 section 2.5.4.5. These tests have been chosen to be similar to the procedure used at the rope-yarn scale for the identification and so, to be representative of a self-heating test. Figure 6.20 is a plot of the loading path of the test.
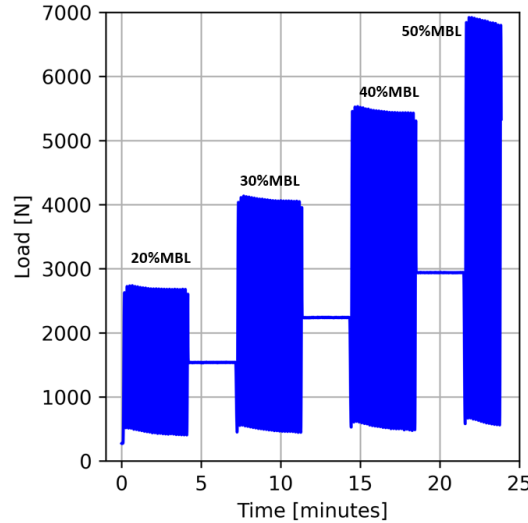
Figure 6.20 – Loading path of the tensile cyclic test on strand in water. Load [N] versus time [minutes]

During these tests, two strains were measured: the axial strain (in the strand axis direction) and the transversal strain (in the strand transverse section) (Figure 6.12). Figure 6.21 shows the results obtained by taking the average of the three tests.

The specific stress[1] versus axial logarithmic strain is plotted on Figure 6.21-left and the transversal logarithmic strain versus axial strain is plotted on Figure 6.21-right. For the validation, we chose to work with the specific stress in N/tex because it is the unit mostly used when studying ropes in tension. Hence, the validation is made using this unit.

[1] The specific stress is defined by $\Sigma = \frac{F}{\overline{\rho_0}}$ with ρ_0 the initial linear density in tex (g/km), that is equal to 27 000 tex for strands.
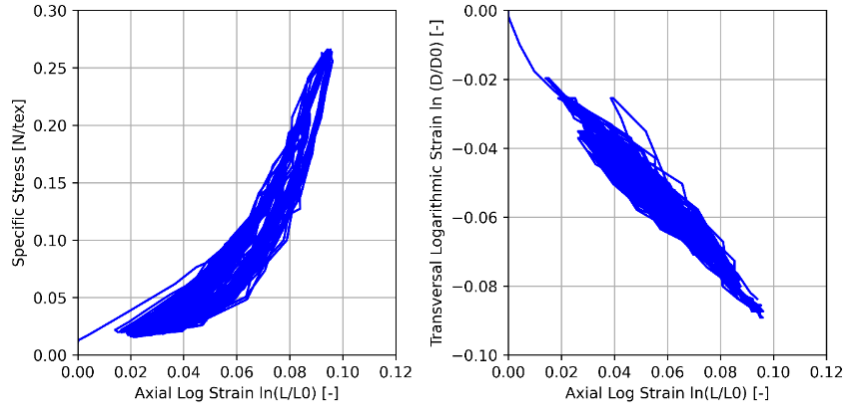
Figure 6.21 – Experimental results of the tensile cyclic tests on strand in water. Left: Specific stress [N/tex] versus axial logarithmic strain [-]. Right: Transversal logarithmic strain [-] versus axial logarithmic strain

On Figure 6.21-right, we observe a fast increase of the transversal strain at the beginning of the curve. This unexpected variation is, in fact, due to the measurement of the initial transversal section D_0. The section is measured all along the length of the strand and the average is calculated to obtain the actual section (explained in chapter 2 section 2.5.4.5). However, D_0 is measured at 2%MBL; at this tension, the strand is not perfectly straight and some curvature is visible on the outline which induces an error on the average and so, an overestimation of the D_0 value. This error on the average disappears when the load increases because the strand under tension becomes straighter.

6.7.2. Simulation of the test and comparison

A simulation of this tensile cyclic test is performed using a quasi-static analysis in *Abaqus-Standard* software and the identified FiBuLa law. The initial state of the strand is taken after the bedding-in, under 2%MBL tension (Figure 6.22; same initial state than for the "3-rod" simulation). The cylinder diameter is $D_0 = 6.36\ mm$ and its length is $L_0 = 150\ mm$ (Figure 6.22). The twist angle of the rope-yarns after the bedding-in is α=22°. The rope-yarns are Z-twisted to form the strand. The initial configuration of the vectors $\overrightarrow{e_{a0}}, \overrightarrow{e_{b0}}$ and $\overrightarrow{e_{c0}}$ is represented in Figure 6.16 ($\overrightarrow{e_{c0}}$ follows the direction of the rope-yarns axis in the initial configuration). The mesh chosen is composed of 76800 C3D8 elements. No mesh convergence study could be performed because of the time constraint.
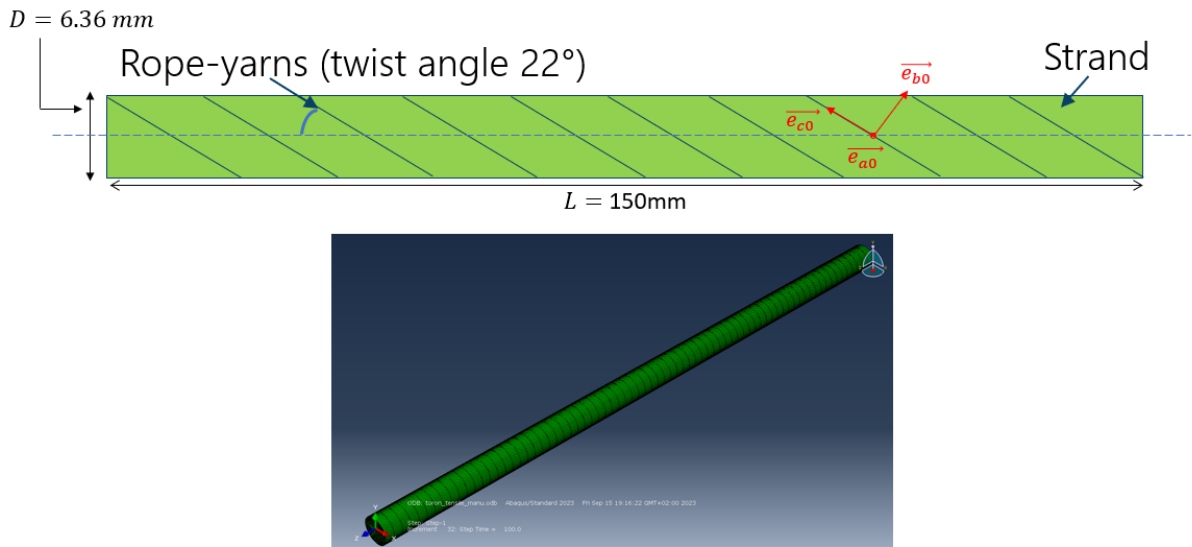
Figure 6.22 - Initial state of the simulation of a tensile cyclic test

As the proposed law is hyperelastic, the simulated load path is only one tensile loading up to 25% strain (no influence of the history of loading). One extremity of the strand is fixed for all degree of freedoms. The other extremity is controlled by displacement along $\vec{z}$ and fixed for the other degrees of freedom.

We compared the stress, the axial and transversal strains of the simulation with the experimental results for the stabilized cycles. The specific stress versus logarithmic axial strain is plotted on Figure 6.23-left and the logarithmic transversal strain versus the logarithmic axial strain is plotted on Figure 6.23-right for the stabilized cycles.
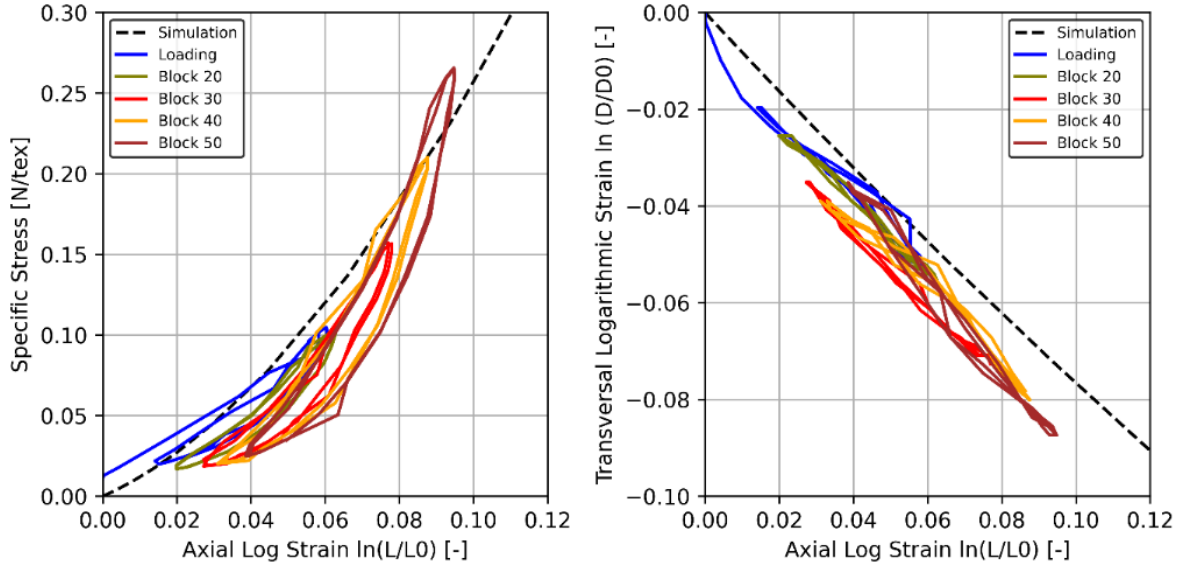
Figure 6.23 – Comparison of the simulation result with the experimental results of a tensile cyclic test on strand in water for the stabilized cycles. Left: Specific stress [N/tex] versus axial logarithmic strain [-]. Right: Transversal logarithmic strain [-] versus axial logarithmic strain

On Figure 6.23-left, we observe that the model overestimates the stiffness of the strand during the first blocks (20%MBL and 30%MBL), then underestimates it for the last two blocks (40%MBL and 50%MBL). However, the range of axial strain is accurate (between 0.00 and 0.12) and the prediction remains very reasonable. The overestimation of the stiffness might be due to the hypothesis that there is no space between the rope-yarns (compact rope-yarns). In reality, the rope-yarns are not completely compacted and some space remains between each rope-yarn leading to a decrease of the mechanical properties.

On Figure 6.23-right, we observe the variation of the transversal logarithmic strain versus axial strain is well described. A slight shift to the right is observed for the simulation. This difference is mainly due to the beginning of the loading. It might be necessary to readjust the experimental D_0 to correct the error made at the beginning of the loading.

This comparison shows that the identified behaviour law describes accurately the behaviour of a strand during a tensile cyclic test in water.

6.7.3. Further analysis of the simulation results

A further analysis of the results obtained by the simulation is now proposed. This analysis gives a first verification of the consistency of the law and proposes a first description of the mechanical response of the rope-yarns during a tensile test.

On Figure 6.24, Figure 6.25 and Figure 6.26 are given some colour maps of different variables of the simulation at the last increment of time 25%.
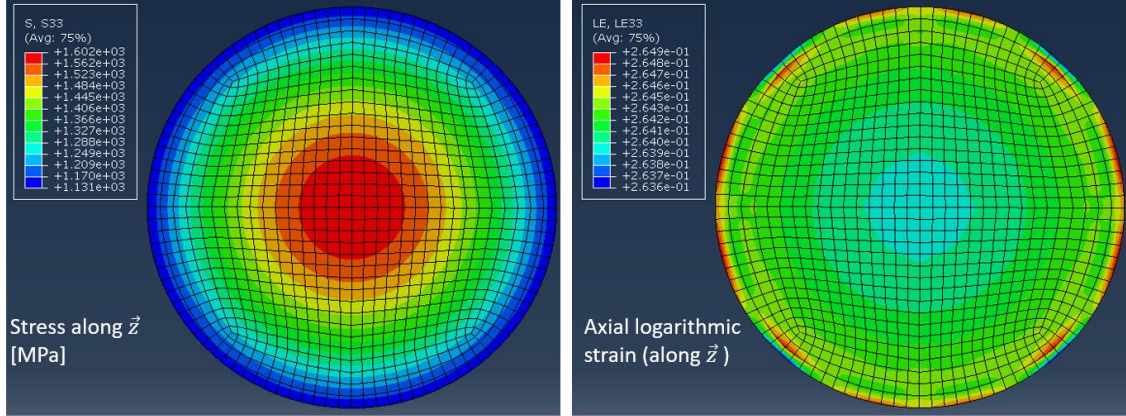
Figure 6.24 – Simulation of the cyclic tensile of a strand: colour maps of the transverse section of the strand. Left: axial Cauchy stress (component ZZ). Right: logarithmic strain along $\vec{z}$ (component ZZ).
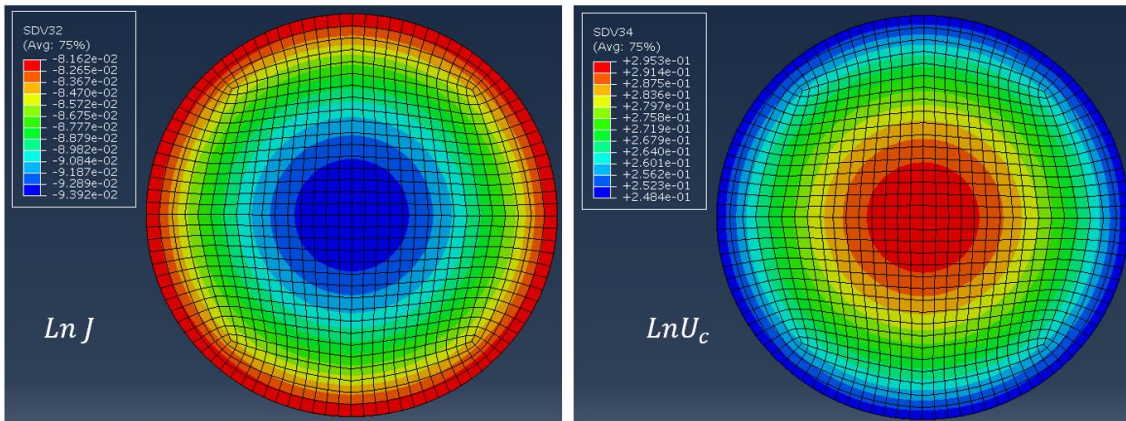
Figure 6.25 - Simulation of the cyclic tensile of a strand: colour maps of the transverse section of the strand. Left: change of volume invariant. Right: Axial elongation invariant.
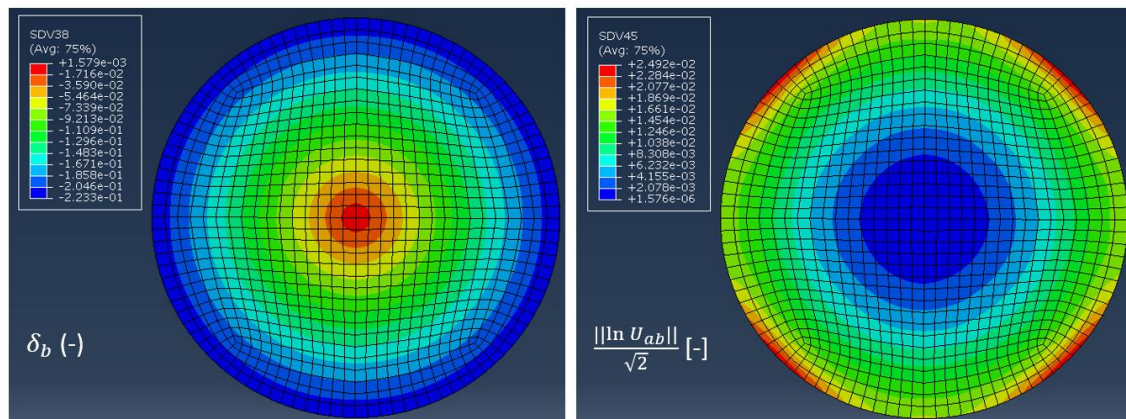
Figure 6.26 - Simulation of the cyclic tensile of a strand. Left: Colour maps of the transverse section of the strand. Shear strain invariant along the axis of the rope-yarns δ_b. Right: Evolution of the shear strain invariant [-] with time [minutes] taken on highlighted node (red circle)

This simulation gives qualitative information of the response of the strand:

- From Figure 6.24- left, the axial stress field is higher at the centre of the strand. This result was expected as the rope-yarns have a decreasing twist angle from the exterior radius to the centre, and they are straight at the centre. The stress increases when the rope-yarns are aligned with the direction of loading because they don't realign and so, they present a higher stiffness. This can also be highlighted by the investigation of the elongation of the rope-yarns inside the strand. Figure 6.27 plots the logarithmic axial elongation of the rope-yarns, at the centre of the strand section and at the left extremity of the strand section, versus the time. The rope-yarns at the centre will elongate more because they present a twist angle of zero.
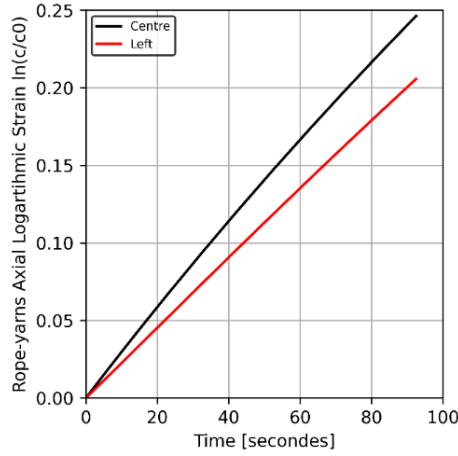
Figure 6.27 – Change of the rope-yarns axial logarithmic strain $\ln \left(\frac{c}{c_0}\right)$ with time [minutes]

- From Figure 6.24- right that presents the logarithmic strain along $\vec{z}$, we observe it is not completely homogenous over the section; but the variation is negligible as it varies from 0.2636 to 0.2649.
- Figure 6.25 presents colour maps of the change of volume invariant $Ln\ J$ and of the axial elongation invariant $LnUc$. The results are in accordance with the evolution of the axial stress. The axial elongation mode is more important at the centre of the strand because the rope-yarns alignment with the loading direction increases. Hence, the rope-yarns will reorient less and elongate more. The change of volume is negative and is higher at the centre. This unusual behaviour is the same as the behaviour observed during the tensile cyclic tests for the rope-yarns. The change of volume is higher at the centre because the elongation is associated with a loss of volume and it is also higher at the centre.
- Figure 6.26-left presents a colour map of the axial shear δ_b (the other invariant δ_a is small during this test and is not presented here). The invariant δ_b, in the bc plan, can be compared to Leech's description of the axial shear illustrated in Figure 6.28 (Leech, 2002). This shear is higher at the perimeter because it is induced by the realignment of the rope-yarn towards the tensile loading direction. This shear is negative because the direction of loading induces a sliding of the rope-yarns in the direction opposite to the direction of the rope-yarns axis $\vec{c_0}$. This result highlights that a cyclic sliding, that could induce friction, at the rope-yarns scale in their preferred direction and along the bc plan, is happening during cyclic uniaxial tensile loading of the strand (only sliding between rope-yarns in the present model, no dissipation). This friction and abrasion may partly explain the observations of broken fibres at the outer diameter of the strands after high-cycle fatigue loadings on the sub-ropes (chapter 5 figure Figure 5.5).
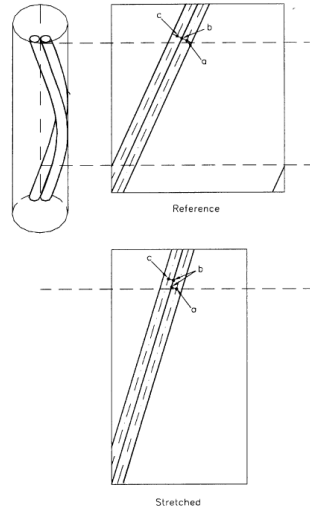
Figure 6.28 – Axial shear described by Leech (Leech, 2002)

- Figure 6.26-right presents a colour map of the norm of the transversal shear strain invariant. It highlights the transversal shear strain reached its maxima at the perimeter of the strand section. These leads to a null transverse shear at the centre of the strand section.

Finally, Figure 6.29 plots the couple $C_{\vec{z}}$ versus axial elongation at the moving extremity of the strand during the simulation.
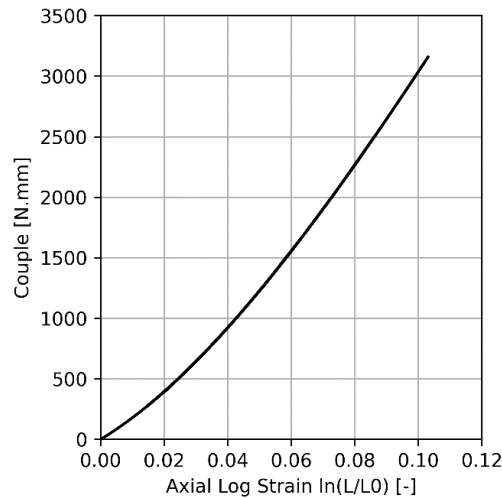
Figure 6.29 – Couple around $\vec{z}$ [$N.mm$] versus axial logarithmic strain $ln(\frac{L}{L_0})$

The predicted moment varies from 0 to 3200 N.mm which is considerable. It was explained, in chapter 2 section 2.5.4.5that, because of the laid construction of a strand, an important couple was applied to the testing machine actuator and two wood beams were added to block the actuator rotation. Hence, in future work, it would be interesting to add a torque sensor to monitor the torsion moment during tensile tests and to compare the experimental result to the simulation.

This first simulation showed that the behaviour law describes accurately the behaviour of a strand. It also checked that the results given by the FiBuLa invariants for the rope-yarns behaviour were consistent. The next section will try to simulate the upper scale.

6.8. First simulation of a sub-rope

This study aims at investigating the feasibility of adapting Charmetant *et al.* approach, developed for a woven material, to a stranded polyamide sub-rope. Hence, this part consists in proposing a complete investigation method on a three-strand sub-rope using the FiBuLa law. A first analysis is performed to assess the advantages of the proposed model to help understand the mechanical and dissipation response of a sub-rope with a given construction. The main objective is to determine if this model, that uses a hyperelastic law, can allow us to separate:

- The polyamide material response at the rope-yarn scale: axial elongation and change of volume invariants of the FiBuLa law (in future work, these strain modes could be defined with visco-elasto-plasticity);
- The inter-strand friction: friction between the meshed solid elements;
- The inter-rope-yarns sliding: shear strain invariants of the FiBuLa law (in future work, these sliding actions could be defined as friction with dissipation).

The method will be validated if the model can provide a realistic description of the geometries of the strands.

6.8.1. Method to simulate a sub-rope

We used the *Abaqus*-Standard dynamic implicit analysis to perform this simulation; this analysis offers an option, called "quasi-static", for approaching a quasi-static simulation. The first difficulty in the simulation of a sub-rope using the FiBuLA law is to obtain its helicoidal construction with the desired parameters (lay-length, twist angle of the strand, twist angle of the rope-yarns inside the strand). To obtain a valid description of the sub-rope behaviour, it is necessary to describe accurately the orientation of the rope-yarns inside the strand and at the contact zones between the strands. In fact, it has been shown the friction coefficient will depend on the inter-fibre angle (Bain, Davies, et al., 2022).

To succeed in this description, we begin the simulation with the three strands straight. Indeed, we will assume a simple helix geometry for the paths of the rope-yarns in this simpler configuration of the straight strands. Then, the stranding process has to be simulated to obtain a 3-strand sub-rope. The last step is to simulate the desired tensile loading path on the sub-rope, in this case, a cyclic loading.

In the initial configuration, the three strands are considered after a bedding-in. This reference state, and the rope-yarn helix geometry, are the same as for the simulation of a tensile test on a strand in section 6.7.2. The length of the strands in the initial state must be chosen according to the lay-length and the simulated number of pitches of the sub-rope.

The following simulation of a sub-rope is based on the use of the rotation-120° symmetry of the 3 strands. Indeed, the mechanical state field in a strand is the same as the two others by rotating around the sub-rope axis by an angle of 120 degrees. We chose to simulate the continuum mechanics on only one strand, called the "master strand", and to duplicate its displacement field according to this rotation-120° symmetry to obtain the response of the two other strands, called "ghost strands". This is carried out in *Abaqus* by linear equations on node displacements (*equation*). The identified FiBuLa law is then implemented into the master strand, and Hooke's law with a null Young modulus is implemented into the two ghost strands (Table 6.5). The role of the ghost strands is only to be part of the contact interaction with the master strand.

Table 6.5 – Method to simulate a sub-rope using a "master strand" and two other "ghost strands" defined by 120° symmetries.

Name	Type	Behavior law	Element nodal force field	Displacement field given by
Strand 1	Master	FiBuLa	Given by FiBuLa	Mechanical equilibrium
Strand 2	Ghost	Hooke law with a null Young modulus	Null	Master strand displacement rotated by +120° around sub-rope axis
Strand 3	Ghost		Null	Master strand displacement rotated by -120° around sub-rope axis

At each extremity of the master strand, the displacements of all nodes of the section are controlled by a rigid body piloted by the displacement and rotation of a supplementary node, Table 6.6. These rigid bodies at the two extremities will block any strain of the section, the Poisson effect for instance. This will lead to side effects but they will vanish with the distance from the extremities. With 4 simulated pitches of the sub-rope, we expected to obtain, in the middle of the sub-rope length, a deformation field not affected by these side effects.

Table 6.6 - Method to simulate a sub-rope using a "master strand" and two other "ghost strands": boundary conditions

Name	Type	Boundary conditions at the two extremity sections
Strand 1	Master	Rigid body piloted by a supplementary node displacement and rotation
Strand 2	Ghost	Nothing
Strand 3	Ghost	Nothing

Hence this method consists of two simulations (Figure 6.30). In the first, starting from a straight strand, we orient it to follow a helix geometry (lay-length, number of pitches, twist angle). To do so, we imposed the displacement of some nodes along the strand axis; two nodes per pitch and the rigid body nodes at the extremities. The idea is to reach a helicoidal geometry by the least displacement node controls, to avoid unnecessary imposed deformation. In this simulation, three parameters are used: the final twist angle of the strand, the length of the strand inside a pitch and the number of pitches. Then, we retrieve the final displacement of each node of the mesh (Figure 6.30-1 and -2).

In the second and final simulation with the three strands:

- Initially, the three strands are in the initial position of the first simulation but the meshes of the ghost strands are rotated by +/- 120° from the mesh of the master strand (Figure 6.30-3). The axes of the three strands are superimposed on the sub-rope axis.
- In a first step: we control all the nodes of the master strand by imposing the displacement field resulting from the first simulation. No contact is defined between the strands during this step (Figure 6.30-5). At the end of this step, the strands form three helices and they are separated from each other, i.e. the positions of the three strands do not overlap at any material point. This last point is critical for the next step.
- In a second step: the contact between the three strands is added. It is a contact with friction. The friction coefficient is fixed at 0.15 based the work of Bain *et al*. The left extremity has the following boundary conditions: a displacement in the $\vec{z}$ direction is applied; it is fixed along $\vec{y}$ and free along $\vec{x}$; its rotation around $\vec{z}$ is fixed while its rotation around $\vec{x}$ and $\vec{y}$ are free. The right extremity is fixed in translation along $\vec{z}$ and all the other degrees of freedom have the same boundary conditions as the left extremity. The initial state of the sub-rope is taken when the three strands are in contact along all their lengths (Figure 6.30-6). This contact can be detected by an increase of the reaction force at the master strand extremity. It is this state that will then be used as the initial state to define the macroscopic axial strain of the sub-rope. This state defines the lay-

length of the sub-rope. To obtain the desired lay-length at this step, it requires several tries to have a definition of the first helix, with no contact, that allows the correct helix to be obtained at the contact.

- The other steps consist in the cyclic loading of the sub-rope and are controlled by displacement of the moving extremity of the master strand along the $\vec{z}$ direction. The other degrees of freedom are the same as during the previous step for both extremities.
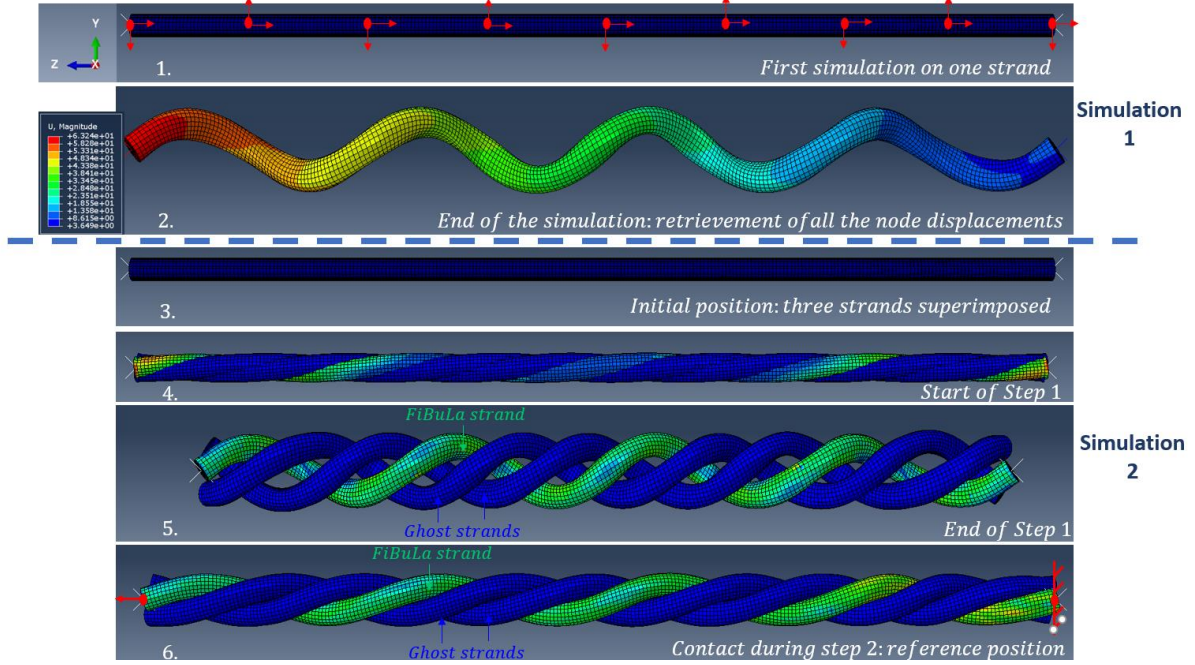
Figure 6.30 – Method used to simulate a three-strand sub-rope that allows a description of the orientation of the rope-yarns inside the strands.

Using this method, the following simulation parameters were used:

- The parameters of the FiBuLa law presented in Table 6.3 are used to define the behaviour of the "FiBuLa strand".
- The "ghost strands" are characterized by a null Young modulus (no stress for any strain).
- The strands are straight and their initial state is taken after a bedding-in procedure. We chose to simulate four pitches. The strand initial length if of L_0=258 mm and the initial diameter, taken after the bedding-in, is D_0=6.36 mm. In the initial straight strand configuration, the rope-yarns twist angle at the surface is $\alpha = 22°$ (Figure 6.16). The final lay-length of the sub-rope, measured on the simulation at the reference state (taken step 2 after full contact) is of 59 mm.
- The mesh chosen consists of 44 8-node linear brick elements C3D8 in the transversal section of the strands. The three-strands model is composed of 33792 C3D8 elements. No convergence study could be performed because of the limited time available.
- The left extremity is piloted by displacement in the $\vec{z}$ direction during the cyclic loading and the right extremity is fixed in the $\vec{z}$ direction. The other degrees of freedom of both extremities are the one described in the methodology part. The cyclic loading is the following: 3 cycles between 10mm and 50mm displacement for the left extremity (Amplitude 1), then two cycles between 10mm and 60mm (Amplitude 2). The displacement imposed is triangular and each step consists of a loading or an unloading ramp.

The next section presents and analyses the results of this simulation.

6.8.2. Simulation results

6.8.2.1. Study at the sub-rope and strand scale

This section investigates the results obtained from the sub-rope simulation using only the outputs calculated by *Abaqus* software (not the FiBuLa law invariants) and proposes some interpretations. Figure 6.31-left plots the load applied on the sub-rope versus time and Figure 6.31-right plots the moment around $\vec{z}$ (torsion) applied on the sub-rope versus time, from step 2 of the simulation to the end.
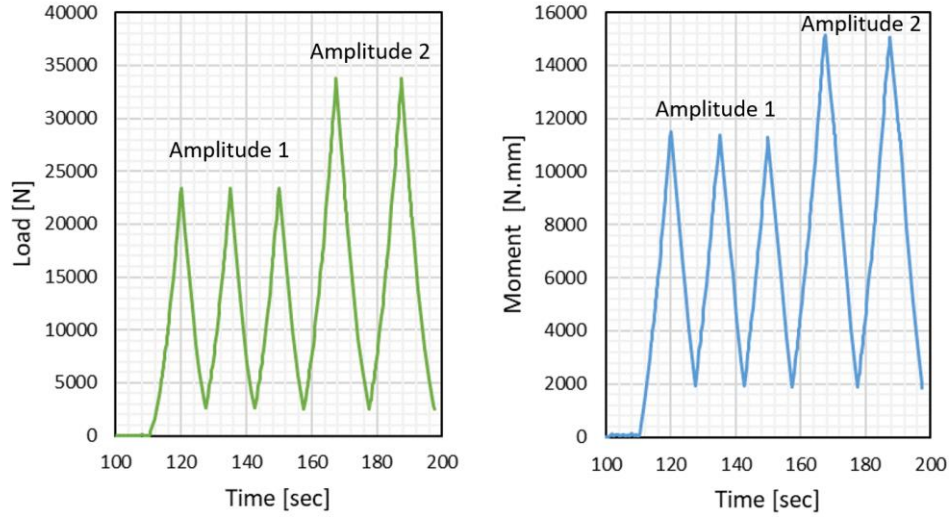
Figure 6.31 – Left: Load applied at the extremity of the sub-rope [N] versus time [second]. Right: Moment around $\vec{z}$ applied at the extremity of the sub-rope [N.mm] versus time [seconds]

We observe that a total torque of $16\,000\ N.mm$ at the top of the sub-rope. This highlights that the torsion plays a role in the mechanical response of the sub-rope.

Figure 6.32 presents a colour map of the logarithmic strain along the sub-rope. We observe irregularities and side effects only on the first pitches at the extremities but they disappear for the two pitches in the middle. Hence, only the mechanical response of these two pitches will be investigated in the following. The measured lay-length of the simulated strand is 59 mm.
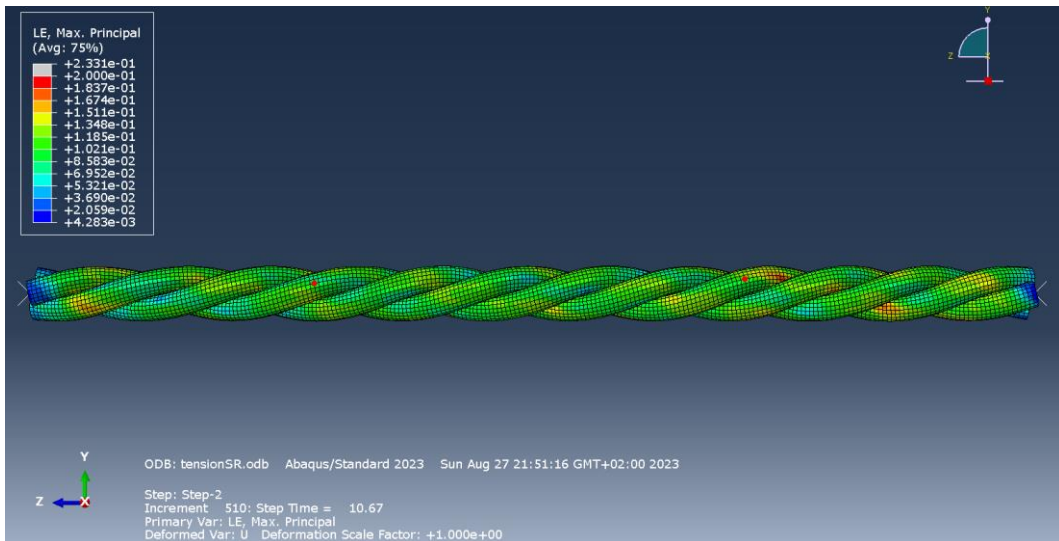
Figure 6.32 – Colour maps of the maximal logarithmic strain eigenvalue [-] along the sub-rope during step 2, after the full contact is set (reference state). Two red points highlight the nodes used for the macroscopic strain calculation.

On Figure 6.32, two red points, with very close y coordinates are highlighted. The z coordinates of these two points at the reference state (Step 2, $t = 10.67 sec$; Figure 6.30-6) and their displacements during the simulation are used to calculate the macroscopic logarithmic strain of the sub-rope. Figure 6.33-left plots this macroscopic logarithmic strain, versus the tensile force on the sub-rope.

A first comparison with the experimental result for a strain monitored fatigue test (studied in chapter 5 section 5.4) is proposed. The experimental test consisted of cycles between 2%MBL and 45%MBL at a frequency of 0.1 Hz. Figure 6.33 presents the experimental result. This cannot be a final validation, as the lay-length of the sub-rope in the experimental test is 55 mm under 2%MBL tension while the simulated lay-length is 59 mm. However, this first comparison can indicate whether the model is realistic. For a load varying between 0 and 17550 N, the range of strain, observed Figure 6.33, is in accordance with the experimental results, Figure 6.33. The simulation predicts a reasonable stiffness. However, as the lay-length simulated is longer, we would have expected a higher stiffness than the experimental results. Hence, the simulation underestimates the stiffness. This could indicate the change in construction observed during the experimental test is not completely predicted by the simulation.

On the simulated load versus strain curve, Figure 6.33 and Figure 6.34-left, we observe that all the cycles remain superimposed, with no visible hysteresis, which is characteristic of a hyperelastic behaviour with low dissipation in the contact area. This result indicates that the inter-strand friction has no major influence is this calculation. The choice of friction coefficient might be questionable and a study of the impact of the friction coefficient would be necessary to conclude.
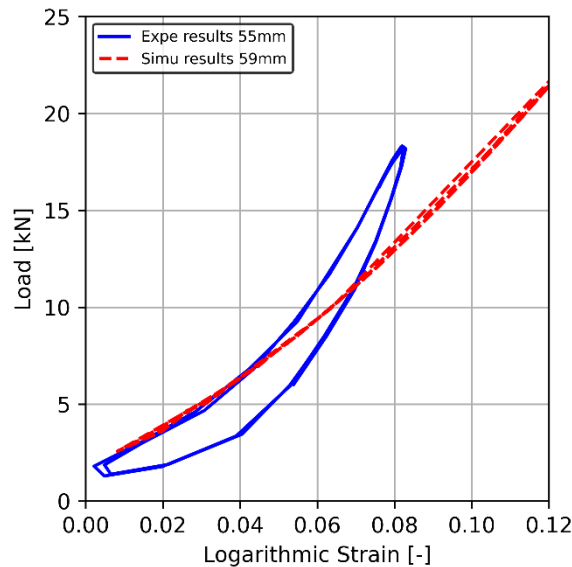
Figure 6.33 – Comparison of the simulation results (red dashed curve; 59mm lay-length sub-rope; during a cyclic test between 10mm and 50mm displacement (Amplitude 1)) with the experimental results (blue curve; 55mm lay-length; during a cyclic test between 2%MBL and 45%MBL): Tensile load [kN] versus the logarithmic strain [-]
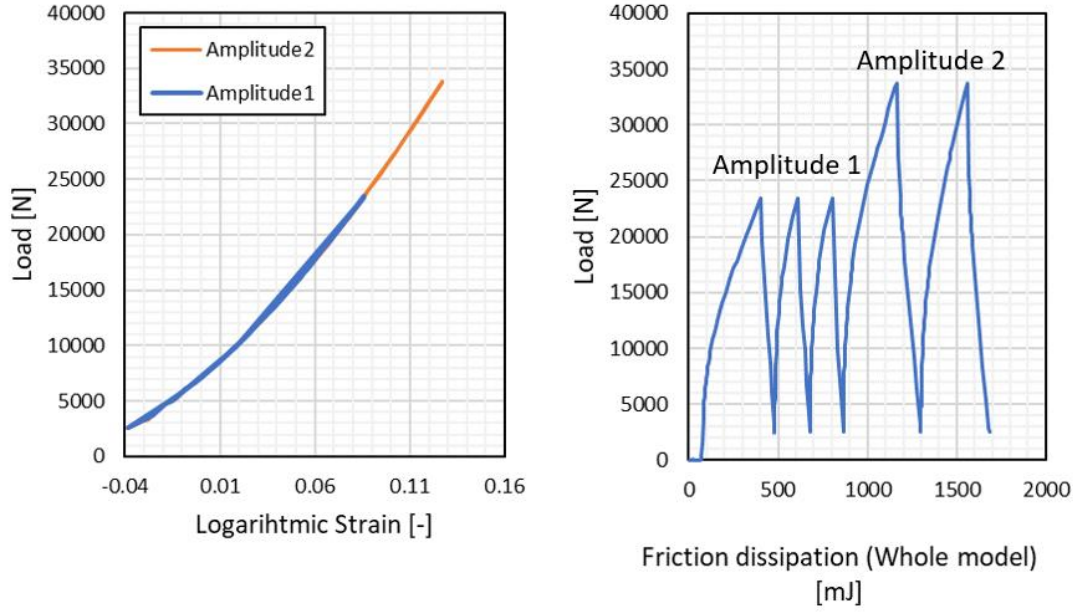
Figure 6.34 – Left: Simulated results of a cyclic test: Load [N] versus logarithmic strain [-]. Right: Tensile load [N] versus the friction dissipation calculated for the whole model by Abaqus software [mJ]

Abaqus calculates the dissipation due to friction for the whole model (Figure 6.34-right). This output allows us to investigate the friction but, the side effects, at the sub-rope extremities, are also included and falsify the results. The simulation of a higher number of pitches could allow to use this calculated dissipation of the whole model with a less important impact of the side effects. We observe, on Figure 6.34-right, that the cumulated dissipation reaches 1.682 J. To investigate the friction effect, the friction coefficient used during this simulation should be varied and investigated. It should be adjusted by considering the direction of the rope-yarns in the contact area. Bain *et al.* showed that the friction angle is an important parameter influencing friction between polyamide fibres; and this model is a precious tool to perform a study of this parameter (Bain, Davies, et al., 2022). In fact, the following section 6.8.2.2 shows that the FiBuLa law used with this mesoscale model can allow to have detailed information on the rope-yarns organization in the contact surfaces.

Another comparison that can be made between the simulation and the experiments focuses on the shape of the strands. The aim of the model was to determine the geometries of the sections, so it must provide a realistic prediction of the shape of the transverse section of the strands in contact. Hence, a comparison of the simulated shape with the tomography scans (Figure 6.35) is proposed. Figure 6.35 presents colour maps of the transverse section of the middle of the sub-rope at different times of the simulation. On Figure 6.35-c, we observe the shape of the strand, at the beginning of the second cycle (at Amplitude 1 at around 700N). This shape is comparable to the shape observed in the tomography scans (Figure 6.35-d). A hole at the centre, along the helix axis, is visible on the simulation and on the tomography scans. This hole is smaller on the tomography scan because of the limited tension to which the sub-rope was subjected during the tomography (in fact, a sub-rope under higher tension will also presents a hole along its helix axis. This hole is due to the tensioning of the strands and their alignment with the loading direction).
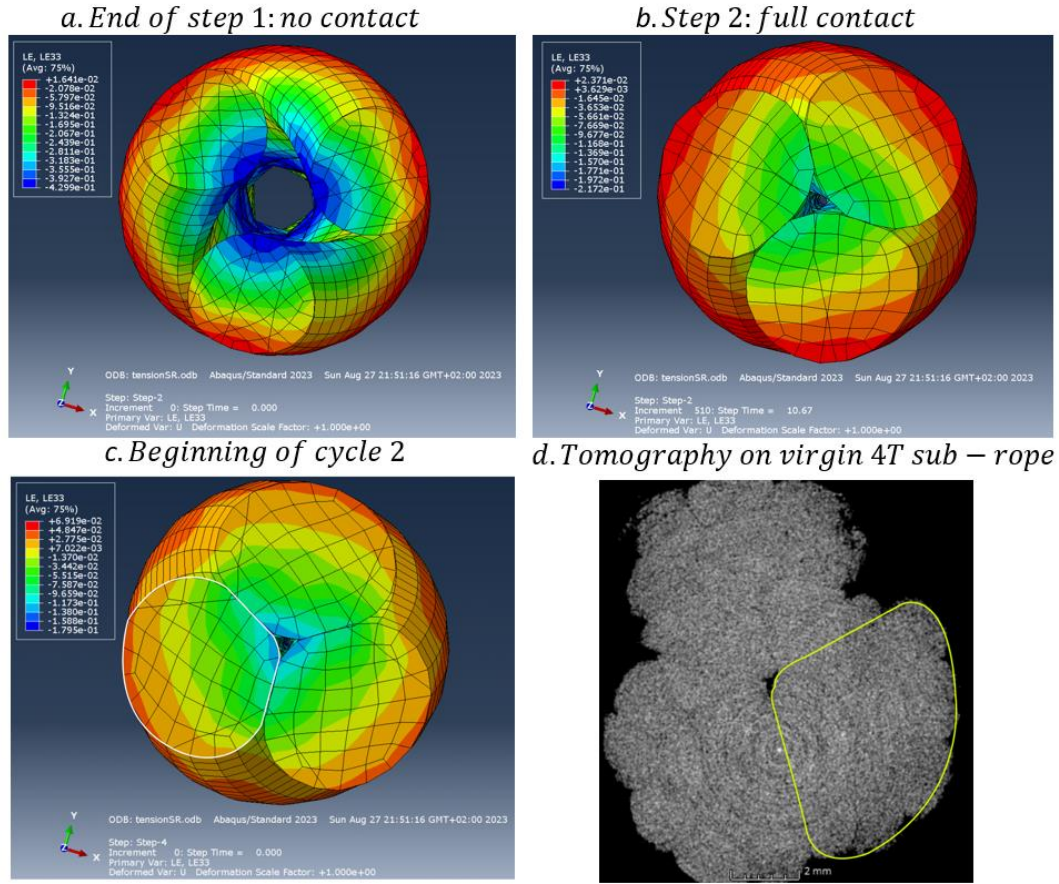
Figure 6.35 – Colour maps of the logarithmic strain [-] along $\vec{z}$ direction of the middle transverse section of the sub-rope at different key steps of the simulation

One objective of this modelling study was to evaluate the contact surfaces and forces. We will focus on the contact between the strands taken from one pitch in the middle of the sub-rope length. Figure 6.36-a presents a colour map of the contact force vector on one strand and Figure 6.36-b presents a colour map of the shear force vector.
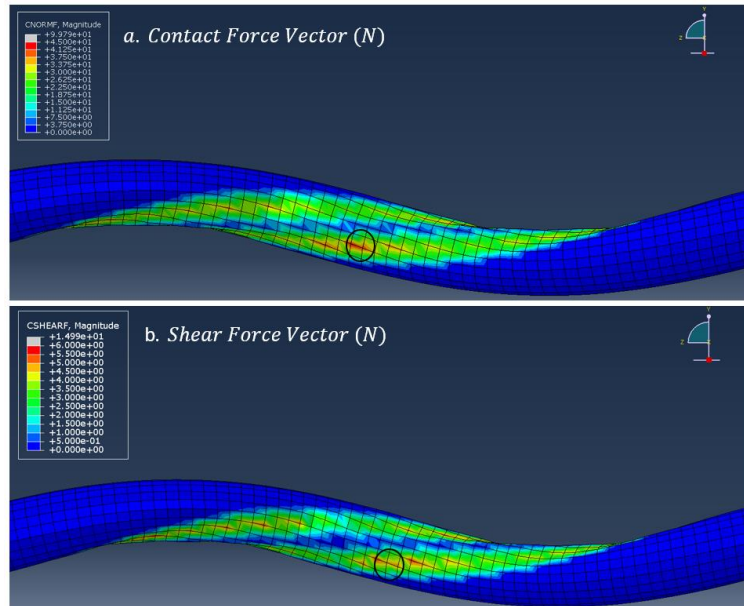
Figure 6.36 – Colour maps of the pitch of the strand. a) contact force vector [N]. b) Shear force vector [N]. Zone with maximal shear and pressure circles in black.

Figure 6.36-a and b, show a maximum pressure and a maximum shear in the circled zone. We plotted the evolution of the contact pressure and the shear stress for one node in this zone (black circle) in Figure 6.37-left and Figure 6.37-right.
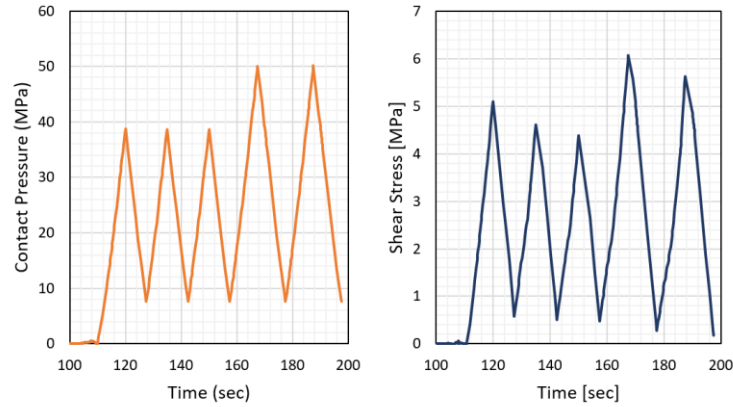
Figure 6.37: Left: Contact pressure [MPa] versus time [second]. Right: Shear stress [MPa] versus time [seconds]. At one node in the zone where the maximal pressure and shear where observe.

We observe a maximum pressure of 50 MPa. On Figure 6.37-right, we observe that the shear stress evolution is the same as the contact pressure. These results show that we can obtain the information of the contact surfaces, pressure and shear stress between the strands. Figure 6.38 is a vector map of the shear force vector.
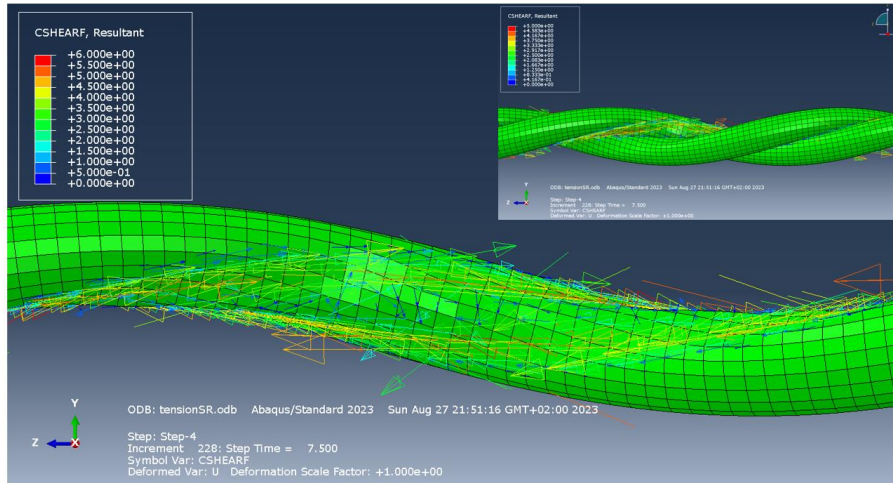
Figure 6.38: Vector maps of the shear magnitude [N] of the FiBuLa strand. Top right: same colour maps with one of the two other strands also represented.

We observe two sliding directions for the vectors at the top and bottom of the contact. Each of these directions of sliding is associated with one of the two strands in contact (illustration of the position of the strand in Figure 6.38-top right). This result indicates that one strand will slide and realign following one direction and the other strand will do the same in the opposite direction.

This first calculation shows that this model provides the necessary information at the strand scale: the geometry of the contact surfaces, the contact forces, the friction dissipation at this scale. Also, it suggests that the friction at this scale (inter-strand friction) doesn't play an important role in the dissipative response of the sub-rope. This is a surprising result that must be further studied in future work.

Two schemes are presented in Figure 6.39 to summarize what was observed at this scale. Now, a study of the rope-yarns scale will be proposed.
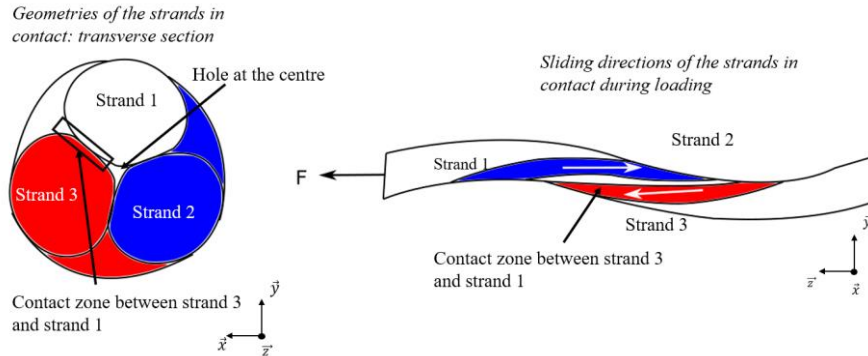
Figure 6.39 – Schemes of the main results at the strand scale obtained from the simulation of the sub-rope. These results are given by the Abaqus software outputs.

6.8.2.2. Study at rope-yarns scale using the FiBuLa law invariants

The FiBula law and its invariants allow us to investigate the behaviour and the sliding at the rope-yarns scale. Colour maps of the invariant of change of volume and of axial elongation, for a bundle of rope-yarns, are presented in Figure 6.40-left and right for the end of cycle 2 (load of 24 kN on the strand). They provide a way to qualitatively evaluate the consistency of the results by comparing them to the tomography and SEM images.
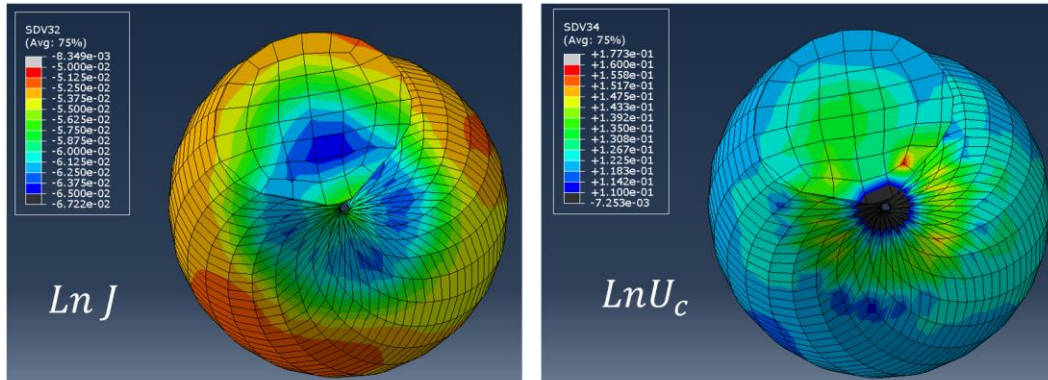
Figure 6.40: Colour maps of the transverse section of a strand. Left: change-of-volume invariants [-]. Right: axial elongation invariant [-].

Both these invariants increase when getting closer to the axis of the sub-rope helix. They reach their maximum, with 6% loss of volume (hence compaction) and with 16% of axial elongation, before the centre of the sub-rope. The contact with the other strands induces a change in the loading of the rope-yarns and so, a change in the distribution of these strain modes. We observe that the rope-yarns are subjected to more tension and more compression at the inner part of the sub-rope. This is coherent with the compaction and rearrangement of the rope-yarns observed in chapter 5 section 5.3.2, at the inner part of the sub-rope. Hence, the mesoscale model, used with the FiBuLa law, provides an accurate description of the heterogenous compaction and change-of-volume, at the rope-yarns scale. It can be a useful tool to investigate these phenomena that play an important role in the fatigue response of ropes.

Figure 6.41 presents colour maps of the invariants associated with shear strains. For each invariant, a colour map of the transverse section and another one along the length of the strand at one pitch, at the end of cycle 2, is presented.
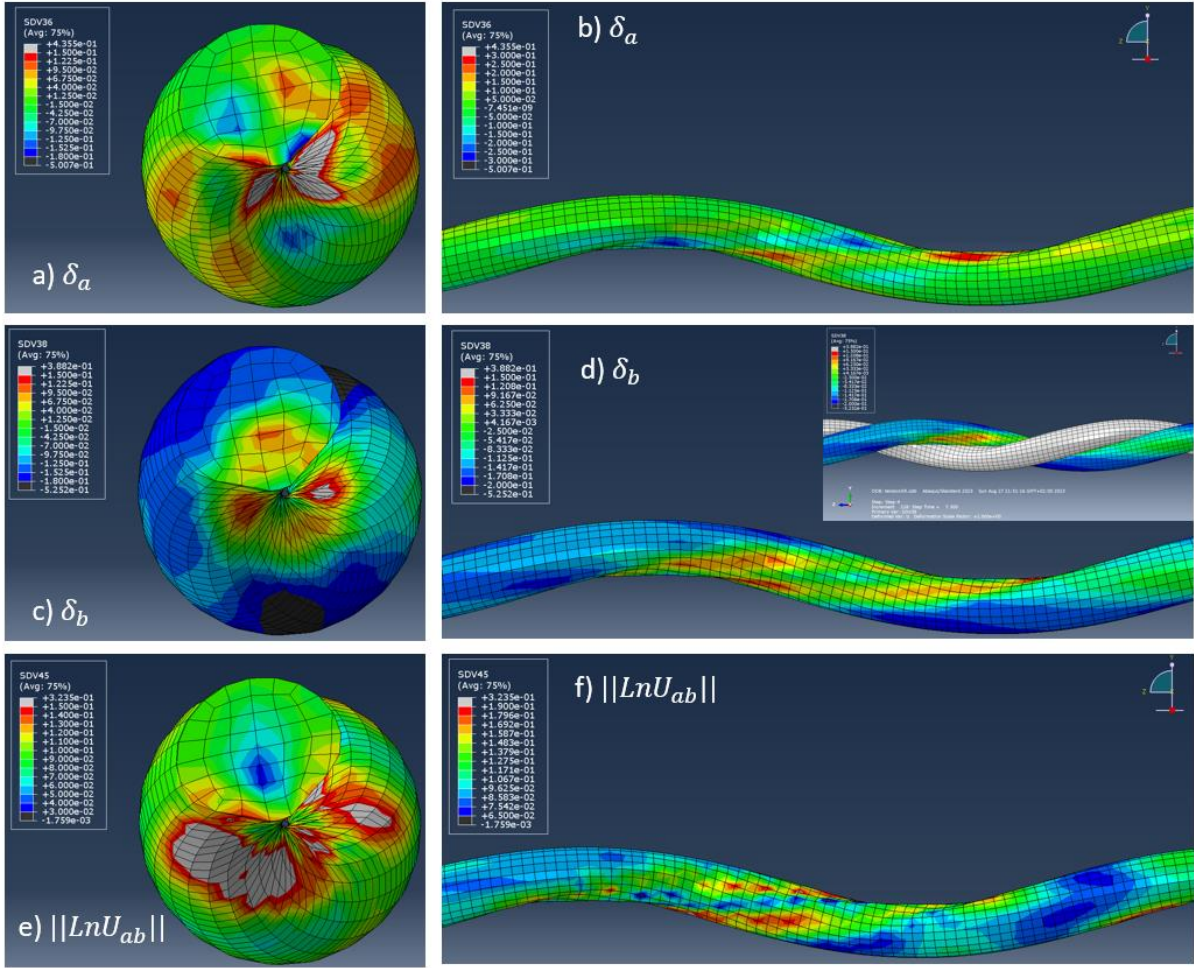
Figure 6.41- Left. Colour maps of the transverse section of a strand. a) and c) longitudinal shear invariants. e) Transversal shear invariant. Right: Colour maps of one pitch of a strand. b) and d) longitudinal shear invariants. f) Transversal shear invariant

The friction strain modes can be studied qualitatively using the FiBuLa law and the meso-model. The main tendencies, revealed by the simulation, for the sliding at the rope-yarns scale (inter-rope-yarns sliding) are summarized by the schemes in Figure 6.42.

The longitudinal shear strain δ_a, in the ac plan, is of the same magnitude as the shear strain δ_b. This was not the case for a tensile test on a strand. In fact, this shear is induced by the contact between the strands. We observe that the directions of the contact shears δ_a (along the length of the strand), on Figure 6.42-b, are in accordance with the sliding directions predicted by *Abaqus* software for the strands in contact, shown in Figure 6.39. The strand 2 will slide in the z^- (right) direction which induces negative shear δ_a of the rope-yarns. On the contrary, the strand 3 will slide in the z^+ (left) direction which induces positive shear δ_a. Hence the results obtained using the shear directions calculated by *Abaqus* contact law are in accordance with the results obtained using one of the invariants of the FiBuLa law. This indicates the consistency and reliability of the proposed FiBuLa law.
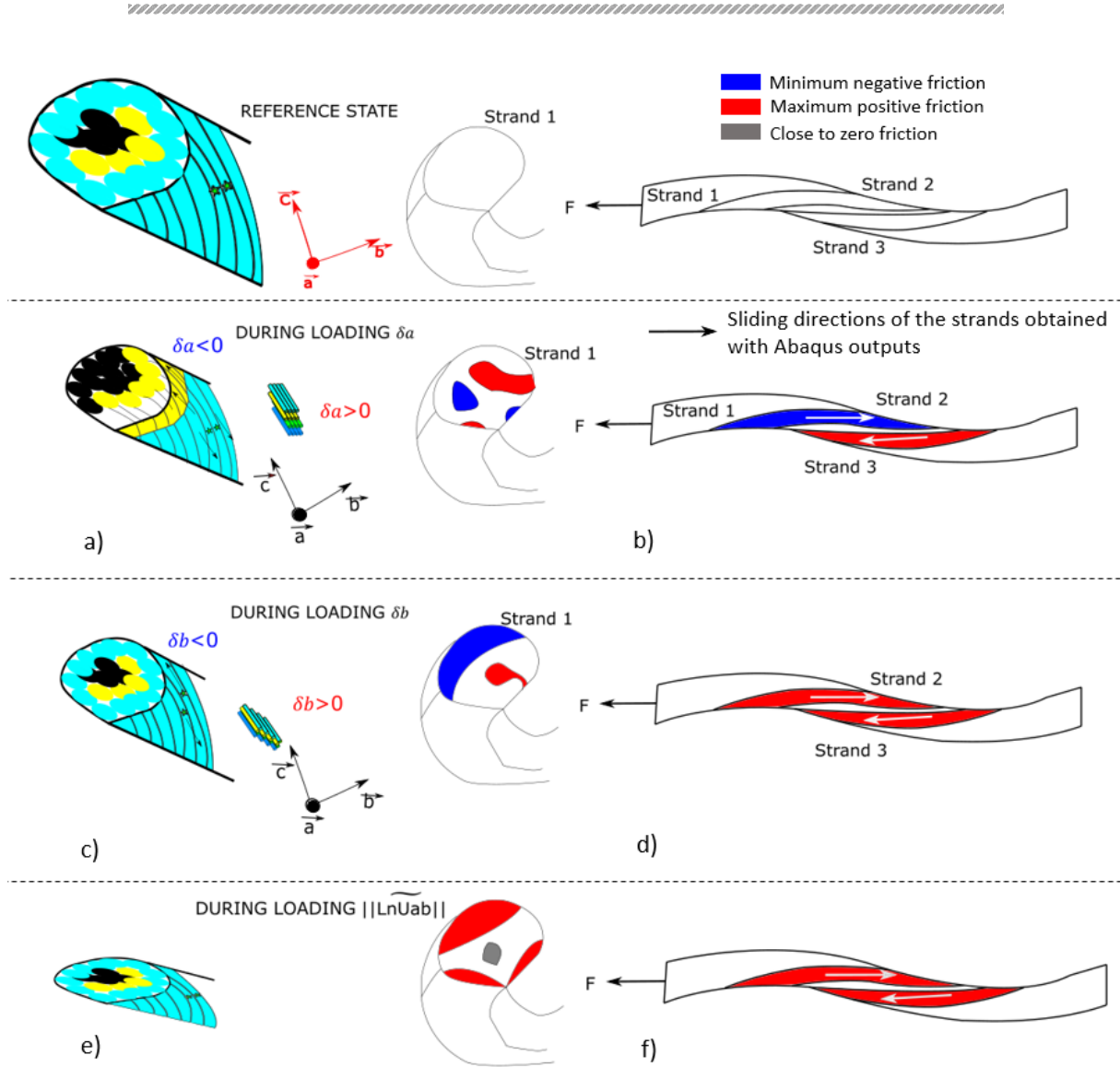
Figure 6.42 – Scheme that indicates the strain modes associated with the shear strain invariants and summarizes the results given by the colour maps of the shear strains invariants.

We observe, on Figure 6.42-c and d, that the longitudinal shear strain δ_b, in the bc plan (which is comparable to the axial shear described by Leech), varies in a similar way to the strand in a tensile test (Figure 6.26). The maximal shear is mostly at the perimeter of the strand section. However, a new zone where this shear strain mode is significant and in opposite value (blue zone, Figure 6.42-d), is revealed by this simulation in the centre of the strand section.

This simulation shows that the contact with the other strands induces shear strains in the bundle of rope-yarns. This is in accordance with what was observed in chapter 5 section 5.3.2, with changes in the surface contact aspect and reorganisation. The mesoscale model, used with the FiBuLa law, can provide important information on the rope-yarns organization, orientation and sliding at the contact surfaces. It can be a useful tool to investigate the friction coefficient variation, which is dependent on the friction angle, and its impact on the dissipation and damage of ropes.

Also, this first simulation reveals the advantage of the more complete description of the strain modes, with two invariants for the longitudinal shear strains. The two longitudinal shear strains, δ_a and δ_b, are of the same magnitude but the maps reveal very different distributions that cannot be described using only one invariant. Hence, decoupling these two longitudinal shear components is interesting for a friction study.

Finally, the transverse shear strain is presented, on Figure 6.42-e and f. It is more important at the contact zones with the other strands. Also, the minimum is reached at the centre which is similar to what was observed during a tensile test on a strand (Figure 6.26-right).

This first simulation highlights the advantages of the proposed FiBuLa law, that adapted the work of Charmetant, to allow a deeper understanding of the mechanical state of the strands and rope-yarns during mechanical loadings on a sub-rope. Analysis of strain and stress fields can allow us to investigate the important parameters for the response of a sub-rope by varying the friction coefficient, the twist angle and lay-length of the strand in the sub-rope, and the twist angle of the rope-yarns inside the strands. Adding dissipation in the shear modes and also visco-elasto-plasticity should allow us to separate the dissipation due to the material from the dissipation due to the friction.

6.9. Conclusion

The previous chapter highlighted the need to improve our understanding of the dissipation and degradation mechanisms of a sub-rope during cyclic tests. This chapter proposed a model approach to quantify and separate the dissipation due to the friction from the dissipation due to the material behaviour. The objectives of the model in its final version will be to evaluate the frictions at two scales: the strands scale and the rope-yarns scale. The chosen method involves modelling each strand by a meshed three-dimensional solid in a finite element analysis software. The strand is considered as a homogeneous material that is defined by a behaviour law that models the transverse-isotropic behaviour of a rope-yarn bundle. At the strand scale, the determination of the contact surfaces, contact forces and friction are needed and will be described by the contact law used in the finite element analysis software. At the rope-yarns scale, the anisotropic law used has to allow us to quantify the friction energies and the dissipative behaviour of the rope-yarns in tension.

We chose to use the method of Charmetant *et al.* for the modelling of a bundle of rope-yarns behaviour because the classical hyperelastic and hypoelastic laws usually give wrong geometries for these types of materials. Hence, the law proposed in this work is an adaptation of the law of Charmetant *et al,* for reinforced woven fabrics. The major advantage of Charmetant's approach is to be able to apply relevant behaviour law for each strain mode. Six strain modes were considered in this model: the axial elongation, the change of volume, two shear strains in the axial direction of the rope-yarns and two transversal shear strains. In his work, Charmetant proposed a set of strain invariants that is limited for a study of the friction between the components of a synthetic rope. So, we proposed new strain invariants that provide a complete description of the strain and so, of the strains that induce friction between the rope-yarns. The proposed law with its invariant has been called the "FiBuLa law" (Fibre Bundle Law).

We proposed an exploratory and feasibility study of this approach involving: the theoretical development; the finite element implementation; a first identification of the parameters; a first validation at a higher scale and a first simulation of a sub-rope in tension. Hence, only hyperelastic laws were used, with no intrinsic dissipation, for this work.

Two experimental set-ups, at the rope-yarn and strand scales, were designed for the identification. They allowed us to identify the 6 parameters associated with the first hyperelastic potentials chosen for the FiBuLa law.

The validation of the proposed law was performed by comparing the simulation of a tensile cyclic test on a strand, to experimental results. The axial and transversal strains were in

accordance with the experimental results. The evolutions of the invariants (describing the rope yarns scale behaviour) during the simulation, and their distribution in the transverse section of the strand, were also in accordance with what is described in literature.

The first simulation of a three-strand twisted sub-rope was also performed. It allowed us to confirm the consistency of the proposed law. No rigorous validation could be made at this scale (future work). However, it was shown that the proposed model was realistic by comparing the simulated load versus axial strain results to experimental results for a different sub-rope construction. Also, the proposed 3D modelling and anisotropic law allowed us to determine the contact geometry and forces between the strands. The results obtained for the invariants of the law (describing the behaviour at the rope-yarns scale) were in accordance with the observations of the state of the sub-rope and its components, after fatigue testing, made using SEM and tomography analysis in chapter 5 of this manuscript. In particular, the change-of-volume invariant allowed to appreciate the heterogenous compaction at the rope-yarns scale. This first simulation highlighted that this mesoscale model, using the FiBuLa law, can be a useful tool to perform studies of the compaction effect observed at the rope-yarns scale, or of the changes in the friction coefficient due to the changes in the orientation of the rope-yarns during cyclic tests. It gives detailed description of the sliding between the rope-yarns which can help us extend our understanding of the mechanical response of ropes.

This first development did not integrate the visco-elasto-plastic behaviour of rope-yarns and the dissipation during slidings between the rope-yarns (transverse shearing and axial shearing). At this stage, only the relative slidings are described. Work is still needed to add all types of dissipation and quantify the friction during loading of the rope. Hence, a future project should add the friction between the rope-yarns by changing the current 2D elastic law for a 2D elasto-plastic law of the Saint-Venant type; an elastic spring in series with a plastic element. The plastic strain will describe the friction during sliding, and the plastic dissipated energy will predict the energy dissipated by friction. A visco-elasto-plastic behaviour at the rope-yarns scale could be added by using a 1D rheological model for the axial elongation behaviour of the rope-yarns instead of the current hyperelastic law proposed.

After such improvements, the model should be able to predict:

- the frictions between the three strands and between the rope-yarns inside the strands;
- their dissipated energies and all deformation within the sub-rope.

This model will be a helpful numerical tool to improve our understanding of the fatigue damage mechanisms. Also, it can give insights on the deformation and elongation that occur during the first loading of synthetic fibre ropes. It may also assist in monitoring developments, such as evaluation of the impact of sensors implanted within the sub-rope. Furthermore, this model is a useful tool for other hierarchical materials made of bundle of fibres.

General conclusions and perspectives

General conclusions

The development of offshore floating wind turbines, at affordable cost, requires the design of innovative mooring solutions and an increase of the knowledge on failure modes, prevention and monitoring. The first platforms will be located in shallow waters and subjected to the swell and the wind. They will require mooring lines that maintain the floater position and withstand the environmental loads. Polyamide 6 ropes are of great interest because of their light weight, high strain to failure, good tension resistance and their dissipative behaviour. The purpose of this thesis was to investigate several areas where knowledge is still required to optimize their use as mooring lines. These can be summarized as follows:

- Their complex visco-elasto-plastic behaviour should be modelled and understood using an appropriate constitutive law;
- They will be subjected to more or less constant loads throughout their whole service life (creep). Hence, their long term creep behaviour should be characterized and the strain generated by creep should be anticipated;
- Mooring lines will be subjected to cyclic loading due to the swell. Hence, their fatigue resistance must be characterized, as well as the failure and damage mechanisms;
- Polyamide 6 sub-ropes are multiscale hierarchical materials. Their non-linear response is due both to their construction, and to behaviour of the polymer fibres. Hence, relying only on experimental studies may limit our understanding of the mechanical response as a large number of parameters need to be examined. Hence, the use of a structural model approach to extend our understanding would be an asset. Also, a model that allows to describe the thermo-mechanical behaviour of ropes and more specifically, that separates the dissipation due to the friction, from the dissipation due to the material would deepen our understanding of their dissipative behaviour and of the damage mechanisms.

The first part of this study was devoted to the state of the art on the modelling, the creep and the fatigue response of synthetic fibre ropes and more specifically, polyamide 6 sub-ropes. The large water uptake and sensitivity to water of polyamide 6 fibre ropes was highlighted and underlined that studies for mooring lines applications shall be performed in water.

An investigation of the constitutive behaviour of polyamide 6 mooring lines via the identification and validation of the POLYAMOOR constitutive law developed by Chevillotte (Chevillotte, 2020; Civier et al., 2023) was then performed. The constitutive model proposed is based on Flory's proposal and its identification was developed using a multi-relaxation test. It combines the following elements:

- A fast spring describing the dynamic behavior,
- A dashpot responsible for the viscous response of the polymer,
- A time-independent part consisting of a ratchet element for the plasticity, and a slow spring responsible for the relaxed elasticity.

A study of a 4T sub-rope, before and after long term creep test (1-year creep at 25%MBL and 1-year recovery at 2%MBL) was performed. The sample after creep presented stiffer mechanical properties than the virgin sample, so a characterization of the properties of the sub-rope subcomponents was performed. It was concluded that it was changes in the construction

geometry at the strand scale (lay-length, diameter, twist angle of the strand) that was responsible for the new properties. The identification of the 11 parameters of the law, was performed on this post creep sample, was performed and showed that the parameter attesting most sensitivity to the changed of the behaviour was the instantaneous stiffness. Another identification, on a higher scale sub-rope (7T), was performed and showed that the law can also describe the behaviour for the case of a more representative construction. A validation of the law on a stochastic loading, more representative of at-sea conditions, was also performed. It was shown that the law provided a good prediction for the dynamic stiffness and the interval of stress-strain. However, the viscous behaviour for long term mechanisms was not properly described by the law and some improvements to the viscosity as defined in the law could be proposed. The POLYAMOOR law was applied to long term creep and it was shown that the relaxation times identified were not adapted to predict this response. The load rate had an influence on the prediction and if the load rate is significantly faster than the load rate used for the identification, it can induce error in the predictions. Finally, the POLYAMOOR law prediction was compared to a strain monitored interrupted fatigue test. The prediction was accurate for the first cycles but did not predict the change in the properties with time, in particular, the evolution of the hysteresis, very probable because the construction in evolving.

An experimental study of the long term creep behaviour of 4T sub-ropes was performed in order to supply missing data and to examine the necessity of running long term creep experiments. It was shown that short term creep tests of up to 3 hours could provide a good prediction of long term creep of up to 2 years using a logarithmic-linear law. The main difference between short and long term creep tests was shown to be the instantaneous strain. Also, it was revealed that short term creep at high loads, comparable to storm events, generated more creep strain than long term creep at lower loads (in-service tension). Hence, short term storm events could be used to characterize the creep over the lifetime of a mooring project. Finally, it was highlighted that the history of loading had an influence on the creep and recovery kinetic of polyamide sub-ropes.

The fifth chapter describes an investigation of the fatigue properties of 4T sub-rope samples. First, the S-N curve proposed by Chevillotte was extended to higher number of cycles and lower loads, reaching 10^5 cycles for a cyclic amplitude from 2%MBL to 25%MBL. The linear trend on a semi-log scale was confirmed for the tested load ranges. Damage and failure mechanisms were investigated using SEM images and X-ray tomography analysis. The failure morphology observed at the fibre scales was in accordance with the previously observed morphology (Bunsell & Hearle, 1971; Ramirez et al., 2006) with a tail present on the broken fibres. The X-ray tomography analysis highlighted a change in the state of the material at the rope-yarns scale, showing that the fibres had rearranged leading to a denser material. Also, a change in the surface aspect was noted and was related to the friction between the fibres of the two strands in contact. This produced a lustering effect similar to observation on other types of synthetic fibre rope (Bain, Marco, et al., 2022). A strain monitored fatigue test performed on a 4T sub-rope sample was performed and it was observed that the hysteresis energy loop increased with the number of cycles. This evolution of hysteresis, and the ratcheting strain also observed, seemed mainly due to the evolution of the construction. A slippage of the splices was also highlighted. Other tests should be performed to validate the repeatability of this results. Finally, a study of the heat-build prediction method was performed. The robustness and repeatability of the heat build-up experimental protocol was validated (same results obtained by three operators). The prediction was adapted using the new data on the fatigue S-N curve and the new data points on the self-heating curve. This new prediction has been chosen to be conservative and its determination is still only graphical. However, it allows a good prediction of the S-N curve and could provide a precious method to limit the experimental difficulties associated with the

characterisation of the fatigue lifetime on ropes, and to offer the possibility of fast screening of multiple parameters. Indeed, testing at 0.1 Hz leads to huge experimental campaigns so it is very important to speed up the characterization. By comparison, one heat build-up test, performed to predict the lifetime at 10^5 cycles, last one day while one fatigue test, at 0.1Hz and reaching 10^5 cycles, last 1 month.

The last chapter of this manuscript describes the development of a 3D mesoscale model of a rope structure, aiming to understand the interactions and displacements between the components of the rope. This method involves modelling each strand by a meshed three-dimensional solid in a finite element analysis software. The strand is considered as a homogeneous material that is defined by a behaviour law that models the transverse-isotropic behaviour of a rope-yarn bundle. The objectives of the model are to evaluate the friction at two scales: the strands and the rope-yarns. At the strand scale, the determination of the contact surfaces, contact forces and friction is needed and will be described by the contact law used in the finite element analysis software. At the rope-yarns scale, the anisotropic law used has to quantify the friction strains and the dissipative behaviour of the rope-yarns. The chosen approach, to define the law of the rope-yarn bundle, is a development of a hyperelastic law proposed by Charmetant *et al.* (Charmetant et al., 2011). It is based on physically motivated invariants, that should describe the different strain modes of the studied material, and allow to choose specific constitutive behaviour laws for each strain mode. The limitation of Charmetant's choice of invariants was the description of the friction modes and this study proposed a new choice of invariants that provide a complete description of the strain and hence, of the friction displacements. This work proposed a feasibility study, both experimental and numerical, of the development, identification and use of this type of law to study the mechanical response of a 3 stranded twisted sub-rope. It was chosen to define the bundle of rope-yarns as a hyperelastic material, so there is no: dissipative behaviour in the shear strain modes and visco-elasto-plastic behaviour. Finally, the FiBuLa law first definition, with the proposed invariants and with hyperelastic potentials for all the strain modes, was proposed. The identification of the FiBuLa law required the development of two innovative experimental set-ups at the strand and rope-yarns scales. A first simulation of a strand, under tensile cyclic loading validated the proposed law and 3D modelling. At the rope-yarns scale, the evolution of the invariants was in accordance with the description of the mechanics of twisted ropes proposed by Leech (Leech, 2002). A first simulation of a sub-rope, with no experimental validation, was proposed. It was shown that the model helps to understand the strain fields at the rope-yarn and strand scales, both for the evolution of the geometry and the evolution of the compacity and change of volume. It provided the contact geometry and forces between the strands.

This work addressed four main questions. Several answers have been found to each of those questions but, some questions still remain unanswered and new questions have also been raised.

Perspectives

First, considering the constitutive law, the validation of the law on a higher scale has showed that the viscous behaviour of the law could be improved. This was confirmed by comparing the predictions with long term creep test results. Two possibilities are available: using the same identification but, for longer relaxations plateau, to identify relaxation times more adapted to longer duration phenomena; proposing a new expression of the viscous behaviour that allows several relaxations times to be defined. Also, it was shown that the fatigue response was properly represented by the law for the first cycles (stiffness, plasticity, hysteresis) but, as the law does not predict any change of construction, it cannot predict the permanent strain, changes in the hysteresis and the increase in stiffness during unloading. It would be interesting to

identify the whole set of parameters on a sample after fatigue testing, in order to evaluate the property changes or, alternatively to define a set of properties more adapted to the behaviour of samples after cyclic loading (after a stabilisation of the construction similar to a bedding-in). This work would be comparable to the work of identifying the parameters on a sample after long term creep. Also, for the final use for dimensioning offshore floating wind moorings, the law should be identified at the correct scale (on higher MBL sub-rope). Finally, in parallel to this study, at-sea tests were started using a buoy moored by monitored polyamide 7T sub-rope lines. Hence, a first in-sea validation of the law, identified at this scale, could be performed using the data recorded on the buoy. These values could be compared predictions using both current design practice (linear stiffness model) and the improved model, to assess the benefits of using the POLYAMOOR law.

The long term experimental creep set-up allowed an investigation of the creep under a maximum load of 39%MBL. This in already an original result, but the equipment was not designed to test higher creep loads nor to study failure of a sub-rope after static creep. Hence, an experimental set-up allowing such test at the sub-rope scale for higher loads, that could reach failure after a certain time, would be interesting. Also, only one sub-rope was characterized after a long term creep test, to evaluate the evolution of its mechanical properties. Hence, choices had to be made and not all the properties could be investigated. It would be interesting to perform a quasi-static tensile test to rupture on one of the remaining sub-rope to determine its residual strength. Another interesting investigation would be to perform an X-ray tomography and SEM analysis on one of the sub-rope after long term creep. A comparison between the state of the material after long term creep and the state of the material after fatigue (observed in this study) could allow a better understanding of the mechanics of the rope, depending on the loading path it is subjected to. Also, it was shown that the construction geometry has changed during the long term creep test and that this was responsible for the higher mechanical properties. Hence, a closer monitoring of the construction during such tests might confirm the results of this study.

The fatigue study on 4T sub-rope samples allowed a significant extension of the S-N curve at the sub-rope scale. It was shown that this scale provided a curve comparable to the results obtained for higher scales. Nevertheless, even the extended S-N curve, only could reached 10^5 cycles and it would be beneficial to continue extending this curve for this sub-rope construction. Even at this scale, performing tests lasting several months raises several experimental difficulties. Investigations on the effect of the test frequency on mechanical and thermal response (heat-build-up, friction, ratchetting) and on the visco-elastic response of the ropes should be performed to allow a higher test frequency. The obtained curve on this construction scale would be conservative. In fact, using a higher scale construction to obtain an extended S-N curve, would require adapting the experimental set-up or testing on other test machines that are more complicated to occupy for long time testing (availability issues).

The strain monitored test highlighted that creep strain, and evolution of the hysteresis loop, could be observed during cyclic loading. Depending on the load ratio, the influence of creep and cyclic loading on the fatigue life of the sub-rope might change. Hence, it would be interesting to perform a fatigue test campaign, with different load ratios. These results could also check the repeatability of the obtained mechanical behaviour under cyclic loading and provide experimental data to validate the mesoscale model at the sub-rope scale.

The investigation of the heat build-up method validated the experimental protocol. Work is still needed to better take into consideration the water effect on the infrared measurements. Also, the approach to propose a prediction is still based on a graphical analysis of the self-heating curve. The main objective in the future is to have a better understanding of the physical

mechanisms and to be able to replace the graphical approach. Hence, the use of an infrared camera with a higher spatial resolution could allow to distinguish the zones with more dissipation. It would also be interesting to develop an experimental set-up that allows to perform such type of tests on smaller scale (strands), to determine the dissipation added by the scale effect. Furthermore, the 3D mesoscale model, developed in chapter 6, aims at improving our understanding of the dissipation by distinguishing the dissipation due to friction from the dissipation due to the material. Therefore, this should also allow us to improve our analysis of the self-heating curve.

The failure and damage analysis raised interesting questions about material reorganization during a fatigue test. We observed a change in the surface aspect, at the fibres scale, that would lead to a change in the friction coefficient and so, a change in the abrasion and hence, the fatigue life. These observations indicated that a smoother surface, hence associated with a lower friction coefficient. This change will also impact the dissipation and so, the self-heating of the material. An interesting study would be to perform interrupted fatigue tests at different lifetimes. To evaluate the change in the self-heating of the sub-rope, it would be interesting to perform a heat build-up protocol, after the interruption of each fatigue test. This could quantify the dissipation with time and the sensitivity of the heat build-up measure to the evolution of the mechanical response of the material. The samples could then be analysed using X-ray tomography analysis and SEM images to characterize the rope structure and organisation changes with time.

In its current state, the proposed mesoscale model has no dissipation in the strain modes associated with friction and no visco-elasto-plastic behaviour in the axial strain mode. Hence, a future project should add the friction between the rope-yarns by changing the current 2D elastic law for a 2D elasto-plastic law of the Saint-Venant type; an elastic spring in series with a plastic element. Then, the plastic strain will describe the friction sliding, and the plastic dissipated energy will predict the dissipated energy by friction. The visco-elasto-plastic behaviour, at the rope-yarns scale, could be added by using a 1D rheological model for the axial elongation behaviour of the rope-yarns instead of the current hyperelastic law proposed. Furthermore, a first simulation of a sub-rope was proposed and showed it could provide a deeper understanding of the mechanics at the different scales. A convergence study of the mesh is also necessary and will have to be performed in future work. The validation of the mesoscale model at the sub-rope scale is still needed and a dedicated experimental campaign is required. The sensitivity of the model to the parameters, such as the friction coefficient between the strands, the lay-length of the sub-rope and the lay-length of the rope-yarns, has to be performed to analyse their influence on the response. This model could be a tool to perform a screening of different construction responses. It can also be a tool for other types of multi-scale hierarchical materials such as other type of synthetic fibre ropes or even human tissues. Indeed, the model developed and implemented during this PhD has already been applied in another study for the investigation of the mechanical response of human shoulder nerves (Perruisseau-Carrier, 2023).

Finally, it may be noted that the work described here is applied to polyamide 6 fibre rope mooring lines. The need to find a suitable low stiffness high strength rope, commercially available in large quantities at low cost, led to this choice by the FOWT industry. However, this may not be the optimum material, and future mooring lines may use other grades of polyamide or alternative synthetic fibre materials. Nevertheless the methodology described here will still be applicable, provided it is based on appropriate identification procedures.

References

Abello, L. S., Marco, Y., Le Saux, V., Robert, G., & Charrier, P. (2013). Fast Prediction of the Fatigue Behavior of Short Fiber Reinforced Thermoplastics from Heat Build-up Measurements. *Procedia Engineering*, *66*, 737–745. https://doi.org/10.1016/j.proeng.2013.12.127

Amaral, G. A. do. (2020). *Analytical assessment of the mooring system stiffness.* Universidade de São Paulo, PhD thesis.

Bain, C. (2020). *Compréhension et modélisation des mécanismes de contact des câbles en polyéthylène haut module*. Thèse de Doctorat, Université Bretagne Loire.

Bain, C., Davies, P., Bles, G., Marco, Y., & Barnet, J. (2020). Influence of bedding-in on the tensile performance of HMPE fiber ropes. *Ocean Engineering*, *203*, 107144. https://doi.org/10.1016/j.oceaneng.2020.107144

Bain, C., Davies, P., Riou, L., Marco, Y., Bles, G., & Damblans, G. (2022). Experimental evaluation of the main parameters influencing friction between polyamide fibers and influence of friction on the abrasion resistance. *The Journal of The Textile Institute*, 1–9. https://doi.org/10.1080/00405000.2022.2105075

Bain, C., Marco, Y., Davies, P., Bles, G., Reinhart, T., & Albouy, P.-A. (2022). An investigation of the appearance of lustering on HMPE fiber ropes. *Applied Ocean Research*, *125*, 103244. https://doi.org/10.1016/j.apor.2022.103244

Banfield, S., & Ridge, I. M. L. (2017). Fatigue durability of nylon rope for permanent mooring design. *OCEANS 2017 - Aberdeen*, 1–9. https://doi.org/10.1109/OCEANSE.2017.8084825

Bles, G. (2023). *Behaviour Law and theoritical development* [Internal Report].

Bles, G., & Kadiri, M. (2020). *Compliant and lasting polyamide mooring line for renewable marine energies* [Internal Report].

Bles, G., Nowacki, W. K., & Tourabi, A. (2009). Experimental study of the cyclic visco-elasto-plastic behaviour of a polyamide fibre strap. *International Journal of Solids and Structures*, *46*(13), 2693–2705. https://doi.org/10.1016/j.ijsolstr.2009.02.015

Bunsell, A. R., & Hearle, J. W. S. (1971). A mechanism of fatigue failure in nylon fibres. *Journal of Materials Science*, *6*(10), 1303–1311. https://doi.org/10.1007/BF00552044

Chailleux, E., & Davies, P. (2003). Modelling the Non-Linear Viscoelastic and Viscoplastic Behaviour of Aramid Fibre Yarns. *Mechanics of Time-Dependent Materials*, *291*, 291–303. https://doi.org/10.1023/B:MTDM.0000007199.01142.f8

Chailleux, E., & Davies, P. (2005). A Non-Linear Viscoelastic Viscoplastic Model for the Behaviour of Polyester Fibres. *Mechanics of Time-Dependent Materials*, *9*(2–3), 147–160. https://doi.org/10.1007/s11043-005-1082-0

Charmetant, A. (2011). *Approches hyperélastiques pour la modélisation du comportement mécanique de préformes tissées de composites*. Thèse de Doctorat, Institut National des sciences appliquées de Lyon.

Charmetant, A., Vidal-Sallé, E., & Boisse, P. (2011). Hyperelastic modelling for mesoscopic analyses of composite reinforcements. *Composites Science and Technology*, *71*(14), 1623–1631. https://doi.org/10.1016/j.compscitech.2011.07.004

Chenal, J.-M., Gauthier, C., Chazeau, L., Guy, L., & Bomal, Y. (2007). Parameters governing strain induced crystallization in filled natural rubber. *Polymer*, *48*(23), 6893–6901. https://doi.org/10.1016/j.polymer.2007.09.023

Chevillotte, Y. (2020). *Characterization of the long-term mechanical behavior and the durability of polyamide mooring ropes for floating wind turbines*. Thèse de Doctorat, Université Bretagne Loire.

Chevillotte, Y., Marco, Y., Bles, G., Devos, K., Keryer, M., Arhant, M., & Davies, P. (2020). Fatigue of improved polyamide mooring ropes for floating wind turbines. *Ocean Engineering*, *199*, 107011. https://doi.org/10.1016/j.oceaneng.2020.107011

Chevillotte, Y., Marco, Y., Davies, P., Bles, G., & Arhant, M. (2018). Fatigue of polyamide mooring ropes for floating wind turbines. *MATEC Web of Conferences*, *165*, 10002. https://doi.org/10.1051/matecconf/201816510002

Chimisso, F. E. G. (2009). *Some experimental results regarding creep behavior on synthetic materials used to produce offshore mooring ropes*. Mechanics of Solids in Brazil, Brazil.

Civier, L., Chevillotte, Y., Bles, G., Damblans, G., Montel, F., Davies, P., & Marco, Y. (2023). Visco-elasto-plastic characterization and modeling of a wet polyamide laid-strand sub-rope for floating offshore wind turbine moorings. *Submitted to Ocean Engineering*.

Civier, L., Chevillotte, Y., Bles, G., Montel, F., Davies, P., & Marco, Y. (2022). Short and long term creep behaviour of polyamide ropes for mooring applications. *Ocean Engineering*, *259*, 111800. https://doi.org/10.1016/j.oceaneng.2022.111800

Colomban, Ph., Herrera Ramirez, J. M., Paquin, R., Marcellan, A., & Bunsell, A. (2006). Micro-Raman study of the fatigue and fracture behaviour of single PA66 fibres: Comparison with single PET and PP fibres. *Engineering Fracture Mechanics*, *73*(16), 2463–2475. https://doi.org/10.1016/j.engfracmech.2006.04.033

Davies, P., Bunsell, A. R., & Chailleux, E. (2010). Tensile fatigue behaviour of PBO fibres. *Journal of Materials Science*, *45*(23), 6395–6400. https://doi.org/10.1007/s10853-010-4721-z

Davies, P., Durville, D., & Vu, T. D. (2016). The influence of torsion on braided rope performance, modelling and tests. *Applied Ocean Research*, *59*, 417–423. https://doi.org/10.1016/j.apor.2016.07.003

Davies, P., Huard, Grosjean, G., & Francois, M. (2000). Creep and Relaxation of Polyester Mooring Lines. *All Days*, OTC-12176-MS. https://doi.org/10.4043/12176-MS

Davies, P., Lacotte, N., Kibsgaard, G., Craig, R., Cannell, D., François, S., Lodeho, O., Konate, K., Mills, S., François, M., Defoy, A.-L., Durville, D., Vu, D., Gilmore, J., & Sherman, D. (2013). Bend Over Sheave Durability of Fibre Ropes for Deep Sea Handling Operations. *Volume 1: Offshore Technology*, V001T01A064. https://doi.org/10.1115/OMAE2013-11332

Del Vecchio, C. J. M. (1992). *Light Weight Materials for Deep Water Moorings*. University of Reading, PhD Thesis.

Deshoulles, Q., Le Gall, M., Dreanno, C., Arhant, M., Priour, D., & Le Gac, P.-Y. (2021). Modelling pure polyamide 6 hydrolysis: Influence of water content in the amorphous phase. *Polymer Degradation and Stability*, *183*, 109435. https://doi.org/10.1016/j.polymdegradstab.2020.109435

DNV. (2021). *DNV-OS-E301 Position mooring*.

DNVGL-RP-E305. (2015). *DNVGL-RP-E305 Design, Testing and Analysis of Offshore Fibre Ropes*.

Doudard, C., Calloch, S., Cugy, P., Galtier, A., & Hild, F. (2005). A probabilistic two-scale model for high-cycle fatigue life predictions. *Fatigue and Fracture of Engineering Materials and Structures*, *28*(3), 279–288. https://doi.org/10.1111/j.1460-2695.2005.00854.x

Durville, D. (2012). Contact-friction modeling within elastic beam assemblies: An application to knot tightening. *Computational Mechanics*, *49*(6), 687–707. https://doi.org/10.1007/s00466-012-0683-0

Falkenberg, E., Åhjem, V., & Yang, L. (2017). Best Practice for Analysis of Polyester Rope Mooring Systems. *Day 3 Wed, May 03, 2017*, D031S034R006. https://doi.org/10.4043/27761-MS

Fancey, K. S. (2005). A mechanical model for creep, recovery and stress relaxation in polymeric materials. *Journal of Materials Science*, *40*(18), 4827–4831. https://doi.org/10.1007/s10853-005-2020-x

Flory, J. F., Ahjem, V., & Banfield, S. J. (2007). A New Method of Testing for Change-in-Length Properties of Large Fiber-Rope Deepwater Mooring Lines. *All Days*, OTC-18770-MS. https://doi.org/10.4043/18770-MS

Flory, J. F., Banfield, S. J., & Berryman, C. (2007). Polyester Mooring Lines on Platforms and MODUs in Deep Water. *All Days*, OTC-18768-MS. https://doi.org/10.4043/18768-MS

Flory, J. F., Banfield, S. J., Ridge, I. M. L., Yeats, B., & Mackay, T. (2016). Mooring systems for marine energy converters. *OCEANS 2016. MTS/IEEE*, 1–13. https://doi.org/10.1109/OCEANS.2016.7761007.

Flory, J. F., & Hagedorn, J. H. (2003). Proper use of fiber ropes on capstans and bitts. *Oceans 2003. Celebrating the Past ... Teaming Toward the Future (IEEE Cat. No.03CH37492)*, 1064-1069 Vol.2. https://doi.org/10.1109/OCEANS.2003.178488

Forest, S. (2022). *Mécanique des milieux continus*. Les Presses des Mines. https://www.cairn-sciences.info/mecanique-des-milieux-continus--9782356718402.htm

François, M., & Davies, P. (2008). Characterization of Polyester Mooring Lines. *Volume 1: Offshore Technology*, 169–177. https://doi.org/10.1115/OMAE2008-57136

Francois, M., & Davies, P. (2023). An empirical model to predict elongation of polyamide mooring lines for floating wind turbines. *Submitted to Ocean Engineering*.

Gasser, T. C., Ogden, R. W., & Holzapfel, G. A. (2006). Hyperelastic modelling of arterial layers with distributed collagen fibre orientations. *Journal of The Royal Society Interface*, *3*(6), 15–35. https://doi.org/10.1098/rsif.2005.0073

Germain, P. (1973). *Cours de Mécanique des Milieux Continus*.

Ghoreishi, S. R. (2005). *Modélisation analytique et caractérisation expérimentale du comportement de câbles synthétiques*. Thèse de Doctorat, Ecole Centrale Nantes.

Ghoreishi, S. R., Cartraud, P., Davies, P., & Messager, T. (2007). Analytical modeling of synthetic fiber ropes subjected to axial loads. Part I: A new continuum model for multilayered fibrous structures. *International Journal of Solids and Structures*, *44*(9), 2924–2942. https://doi.org/10.1016/j.ijsolstr.2006.08.033

Ghoreishi, S. R., Davies, P., Cartraud, P., & Messager, T. (2007). Analytical modeling of synthetic fiber ropes. Part II: A linear elastic model for 1+6 fibrous structures. *International Journal of Solids and Structures*, *44*(9), 2943–2960. https://doi.org/10.1016/j.ijsolstr.2006.08.032

Goskoy, M. (1986). *A study of yarn-on-yarn abrasion*. Universisty of Manchester Institute of Science and Technology, PhD thesis.

Gros, A., Tosaka, M., Huneau, B., Verron, E., Poompradub, S., & Senoo, K. (2015). Dominating factor of strain-induced crystallization in natural rubber. *Polymer*, *76*, 230–236. https://doi.org/10.1016/j.polymer.2015.08.058

Guimarães, G. B., & Burgoyne, C. J. (1992). Creep behaviour of a parallel-lay aramid rope. *Journal of Materials Science*, *27*(9), 2473–2489. https://doi.org/10.1007/BF01105061

Guo, Z., Peng, X., & Moran, B. (2007). Large deformation response of a hyperelastic fibre reinforced composite: Theoretical model and numerical validation. *Composites Part A: Applied Science and Manufacturing*, *38*(8), 1842–1851. https://doi.org/10.1016/j.compositesa.2007.04.004

Heiberg, G., Berge, H.-E., & Barros, P. (2021, August 1). Research project examines mooring design for floating offshore wind. *Offshore*. https://www.offshore-mag.com/renewable-energy/article/14206579/dnv-energy-systems-research-project-examines-mooring-design-for-floating-offshore-wind

Herrera-Ramirez, J.-M. (2004). *Les mécanismes de fatigue dans les fibres thermoplastiques*. Thèse de Doctorat, Ecole Nationale Supérieure des Mines de Paris.

Hobbs, R. E., & Ridge, I. M. L. (2018). A new estimate of the yarn-on-yarn friction coefficient. *The Journal of Strain Analysis for Engineering Design*, *53*(4), 191–196. https://doi.org/10.1177/0309324718760883

Hoger, A. (1986). *The material time derivative of logarithmic strain. 22*, 1019–1032. https://doi.org/10.1016/0020-7683(86)90034-X

Huang, W., Liu, H., Lian, Y., & Li, L. (2013). Modeling nonlinear creep and recovery behaviors of synthetic fiber ropes for deepwater moorings. *Applied Ocean Research*, *39*, 113–120. https://doi.org/10.1016/j.apor.2012.10.004

Huang, W., Liu, H., Lian, Y., & Li, L. (2015). Modeling nonlinear time-dependent behaviors of synthetic fiber ropes under cyclic loading. *Ocean Engineering*, *109*, 207–216. https://doi.org/10.1016/j.oceaneng.2015.09.009

Humeau. (2017). *Contribution to the study of coupling between moisture diffusion and mechanical stress, in high performance marine materials*. Thèse de Doctorat, Université Bretagne Loire.

Humeau, C., Davies, P., LeGac, P. Y., & Jacquemin, F. (2018). Influence of water on the short and long term mechanical behaviour of polyamide 6 (nylon) fibres and yarns. *Multiscale and Multidisciplinary Modeling, Experiments and Design*, *1*(4), 317–327. https://doi.org/10.1007/s41939-018-0036-6

Hunt, D. G., & Darlington, M. W. (1978). Accurate measurement of creep of nylon-6,6 at constant temperature and humidity. *Polymer*, *19*(8), 977–983. https://doi.org/10.1016/0032-3861(78)90209-4

Hunt, D. G., & Darlington, M. W. (1979). Prediction of creep of nylon-6,6 at constant stress, temperature and moisture content. *Polymer*, *20*(2), 241–246. https://doi.org/10.1016/0032-3861(79)90228-3

Huntley, M. B. (2016). Fatigue and modulus characteristics of wire-lay nylon rope. *OCEANS 2016 MTS/IEEE Monterey*, 1–6. https://doi.org/10.1109/OCEANS.2016.7761501

Jegou, L., Marco, Y., Le Saux, V., & Calloch, S. (2013). Fast prediction of the Wöhler curve from heat build-up measurements on Short Fiber Reinforced Plastic. *International Journal of Fatigue*, *47*, 259–267. https://doi.org/10.1016/j.ijfatigue.2012.09.007

Kanzenbach, L., Kießling, R., Stockmann, M., & Ihlemann, J. (2017). Development of a compression chamber for the determination of the bulk modulus. *Materials Today: Proceedings*, *4*(5), 5839–5842. https://doi.org/10.1016/j.matpr.2017.06.055

Kenney, M. C., Mandell, J. F., & McGarry, F. J. (1985). Fatigue behaviour of synthetic fibres, yarns, and ropes. *Journal of Materials Science*, *20*(6), 2045–2059. https://doi.org/10.1007/BF01112288

Lai, J., & Bakker, A. (1996). 3-D schapery representation for non-linear viscoelasticity and finite element implementation. *Computational Mechanics*, *18*, 182–191. https://doi.org/10.1007/BF00369936

Le Clerc, C., Monasse, B., & Bunsell, A. R. (2007). Influence of temperature on fracture initiation in PET and PA66 fibres under cyclic loading. *Journal of Materials Science*, *42*(22), 9276–9283. https://doi.org/10.1007/s10853-007-1864-7

Le Gac, P.-Y., Albouy, P.-A., & Sotta, P. (2019). Strain-induced crystallization in a carbon-black filled polychloroprene rubber: Kinetics and mechanical cycling. *Polymer*, *173*, 158–165. https://doi.org/10.1016/j.polymer.2019.04.019

Le Saux, V. (2017). *Celenos users manual, Internal report.* [Rapport interne]. ENSTA Bretagne.

Le Saux, V., Marco, Y., Calloch, S., Doudard, C., & Charrier, P. (2010). Fast evaluation of the fatigue lifetime of rubber-like materials based on a heat build-up protocol and micro-tomography measurements. *International Journal of Fatigue*, *32*(10), 1582–1590. https://doi.org/10.1016/j.ijfatigue.2010.02.014

Lechat, C. (2007). *Comportement mécanique de fibres et d'assemblages de fibres en polyester pour câbles d'amarrage de plates-formes offshore*. Thèse de Doctorat, Ecole Des Mines de Paris.

Lechat, C., Bunsell, A. R., & Davies, P. (2011). Tensile and creep behaviour of polyethylene terephthalate and polyethylene naphthalate fibres. *Journal of Materials Science*, *46*(2), 528–533. https://doi.org/10.1007/s10853-010-4999-x

Lechat, C., Bunsell, A. R., Davies, P., & Piant, A. (2006). Mechanical behaviour of polyethylene terephthalate & polyethylene naphthalate fibres under cyclic loading. *Journal of Materials Science*, *41*(6), 1745–1756. https://doi.org/10.1007/s10853-006-2372-x

Leech, C. M. (2002). The modelling of friction in polymer fibre ropes. *International Journal of Mechanical Sciences*, *44*, 621–643. https://doi.org/10.1016/S0020-7403(01)00095-9

Leech, C. M., & Hearle, J. W. S. (1993). *Modelling Tension and Torque properties of fibre ropes and splices.* International offshore and polar engineering conference, Singapore. https://api.semanticscholar.org/CorpusID:55471343

Leveuf, L., Marco, Y., Le Saux, V., Navrátil, L., Leclercq, S., & Olhagaray, J. (2018). Fast screening of the fatigue properties of thermoplastics reinforced with short carbon fibers based on thermal measurements. *Polymer Testing*, *68*, 19–26. https://doi.org/10.1016/j.polymertesting.2018.03.045

Lian, Y., Liu, H., Huang, W., & Li, L. (2015). A creep–rupture model of synthetic fiber ropes for deepwater moorings based on thermodynamics. *Applied Ocean Research*, *52*, 234–244. https://doi.org/10.1016/j.apor.2015.06.009

Lian, Y., Liu, H., Li, L., & Zhang, Y. (2018). An experimental investigation on the bedding-in behavior of synthetic fiber ropes. *Ocean Engineering*, *160*, 368–381. https://doi.org/10.1016/j.oceaneng.2018.04.071

Mandell, J. F. (1987). Modeling of Marine Rope Fatigue Behavior. *Textile Research Journal*, *57*(6), 318–330. https://doi.org/10.1177/004051758705700602

Marcellan, A., Bunsell, A. R., Laiarinandrasana, L., & Piques, R. (2006). A multi-scale analysis of the microstructure and the tensile mechanical behaviour of polyamide 66 fibre. *Polymer*, *47*(1), 367–378. https://doi.org/10.1016/j.polymer.2005.10.093

Marco, Y., Masquelier, I., Le Saux, V., & Charrier, P. (2017). Fast prediction of the wöhler curve from thermal measurement for a wide range of NR and SBR compounds. *Rubber Chemistry and Technology*, *90*(3), 487–507. https://doi.org/10.5254/rct.16.83755

McKenna, H. A., Hearle, J. W. S., & O'Hear, N. (2004). *Handbook of fibre rope technology*. Woodhead.

Mitchell J.C, & Meier D.J. (1968). Rapid stress-induced crystallization in natural rubber. *Journal of Polymer Science*, *6*, 1689–1703. https://doi.org/10.1002/pol.1968.160061001

Mukhopadhyay. (2009). Manufacturing, properties and tensile failure of nylon fibres. In *In: Handbook of tensile properties of textile and technical fibres* (A.R.Bunsell-Woodhead publishing in textiles, pp. 197–222). The textile institute.

Naouar, N., Vidal-Salle, E., Maire, E., Schneider, J., & Boisse, P. (2016). Simulation E.F. à l'échelle mésoscopique de la déformation de renforts composite à partir de microtomographie à rayon X. *Matériaux & Techniques*, *104*(4), 409. https://doi.org/10.1051/mattech/2016029

NI 432 Dt R02 E Bureau Veritas. (2007). *Certification of Fibre Ropes for Deepwater Offshore Services.* [Technical Report].

Offshore Wind Europe. (2021). *Wind energy in Europe: 2022 Statistics and the outlook for 2023-2027.* https://windeurope.org/intelligence-platform/product/wind-energy-in-europe-2022-statistics-and-the-outlook-for-2023-2027/

Oland, E., Schlanbusch, R., & Falconer, S. (2020). Condition Monitoring Technologies for Synthetic Fiber Ropes—A Review. *International Journal of Prognostics and Health Management*, *8*(2). https://doi.org/10.36001/ijphm.2017.v8i2.2619

Oudet, C. H., & Bunsell, A. R. (1987). *Effects of structure on the tensile, creep and fatigue properties of polyester fibres*. *22*, 4292–4298. https://doi.org/10.1007/BF01132020

Pal, S. K., Thakare, V. B., & Singh, G. (2007). Creep behaviour of braided cordages made of high performance fibres for aerospace applications. *INDIAN J. FIBRE TEXT. RES.*

Pang, J. W. C., & Fancey, K. S. (2006). An investigation into the long-term viscoelastic recovery of Nylon 6,6 fibres through accelerated ageing. *Materials Science and Engineering: A*, *431*(1–2), 100–105. https://doi.org/10.1016/j.msea.2006.05.052

Parsey, M. R. (1983). *The Fatigue Resistance And Hysteresis Of Man-Made Fibre Ropes*. SPE-11908-MS. https://doi.org/10.2118/11908-MS

Péron, M., Jacquemin, F., Casari, P., Orange, G., Bailleul, J.-L., & Boyard, N. (2018). Thermomechanical characterization of a low viscosity PA66 thermoplastic matrix and associated continuous glass fiber composite under processing conditions. *Journal of Composite Materials, 53 (22)*, pp.3169-3186. https://doi.org/10.1177/0021998319862344

Perruisseau-Carrier, A. (2023). *Modélisation et simulation numérique du comportement mécanique du plexus brachial pour la réparation nerveuse Clinique*. University of Strasbourg, PhD Thesis.

Pham, H., Cartraud, P., Schoefs, F., Soulard, T., & Berhault, C. (2019). Dynamic modeling of nylon mooring lines for a floating wind turbine. *Applied Ocean Research*, *87*, 1–8. https://doi.org/10.1016/j.apor.2019.03.013

Ramirez, J. M. H., Bunsell, A. R., & Colomban, Ph. (2006). Microstructural mechanisms governing the fatigue failure of polyamide 66 fibres. *Journal of Materials Science*, *41*(22), 7261–7271. https://doi.org/10.1007/s10853-006-0421-0

Raoof, M., & Kraincanic, I. (1998). *Prediction of coupled axial/ torsional coefficients of locked-coil ropes. 69*, 1166–1182. https://doi.org/10.1016/S0045-7949(98)00128-X

Rosa, G. L., & Risitano, A. (2000). Thermographic methodology for rapid determination of the fatigue limit of materials and mechanical components. *International Journal of Fatigue*. https://doi.org/10.1016/S0142-1123(99)00088-2

Santharam, P., Marco, Y., Le Saux, V., Le Saux, M., Robert, G., Raoult, I., Guévenoux, C., Taveau, D., & Charrier, P. (2020). Fatigue criteria for short fiber-reinforced thermoplastic validated over various fiber orientations, load ratios and environmental conditions. *International Journal of Fatigue*, *135*, 105574. https://doi.org/10.1016/j.ijfatigue.2020.105574

Schmieder, A., Heinze, T., & Michael, M. (2015). Failure Analysis of High Strength Fiber Ropes. *Materials Science Forum*, *825–826*, 891–898. https://doi.org/10.4028/www.scientific.net/MSF.825-826.891

Seo, M., Wu, H. C., Chen, J., Toomey, C. S., & Backer, S. (1997). *Wear and Fatigue of Nylon and Polyester Mooring Lines*. *67*(7). https://doi.org/10.1177/004051759706700701

Sibellas, A., Adrien, J., Durville, D., & Maire, E. (2019). *Experimental study of the fiber orientations in single and multi-ply continuous filament yarns*. *111*, 646–659. https://doi.org/10.1080/00405000.2019.1659471

Sibellas, A., Rusinowicz, M., Adrien, J., Durville, D., & Maire, E. (2020). *The importance of a variable fibre packing density in modelling the tensile behaviour of single filament yarns*. https://doi.org/10.1080/00405000.2020.1781347

Sørum, S. H., Fonseca, N., Kent, M., & Faria, R. P. (2023). Assessment of nylon versus polyester ropes for mooring of floating wind turbines. *Ocean Engineering*, *278*, 114339. https://doi.org/10.1016/j.oceaneng.2023.114339

Sorum, S. H., Fonseca, N., Kent, M., & Faria, R. P. (2023). Modelling of Synthetic Fibre Rope Mooring for Floating Offshore Wind Turbines. *Journal of Marine Science and Engineering*, *11*(1), 193. https://doi.org/10.3390/jmse11010193

Terzolo, A., Bailly, L., Orgéas, L., Cochereau, T., & Henrich Bernardoni, N. (2022). A micro-mechanical model for the fibrous tissues of vocal folds. *Journal of the Mechanical Behavior of Biomedical Materials*, *128*, 105118. https://doi.org/10.1016/j.jmbbm.2022.105118

University of Stratchlyde. (2019). *Offshore wind, ready to float? Global UK trends in the floating offshore wind market*. https://doi.org/10.17868/69501

Vlasblom, M., Boesten, J., Leite, S., & Davies, P. (2012). Creep and stiffness of HMPE fiber for permanent deepwater offshore mooring. *2012 Oceans - Yeosu*, 1–7. https://doi.org/10.1109/OCEANS-Yeosu.2012.6263399

Vu, T. D. (2014). *Lifetime of fibre ropes for deep sea handling*. Thèse de Doctorat, Université de Bretagne Occidentale.

Vu, T. D., Durville, D., & Davies, P. (2015). Finite element simulation of the mechanical behavior of synthetic braided ropes and validation on a tensile test. *International Journal of Solids and Structures*, *58*, 106–116. https://doi.org/10.1016/j.ijsolstr.2014.12.022

Wang, Y., Jiao, Y., Wu, N., Xie, J., Chen, L., & Wang, P. (2022). An efficient virtual modeling regard to the axial tensile and transverse compressive behaviors of the twisted yarns. *Journal of Industrial Textiles*, *52*, 152808372211373. https://doi.org/10.1177/15280837221137353

Weller, S. D., Banfield, S. J., & Canedo, J. (2018). Parameter Estimation for Synthetic Rope Models. *Volume 1: Offshore Technology*, V001T01A072. https://doi.org/10.1115/OMAE2018-78606

Weller, S. D., Davies, P., Vickers, A. W., & Johanning, L. (2014). Synthetic rope responses in the context of load history: Operational performance. *Ocean Engineering*, *83*, 111–124. https://doi.org/10.1016/j.oceaneng.2014.03.010

Weller, S. D., Davies, P., Vickers, A. W., & Johanning, L. (2015). Synthetic rope responses in the context of load history: The influence of aging. *Ocean Engineering*, *96*, 192–204. https://doi.org/10.1016/j.oceaneng.2014.12.013

Weller, S. D., Johanning, L., Davies, P., & Banfield, S. J. (2015). Synthetic mooring ropes for marine renewable energy applications. *Renewable Energy*, *83*, 1268–1278. https://doi.org/10.1016/j.renene.2015.03.058

Wielhorski, Y., & Durville, D. (2015). *Finite element simulation of a 3D woven fabric: Determination of the initial configuration and characterization of the mechanical behavior*. Texcomp-12 Conference, May 2015, Rayleigh, NC,, United States. https://hal.science/hal-01361252

Woellwarth, L. (2020, October 3). Floating wind: What are the mooring options？ *Energy Global*. https://www.energyglobal.com/special-reports/03112020/floating-wind-what-are-the-mooring-options/

Appendixes

Appendix A. Figures associated to the identification of the POLYAMOOR law for a virgin 4T sub-rope.

In this section, the full identification and figures associated to the identifications of the POLYAMOOR law for a virgin 4T sub-ropes are presented.

The identification method presented in Chapter 3 section 3.2 was followed.

First, the instantaneous elasticity is identified. Figure 0.1 plots an example of the obtained instantaneous moduli versus the specific stress. The associated linear identification is also plotted.
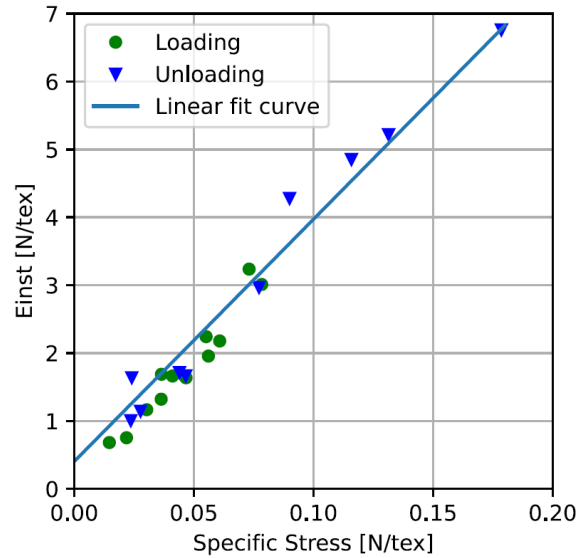
Figure 0.1 - Short-term elasticity modulus (E_{inst}) versus the specific stress at the beginning of the sudden change, i.e. at every re-loading after a relaxation, a creep or a recovery, for a 4T sub-rope

This result can be expressed as:

$$E_{inst} = a \cdot \Sigma + b = \frac{d\Sigma}{d\varepsilon}$$

Eq. 192

Then, the fully relaxed behaviour was identified using the relaxation plateaus. Figure 0.2 plots the fully relaxed behaviour stress versus the fully relaxed behaviour logarithmic strain.
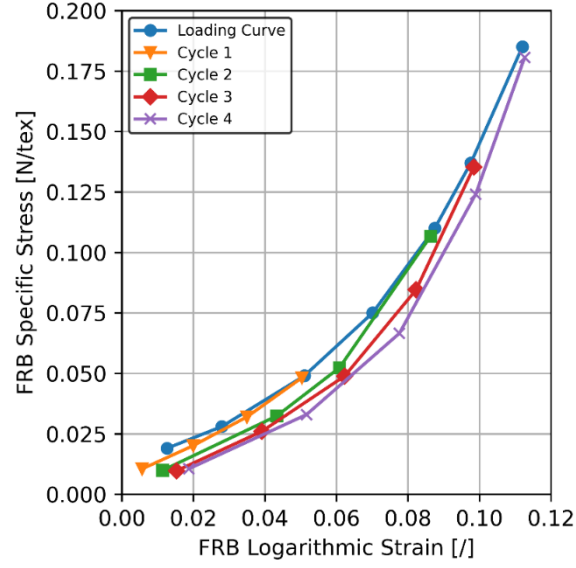
Figure 0.2 - Fully relaxed behavior (FRB) measured on 4T sub-ropes

Then, the tangent modulus associated to the fully relaxed behaviour $M_{FRB} = \dfrac{d\Sigma_{FRB}}{d\varepsilon_{FRB}}$ can be determined between two measured relaxed states of the same cycle. Figure 0.3 plots the obtained FRB modulus versus the mean stress at the middle of two corresponding relaxed state.
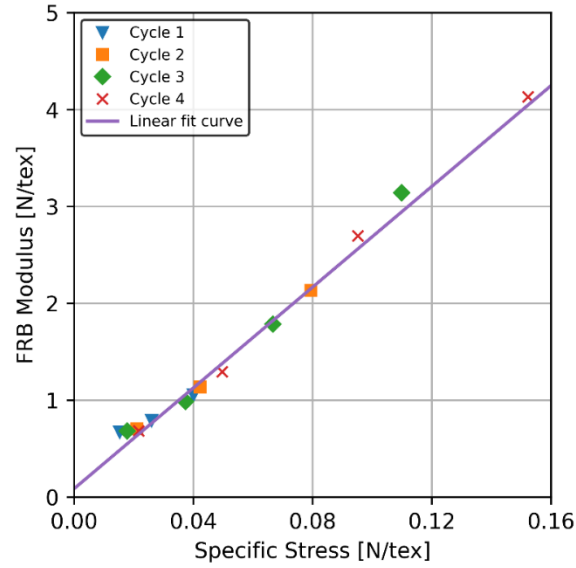
Figure 0.3 - Fully relaxed behaviour tangent modulus $M_{FRB} = \dfrac{d\Sigma_{FRB}}{d\varepsilon_{FRB}}$ versus the associated specific stress for 4T sub-ropes

This result can be expressed as:

$$M_{FRB} = c \cdot \Sigma_{FRB} + g = \frac{d\Sigma_{FRB}}{d\varepsilon_{FRB}}$$

Eq. 193

The plasticity is identified according to the equation:

$$\varepsilon_p = \varepsilon_{FRB} - d^{-1}(\Sigma_{FRB})$$

Eq. 194

The plastic strain is a function of the maximum stress Σ_{FRB}. The obtained plastic strain against the specific stress is plotted in Figure 0.4.
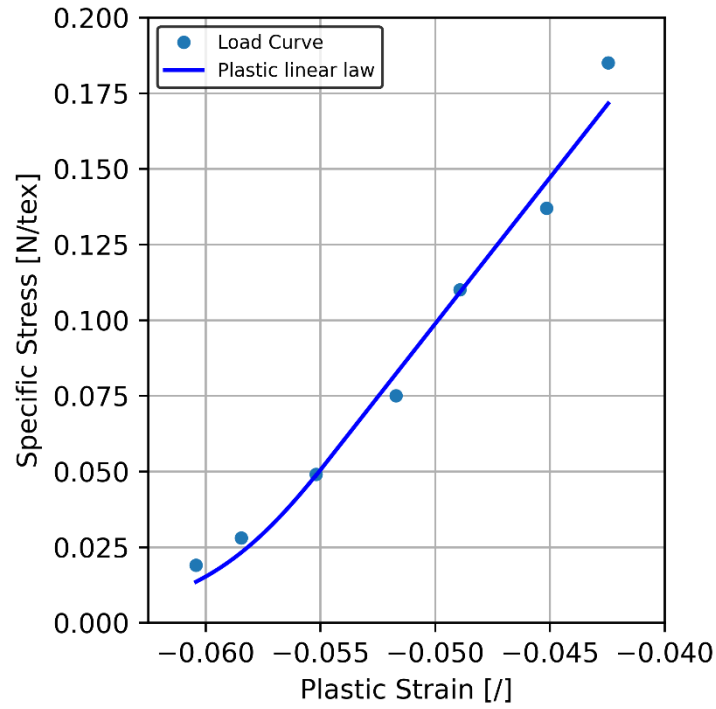
Figure 0.4 - Plastic strain calculated versus the specific stress, for 4T sub-rope

Finally, the viscosity was identified. The figures are presented in chapter 3 of this manuscript in details for a virgin 4T sub-rope.

Appendix B. Figures associated to the identification of the POLYAMOOR law for a virgin 7T sub-rope.

First, a comparison of the behaviour of the 4T virgin sub-rope and the 7T virgin sub-rope is presented in Figure 0.5.
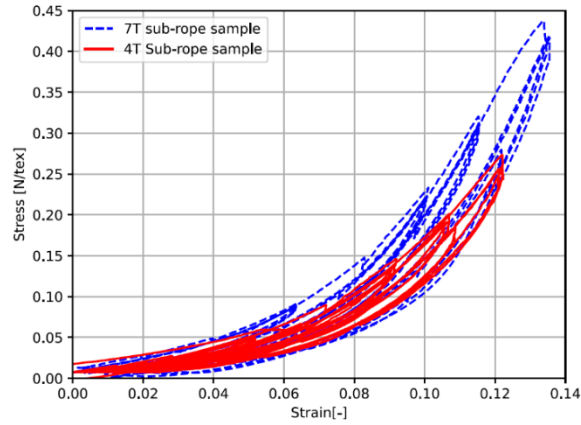
Figure 0.5 - Specific stress [N/tex] versus logarithmic strain [-] of the 4T and the 7T sub-rope samples

In this section, the full identification and figures associated to the identifications of the POLYAMOOR law for a virgin 4T sub-ropes are presented.

The identification method presented in Chapter 3 section 3.2 was followed.

First, the instantaneous elasticity is identified. Figure 0.6 plots an example of the obtained instantaneous moduli versus the specific stress. The associated linear identification is also plotted.
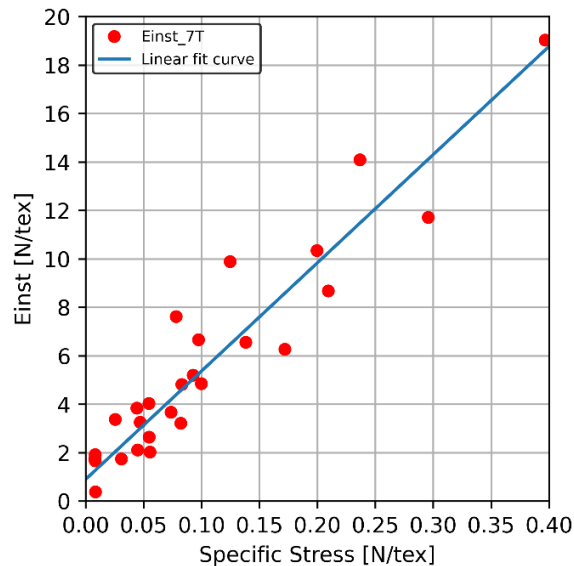

Figure 0.6 - Instantaneous modulus [N/tex] versus Specific Stress [N/tex].

This result can be expressed as:

$$E_{inst} = a \cdot \Sigma + b = \frac{d\Sigma}{d\varepsilon}$$

Then, the fully relaxed behaviour was identified using the relaxation plateaus. Figure 0.7 plots the fully relaxed behaviour stress versus the fully relaxed behaviour logarithmic strain.
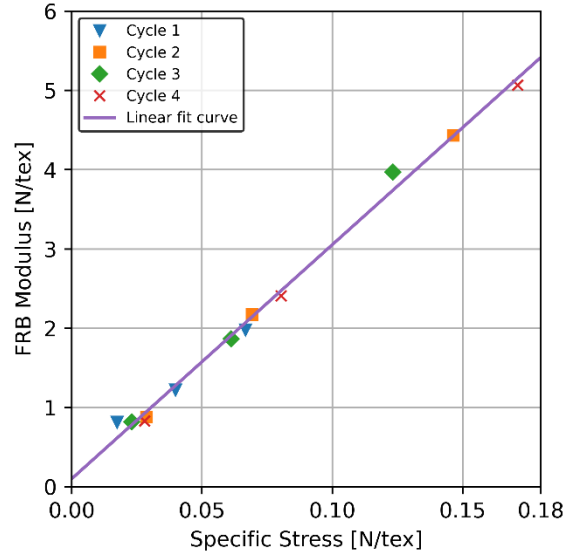

Figure 0.7 - FRB modulus [N/tex] versus Specific Stress [N/tex]

Figure 0.8 presents the plastic strain behaviour identified for 4T and a 7T sub-rope samples.
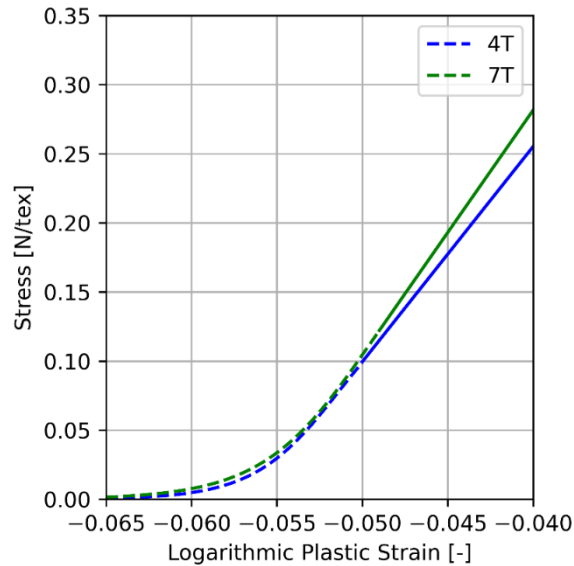
Figure 0.8 - Comparison of the plastic strain behaviour for a 4T and 7T sub-rope behaviour. Specific Stress [N/tex] versus logarithmic plastic strain [-]

Finally, the viscosity was identified. Figure 0.9 presents the viscous behaviour identified on the 7T sub-rope sample. The viscous stress remains low during the first loadings of the loading curve and a sudden increase in viscous stress for the last 3 loadings is observed. This attests the difficulty to identify the viscous behaviour for all the plateau.
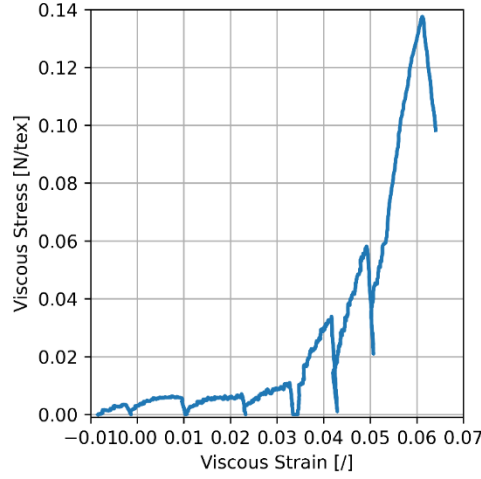
Figure 0.9 – Viscous stress [N/tex] versus viscous strain [-] identified for a 7T sub-rope sample

Figure 0.10t presents the identification of W1 and W2 parameters.
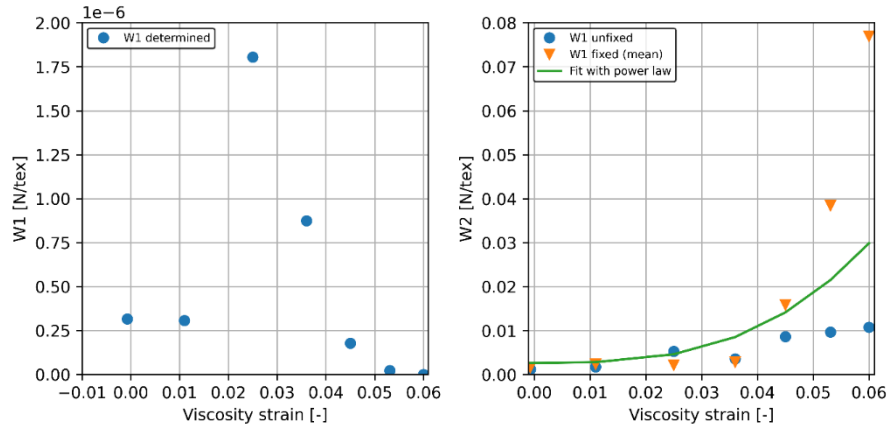
Figure 0.10 - W1 [N/tex] and W2 [N/tex] parameters identified on Figure 0.9 for a 7T sub-rope sample

Again, we can observe on Figure 0.10 that the parameters associated with the dashpot are more complicated to identify than for a virgin 4T sub-rope sample. We observe in Figure 0.10-left that the variation of the W1 parameter is complicated. This leads to a less precise identification of W2 parameters in Figure 0.10-right. However, it still allows a good prediction of the relaxations and recoveries as shown in chapter 3 section 3.4.

Appendix C. Charmetant's Model description

Charmetant *et al.* (Charmetant et al., 2011) proposed and validated an anisotropic hyperelastic model for the mechanical behaviour of textile composite reinforcements. Fabrics are materials that consist of yarns combined together following textile architecture: woven, knitted, braided or non-crimped fabrics. The modeller has to choose how many scales are to be modelled. In Charmetant's work, the mesoscopic scale is chosen (Figure 0.11). This scale describes the weave as interlaced tows, respectively the warp and the weft yarns. Hence, their working scale corresponds to the yarn dimensions (Figure 0.11). The warp and weft yarns are meshed with solid finite elements. The behaviour law of these elements is hyperelastic and based on specific physically motivated invariants. In order to choose these specific invariants, Charmetant *et al.* first analysed the behaviour of the yarns.
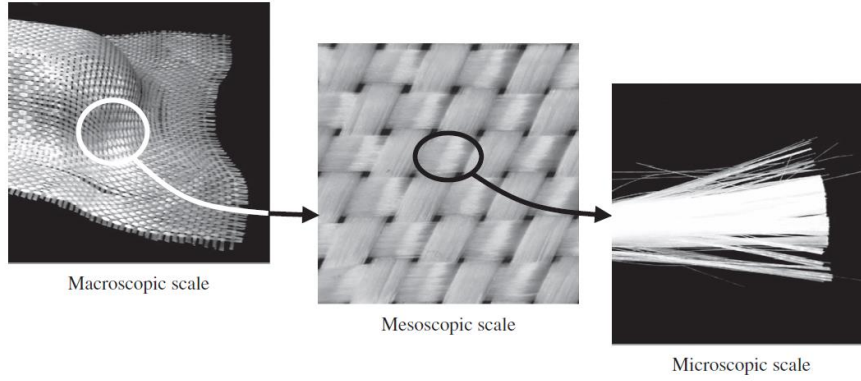
Figure 0.11 - Different scales of a woven reinforcement (Charmetant et al., 2011)

They considered the yarns as an assembly of oriented fibres in approximately the same direction, i.e. a fibre bundle. This fibre bundle was considered as a homogeneous material. The material preferred direction is the fibre one. Then the yarns are considered to be made of this homogeneous material that is modelled as a transverse-isotropic material. They decomposed the deformation gradient of the yarn material, related to their interaction at the microscopic scale, to define the constitutive law. Four deformations modes were considered: the elongation in the fibre direction, the compaction in the transverse section of the yarn, the distortion (shear) in the transverse section and the shear along the fibre direction. Each of these strain modes is associated with a dedicated behaviour law that is experimentally identified. The proposed model does not consider any coupling between the deformation modes.

Their approach is based on a decomposition of the deformation gradient to determine strain physically-based invariants. The use of an orthonormal basis defined as $\left(\vec{M}, \vec{N_1}, \vec{N_2}\right)$ allows the components of the deformation gradient $\tilde{F}$ of transversely isotropic material to be written in the form:

$$[F]_{(\vec{M},\vec{N_1},\vec{N_2})} = \begin{bmatrix} f_m & f_{m1} & f_{m2} \\ 0 & f_{11} & 0 \\ 0 & 0 & f_{22} \end{bmatrix}_{(\vec{M},\vec{N_1},\vec{N_2})} \qquad \text{Eq. 196}$$

The vector $\vec{M}$ represents the preferred direction (fibre axis).

The four deformation modes of the yarn are separated thanks to a multiplicative split of the deformation:

$$\tilde{F} = \widetilde{F_{elong}} \cdot \widetilde{F_{comp}} \cdot \widetilde{F_{dist}} \cdot \widetilde{F_{sh}}$$

where $\widetilde{F_{elong}}, \widetilde{F_{comp}}, \widetilde{F_{dist}}$ and $\widetilde{F_{sh}}$ respectively describe the elongation of the yarn along the fibre direction, the compaction and distortion of the yarn in the transverse direction, and the longitudinal shear of the yarn.

Charmetant *et al.* worked with the Cauchy-Green deformation tensor defined by:

$$\tilde{C} = \tilde{F}^T \tilde{F}$$

The classical associated invariants are:

$$I_1 = trace(\tilde{C})$$
$$I_2 = \frac{1}{2}\left(trace(\tilde{C})^2 - trace(\tilde{C}^2)\right)$$
$$I_3 = \det(\tilde{C})$$

$$I_4 = \tilde{C}:\widetilde{M_0}$$
$$I_5 = (\tilde{C} \cdot \tilde{C}):\widetilde{M_0}$$

For each deformation mode, a dedicated scalar invariant is defined as a function of the classical invariants of the Cauchy-Green deformation tensor $\tilde{C}$:

$$I_{elong} = \frac{1}{2}\ln(I_4)$$
$$I_{comp} = \frac{1}{4}\ln\left(\frac{I_3}{I_4}\right)$$
$$I_{shear} = \sqrt{\frac{I_5}{I_4^2} - 1}$$

$$I_{dist} = \frac{1}{2}\ln\left(\frac{I_1 I_4 - I_5}{2\sqrt{I_3 I_4}} + \sqrt{\left(\frac{I_1 I_4 - I_5}{2\sqrt{I_3 I_4}}\right)^2 - 1}\right)$$

Appendix D. Derivative of the axial shear strain invariants δ_a and δ_b

From chapter 6, we have: $\delta_a = \dfrac{c_0}{c} \dfrac{\vec{a} \cdot \vec{e_c}}{a_0}$

$$\Rightarrow \ln \delta_a = \ln \frac{c_0}{a_0} + \ln(\vec{a} \cdot \vec{c}) - \ln(\vec{c} \cdot \vec{c})$$

$$\frac{\dot{\delta}_a}{\delta_a} = \frac{\vec{a} \overset{.}{\cdot} \vec{c}}{\vec{a} \cdot \vec{c}} - \frac{\vec{c} \overset{.}{\cdot} \vec{c}}{\vec{c} \cdot \vec{c}}$$

With $\vec{a} \overset{.}{\cdot} \vec{c} = \dot{\vec{a}} \cdot \vec{c} + \vec{a} \cdot \dot{\vec{c}} = (\tilde{L} \cdot \vec{a}) \cdot \vec{c} + \vec{a} \cdot (\tilde{L} \cdot \vec{c}) = \vec{a} \cdot (\tilde{L}^T \cdot \vec{c}) + \vec{a} \cdot (\tilde{L} \cdot \vec{c})$

Because of Eq 6 chapter 6, we obtain:

$$\vec{a} \overset{.}{\cdot} \vec{c} = 2 \cdot \vec{a} \cdot (\tilde{D} \cdot \vec{c}) = 2 \cdot \tilde{D} : (\vec{a} \otimes \vec{c})$$

And

$$\vec{c} \overset{.}{\cdot} \vec{c} = 2 \cdot \vec{c} \cdot (\tilde{D} \cdot \vec{c}) = 2 \cdot \tilde{D} : (\vec{c} \otimes \vec{c})$$

Hence,

$$\frac{\dot{\delta}_a}{2\delta_a} = \left(\frac{\vec{a} \otimes \vec{c}}{\vec{a} \cdot \vec{c}} - \frac{\vec{c} \otimes \vec{c}}{\vec{c} \cdot \vec{c}} \right) : \tilde{D}$$

Also: $\overrightarrow{a_\pi} = \widetilde{P_c} \cdot \vec{a} = \vec{a} - \left(\frac{(\vec{a} \cdot \vec{c}) \cdot \vec{c}}{\vec{c} \cdot \vec{c}} \right) = (\vec{a} \cdot \vec{c}) \cdot \left[\frac{\vec{a}}{(\vec{a} \cdot \vec{c})} - \frac{\vec{c}}{\vec{c} \cdot \vec{c}} \right]$

Hence,

$$\frac{\dot{\delta}_a}{2\delta_a} = \left(\frac{\overrightarrow{a_\pi} \otimes \vec{c}}{\vec{a} \cdot \vec{c}} \right) : \tilde{D}$$

$$\dot{\delta}_a = 2 \frac{c_0}{a_0} \left(\frac{(\vec{a} \cdot \vec{c})}{\vec{c} \cdot \vec{c}} \right) \left(\frac{\overrightarrow{a_\pi} \otimes \vec{c}}{\vec{a} \cdot \vec{c}} \right) : \tilde{D}$$

$$\dot{\delta}_a = 2 \frac{c_0}{c \cdot a_0} (\overrightarrow{a_\pi} \otimes \overrightarrow{e_c}) : \tilde{D}$$

And we know: $\overrightarrow{a_\pi} = \tilde{F}_\pi \cdot \overrightarrow{a_0}$ and $\vec{c} = \tilde{F}_\pi \cdot \overrightarrow{c_0}$ hence, $\overrightarrow{e_c} = \frac{c_0}{c} \tilde{F}_\pi \overrightarrow{e_{c0}}$

$$\dot{\delta}_a = 2 \left(\frac{c_0}{c} \right)^2 \frac{1}{a_0} \left(\tilde{F}_\pi \cdot (\overrightarrow{a_0} \otimes \vec{e}_{c0}) \cdot \tilde{F}_\pi^{\,T} \right) : \tilde{D}$$

$$\dot{\delta}_a = 2 \left(\frac{c_0}{c} \right)^2 \left(\tilde{F}_\pi \cdot (\vec{e}_{a0} \otimes \vec{e}_{c0}) \cdot \tilde{F}_\pi^{\,T} \right) : \tilde{D}$$

Because $2\tilde{A} : \tilde{D} = (\tilde{A} + \tilde{A}^T) : \tilde{D}$:

$$\dot{\delta}_a = \left(\frac{c_0}{c} \right)^2 \left(\tilde{F}_\pi \cdot (\vec{e}_{a0} \otimes \vec{e}_{c0} + \vec{e}_{c0} \otimes \vec{e}_{a0}) \cdot \tilde{F}_\pi^{\,T} \right) : \tilde{D}$$

and with $\vec{e}_{a0} \otimes \vec{e}_{c0} + \vec{e}_{c0} \otimes \vec{e}_{a0} = \widetilde{D_5} \cdot \sqrt{2}$

Finally: $\dot{\delta}_a = \sqrt{2} \left(\frac{c_0}{c} \right)^2 \left[\widetilde{Q_{(\tilde{F}_\pi)}} : \widetilde{D_5} \right] : \tilde{D}$. The same demonstration allows to obtain $\dot{\delta}_b$.

Appendix E. Proof of an expression needed for the stress tensor associated with the distortion strain mode of $\widetilde{W'_{ab}}$

$$\left[\tilde{\tilde{Q}}_{(\widetilde{P_c}.\widetilde{R_\pi})}:\widetilde{\widetilde{\gamma_{(U_\pi)}}} - \frac{1}{2}\left(\tilde{P_c} \otimes \widetilde{P_{c0}}\right)\right]:\widetilde{W'_{ab}} = \tilde{\tilde{Q}}_{(\widetilde{R_\pi})}:\widetilde{\widetilde{\gamma_{(U_\pi)}}}:\widetilde{W'_{ab}}$$

This last equation can be demonstrated:

Indeed: We first have:

$$\left(\tilde{P_c} \otimes \widetilde{P_{c0}}\right):\widetilde{W'_{ab}} = \tilde{\emptyset}$$

Because: $\widetilde{P_{c0}} = \tilde{I} - \vec{e}_{c0}\otimes\vec{e}_{c0} = \begin{bmatrix} 1 & 0 & 0 \\ 0 & 1 & 0 \\ 0 & 0 & 0 \end{bmatrix}_{\overrightarrow{e_{a0}},\overrightarrow{e_{b0}},\overrightarrow{e_{c0}}} = \sqrt{2}\widetilde{D_1}$

With: $\widetilde{W'_{ab}} = W'_{ab11}\sqrt{2}\widetilde{D_2} + W'_{ab12}\sqrt{2}\widetilde{D_4}$

Hence: $\widetilde{P_{c0}}:\widetilde{W'_{ab}} = 2W'_{ab11}\left(\widetilde{D_1}:\widetilde{D_2}\right) + 2W'_{ab12}\left(\widetilde{D_1}:\widetilde{D_4}\right) = \emptyset$

Secondly, we have: $\widetilde{R_\pi} \cdot \vec{e}_{c0} = \vec{e}_c$

Because: $\widetilde{R_\pi} \cdot \vec{e}_{c0} = \widetilde{R_\pi} \cdot \left[\left(\frac{c_0}{c}\right)\widetilde{U_\pi} \cdot \vec{e}_{c0}\right] = \frac{c_0}{c}\widetilde{F_\pi} \cdot \vec{e}_{c0} = \frac{1}{c} \cdot \widetilde{G_\pi} \cdot \tilde{F} \cdot \overrightarrow{C_0} = \frac{\widetilde{G_\pi}\cdot\vec{c}}{c} = \frac{\vec{c}}{c} = \vec{e}_c$

Then, we have: $\tilde{P_c} = \widetilde{R_\pi} \cdot \widetilde{P_{c0}} \cdot \widetilde{R_\pi}^T$

Because: $\widetilde{R_\pi} \cdot (\tilde{I} - \vec{e}_{c0}\otimes\vec{e}_{c0}) \cdot \widetilde{R_\pi}^T = \widetilde{R_\pi} \cdot \widetilde{R_\pi}^T - \left(\widetilde{R_\pi} \cdot \vec{e}_{c0}\right) \otimes \left(\widetilde{R_\pi} \cdot \vec{e}_{c0}\right) = \tilde{I} - \vec{e}_c\otimes\vec{e}_c = \tilde{P_c}$

Thirdly, we have: $\widetilde{Q_{P_{c0}}}:\widetilde{\widetilde{\gamma_{(U_\pi)}}}:\widetilde{W'_{ab}} = \widetilde{P_{c0}} \cdot \left(\widetilde{\widetilde{\gamma_{(U_\pi)}}}:\widetilde{W'_{ab}}\right) \cdot \widetilde{P_{c0}} = \widetilde{\widetilde{\gamma_{(U_\pi)}}}:\widetilde{W'_{ab}}$

Indeed: we call $\left(\overrightarrow{U_{\pi i}}\right) = \left(\overrightarrow{U_{\pi 1}}, \overrightarrow{U_{\pi 2}}, \vec{e}_{c0}\right)$ a basis eigen vector of the tensor $\widetilde{U_\pi}$ and $(\lambda_{\pi 1}, \lambda_{\pi 2}, \frac{c}{c_0})$, the associated eigen values.

Then: $\widetilde{\widetilde{\gamma_{(U_\pi)}}} = \begin{bmatrix} 1 & 0 & 0 & 0 & 0 & 0 \\ 0 & 1 & 0 & 0 & 0 & 0 \\ 0 & 0 & 1 & 0 & 0 & 0 \\ 0 & 0 & 0 & g(\lambda_{\pi 1}, \lambda_{\pi 2}) & 0 & 0 \\ 0 & 0 & 0 & 0 & g(\lambda_{\pi 1}, \frac{c}{c_0}) & 0 \\ 0 & 0 & 0 & 0 & 0 & g(\lambda_{\pi 2}, \frac{c}{c_0}) \end{bmatrix}_{VM\widetilde{(\overrightarrow{U_{\pi i}})}}$

And: $\widetilde{W'_{ab}} = \begin{bmatrix} W'_{ab11} & W'_{ab12} & 0 \\ W'_{ab12} & -W'_{ab11} & 0 \\ 0 & 0 & 0 \end{bmatrix}_{(\overrightarrow{e_{a0}},\overrightarrow{e_{b0}},\overrightarrow{e_{c0}})} = \begin{bmatrix} x & y & 0 \\ y & -x & 0 \\ 0 & 0 & 0 \end{bmatrix}_{\overrightarrow{U_{\pi i}}} = \begin{pmatrix} x \\ -x \\ 0 \\ y\sqrt{2} \\ 0 \\ 0 \end{pmatrix}_{VM\widetilde{(\overrightarrow{U_{\pi i}})}}$

Hence: $\widetilde{\widetilde{\gamma_{U_\pi}}}:\widetilde{W'_{ab}} = \begin{pmatrix} x \\ -x \\ 0 \\ y\sqrt{2}g(\lambda_{\pi 1},\frac{c}{c_0}) \\ 0 \\ 0 \end{pmatrix}_{VM_{\overrightarrow{(U_{\pi\iota})}}} = \begin{bmatrix} x & y\sqrt{2}g(\lambda_{\pi 1},\frac{c}{c_0}) & 0 \\ y\sqrt{2}g(\lambda_{\pi 1},\frac{c}{c_0}) & -x & 0 \\ 0 & 0 & 0 \end{bmatrix}_{\overrightarrow{U_{\pi\iota}}}$

With: $\widetilde{P_{c0}} = \tilde{I} - \vec{e}_{c0}\otimes\vec{e}_{c0} = \begin{bmatrix} 1 & 0 & 0 \\ 0 & 1 & 0 \\ 0 & 0 & 0 \end{bmatrix}_{\overrightarrow{U_{\pi\iota}}}$

Hence: $\widetilde{P_{c0}} \cdot \left(\widetilde{\widetilde{\gamma_{(U_\pi)}}}:\widetilde{W'_{ab}} \right) = \left(\widetilde{\widetilde{\gamma_{(U_\pi)}}}:\widetilde{W'_{ab}} \right)$ and $\widetilde{P_{c0}} \cdot \left(\widetilde{\widetilde{\gamma_{(U_\pi)}}}:\widetilde{W'_{ab}} \right) \cdot \widetilde{P_{c0}} = \widetilde{\widetilde{\gamma_{(U_\pi)}}}:\widetilde{W'_{ab}}$ Therefore:

$$\left[\widetilde{\tilde{Q}}_{(\widetilde{P_c}.\widetilde{R_\pi})}:\widetilde{\widetilde{\gamma_{(U_\pi)}}} - \frac{1}{2}\left(\widetilde{P_c} \otimes \widetilde{P_{c0}}\right)\right]:\widetilde{W'_{ab}} = \widetilde{\tilde{Q}}_{(\widetilde{R_\pi}\cdot\widetilde{P_{c0}})}:\widetilde{\widetilde{\gamma_{(U_\pi)}}}:\widetilde{W'_{ab}} - \frac{1}{2}\left(\widetilde{P_c} \otimes \widetilde{P_{c0}}\right):\widetilde{W'_{ab}}$$

$$\left[\widetilde{\tilde{Q}}_{(\widetilde{P_c}.\widetilde{R_\pi})}:\widetilde{\widetilde{\gamma_{(U_\pi)}}} - \frac{1}{2}\left(\widetilde{P_c} \otimes \widetilde{P_{c0}}\right)\right]:\widetilde{W'_{ab}} = \widetilde{R_\pi} \cdot \widetilde{P_{c0}} \cdot \left(\widetilde{\widetilde{\gamma_{(U_\pi)}}}:\widetilde{W'_{ab}} \right) \cdot \widetilde{P_{c0}} \cdot \widetilde{R_\pi}^T$$
$$= \widetilde{R_\pi} \cdot \left(\widetilde{\widetilde{\gamma_{(U_\pi)}}}:\widetilde{W'_{ab}} \right) \cdot \widetilde{R_\pi}^T$$

Hence: $\left[\widetilde{\tilde{Q}}_{(\widetilde{P_c}.\widetilde{R_\pi})}:\widetilde{\widetilde{\gamma_{(U_\pi)}}} - \frac{1}{2}\left(\widetilde{P_c} \otimes \widetilde{P_{c0}}\right)\right]:\widetilde{W'_{ab}} = \widetilde{\tilde{Q}}_{(\widetilde{R_\pi})}:\widetilde{\widetilde{\gamma_{(U_\pi)}}}:\widetilde{W'_{ab}}$.

Appendix F. First implementation and validation of the FiBuLa law

During this PhD, a considerable time has been dedicated to write the sub-routine of an anisotropic law for a bundle of rope-yarns in FORTRAN. The first implementation of the law was done by using linear functions for the conjugated stresses $W''^J_{Jc}, W'^c_{Jc}, W'_{ab} W'_\delta$. Hence, the associated potentials were chosen quadratic. The aim was to validate the law with simple potentials and usual parameters before adding the potential identified experimentally on polyamide 6 rope-yarns and the associated parameters.

The potentials were defined as follows:

$$W'^J_{Jc} = \frac{P_J}{\rho_0} \cdot \ln J$$

<div align="right">Eq. 201</div>

$$W'^c_{Jc} = \frac{P_c}{\rho_0} \cdot \ln Uc$$

<div align="right">Eq. 202</div>

$$\widetilde{W'_{ab}}\left(\theta, \widetilde{LnU_{ab}}\right) = \frac{G_{ab}}{\rho_0} \cdot \widetilde{LnU_{ab}}$$

<div align="right">Eq. 203</div>

$$\widetilde{W'}_\delta(\theta, \widetilde{\varepsilon}_\delta) = \frac{G_\delta}{\rho_0} \cdot \widetilde{\varepsilon}_\delta$$

<div align="right">Eq. 204</div>

Using this set of parameters:

Table 0.1- Initial set of parameters used for the linear definitions of the conjugate stresses in the first implementations

P_J (MPa)	P_C (MPa)	G_{ab} (MPa)	G_δ (MPa)
12000	3300	0.015	3

Four elementary tests were performed to check the validity of the implementation of the UMAT subroutine and also to check the consistency between the law and the result given by the model. These tests were realized on one 8-node linear brick element C3D8 on Abaqus/implicit (Figure 0.12). Each of the four tests correspond to a deformation mode. We check if the deformation is homogeneous in the element and if the behaviour is linear in small deformation with the exact values of the parameters used (Table 0.1). The rope-yarns are considered parallel and align in the direction $\vec{x}$.

Figure 0.12 shows the elementary tests and the obtained deformed shapes at the end of the simulations. It shows that the deformation is homogeneous for all the tests.
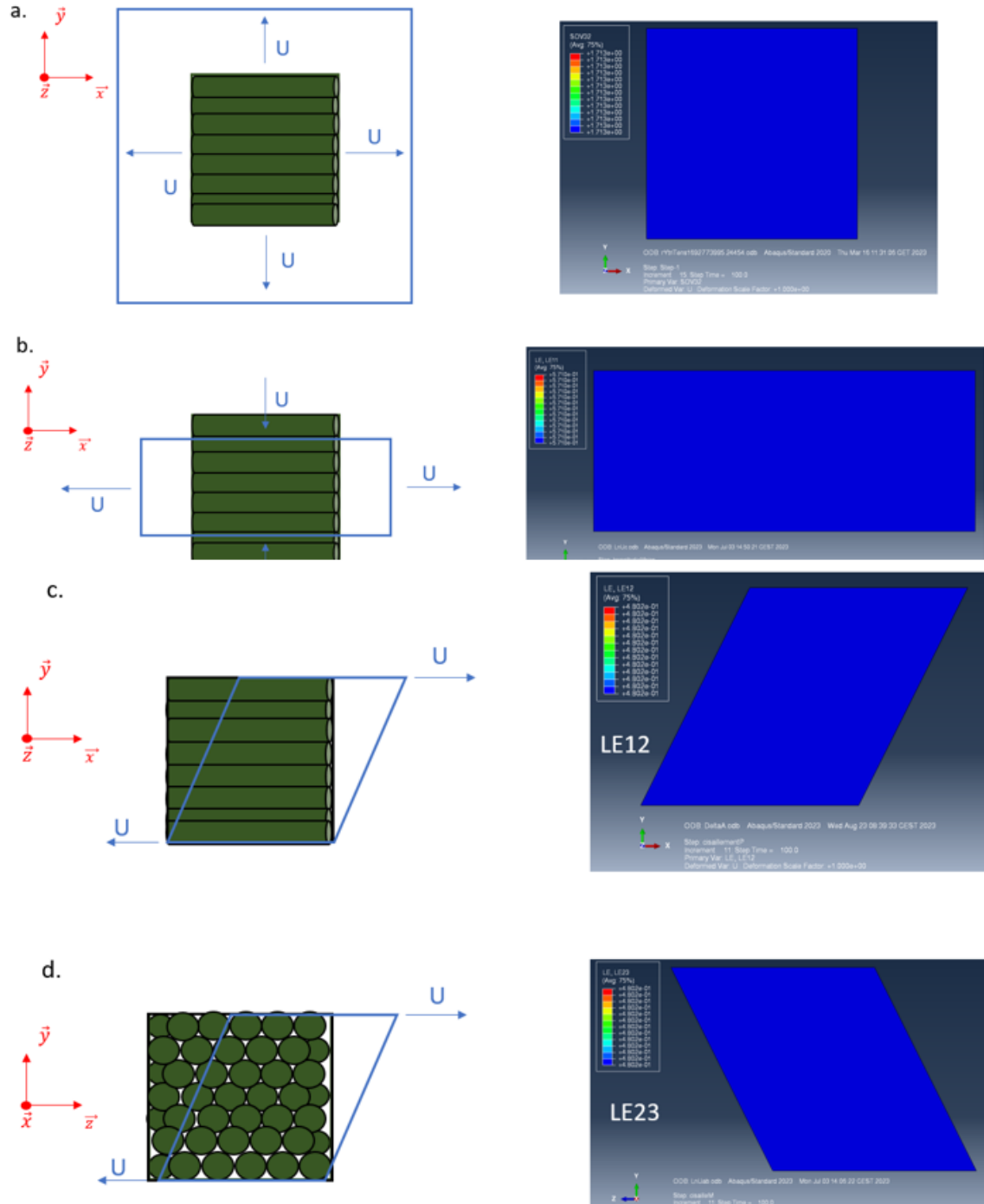
Figure 0.12 – Tests to check the implementation and consistency of the law (a) Change of volume (b) Elongation (c) Longitudinal shear (d) Transversal shear

Also, the behaviour at small strain are linear and the slope are equal to the entered parameters (Table 0.1) as shown in Figure 0.13. This allows to validate the implementation of the law and the consistency of the law.

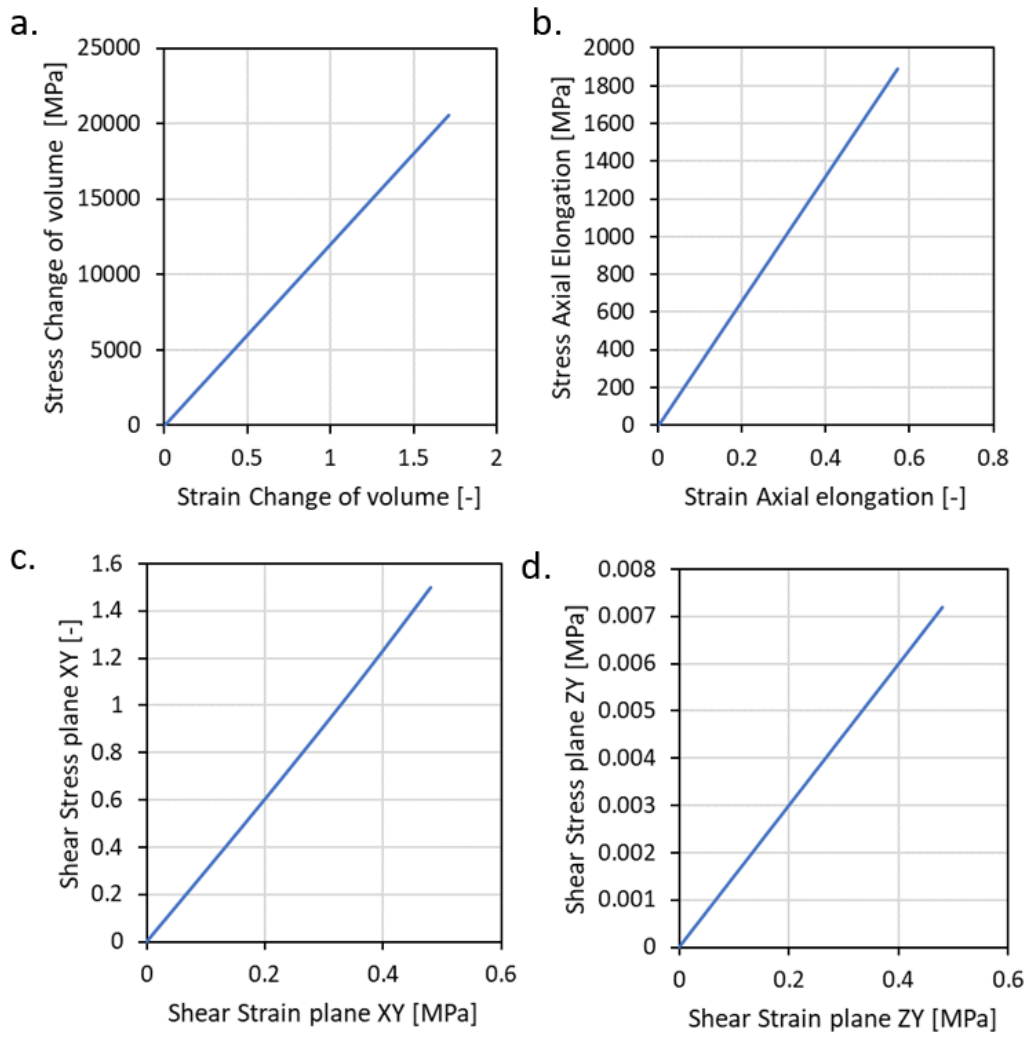*Figure 0.13 – Results of the simulation tests to check the validity of the law. Stress versus strain for each deformation modes. (a) Change of volume (b) Elongation (c) Longitudinal shear (d) Transversal shear*

Appendix G. Résumé en français

L'éolien offshore est bien établi en Europe avec la plus grande ferme opérationnelle combinant des systèmes d'ancrages posés et des fondations flottantes (Offshore Wind Europe, 2021). Actuellement, on recense 123 fermes offshores dans 12 pays Européens. L'objectif visé est de fournir 160 GW de capacité offshore d'ici à l'année 2030 (Offshore Wind Europe, 2021). En France, les trois premières éoliennes flottantes sont en construction et doivent être installées en 2024 par l'entreprise SBM. La solution proposée est une technologie sur câbles tendus (nommée TLP pour « taut-leg mooring line »). Cette solution est utilisée historiquement dans l'Oil&Gaz ; elle autorise peu de mouvements. Un projet de flotteur pilote, FLOATGEN, a été installé au site du SEM-REV. La solution d'ancrage proposée est composée de 6 lignes d'ancrage en polyamide. Le nombre de projets augmentent et les constructeurs de turbines et de flotteurs développent différents modèles de flotteurs et de systèmes d'ancrage pour les différentes conditions (mer, vent, flottabilité) (Heiberg et al., 2021). Les quatre technologies principales sont représentées sur la Figure 0.14. On distingue :

- Les plateformes Spar : un large cylindre vertical, constitué d'un matériau plus dense que l'eau, permet de maintenir la stabilité.
- Les plateformes à ancrage tendus : elles sont ancrées verticalement par des matériaux raides et tendus. Aucun déplacement n'est toléré.
- Les plateformes semi-submersibles : la structure de la plateforme flottante est caractérisée par un large pont. La raideur de la structure dépend de la colonne d'eau et du système d'ancrage.

Figure 0.14 – Principales technologies de flotteurs pour les éoliennes offshores. Gauche (2) : posées. Droite (3): flottantes.

Pour les solutions Spar et les plateformes semi-submersibles, les lignes d'ancrage peuvent être composées de matériaux synthétiques flexibles comme le polyester ou le polyamide 6. Le choix du matériau d'ancrage aura un impact important sur le dimensionnement de la structure flottante. Il est nécessaire d'accélérer le développement de solution d'ancrages innovantes et rentables. Pour cela, la maîtrise et la connaissance des modes de rupture, de la prévention et du suivi en service doivent être approfondies.

Les systèmes de flotteurs développés pour les énergies marines renouvelables en eaux peu profondes (< 200 m) requièrent un ancrage qui assure le maintien de la station et la diminution des effets combinés de la houle, du vent et des chargements dus à la plateforme. Les lignes d'ancrage en polyamide 6 (PA6) s'imposent face à leurs homologues en polyester grâce à leur importante élongation à rupture (20%). Combinées à leur résistance en traction, les propriétés de ces lignes permettraient le maintien et l'amortissement requis (Chailleux & Davies, 2003; Flory, Banfield, et al., 2007). Ces lignes sont déjà utilisées pour des applications de courtes

durées (3 ans) comme l'accostage des bateaux. Ces utilisations limitées dans le temps étaient dues à la durée de vie en fatigue limitée des lignes en polyamide 6 qui devaient être changées tous les 3 ans. Les lignes d'ancrage seront soumises à des efforts constants et des chargements dynamiques pendant toute leur durée de vie. Elles doivent donc avoir une bonne résistance au fluage long terme et à la fatigue. De nouvelles constructions, associées à des revêtements innovants pour diminuer le frottement, ont été proposées par les constructeurs. Des travaux (Banfield & Ridge, 2017; Chevillotte, 2020) ont permis de montrer que leur durabilité et leur tenue en fatigue remplissent les normes attendues. La mise en œuvre industrielle requiert encore de confirmer la faisabilité et la robustesse de l'usage du polyamide comme ligne d'ancrage. Ce travail de thèse s'intègre dans un projet d'étude du comportement des lignes d'ancrage en polyamide et de développement de solutions de monitoring, nommé MONAMOOR, piloté par France Energies Marines. Ce projet est une continuation directe du projet POLYAMOOR et de la thèse associée menée par Chevillotte (Chevillotte, 2020). Ce premier projet avait entamé les investigations sur les verrous scientifiques et industriels associés aux lignes d'ancrage en polyamide.

La première partie de cette étude est dédiée à un état de l'art sur les sujets abordés pendant la thèse. Il est montré que le polyamide se caractérise par une importante prise en eau associée à un changement significatif de ses propriétés mécaniques. Ainsi, pour réaliser une étude sur leur utilisation comme ligne d'ancrage, il est nécessaire d'étudier leur comportement en eau. Par ailleurs, le développement de modèle pour décrire des cordages synthétiques (polyester, polyamide) est principalement motivé par le dimensionnement de ligne d'ancrage. Néanmoins, peu de modèles peuvent être utilisés pour étudier les comportements viscoélastiques et viscoplastiques de ces cordage synthétiques. Ces comportements dépendant du temps sont cruciaux pour le polyamide qui se caractérise par un comportement visqueux important. Dans ce contexte, Chevillotte a développé une loi constitutive 1D, caractérisée sur une échelle de sous-cordage de laboratoire, et implémentable en éléments finis. Cette loi doit encore être validée sur des échelles plus représentatives des cordages échelle 1. Leur comportement au fluage long terme en eau a été peu étudié sur les échelles supérieures (sous-cordage, cordage). La revue de la littérature montre la difficulté expérimentale associée à ce type d'étude. Dans ce contexte, Chevillotte a conçu un banc expérimental dédié à l'étude du fluage long terme, en eau, sur des échelles de sous-cordage de laboratoire. Des essais de fluage et de recouvrement long terme ont été commencés pendant ce premier projet et permettent d'avoir aujourd'hui plus de trois ans de données expérimentales.

Les connaissances sur le comportement en fatigue permettent de montrer que deux mécanismes pilotent majoritairement la rupture en fatigue : le fluage à l'échelle des filaments et des fibres pour les chargements élevés ; les phénomènes d'abrasion (externe et interne) pour les chargements plus faibles. Les études montrent que la construction a un impact important sur la résistance à l'abrasion et donc, sur la durée de vie en fatigue aux plus faibles valeurs de chargements (plus représentatifs des conditions en service la majeure partie du temps). Les nouvelles constructions de cordages toronnés, associées aux nouveaux revêtements, ont été développées pour augmenter la durée de vie et des études montrent que ces cordages peuvent avoir une durée de vie comparable au polyester. L'étude expérimentale de la fatigue à l'échelle des sous-cordages et des cordages est compliquée. L'usage de machines expérimentales qui peuvent accueillir de longs échantillons et qui disposent d'une course de vérin importante, est nécessaire. De plus, la nécessité de réaliser ces essais en eau complexifie d'autant plus la démarche expérimentale. Une autre contrainte associée à l'étude des lignes d'ancrage est la faible fréquence de sollicitation associée à cette application : 0.1 Hz pour être représentatif de la fréquence de la houle. La littérature montre que des données pour des chargements plus faibles, associées à un nombre de cycles plus important, sont manquantes. De plus, les

connaissances sur les mécanismes d'endommagement lors de sollicitations cycliques à plus faible charge et caractérisés majoritairement par de l'abrasion sont encore à approfondir. Pour finir, la revue de littérature a montré que les modèles volumiques 3D développés pour les cordages ne considéraient pas le comportement complexe visco-élasto-plastique des fibres en polyamide (Durville, 2012; Ghoreishi, Cartraud, et al., 2007). Ainsi, ce type de modèles ne peut pas être utilisé pour étudier à la fois l'impact de la construction et l'impact du comportement complexe du matériau. Cela est limitant car la visco-elasto-plasticité des filaments a une contribution importante dans la réponse du cordage. Récemment, des efforts ont été réalisés dans la recherche pour développer des modèles hyperélastiques pour décrire le comportement de matériaux caractérisés par de grandes transformations. Un modèle développé par Charmetant *et al.* (Charmetant et al., 2011)*,* pour des renforts tissés, propose de choisir des invariants avec un sens physique qui permettent d'étudier en détail la réponse de la construction au chargement. Il est aussi possible d'ajouter une loi de comportement spécifique dans chacun des modes de déformations. Ce type de modèle peut permettre une analyse précieuse de la réponse de la construction combinée à la réponse du matériau.

Le second chapitre a introduit les matériaux et méthodes utilisés dans cette étude. Pour ce travail, un sous-cordage composé de 3 torons toronnés (charge minimale à rupture de 4T) (Figure 0.15) et un sous-cordage d'une échelle supérieure, plus représentative (charge minimale à rupture de 7T) ont été étudiés.
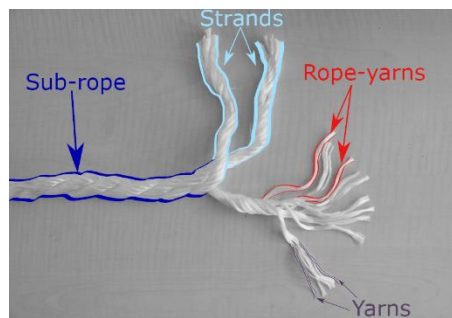

Figure 0.15 – Les différentes échelles d'un sous-cordage toronné, échelle laboratoire, constitué de 3 torons (rupture à 4T). « Sub-rope » signifie « sous-cordage » ; « strands » signifie « toron » ; « rope-yarns » signifie « brins assemblés » et « yarns » signifie « fil ».

Les cordages sont des matériaux qui présentent une construction hiérarchique et multi-échelles. Une étude complète de ces matériaux nécessite donc d'étudier chaque échelle. Les essais à l'échelle locale (fibres) permettent d'identifier la contribution du matériau, alors que les essais à l'échelle macroscopique (sous-cordage et cordage) incluent la contribution de la construction à la réponse mécanique. Chaque échelle est associée à une gamme de chargements et de déplacements spécifiques qui requièrent des dispositifs expérimentaux dédiés. Nous avons étudié trois échelles pendant notre étude : l'échelle des sous-cordage, des torons et celle des brins assemblés (Figure 0.15). Ainsi, des moyens expérimentaux associés à l'échelle du sous-cordage sont d'abord présentés et une seconde partie présente des moyens d'essais associés aux échelles du toron (« strands ») et du brin assemblé (« rope-yarns »).

Le chapitre 3 est dédié à l'étude du comportement constitutif de sous-cordages de polyamide 6 toronnés et constitués de 3 torons. Cette étude se concentre sur la présentation, l'identification et la validation de la loi de comportement « POLYAMOOR » développée par Chevillotte et basée sur la proposition de Flory (Flory, 2007). Son développement est basé sur la caractérisation de la réponse mécanique d'un sous-cordage 4T lors d'un essai de multi-relaxations. Ce modèle rhéologique est représenté sur la Figure 0.16. Il est composé des éléments suivants :

- Un ressort rapide pour le comportement dynamique
- Un amortisseur responsable de la réponse visqueuse du polymère
- Une partie indépendante du temps composée d'un rochet pour la plasticité et d'un ressort pour l'élasticité retardée (i.e relaxée).
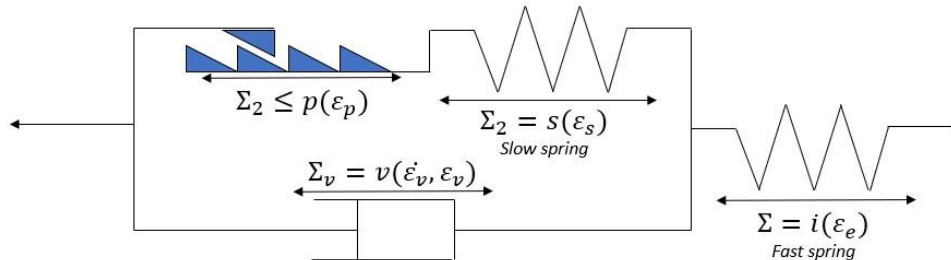

Figure 0.16 – La loi constitutive POLYAMOOR

Ce modèle comprend 11 paramètres qui peuvent tous être identifiés sur un seul essai de multi-relaxations. Les lignes d'ancrage en polyamide devront rester en service pour des durées de 20 ans. Ainsi, l'évolution des propriétés mécaniques au cours du vieillissement est critique et l'évolution des paramètres de la loi au cours d'un vieillissement doit être évaluée. Une identification de la loi sur un échantillon de l'échelle de laboratoire ayant subi un fluage de deux ans en eau douce est donc réalisée. Le sous-cordage vieilli présente des propriétés mécaniques plus élevées qui semblent être majoritairement dues à une évolution de sa construction à l'échelle macroscopique.

La loi 1D doit permettre de décrire le comportement d'un cordage échelle 1. Une identification des paramètres sur un sous-cordage d'une échelle supérieure, caractérisé par une construction plus proche de l'échelle 1, est réalisée. Une validation de la loi sur cette échelle avec un essai stochastique représentatif des sollicitations en mer est proposée. La loi prédit correctement l'évolution de la raideur dynamique au cours de l'essai. En revanche, la loi actuelle ne possède pas de temps de relaxations adaptés à un comportement long terme car elle a été identifiée sur des essais multi-relaxations avec des paliers de maximum 30 minutes. L'identification de plusieurs temps de relaxations sur des temps longs et l'ajout de branches au modèle 1D est possible.

Le quatrième chapitre est une étude approfondie du comportement au fluage long terme. La rupture du cordage en fluage est considérée comme un dommage statique lors duquel la corde rompt après une certaine durée à contrainte constante. Le fluage sur un temps long et pour des contraintes importantes génère des déformations au sein du matériau qui ne sont pas totalement recouvrables. La réponse à ce type de fluage est encore mal connue. Par conséquent, sa caractérisation est nécessaire car la durée de vie attendue de ces ancrages est de 20 ans.

Dans l'objectif de prévoir le comportement au fluage des lignes en PA6, un banc d'essai a été conçu et mis en œuvre par Chevillotte; des essais de fluage longue durée sont en cours depuis bientôt deux ans. Le banc de fluage permet de tester 3 éprouvettes de type « sous cordage » caractérisé par une force à rupture de 4T (notée MBL : minimal breaking load) simultanément. Certains des essais réalisés sont toujours en cours après plus de 3 ans de mesures, sont des fluages à 25 %, 38 % et 50 % de MBL recouvrement sous une contrainte de 0.013 N. La Figure 0.17 présente la comparaison de ces essais de fluage longs à des essais de fluage courts aux mêmes chargements (3h).
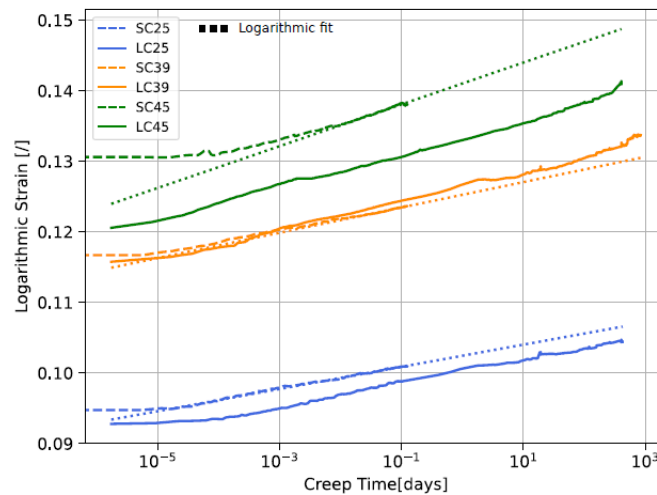
Figure 0.17 – Superposition des résultats d'essais de fluage long termes et court termes : déformation logarithmique de fluage [-] en fonction du temps [jours]. Extrapolation avec un fit par une loi logarithmique linéaire.

Ces données sur une longue durée, permettent de déterminer que les phénomènes de fluage et de recouvrement suivent une loi logarithmique de la forme :

$$\varepsilon_c = A \cdot \ln(time) + B$$

<div align="right">***Eq. 205***</div>

La constante A (exprimée [/]/ln(jours)) représente la vitesse de fluage. Les cinétiques de fluage et de recouvrement sont comparables. On observe aussi que des fluages courts peuvent permettre de prédire des fluages longs de 3 ans avec loi logarithmique linéaire. Un essai de « fluage cyclique » a été réalisé pour déterminer si le fluage généré lors d'un fluage court à charge élevée (représentatif d'une tempête), générait plus de déformation qu'un fluage plus long à une charge plus faible (représentatif d'un chargement à la tension de service). Il a été montré que le fluage généré par des effets tempêtes est plus significatifs. Par ailleurs cet essai a permis de mettre en évidence l'impact de l'histoire de chargement sur les cinétiques de fluage et de recouvrement. En effet, le deuxième fluage à haute charge était caractérisé par une cinétique de fluage bien plus faible que le premier.

La comparaison de ces données expérimentales précieuses à une simulation avec la loi POLYAMOOR est l'occasion de trancher sur la nécessité de développer des modèles complémentaires. Le modèle POLYAMOOR, identifié sur des essais courtes durées (multi-fluage), doit être prédictif. La loi actuelle ne possède pas de temps de relaxation adaptés à un comportement long terme car elle a été identifiée sur des essais multi-fluage avec des paliers de maximum 30 minutes.

Le cinquième chapitre propose une étude des propriétés en fatigue de sous-cordages de polyamide 6 échelle 4T. Dans un premier temps, la courbe S-N proposée par Chevillotte a été étendue à de plus haut nombres de cycles et de plus faibles gammes de chargement. Le point de plus haut nombre de cycles atteint 10^5 cycles pour un chargement de 25%MBL.

Une comparaison des résultats obtenus pour l'échelle 4T à des résultats obtenus sur une échelle 7T (Chevillotte) ainsi qu'à des résultats obtenus sur des cordages toronnés lors d'une étude récente est proposée Figure 0.18.
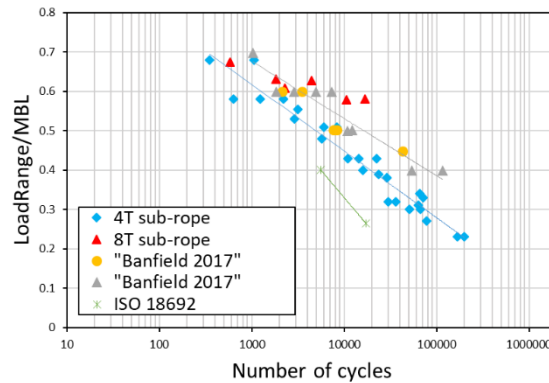
Figure 0.18 – Résultats des essais de fatigue sur une échelle 4T et comparaison avec les résultats sur une échelle 8T (Chevillotte et al., 2018) et sur d'autres constructions toronnées (Banfield & Ridge, 2017)

La tendance linéaire en échelle semi-logarithmique est confirmée pour les chargements testés. Les différences de comportement semblent être majoritairement dues à la construction du cordage 4T, destinée à l'étude en laboratoire. Elle est caractérisée par un pas plus faible et un angle de toronnage plus important. Cette construction favorise l'endommagement par abrasion car les mouvements des torons les uns par rapport aux autres sont augmentés. Néanmoins, on constate que les résultats à l'échelle 4T sont proches des résultats de Banfield *et al*. Ils sont plus conservatifs. Ainsi, prolonger les études sur cette échelle peut s'avérer une solution pertinente et plus accessible expérimentalement.

Une étude de l'endommagement lors de la fatigue a aussi été réalisée. Des tomographies et des analyses au SEM ont permis de comparer l'état du matériau d'un sous-cordage 4T vierge et d'un sous-cordage 4T après un essai de fatigue. Les coupes de la section axiale, respectivement avec tension et sans tension, sont présentées Figure 0.19. et Figure 0.20..
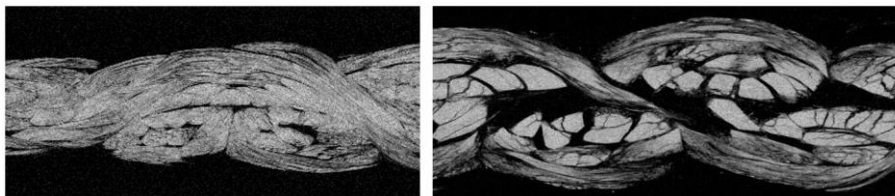

Figure 0.19 – Tomographies de la section axiale d'un cordage 4T vierge sans tensions. Gauche: Echantillon vierge. Droite: Echantillon après un essai de fatigue (essai de fatigue à 29%MBL).
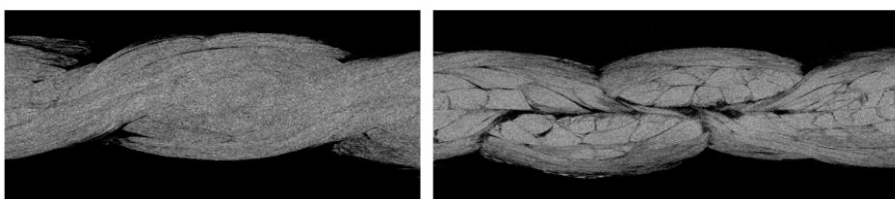
Figure 0.20 - Tomographies de la section axiale d'un cordage 4T vierge sous tensions. Gauche: Echantillon vierge. Droite: Echantillon après un essai de fatigue (essai de fatigue à 29%MBL).

On constate que les brins assemblés du sous-cordage 4T sont plus compacts et denses. Une étude approfondie au MEB a permis de montrer, qu'à l'échelle des fibres, un réarrangement s'est produit rendant la construction plus compacte. Les surfaces de contacts entre les torons ont aussi évolué et on constate un meilleur alignement des fibres qui les constituent qui peut tendre à diminuer leur rugosité. Par ailleurs, des arrachements de matière sont aussi observables. Ce phénomène est comparable au lustrage qu'avait observé Bain *et al.* sur d'autres types de fibres synthétiques.

Un essai de fatigue avec un suivi de la déformation a permis de mettre en évidence l'évolution de la construction au cours d'un essai de fatigue sur les sous-cordages 4T. L'aire de boucle et le module au déchargement ont augmenté avec les nombres de cycles. Ces deux évolutions sont associées majoritairement à des changements de la construction. Les épissures ont glissé ce qui met en évidence l'importance d'avoir des épissures suffisamment longues pour conserver un état de torsion constant au cours de l'essai. Ici, cet effet peut remettre en question les résultats de fatigue à l'échelle 4T. Néanmoins, ces résultats seront toujours conservatifs par rapport aux constructions des échelles supérieures.

Finalement, une étude sur l'auto-échauffement a été réalisée pour vérifier la répétabilité et la robustesse du protocole expérimental.

La répétabilité du protocole expérimental est donc confirmée. Par ailleurs, la courbe d'auto-échauffement sur un cordage 4T a été enrichie et une analyse plus claire peut être proposée. En effet, la prédiction par la méthode d'auto-échauffement consiste à analyser les changements de régimes de la dissipation. Nos connaissances sur les régimes de dissipation sur les cordages sont trop encore trop minimes pour permettre de dépasser l'approche graphique. Une nouvelle détermination de transition entre le premier et le second régime de dissipation est proposée. Nous associons cette transition de régime à une durée de vie en fatigue (nombre de cycles) empiriquement. Jusque-là, il a été observé que cette transition de régime était associée à une durée de 10^6 cycles pour plusieurs familles de matériaux. Les cordages sont des matériaux multi-échelle et cet aspect peut les différencier du comportement des matériaux jusque là étudiés. Pour s'assurer d'être conservatif sur notre prédiction par la méthode d'auto-échauffement, nous proposons d'associer la transition de régime à une durée de vie de 10^5 cycles. Le critère énergique utilisé permet de relier le nombre de cycles à rupture à la dissipation selon l'expression :

$$\Delta^* N^b = C$$

Eq. 206

Nous avons donc une relation entre le nombre de cycles à rupture et la dissipation moyenne. Un fit par un polynôme d'ordre 3, entre la dissipation moyenne et le nombre de cycle à rupture, nous permet donc de prédire la durée de vie en fatigue à partir de la dissipation.

La Figure 0.21. présente la prédiction par la méthode d'auto-échauffement de la courbe S-N proposée dans cette étude.
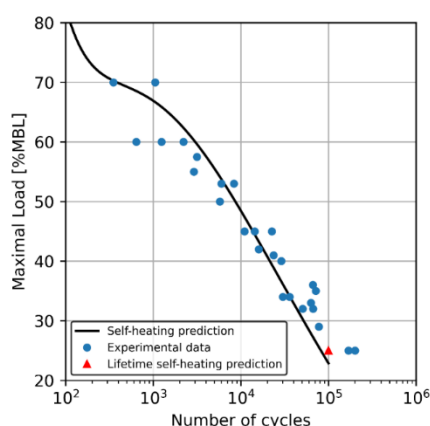

Figure 0.21 – Courbe S-N de fatigue prédite en utilisant la méthode de prédiction auto-échauffement basée sur un critère énergétique (ligne noire continue et triangle noir). Comparaison avec les données expérimentales (cercles bleus).

On constate que la prédiction est en accord avec les résultats expérimentaux. Cette prédiction est conservative et pourrait sous-estimer la durée de vie pour les plus hauts nombres de cycles. L'objectif, à terme, serait de dépasser l'approche graphique par une compréhension des phénomènes physiques et/ou mécaniques associés la dissipation. Une piste pour identifier la source de dissipation est le développement d'un modèle qui nous permettrait de séparer les dissipations dues au frottement des dissipations dues au matériau.

Le sixième chapitre de cette étude est dédié au développement d'un modèle à l'échelle mésoscopique d'un sou-cordage toronné. Cela répond au besoin de mieux comprendre l'influence de la construction sur la réponse mécanique. L'étude du chapitre 5 a mis en évidence la nécessité de quantifier les dissipations dues au frottement. Deux mécanismes contribuent à la dissipation ; la visco-élasticité du matériau et les frictions entre les sous-composants du cordage :

$$\Delta^* = \Delta^*_{material} + \Delta^*_{friction}$$

<div align="right">*Eq. 207*</div>

Le développement d'une loi de comportement basée sur l'échelle mésoscopique d'un cordage, puis son implémentation dans un logiciel d'éléments finis, permettraient une meilleure compréhension de ce comportement, notamment, des phénomènes de dissipation dus aux frictions internes entre composants. Ces derniers sont déterminants car ils sont à l'origine de l'endommagement par fatigue de ces cordages synthétiques. Leur structure mésoscopique peut être décrite par une architecture hiérarchique : sous-cordage, torons, brins, fils, filaments. Un modèle numérique d'un cordage est nécessaire pour l'étude.

L'approche de modélisation proposée s'inspire du travail de Charmetant *et al.* pour des renforcements composites (Charmetant et al., 2011). Les torons sont ainsi modélisés par trois cylindres hélicoïdaux en contact les uns avec les autres. Dans les éléments volumiques de ces torons, une loi de comportement simulant un matériau homogène équivalent, qui rend compte de l'anisotropie due aux brins, est mise en place (ceux-ci constituent le toron). La loi de comportement proposée est basée sur l'approche de Charmetant et consiste à modéliser une particule de matière constituée d'un amas de brins rectilignes identiques les uns accolés aux autres. Les distances entre brins sont supposées négligeables et la dissipation intrinsèque est supposée nulle. L'orientation des brins dans le toron est prise en compte selon la description de Leech (Leech, 2002). La décomposition des modes de déformations de l'amas de brin est alors nécessaire. Ces modes sont directement reliés au comportement intrinsèque des brins ainsi qu'à leur interaction. Quatre modes de déformations sont considérés : $\widetilde{R_\pi}$ la rotation des brins, $\widetilde{U_{ab}}$ la déformation due au réarrangement des brins les uns par rapport aux autres dans le plan perpendiculaire à l'axe des brins (sans changement de volume), $\widetilde{U_c}$ la déformation axiale des brins, $\widetilde{U_{vol}}$ la déformation de changement de volume, et $\widetilde{K_\pi^{-1}}$ les déformations de glissement des brins les uns sur les autres dans la direction de l'axe des brins. Pour chaque mode de déformation, une loi de comportement dédiée et pertinente sera proposée. L'énergie libre massique est supposée être la somme des potentiels massiques dédiés à chacun de ces modes de déformations. Cette loi de comportement permet de distinguer les modes de déformation associés à de la friction ($\widetilde{U_{ab}}$, $\widetilde{K_\pi^{-1}}$) de ceux associés à la matière des filaments ($\widetilde{U_c}$, $\widetilde{U_{vol}}$). Cette loi se distingue de l'approche de Charmetant par un nombre d'invariants plus élevés pour décrire les deux modes de friction. Cette description plus exhaustive devrait permettre une meilleure compréhension des phénomènes de friction et à terme, d'inclure une plasticité dédiée aux modes de friction. Ce premier travail propose une étude de faisabilité à la fois théorique, expérimentale et numérique, de cette approche de modélisation. Ainsi, les comportements en déformation seront hyperélastiques (pas de dissipation ni de viscoélasticité). L'objectif à terme

sera de rajouter cette complexité dans le comportement si cette première étude se révèle fructueuse.

Pour établir cette loi pour un amas de brins assemblés, nous avons suivi la procédure suivante :

- Définition des échelles visées pour la modélisation
- Proposition d'une décomposition pour le tenseur de déformation $\tilde{F}$
- Choix d'invariants spécifiques avec un sens physique pour décrire chaque mode de déformation. L'énergie libre spécifique ψ, sera exprimée en fonction de ces invariants (Figure 0.22).
- Calcul des dérivées par rapport au temps de chacun de ces invariants (sous la forme d'un produit contracté avec $\widetilde{D}$), dans l'objectif de résoudre $\dot{\psi} = \tilde{\Sigma} : \widetilde{D} - s \cdot \dot{\theta} - \varphi_1$
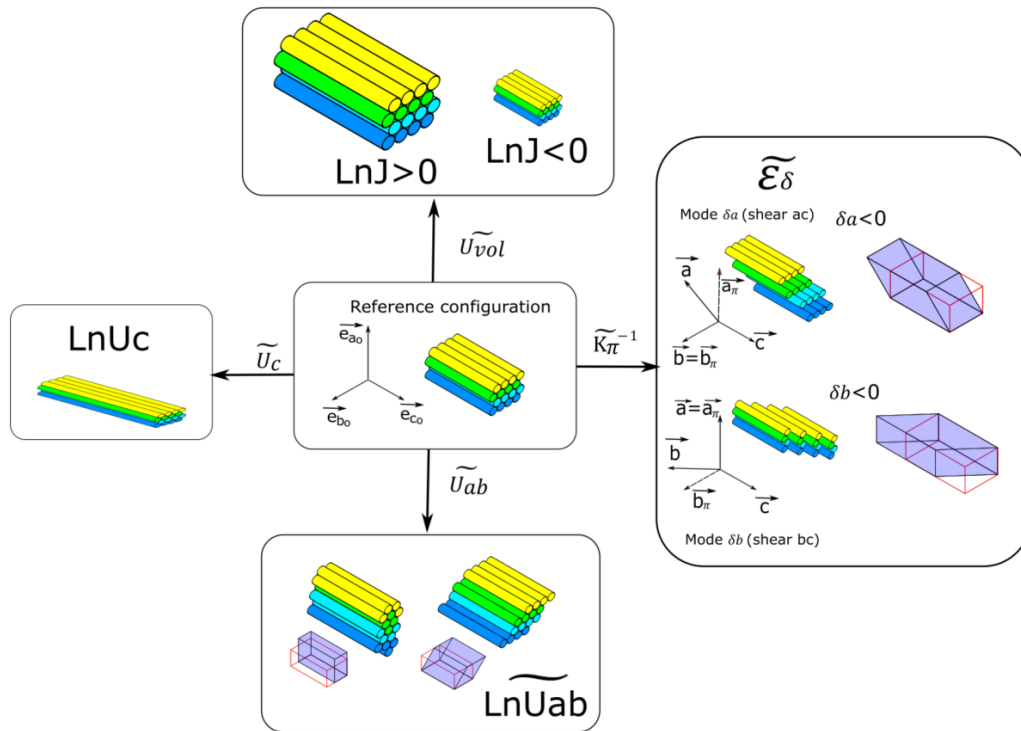- Résoudre l'équation pour obtenir une relation entre la contrainte et la déformation.

Figure 0.22 – Décomposition de la déformation et choix d'invariants avec un sens physique pour décrire chaque mode de déformation

Finalement, la loi de contrainte-déformation, en fonction de la contrainte de Cauchy, obtenue est la suivante :

$$\widetilde{R_\pi}^T \cdot \tilde{T} \cdot \widetilde{R_\pi} = \frac{1}{J}[\rho_0 W'^J{}_{Jc}\tilde{I} + \rho_0 W'^c{}_{Jc}\left((\overrightarrow{e_{c0}} \otimes \overrightarrow{e_{c0}}) - \frac{1}{3}\tilde{I}\right) + \tilde{\tilde{\gamma}}_{(\widetilde{U_{ab}})}$$
$$: \rho_0\widetilde{W'_{ab}} + \left(\frac{c}{c_0}\right)^2 \widetilde{U_\pi} \cdot \rho_0 \widetilde{W'}_\delta \cdot \widetilde{U_\pi}]$$

Eq. 208

Pour l'identification des fonctions pour définir les potentiels, et des paramètres associés, deux moyens expérimentaux ont été conçus à l'échelle des brins assemblés et des torons pendant ce travail de thèse.

Pour identifier le comportement couplé de l'élongation axiale et du changement de volume des brins, des essais de traction cycliques en eau ont été réalisés. A partir de la mesure de deux déformations, axiale et transverse, une identification du potentiel W_{Jc} est proposée sous cette forme :

$$\rho_0 W_{Jc}(\ln J, LnU_c) = a \cdot \ln J^2 + b \cdot \ln J \cdot LnU_c + f(LnU_c)$$

Avec

$$f(LnU_c) = c \cdot LnU_c^2 + d \cdot LnU_c^3$$

Le jeu de paramètres identifiés avec ces essais est le suivant :

$$a = 3000 \, MPa, b = 3459 \, MPa, c = 1371 \, MPa \, and \, d = 3878 \, MPa$$

Deux expressions quadratiques ont été choisies pour les potentiels qui décrivent les comportements des modes de déformation en cisaillement.

$$W_{ab}(\theta, \widetilde{LnU_{ab}}) = \frac{1}{2} G_{ab} \cdot \widetilde{LnU_{ab}}^2$$

$$W_\delta(\theta, \widetilde{\varepsilon_\delta}) = \frac{1}{2} G_\delta \cdot \widetilde{\varepsilon_\delta}^2$$

Pour identifier les deux paramètres G_{ab} et G_δ, un essai de compression diamétrale, avec « 3 rouleaux », a été conçu à l'échelle du toron. L'étude de la section de contact à l'aide de mesures par scanner 3D a été réalisée. Une identification inverse a été mise en place en simulant le même essai avec le logiciel Abaqus. L'objectif était de faire varier les deux paramètres jusqu'à obtenir la section de contact avec les propriétés géométriques les plus proches des mesures expérimentales (Figure 0.23). Finalement les deux paramètres obtenus sont les suivants : $G_{ab} = 0.06 \, MPa$ and $G_\delta = 2 \, MPa$.
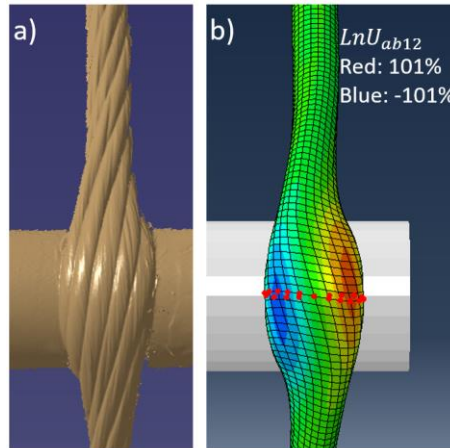

Figure 0.23 – Identification indirecte pour les comportements en cisaillement. Gauche : Mesure par scanner 3D de la section centrale au contact. Droite : Fin de la simulation du même essai et comparaison de la section centrale au contact.

Une première validation de l'identification de la loi a été réalisée en confrontant les résultats d'une simulation d'un essai de traction cyclique sur un toron à des résultats expérimentaux. La comparaison des déformations axiales et transverses a permis de montrer que les prédictions de la loi sont en accord avec l'expérimental. Par ailleurs, l'étude des champs de distributions des invariants de déformation, qui décrivent les déformations de l'amas de brins assemblés, sont en cohérence avec les descriptions de la mécanique des ensembles toronnés proposées dans la littérature (Leech, 2002).

Une première simulation d'un sous-cordage toronné avec 3 torons est réalisée. Cette simulation ne constitue pas une réelle validation car nous n'avons pas la base expérimentale adéquate. L'objectif est d'évaluer la faisabilité d'une simulation d'un essai cyclique de cette échelle avec la loi identifiée. La méthode pour réaliser ce calcul se divise en 5 étapes majeures représentées Figure 0.24.
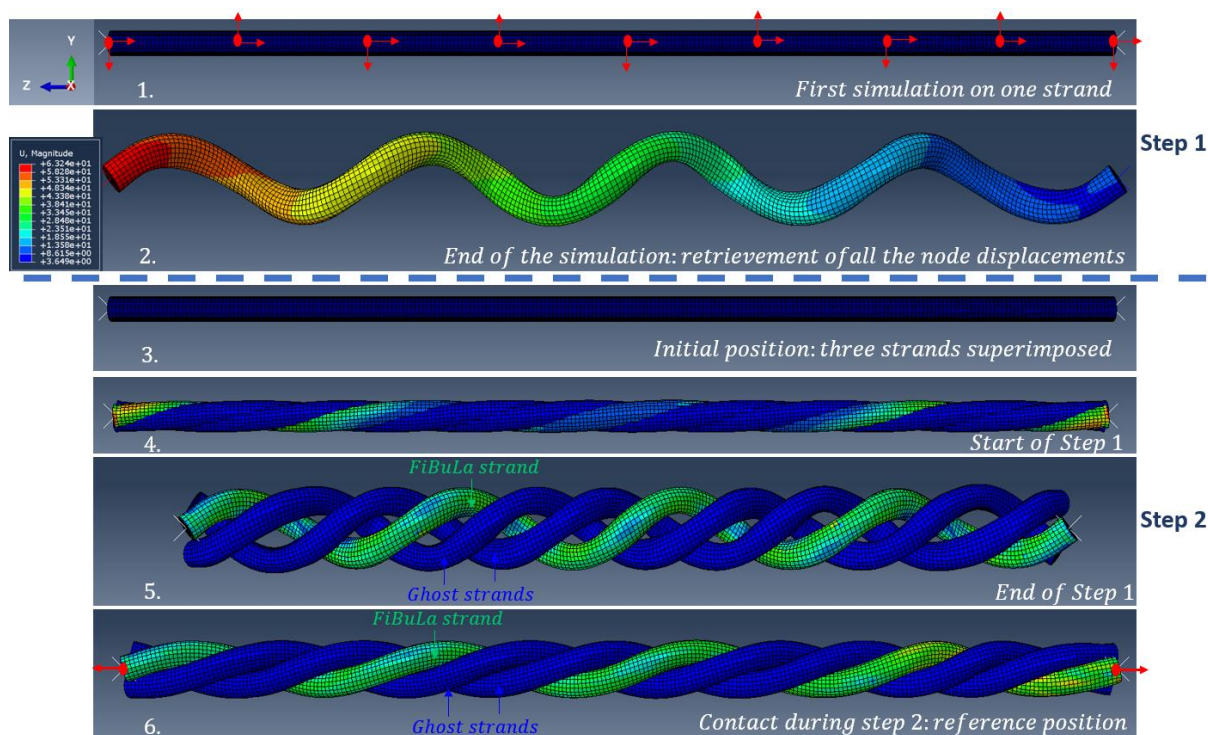
Figure 0.24 – Méthode utilisée pour simuler un sous-cordage constitué de trois torons qui permet de décrire l'orientation des brins assemblées dans les torons

Les résultats de la simulation sont divers et sont très prometteurs pour la compréhension de la réponse mécanique. Figure 6.36Figure 0.25 montre par exemple les champs de pression de contact obtenus au niveau d'un contact entre les torons. Cela montre que l'on peut obtenir cette information nécessaire à la quantification de la friction à l'échelle des torons. Figure 0.26 montre les directions des glissements des torons lors d'un cyclage. Cela montre que l'on peut avoir les informations sur les réarrangements lors d'un cycle.
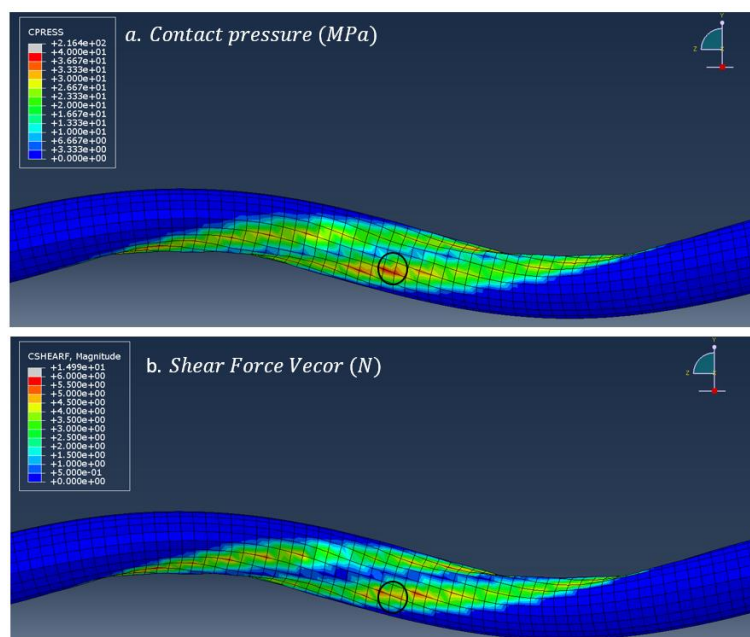

Figure 0.25 – Carte de couleurs d'un pas du sous-cordage pour un toron. a) Pression de contact [MPa]. b) Amplitude du vecteur de cisaillement [N]. Zones avec les valeurs maximales entourées en noire.
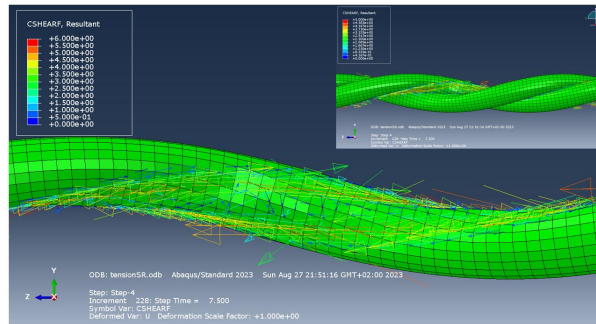
Figure 0.26: Carte de vecteur de l'amplitude de cisaillement [MPa]. En haut à droite: même carte de vecteurs avec un autre toron affiché

Finalement, les invariants qui décrivent les déformations à l'échelle des brins assemblés montrent aussi que l'on peut avoir des informations sur la répartition et les directions des cisaillements et des frictions à cette échelle.

Cette étude montre la faisabilité et les apports de cette approche de modélisation. Des travaux futurs ajouteront de la dissipation dans les modes de friction et de la viscoélasticité dans le mode de déformation en élongation des brins assemblés.

Ce travail a permis d'apporter des réponses dans plusieurs thématiques et d'approfondir les connaissances du comportement des cordages en polyamide 6. Néanmoins, ces travaux ont aussi mis en évidence des axes à approfondir dans le futur. Dans un premier temps, la loi constitutive proposée devra être identifiée et validée à l'échelle 1. Par ailleurs, l'expression de la viscosité est limitée à la prédiction de phénomènes aux temps courts et devra être modifiée pour prédire les comportements long termes. Le fluage long terme a été bien approfondi pour des gammes de chargement allant jusqu'à 39%MBL. Des études sur des chargements plus élevés seraient intéressantes pour compléter cette étude.

L'étude sur la fatigue a permis de mettre en évidence certains changements de constructions et d'arrangements aux différentes échelles. Une campagne d'essais avec suivi des déformations et pour des ratios de chargement variables permettraient d'étudier l'effet du ratio sur le fluage cyclique et l'évolution de l'hystérèse. De même, la réalisation d'essais de fatigue interrompus, suivis d'une mesure d'auto-échauffement et d'analyses par tomographie et MEB, permettrait d'investiguer la cinétique des mécanismes d'endommagement, mais aussi d'évaluer si ces endommagements modifient de façon significative la dissipation du sous-cordage. Cette étude a tout de même montré que les travaux sur l'échelle 4T de sous-cordage, adaptée aux laboratoires, reste pertinente et peut permettre d'obtenir des résultats conservatifs. La méthode d'auto-échauffement devra être encore approfondie et pourrait devenir un outil précieux pour qualifier la durée de vie en fatigue de différentes constructions de cordage pour des temps long et des coûts d'essais réduits.

Enfin, l'ajout d'un comportement visco-elasto-plastique et d'une dissipation dans le modèle méso-scopique devra être réalisé. Le modèle devra ensuite être validé à l'échelle du sous-cordage à l'aide d'une campagne expérimentale dédiée. Une étude du comportement de différentes constructions pourra être réalisée en faisant varier la construction simulée ainsi que les coefficients de frottements choisis à l'échelle des torons et des brins assemblés.

Titre : Caractérisation et modélisation de la fatigue et de la durabilité de ligne d'ancrages en polyamide pour les éoliennes offshore flottantes

Mots clés : polyamide 6, cordage toronné, modèle constitutif, fatigue, fluage, analyse méso-scopique, loi de comportement hyper-élastique.

Résumé : Grâce à une résistance équivalente à celle du polyester, et à une élongation à rupture plus importante (20%), les lignes en polyamide 6 se distinguent pour l'ancrage de flotteurs d'éoliennes offshore en eaux peu profondes (< 200 m). Un premier verrou réside dans la complexité de leur comportement mécanique non linéaire. Cette étude propose de valider et d'améliorer un modèle de comportement 1D composé de quatre éléments ressort-rochet-amortisseur qui permet une description précise du comportement d'une ligne en polyamide 6. Cette loi permettrait un premier dimensionnement des lignes d'ancrage. Ces lignes seront sous tension pendant toute leur durée de vie en service. Elles seront soumises à des sollicitations cycliques dues à la houle et aux mouvements de la plateforme. Un second verrou réside donc dans leur durabilité en fluage et en fatigue. Deux études expérimentales dédiées respectivement, à leur comportement en fluage long terme et à leur durée de vie en fatigue, sont donc présentées. Afin d'améliorer la compréhension des mécanismes de dégradation et de dissipation en fatigue, le développement d'une loi de comportement basée sur l'échelle mésoscopique d'un cordage et son implémentation dans un logiciel d'éléments finis sont présentés. Le modèle 3D final doit permettre une meilleure analyse du comportement non linéaire et, notamment, des phénomènes de dissipation dus aux frictions internes entre composants.

Title : Characterization and modelling of the fatigue and durability of polyamide mooring lines for offshore floating wind turbines

Keywords : polyamide 6, laid strand rope, constitutive model, fatigue, creep, mesoscopic analysis, hyper-elastic behaviour laws.

Abstract : Polyamide 6 fibre ropes are of interest for floating offshore wind turbines mooring lines thanks to their low stiffness, good tensile strength and high strain to failure (20%). The complex visco-elasto-plastic behaviour of polyamide 6 ropes is not fully understood. The development of a reliable model for the mechanical behaviour of polyamide 6 fibres is essential for permanent mooring applications. This study proposes to validate and improve a 1D constitutive law composed of four spring-ratchet and dashpot elements, that aims at completely describing the complex behavior of polyamide 6 fibre elements. The mooring lines will be under tension during all their service life and submitted to cyclic loading due to the waves and the movements of the plateform. Hence, they should show durability in terms of creep and fatigue life. Two experimental studies, respectively on long term creep behaviour and fatigue durability, are presented in this study. Also, to extend our understanding of the dissipation and degradation mechanisms in fatigue, the developement of a behaviour law based on the mesoscopic scale of a rope and its implementation in finite element analysis are presented. The final 3D model should allow a better understanding of the non linear behaviour and help to assess the dissipated energy due to the internal friction between components.